



Universiteit Gent  
Faculteit Ingenieurswetenschappen  
Vakgroep Informatietechnologie

## Label-free Silicon Photonics Biosensor Platform with Microring Resonators

Labelvrij fotonisch biosensorplatform met silicium-op-isolator  
microring resonatoren

---

Katrien De Vos



Proefschrift tot het bekomen van de graad van  
Doctor in de Ingenieurswetenschappen:  
Fotonica  
Academiejaar 2009-2010



**Promotoren:**

Prof. Dr. Ir. Peter Bienstman

Prof. Dr. Ir. Roel Baets

**Examencommissie:**

Prof. Dr. Ir. Daniël De Zutter (voorzitter)

Universiteit Gent, INTEC

Prof. Dr. Ir. Peter Bienstman (promotor)

Universiteit Gent, INTEC

Prof. Dr. Ir. Selim Ünlü

Boston University (VS)

Prof. Dr. Ir. Jan Vanfleteren

Universiteit Gent, ELIS

Prof. Dr. Ir. Roel Baets (promotor)

Universiteit Gent, INTEC

Dr. Ir. Wim Bogaerts (secretaris)

Universiteit Gent, INTEC

Prof. Dr. Peter Dubrueel

Universiteit Gent, Vakgroep Organische Chemie

Dr. Ir. Paul Jacobs

Zelfstandig expert

Universiteit Gent  
Faculteit Ingenieurswetenschappen

Vakgroep Informatietechnologie  
Sint-Pietersnieuwstraat 41, B-9000 Gent, België

Tel.: +32-9-264.33.39

Fax.: +32-9-264.35.93

Dit werk kwam tot stand in het kader van een specialisatiebeurs van het IWT-Vlaanderen (Instituut voor de aanmoediging van Innovatie door Wetenschap en Technologie in Vlaanderen). De auteur dankt epixfab ([www.epixfab.eu](http://www.epixfab.eu)) voor fabricage van de chips. Er werden fondsen verkregen via het UGent GOA project B/05958/01 en IAP6-10 Photonics@be.



PhD.Final  
 PhD.Final1  
 Phd.Final1.2  
 Phd.AbsolutelyFinal

*THX.*

Prof. Peter Bienstman en Prof. Roel Baets

**Input, orientatie & advies  
 Bos door de bomen  
 Vertrouwen**

Alle collega's en oud-collega's\*

**Hoogtechnologische omgeving  
 Enthousiasme  
 Nooit teveel gevraagd  
 Intens luistermateriaal**

Het bioteam voor de sensorbesprekingen. Tom Claes in  
 het bijzonder, om me vooruit te stuwten door me op de  
 hielen te zitten

Wouter, Peter, Stijn en Marie en de senseomomenten

Yannick voor het programmeerwerk, Cristina, Jeroen,  
 Michiel en Elena als ijverige thesisstudenten

\*enkel om stylistische  
 redenen als groep  
 beschouwd, want elk apart  
 heel bijzonder

Steven, Liesbet, Jeroen, Luc, Ilse, Ilse, Karien,  
 Bernadette, Kristien, Hendrik

Wim Bogaerts, voor 878 mails

Irene Bartolozzi, Stepan Popelka, Jordi Girones Molera  
 and Prof. Em. Etienne Schacht for a fruitful collaboration

BU colleagues and Prof. Selim Ünlü

**Valuable advise  
 Critical reflections  
 Great time**

Mama en papa

Om er te zijn als het nodig was  
 En er niet te zijn als het niet nodig was

Stefanie en Laurens

Sarah

Om alle stukjes te doen passen  
 en meer



Katrien De Vos, Gent, 2010



# Table of Contents

<b>Nederlandse samenvatting</b>	<b>ix</b>
<b>English summary</b>	<b>xvii</b>
<b>1 Introduction</b>	<b>1-1</b>
1.1 Affinity biosensors . . . . .	1-1
1.2 Application areas . . . . .	1-5
1.2.1 Drug discovery . . . . .	1-6
1.2.2 Point-of-care diagnostics . . . . .	1-6
1.2.3 Environmental control and food testing . . . . .	1-7
1.3 Silicon-on-insulator microring biosensor platform . . . . .	1-7
1.3.1 Towards integrated optical biosensors . . . . .	1-7
1.3.2 Working principle . . . . .	1-9
1.3.3 Silicon photonics for biotechnology . . . . .	1-9
1.4 Outline of the manuscript . . . . .	1-13
1.5 Competing technologies . . . . .	1-14
1.5.1 Optical biosensors . . . . .	1-15
1.5.2 Mechanical biosensors . . . . .	1-19
1.5.3 Electrical biosensors . . . . .	1-21
1.6 Conclusion . . . . .	1-22
References . . . . .	1-24
<b>2 Evanescent field sensing with SOI microring resonators</b>	<b>2-1</b>
2.1 SOI microring resonators . . . . .	2-2
2.1.1 Photonic waveguides . . . . .	2-3
2.1.2 Coupling section . . . . .	2-5
2.1.3 Spectral characteristics . . . . .	2-9
2.1.4 Performance of SOI ring resonators . . . . .	2-13
2.2 Sensitivity . . . . .	2-19
2.2.1 Resonance wavelength shift . . . . .	2-21
2.2.2 Optical model for biomolecular interaction . . . . .	2-22
2.2.3 SOI ring resonator sensitivity . . . . .	2-24
2.3 Measurement resolution . . . . .	2-25
2.3.1 Simulation method . . . . .	2-26
2.3.2 Resolution versus instrumentation . . . . .	2-27

---

2.3.3	Resolution versus resonance shape . . . . .	2-32
2.3.4	Add-drop or all-pass resonator? . . . . .	2-33
2.3.5	Conclusion . . . . .	2-37
2.4	Detection limit . . . . .	2-38
2.5	Other sensor configurations . . . . .	2-39
2.6	Conclusion . . . . .	2-43
	References . . . . .	2-45
<b>3</b>	<b>Dual polarization ring resonator sensor</b>	<b>3-1</b>
3.1	Introduction . . . . .	3-1
3.2	Measurement principle . . . . .	3-3
3.3	Design considerations . . . . .	3-3
3.3.1	Sensor quality defined by detection limit and accuracy . . . . .	3-3
3.3.2	Waveguide design . . . . .	3-5
3.4	Implementation: SOI ring resonator with polarization duplexer . . . . .	3-9
3.5	Conclusion . . . . .	3-12
	References . . . . .	3-14
<b>4</b>	<b>(Bio)Chemistry for engineers</b>	<b>4-1</b>
4.1	Biomolecular interactions at surfaces . . . . .	4-2
4.1.1	General model . . . . .	4-2
4.1.2	Mass transport to the surface . . . . .	4-4
4.1.3	Bulk refractive index effect . . . . .	4-5
4.1.4	Molecular interactions studied with label-free biosensors . . . . .	4-7
4.2	Surface characterization techniques . . . . .	4-7
4.3	Protein coupling to a silicon surface . . . . .	4-10
4.3.1	One-step modification: reaction with aminosilane . . . . .	4-11
4.3.2	Two-step modification: reaction with poly(ethylene glycol) . . . . .	4-13
4.3.3	From biotin to other proteins . . . . .	4-18
4.4	Conclusion . . . . .	4-22
	References . . . . .	4-24
<b>5</b>	<b>Microfluidics</b>	<b>5-1</b>
5.1	Basic concepts . . . . .	5-2
5.1.1	Introduction . . . . .	5-2
5.1.2	Laminarity . . . . .	5-4
5.1.3	Modeling . . . . .	5-4
5.1.4	Lab-on-a-chip . . . . .	5-6
5.1.5	Time to accumulate a threshold number of molecules . . . . .	5-7
5.2	Fabrication . . . . .	5-9
5.2.1	Excimer laser photoablation of PMMA . . . . .	5-10
5.2.2	Casting of PDMS . . . . .	5-13
5.3	Integration with SOI chips . . . . .	5-14
5.3.1	Direct bonding using plasma activation of the surface . . . . .	5-15
5.3.2	Adhesive bonding with stamp-and-stick method . . . . .	5-15

---

5.4	Conclusion . . . . .	5-16
	References . . . . .	5-18
<b>6</b>	<b>Optical read-out</b>	<b>6-1</b>
6.1	Signal stability and temperature dependence . . . . .	6-1
6.2	Sources and detectors . . . . .	6-2
6.3	Grating couplers . . . . .	6-3
6.4	Measurement setups: fiber-based, camera-based . . . . .	6-5
6.4.1	Fiber-based setup . . . . .	6-5
6.4.2	Infra-red camera setup with fiber illumination . . . . .	6-5
6.4.3	Infra-red camera setup with flood illumination . . . . .	6-8
6.5	Noise . . . . .	6-12
6.6	Conclusion . . . . .	6-13
	References . . . . .	6-16
<b>7</b>	<b>Biosensor measurement results</b>	<b>7-1</b>
7.1	Introduction . . . . .	7-1
7.2	Bulk RI sensing . . . . .	7-2
7.3	Layer thickness sensing . . . . .	7-2
7.4	Avidin-biotin characterization . . . . .	7-4
7.4.1	One-step modification . . . . .	7-4
7.4.2	Two-step modification . . . . .	7-5
7.5	Protein detection and multiplexing . . . . .	7-8
7.5.1	SOI biosensor platform for multiplexed protein detection . . . . .	7-8
7.5.2	Chemistry optimization steps . . . . .	7-11
7.5.3	Multiplexing . . . . .	7-13
7.6	Conclusion . . . . .	7-14
	References . . . . .	7-18
<b>8</b>	<b>Perspectives</b>	<b>8-1</b>
8.1	Towards lower detection limit, higher level of integration and reduced cost . . . . .	8-1
8.2	DNA hybridization . . . . .	8-3
8.2.1	DNA functionalization . . . . .	8-3
8.2.2	DNA preliminary results . . . . .	8-4
8.3	Fiber probe sensor . . . . .	8-5
8.3.1	Motivation . . . . .	8-5
8.3.2	Implementation . . . . .	8-7
8.3.3	Fabrication . . . . .	8-7
8.4	Conclusion . . . . .	8-9
	References . . . . .	8-10
<b>9</b>	<b>Conclusions</b>	<b>9-1</b>

---

<b>A</b>	<b>Microfluidics processing</b>	<b>A-1</b>
A.1	Introduction . . . . .	A-1
A.2	PDMS microfluidics fabrication . . . . .	A-1
A.3	Surface preparation . . . . .	A-2
A.4	Bonding . . . . .	A-3
	. . . . .	A-1
<b>B</b>	<b>Publications</b>	<b>B-1</b>
B.1	Patent applications . . . . .	B-1
B.2	International Journals . . . . .	B-1
B.3	International Conferences . . . . .	B-2
B.4	National Conferences . . . . .	B-4

# List of Acronyms

BSA	Bovine Serum Albumin
DSC	Disuccinimidyl Carbonate
DIW	De-ionized water
Hu-IgG	Human Immunoglobuline
HSA	Human Serum Albumin
MZI	Mach-Zehnder interferometer
OSA	Optical Spectrum Analyzer
PBS	Phosphate Buffer Solution
PDMS	Poly(dimethylsiloxane)
PEG	Poly(ethylene glycol)
PMMA	Poly(methyl methacrylate)
RIU	Refractive Index Units
SAM	Self-Assembled Monolayer
SEM	Scanning Electron Microscope
SOI	Silicon-On-Insulator
WGM	Whispering Gallery Mode
XPS	X-ray Photoelectron Spectroscopy



# Nederlandse samenvatting

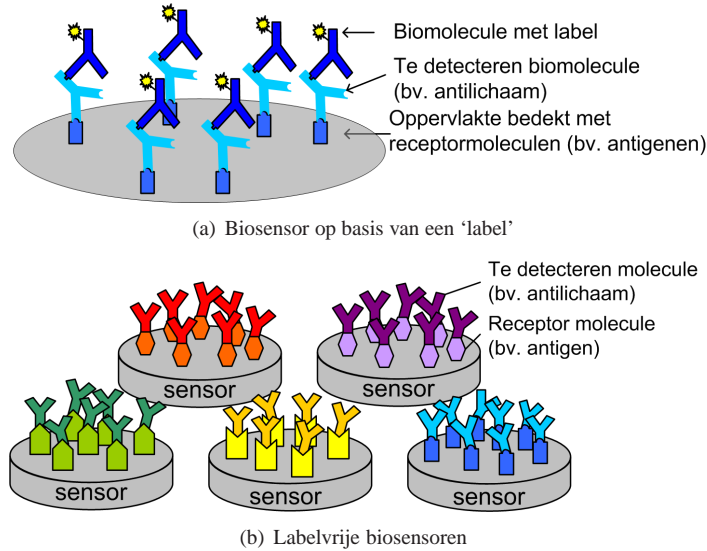
## Biosensoren en silicium fotonica

Tijdens dit doctoraatsproject bestudeerden we wat er gebeurt als twee veelbelovende, maar heel verschillende onderzoeksgebieden samengebracht worden.

Fotonica is het vakgebied dat 'licht' bestudeert, in veel vormen en toepassingen. Licht kan uit verschillende kleuren of golflengtes bestaan. Het kan op verschillende manieren geleid worden, bijvoorbeeld door een opeenvolging van spiegels of door een glasvezel. Het kan gemanipuleerd worden; versterkt, verzwakt, vertraagd, versneld... In het vakgebied 'silicium fotonica' wordt licht geleid en gemanipuleerd in kleine silicium chips, zoals we kennen uit de elektronica.

Biosensoren worden gebruikt in de biotechnologie. Ze dienen voor het bestuderen van interacties tussen moleculen en voor het detecteren van moleculen in lichaamsvloeistoffen zoals bloed en serum. Dit is niet triviaal, omdat biomoleculen erg klein zijn en in zeer lage concentraties voorkomen (pg/ml tot ng/ml). Bovendien komen ze voor in vloeistoffen die ook duizenden andere moleculen kunnen bevatten in veel hogere concentraties. Biologisch moleculair onderzoek steunt vandaag voornamelijk op het detecteren van een *label* dat vastgehecht wordt aan de molecule, het virus of de cel die men wil bestuderen. Dit is geïllustreerd in Fig. 1(a). Fluorescente en radioactieve labels, alsook nanodeeltjes, zijn courant gebruikte indicatoren omdat ze gemakkelijk gedetecteerd kunnen worden en dus indirect de aanwezigheid van de gezochte biomolecule kunnen aantonen. Hoewel gelabelde methodes sterk ingeburgerd en heel gevoelig zijn, vertonen ze enkele grote nadelen. Wanneer een biomolecule aan een label bindt, kan de vorm en de functionaliteit ervan beïnvloed worden. Het labelen zelf is duur, tijdrovend en moet in een gecontroleerde omgeving gebeuren. Bovendien is het quasi onmogelijk om een kwantitatieve meting uit te voeren, of om moleculaire interacties in de tijd te volgen.

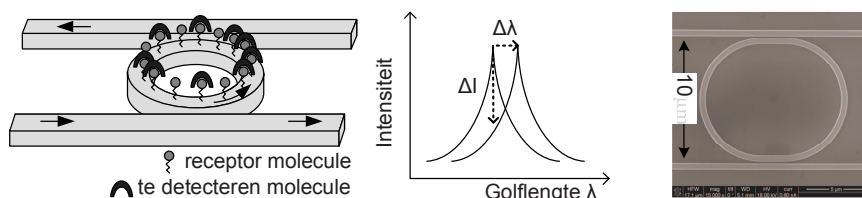
Om deze redenen ontstond het laatste decennia een trend naar de ontwikkeling van *labelvrije* detectiemethodes. Zoals illustratie 1(b) toont, bestaat een labelvrije biosensor uit een sensor die de aanwezigheid van een molecule direct kan detecteren, zonder tussenkomst van een label. Dit gebeurt dan op basis van de fysieke eigenschappen van die molecule. Optische biosensoren bijvoorbeeld, sturen licht door de biomoleculen waarbij deze het licht 'vertragen'. De biosensor zet deze vertraging om in een uitleesbaar signaal. In dit werk bestuderen we een affiniteitgebaseerde biosensor. Aan het oppervlak van de sensor worden receptoren gehecht.



**Figuur 1:** Illustratie van biosensoren op basis van 'labels' en 'labelvrije' biosensoren.

Deze vertonen een hoge affiniteit voor de biomoleculen die men wil detecteren en zullen er dus een binding mee aangaan. Dit zal resulteren in een signaal aan de uitgang van de sensor. Op die manier kan de binding gevolgd worden in de tijd en bij het plaatsen van verschillende sensoren in een matrix kunnen verschillende biomoleculen tegelijk worden gedetecteerd. Labelvrije biosensoren kunnen voor een doorbraak zorgen in verschillende toepassingsgebieden, o.m. voor de ontwikkeling van geneesmiddelen, omgeving- of voedselcontrole en voor draagbare toestellen voor ziektediagnose, zogenaamde point-of-care systemen.

Labelvrije biosensoren die vandaag verkrijgbaar zijn, bestaan uit losstaande optische componenten die het licht geleiden. Hierdoor zijn ze groot en zwaar en moeten ze mechanisch stabiel, dus in labomgevingen, geplaatst worden. Deze toestellen kunnen niet uitgebreid worden naar systemen die grote hoeveelheden moleculen simultaan kunnen detecteren, zonder aan gevoeligheid of kostprijs in te boeten. Daarom is er de laatste jaren onderzoek naar het integreren van labelvrije biosensoren op kleine chips, bijvoorbeeld fotonische chips. Fotonische geïntegreerde circuits bestaan uit geminiaturiseerde componenten die licht kunnen geleiden, opslaan of manipuleren. Alle componenten van de chip worden in een stap gefabriceerd en zijn automatisch goed gepositioneerd ten opzichte van elkaar. Vermenigvuldigen van de detectie kan eenvoudigweg gebeuren door meerdere sensoren in een matrix te plaatsen en ze met de bron en de detector te verbinden door middel van golfgeleiders. Maar, nog belangrijker, bieden deze chips de mogelijkheid om verder geïntegreerd te worden met elektronische of biologische functies. Uiteindelijk zullen alle labostappen, nodig ter bestudering van



**Figuur 2:** Werkingsprincipe van een ringresonator biosensor.

een bloed- of serumstaal, door één chip uitgevoerd worden. Dit is het zogenaamde *laboratorium-op-een-chip* concept.

Het werkingsprincipe van de geïntegreerde biosensor die in dit werk is bestudeerd, is geïllustreerd in Fig. 2. In een ringresonator kunnen optische golven circuleren als hun golflengte voldoet aan de volgende vergelijking:

$$\lambda_{res} = \frac{Ln_{eff}}{m}$$

waarbij  $L$  de omtrek van de ring is,  $m$  een geheel getal en  $n_{eff}$  de effectieve brekingsindex van de circulerende mode. Als de brekingsindex aan het oppervlak van de ring verandert door het binden van een biomolecule, zal de resonantiegolflengte verschuiven. Deze verschuiving is een kwantitatieve maat voor het aantal moleculaire bindingen in de omgeving van de ring en kan dus gebruikt worden als uitgangssignaal van de biosensor.

Silicium-op-isolator als materiaalplatform voor geïntegreerde fotonische circuits biedt verschillende voordelen. Door het hoge brekingsindexcontrast van het materiaal, kan licht opgesloten worden in structuren met dimensies kleiner dan een micrometer. Licht zal geleid worden doorheen heel kleine bochten, wat leidt tot ringresonatoren met potentieel heel kleine oppervlaktes (orde  $30 \mu m^2$ ). Er zijn slechts kleine hoeveelheden biomoleculen nodig om deze oppervlakte volledig te bedekken, terwijl de verschuiving van de golflengte niet schaalt met deze oppervlakte. Bijgevolg kunnen potentieel heel kleine hoeveelheden biomoleculen gedetecteerd worden. Een vierkante millimeter op de chip kan meer dan 1,000 sensoren bevatten. Als elke sensor met receptoren van een verschillende soort is bedekt, kan een enorm aantal verschillende biomoleculen, bijvoorbeeld antilichamen ter bepaling van een bepaalde aandoening, tegelijk worden gedetecteerd. Een ander belangrijk voordeel van silicium als fotonisch materiaal platform, is dat het kan gestructureerd worden met bestaande apparatuur die ontwikkeld werd voor fabricage van CMOS componenten, meer bepaald 193 nm optische projectielithografie en droog plasma-etsen. Dit maakt massaproductie mogelijk, wat leidt tot een enorme kostenreductie per chip zodat de chips als wegwerpproducten kunnen geleverd worden.

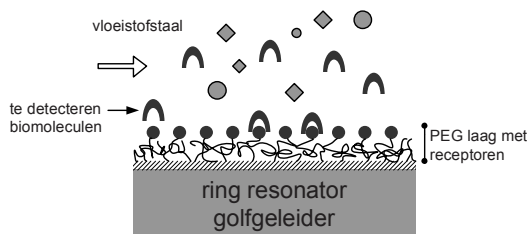
## Theoretische studie

We maakten een theoretische analyse van de intrinsieke capaciteiten van SOI ring-resonator biosensoren, waarbij drie criteria werden onderzocht: de meetresolutie, de gevoeligheid en de detectielimiet. De meetresolutie komt overeen met de kleinste golflengteverschuiving die met voldoende nauwkeurigheid kan gemeten worden. Deze hangt af van de vorm van de resonantiecurve en van de eigenschappen van de meettoestellen (zoals golflengtestap en ruis). De meetresolutie kan veel kleiner zijn dan de breedte van de resonantiepiek of -dip, door gebruik van een gepast fittingalgoritme. Het reduceren van de ruis en het vergroten van de Q-factor van de resonantie zijn de belangrijkste manieren om kleine waarden voor de meetresolutie te verkrijgen. De Q-factor, die een maat is voor de breedte van de resonantie, is beperkt door de propagatieverliezen in de ring, veroorzaakt doordat water licht met golflengtes rond 1550 nm sterk absorbeert. We berekenden een meetresolutie van 0.67 pm voor de SOI ringresonatoren. De gevoeligheid van de sensor weerspiegelt de grote van de golflengteverschuiving wanneer veranderingen aan het oppervlak plaatsvinden. We bestudeerden deze factor voor verschillende omgevingsinvloeden, voor verschillende afmetingen van de golfgeleider en voor verschillende polarisaties van het licht. De detectielimiet (DL) wordt dan bepaald uit de verhouding van de meetresolutie en de gevoeligheid. We berekenden de detectielimiet voor homogene veranderingen van de hele sensoromgeving ( $DL=10^{-6}$  RIU), voor moleculaire oppervlakedichtheid en voor moleculaire massa. Het SOI sensorsysteem kan een oppervlakedichtheid van  $5.02 \text{ pg/mm}^2$  detecteren, dit komt overeen met ongeveer 158 ag moleculen gebonden aan het ringoppervlak.

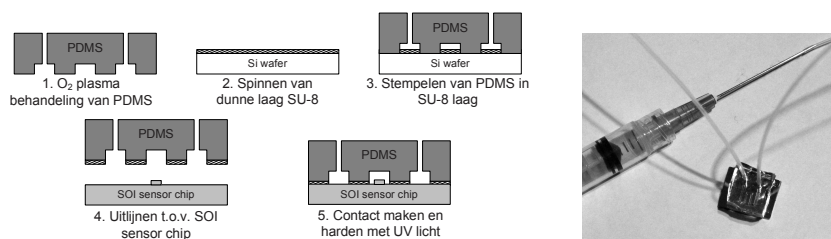
## Biosensor platform: chemie, fluidica en uitlezing

Om de theoretische resultaten experimenteel te bewijzen, werd een biosensor platform uitgebouwd, bestaande uit de fotonische chip zelf, bindingschemie, een vloeistofstelsel en uitleesapparatuur.

De gevoeligheid van de biosensor is afhankelijk van de dichtheid van de receptoren op het oppervlak. De bindingschemie die de receptoren aan het siliciumoppervlak van de golfgeleiders moet koppelen is een cruciaal onderdeel van de biosensor. Ze moet ervoor zorgen dat receptoren efficiënt worden gebonden, en ze moet tegelijk interactie van andere moleculen in het vloeistofstaal met het oppervlak tegengaan (zogenaamde niet-specifieke interactie). De chemische laag moet stabiel en homogeen zijn, en mag het transport van de moleculen naar de oppervlakte niet in de weg staan. Courant gebruikte bindingschemie bestaat erin de siliciumgolfgeleiders te bedekken met een silaanlaag met een functionele groep aan het uiteinde. We onderzochten deze methode, maar de silaanlagen bleken onvoldoende immuun tegen niet-specifieke interactie. Een betere methode werd ontwikkeld. Die bestond erin een extra polymeerlaagje van enkele nanometers dik aan te brengen. Twee heterobifunctionele poly(ethylene glycol) (PEG) lagen met verschillende functionele groepen werden onderzocht:  $\alpha$ -sulfanyl- $\omega$ -carboxy



**Figuur 3:** Golfgeleider met PEG laag voor binding van receptor moleculen en voor het verhinderen van niet-specifieke interacties.

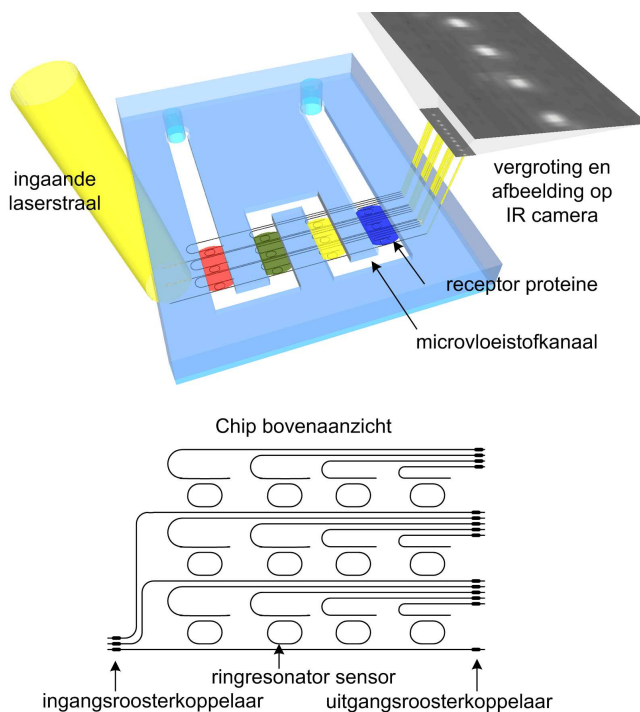


**Figuur 4:** Stempelprocedure voor het verpakken van SOI fotonische chips met PDMS microvloeistofkanalen.

PEG (HS-PEG-COOH) en diamino-PEG( $\text{H}_2\text{N}$ -PEG-NH-Boc). Dit wordt schematisch weergegeven in Fig. 3. De polymeerlagen verlaagden de niet-specifieke interactie in hoge mate zodat het systeem nu moleculen kan detecteren in een lichaamsvloeistof met een veel verschillende componenten.

De vloeistoffen moeten met gelijke snelheid over alle sensoren op de chip worden geleid. Hiervoor gebruikten we vloeistofkanalen met dimensies van enkele tientallen micrometers, zogenaamde microfluidische kanalen. Alvorens de kanalen op de chip aan te brengen, zullen de verschillende receptormoleculen op de sensoren worden aangebracht. Tijdens het binden van de kanalen moet er dus voor gezorgd worden dat de receptormoleculen niet beschadigd geraken door agressieve oppervlaktebehandelingen, hoge temperaturen of lijm. Om deze redenen gebruiken we een stempelprocedure om de chip te verpakken met de kanalen. Deze procedure is geïllustreerd in Fig. 4, er wordt ook een foto van het afgewerkt geheel getoond.

Na de chemische behandeling en het verpakken van de chip met microvloeistofkanalen, kan de detectie gebeuren en moet de chip uitgelezen worden. We maken gebruik van geïntegreerde roosterkoppelaars om het licht van de horizontale golfgeleider naar de verticale richting te koppelen, waar het verder geleid wordt door optische vezels of in de vrije ruimte. In tegenstelling tot commerciële biosensoren, is het uitleessysteem hier volledig ontkoppeld van het sensormechanisme en kunnen beide afzonderlijk geoptimaliseerd worden. De tolerantie op de posities van de componenten is veel groter wat belangrijk is voor draagbare toepassingen. We installeerden en bestudeerden een uitleessysteem met simultane belichting van ver-

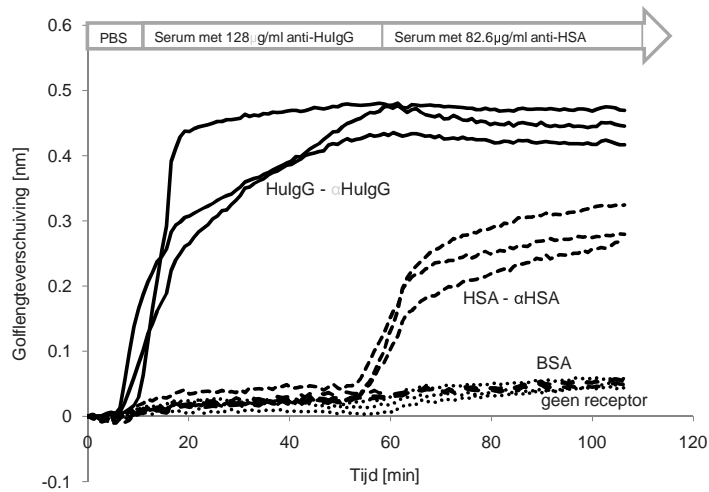


**Figuur 5:** Illustratie van een verpakte SOI sensor chip met een matrix van sensoren in de meetopstelling.

schillende ingangsgolfgeleiders en een infrarood camera voor simultane uitlezing van verschillende uitgangsgolfgeleiders. Dit systeem heeft een laag ruisniveau en biedt de mogelijkheid tot het uitlezen van meer dan 1,000 sensoren tegelijkertijd. Een illustratie is weergegeven in Fig. 5.

## Experimentele resultaten

Voor het testen van het SOI biosensor platform, gebruikten we in eerste instantie avidine en biotine. Dit zijn twee stabiele biomoleculen die een hoge affiniteit voor elkaar vertonen en daarom als modelmoleculen worden gebruikt voor de karakterisering van het systeem. De detectielimiet bleek ongeveer 3.8 ng/ml avidine concentratie te bedragen. Voor simultane detectie van meerdere moleculen, werd een matrix van ringen bedekt met een homogene polymeerlaag. Daarop werden vervolgens drie verschillende receptormoleculen aangebracht (ook aangeduid op Fig. 10): Hu-IgG, HSA en BSA. De vierde kolom van de matrix werd vrijgelaten en als referentie gebruikt. Fig. 6 toont het resultaat van een karakterisatie-experiment. Wanneer serums met verschillende antilichamen over de chip werden gevloeid, kunnen deze antilichamen worden gedetecteerd aan de hand van het sig-



**Figuur 6:** Experimenteel resultaat met drie verschillende receptoren (Hu-IgG, HSA en BSA) op een matrix van ring resonatoren. Twee vloeistoffen met de complementaire biomoleculen (anti-Hu-IgG en anti-HSA) werden over de chip geleid en de desbetreffende ringresonatoren vertonen een duidelijk signaal aan de uitgang wanneer binding optreedt.

naal van de overeenstemmende ringresonatoren.

Nu een basis biosensor platform met SOI ringresonatoren is uitgebouwd en een theoretische studie werd voltooid, kan het systeem verder worden geoptimaliseerd om de detectielimiet te verlagen, bijvoorbeeld met andere componenten of betere uitleesapparatuur. Verdere integratie met microvloeistofsystemen en elektronica kan uiteindelijk leiden tot SOI fotonische wegwerpbiochips, bijvoorbeeld voor gebruik in draagbare toestellen voor ziektediagnose.



# English summary

## **Silicon photonics and biosensors**

Biosensors provide the ability to study interactions between biomolecules and to detect analytes from body fluids, manufacturing processes or environmental samples. The development of this technique is challenging, because biomolecules are extremely small and sometimes present within a sample at very low concentrations (pg/ml to fg/ml) that simultaneously contains thousands of other molecules at much higher concentrations. Biological research has historically relied upon attachment of a *label* to one or more of the molecules, viruses or cell being studied. Commonly used labels are fluorescent dyes, radioactive molecules or nanoparticles. These are easily measurable and serve to indicate the presence of the analyte to which they have been attached indirectly. While labeled detection methods can be sensitive down to a single molecule, labels can structurally and functionally alter the assay and the labeling process is labor intensive and costly. Quantification is difficult since the bias label intensity level is dependent on all working conditions. Moreover, a labeled assay can only be performed in an 'end-point' fashion so that no kinetic information on the biomolecular interaction can be obtained. Due to these considerations, there has been a drive to reduce assay cost and complexity while providing more quantitative information with high throughput. *Label-free* biosensors measure the presence of a biomolecule directly through some physical property. The type of label-free biosensor we studied is an affinity-based biosensor: a so-called 'receptor' or 'ligand' is attached to the surface of a sensor that responds to the affinity interaction of the receptor with an analyte. The formation of complexes can thus be monitored continuously and many interactions can be followed simultaneously. Emerging applications include point-of-care diagnostics, drug development, environmental control and food monitoring. Point-of-care systems are designed to process clinical samples for a number of different types of biomarkers and to work in a variety of settings.

Optical label-free biosensors make use of the fact that biological molecules reduce the propagation velocity of electromagnetic fields that pass through them, which is translated into a quantifiable signal proportional to the amount of biological material present on the sensor surface. Commercially available optical label-free biosensors exist mainly in free-space beam sensing configurations, where discrete components such as mirrors and lenses are used. Coupling light from one component to another in free-space setups typically requires accurate and therefore

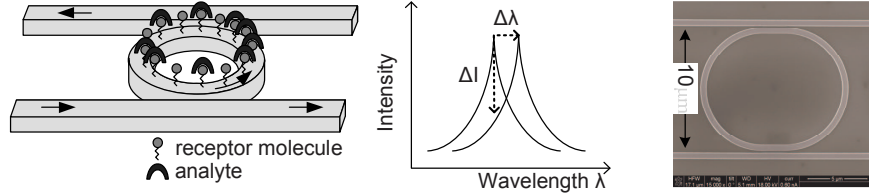


**Figure 7:** Basic principle of a ring resonator biosensor.

time consuming and expensive mechanical alignment. For that reason portability of the equipment is low and its use is limited to dedicated lab or clinical environments. Expanding the optical sensing principle to multiplexed sensing is not straightforward with these tools, as the complexity and cost of the optical components of the read-out equipment scales with the degree of multiplexing. Over the past decade, there has been a vast research effort in integration of optical label-free biosensors on photonic chips. Photonic integrated circuits (PIC) consist of optical components, such as light sources, detectors, or sensors, that are integrated on one single chip. The integrated approach allows for a significant simplification of the optical system, since the light routing and processing can be accomplished by a waveguide circuit that is fabricated by a collective lithography process. The sensing part is fully decoupled from the optical read-out part and can thus be optimized separately. Extension to multiplexed sensor arrays is simply attained by arraying one sensor next to the other and connecting them with source and detector through integrated waveguides. Most importantly, additional levels of integration with electronic and biologic functions are possible. The ultimate goal is to integrate several laboratory functions in a single chip, a so-called lab-on-a-chip.

The working principle of the integrated optical label-free biosensor we studied is illustrated in Fig. 7. A ring resonator supports circulating waveguide modes with resonant wavelengths that are related to the effective optical path length within the resonator:

$$\lambda_{res} = \frac{Ln_{eff}}{m}$$

where  $L$  is the circumference of the ring,  $m$  is an integer and  $n_{eff}$  the effective refractive index of the circulating mode. When the refractive index near the ring resonator surface is modified due to the capture of target molecules on the surface,  $n_{eff}$  will change which in turn leads to a shift in the resonance wavelength  $\lambda_{res}$ . This wavelength shift is a quantitative measure for the number of binding events near the surface.

Silicon-on-insulator (SOI) as a material platform for on-chip biosensors offers several advantages. SOI waveguides confine light within sub-micron structures because of the high omni-directional index contrast. This results in very sharp bending structures and in micron-scale ring resonators, which is of importance when detecting very small amounts of molecules. The resonance wavelength shift does not scale with the size of the cavity, hence the smaller the cavity, the less

molecules are needed to cover its entire surface, while the response does not decrease with decreasing surface area. Moreover, not only the small surface area, but also the high mode confinement itself is beneficial for highly sensitive detection. Due to the high integration density of structures in SOI, one square millimeter on a photonics chip can contain over 1,000 biosensors. When each of them is covered with different receptor molecules, large sets of biomarkers can be screened simultaneously within very small sample volumes. Last but not least, using silicon as a photonics platform offers the advantage of reuse of extensively developed CMOS processing technology, in particular 193 nm optical projection lithography and dry etching. This allows for mass production and economics of scale. For point-of-care diagnostics the availability of cheap disposables is a prior requirement, since reuse of the sensor chip is excluded. Also in drug discovery where immense numbers of test assays are run, cheap disposables can increase efficiency and keep down the development costs of the drugs.

## Theoretical study

We performed a theoretical study of the intrinsic biosensing capacities of SOI ring resonators. Three important characteristics were investigated: the measurement resolution, the sensitivity and the detection limit. The measurement resolution corresponds to the minimum wavelength shift that can be accurately measured. It depends on the shape of the resonance spectrum and on equipment factors such as wavelength step and noise. It can be much smaller than the light source line width and the resonance peak width by using a peak fitting algorithm. Suppressing intensity noise and increasing the Q-factor are important to obtain a good measurement resolution. The Q-factor however, is limited by propagation losses in the ring mainly caused by the large absorption of water at 1550 nm wavelength. The measurement resolution of our devices was found to be 0.67 pm on average. The sensitivity of a biosensor reflects its response to environmental changes. It was studied for various waveguide dimensions and various types of environmental changes (bulk refractive index changes and molecular layer changes that can correspond to a thickness or a density increase). The detection limit of a biosensor includes the effect of the two other parameters: it is the ratio of the measurement resolution to the sensitivity. We calculated the detection limit of SOI biosensors for bulk index sensing, layer detection, surface coverage and absolute mass and find the current system being capable of detecting a surface coverage of 5.02 pg/mm<sup>2</sup>, corresponding to a total molecular mass of about 158 ag on the ring surface.

## Platform: chemistry, fluidics and read-out

For experimental verification of the theory, we built a biosensor platform consisting of the photonics chip itself, coupling chemistry, a fluidic sample delivery system and read-out equipment. All parts were developed with a focus on low

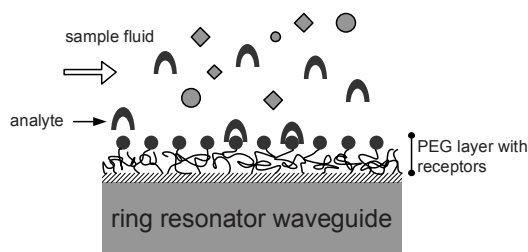


**Figure 8:** Waveguide with PEG coating for receptor binding and reduction of non-specific interaction with other molecules in the sample.

detection limit and high throughput biosensing.

The intrinsic sensitivity of the biosensor is reduced when the density of the receptor molecules at its surface is not optimal. Thus, the properties of a biosensor critically depend on the quality of the receptor layer. The coupling chemistry has to allow for immobilization of receptor molecules and at the same time effectively block non-specific interactions with the macromolecular components of the sample. It must be stable, homogeneous and must not hinder transport of the chemical or biological compounds to the transducer surface. Silanization of a silicon oxide layer on top of the silicon waveguide is a straightforward coupling procedure for dense receptor coverage. However, silanes perform poorly in terms of non-specific interactions with proteins in the analyte solution. To reduce the non-specific interaction, we coupled thin poly(ethylene glycol) (PEG) layers to the silane coating. We investigated two heterobifunctional PEG layers with different reactive groups:  $\alpha$ -sulfanyl- $\omega$ -carboxy PEG (HS-PEG-COOH) and monoprotected diamino-PEG (H<sub>2</sub>N-PEG-NH-Boc). This is schematically shown in Fig. 8. The PEG layers are a few nanometers thick and show good homogeneity. We will present various characterization experiments to verify the effectiveness of the coatings towards non-specific interaction reduction.

In order to deliver a sample liquid to an array of ring resonators, it is important that the flow characteristics are equal over the entire chip. The need for compact fluidics in which the flow velocity is similar at all locations on the chip implies the use of channels with dimensions in the order of a few tenths of microns, so-called 'microfluidics'. Different receptor molecules are spotted on the chip before microfluidic channels are mounted. This is in contrast with the approach in which receptor molecules are coupled to the surface after bonding the channels, which requires a more complex channel network with multiple in- and outlets. Our approach asks for a low-temperature bonding process during which no contact is allowed between an adhesive glue and the receptor molecules on the SOI chip. We use a stamp-and-stick method to transfer PDMS channels on the SOI chip without damaging the fragile receptor molecules. This is illustrated in Fig. 9 together with a picture of the finished device.

The chips with chemistry coating and packaged with PDMS microfluidics, are

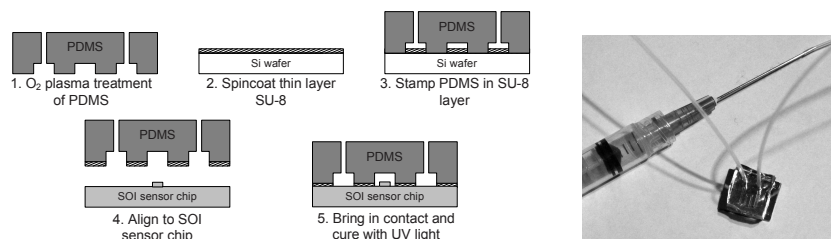


**Figure 9:** Stamp-and-stick procedure for packaging an SOI photonic chip with PDMS microfluidics and a picture of the finished device.

subsequently placed in a read-out setup. Integrated grating couplers couple light from the horizontal waveguides to the vertical direction where it is further guided through single-mode optical fibers or in free-space. A system consisting of flood illumination of multiple input waveguides and imaging of multiple output gratings with an infra-red (IR) camera offers a good trade-off between a high degree of multiplexing and low noise. The chip with read-out system is schematically shown in Fig. 10. The read-out system of an integrated optical biosensor is fundamentally different from the read-out system of commercial free-space biosensors like Biacore SPR. Here, read-out is completely decoupled from the detection, offering a much higher degree of multiplexing and a much higher alignment tolerance. The latter is important for portable applications and reduces the cost of the overall system.

## Biosensor experiments

Using the platform, we performed a number of experiments to characterize the SOI microring biosensor. Avidin/biotin was initially used as a model biomolecular pair. The detection limit of the system was determined to be around 3.8 ng/ml. For multiplexed protein detection experiments, an array of microrings was covered homogeneously with a PEG layer, on top of which different proteins were spotted on different ring resonators (see Fig. 10). Fig. 11 shows the result of a proof-of-principle multiplexed sensing experiment. Three different proteins are spotted on the resonators: Hu-IgG, HSA and BSA. The fourth column of resonators was left for reference. When flowing diluted serums with different antibodies (anti-Hu-IgG and anti-HSA) across the chip, the analytes could be detected with high specificity. Now that a basic biosensor platform has been installed and SOI microring biosensors have been characterized, other filter configurations and better read-out schemes can be developed to obtain lower detection limits. Higher levels of integration, with microfluidics and optoelectronic components, are investigated as well. This will ultimately lead to integration of a disposable SOI photonics biochip in a point-of-care diagnostic tool.

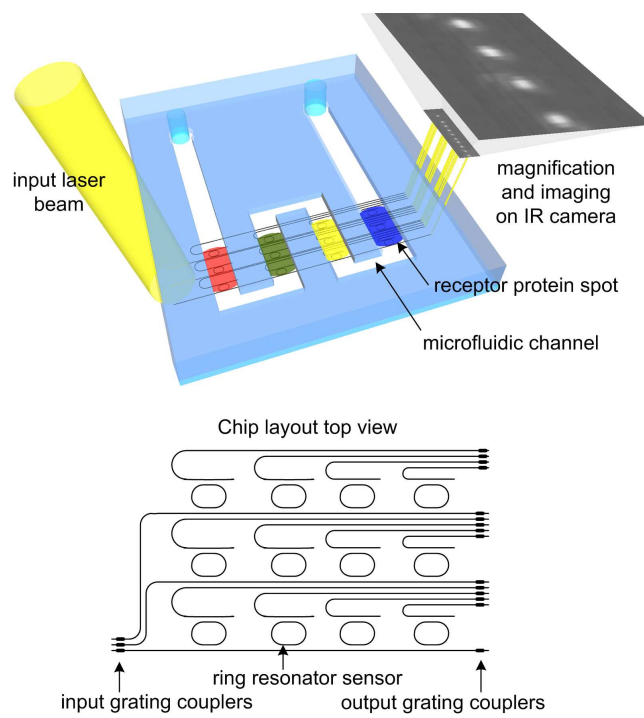


**Figure 10:** Illustration of the packaged SOI chip, containing an array of SOI microring resonators, implemented in a read-out system.

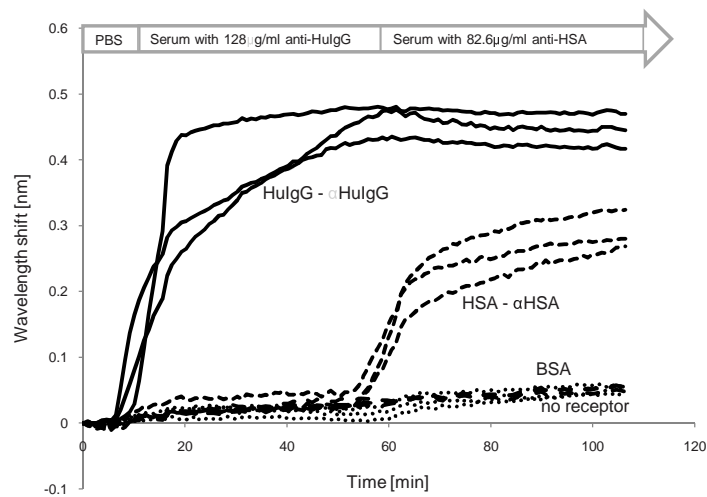


**Figure 11:** Experiment with three different receptor molecules spotted on the SOI chip: Hu-IgG, HSA, and BSA. Two serums were pumped over the sensors, containing 128 µg/ml anti-Hu-IgG and 1.9 mg/ml other proteins, and 82.6 µg/ml anti-HSA and 1.5 mg/ml other proteins. The resonators spotted with the complementary proteins responded sharply, while the response of the other resonators remained low.



# 1

## Introduction

In this PhD project we studied and developed a label-free biosensor based on a silicon-on-insulator photonic chip. The sensor itself consists of an integrated optical resonator that responds when biomolecules interact at its surface. It was a multidisciplinary project during which different research fields like chemistry, fluidics and optics were combined to obtain a sensitive, disposable biochip for multiplexed protein detection. We closely collaborated with the *Polymer Material Research Group* at *Ghent University* with Prof. Em. Etienne Schacht in the framework of a UGent GOA project.

This chapter serves to set the context of this work. It will give an answer to the questions “Label-free biosensing: what, why and what for?” in sections 1.1 and 1.2. Section 1.3 introduces the device that we studied: a silicon-on-insulator (SOI) ring resonator biosensor. We will briefly introduce the field of SOI photonics and its connection with biology. The working principle of the device will be explained as well as its main assets. The outline of the rest of the manuscript is given in section 1.4. The chapter concludes with an overview and discussion of competing technologies in section 1.5.

### 1.1 Affinity biosensors

A biosensor provides the ability to study interactions between biomolecules, to observe the activity of cells, and to specifically detect analytes from body fluids, manufacturing processes, or environmental samples. The development of tech-

nology to meet these requirements is challenging because biochemical analytes are extremely small and sometimes present within a sample at concentrations in the fg/ml to pg/ml concentration range that simultaneously contains thousands of other molecules at concentrations orders of magnitude greater. The analytes to detect can include drug compounds with molecular weights below 500 Da<sup>1</sup>, DNA oligomers, peptides, enzymes, antibodies, viral particles... An additional challenge arises from the need to perform many thousands of individual measurements. For example, researchers working in pharmaceutical discovery and life science research seek to perform large numbers of assays<sup>2</sup> in parallel [1].

Due to the difficulty in detecting biological analytes directly through their intrinsic physical properties (such as mass, size, electrical impedance, or dielectric permittivity), biological research has historically relied upon attachment of some sort of 'label' to one or more of the molecules, viruses or cells being studied. The label is designed to be easily measured and indirectly indicates the presence of the analyte to which it has been attached. For example, many commercially available fluorescent dyes can be conjugated with DNA, proteins, or cells so that, when illuminated with a laser at the excitation wavelength of the fluorophore, light is emitted at a characteristic wavelength. An example is illustrated in Fig. 1.1(a). ELISA (enzyme-linked immunosorbent assay) allows for screening of an antigen<sup>3</sup> in a sample (e.g. the blue antigen in the figure). In brief, the sample is adsorbed to a surface first. The surface is then treated with a solution containing the primary antibody - an antibody against the antigen of interest. Unbound antibody is washed away and the surface is treated with a solution containing antibodies against the primary antibody. These have been linked to fluorescent labels. The fluorescent signal is proportional to the concentration of the antibody of interest in the sample.

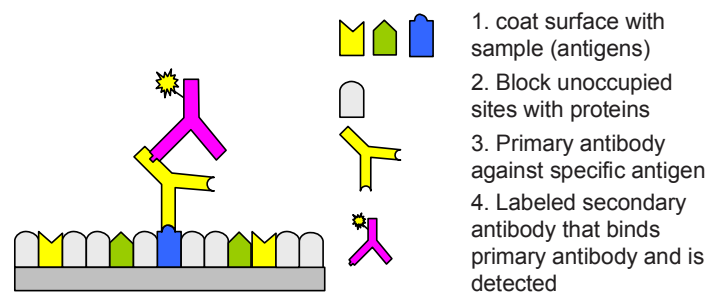
Though labels have been central to implementing nearly all biochemical and cell-based assays, the labels themselves pose several potential problems. For example, though the detection of *radioactive labels* can be performed with tremendous sensitivity, their usage requires specially outfitted 'hot labs' and the generation of large quantities of contaminated reagents and labware that must be properly disposed. With advanced microscopy, fluorescence can be detected down to very small amounts [2]. However, the emission efficiency of *fluorescent labels* is degraded by time and exposure to light (including room light and the laser excitation

---

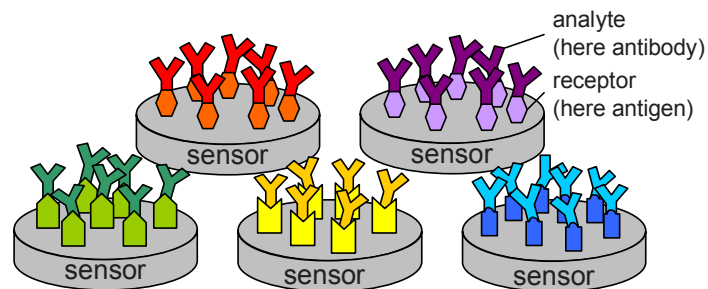
<sup>1</sup> 1 Dalton (Da) is the atomic mass unit corresponding to one twelfth of the mass of an isolated atom of carbon-12 (<sup>12</sup>C) at rest and in its ground state.

<sup>2</sup> An assay is a procedure in molecular biology for testing and/or measuring the activity of a drug or biochemical substance in an organism or organic sample.

<sup>3</sup> Antibody/Antigen: Antibodies or immunoglobulins (Ig) are the proteins at the heart of the human immune system. They bind bacteria, viruses or other foreign molecules and target them for destruction. An antigen is any molecule or pathogen capable of eliciting an immune response, it may be a virus, a bacterial cell wall or another macromolecule. An individual antibody binds only one particular antigen, more specifically, it binds to one particular molecular structure within the antigen.



(a) Labeled biosensing



(b) Label-free biosensing

**Figure 1.1:** Illustration of labeled and label-free biosensors. Labeled biosensing relies on attachment of a label to the analyte and is illustrated with the ELISA principle. The label (fluorescent, radioactive, nanoparticle, ...) can easily be measured and indirectly indicates the presence of the analyte to which it has been attached. Label-free affinity biosensing relies on a receptor molecule attached to a transducer that responds to affinity binding between receptor and analyte.

light) by photobleaching, reducing the ability to supply highly quantitative measurements and requiring that assays be read in an ‘end point’ fashion so that kinetic information from an assay is lost. Quenching and self-quenching may also reduce the efficacy of fluorescent tags in an unpredictable manner [3]. In practice, label-based assays require a high degree of development to assure that the label does not block an important active site on the tagged molecule or modify the molecular conformation.

Due to the above considerations, there has been a drive to reduce assay cost and complexity while providing more quantitative information with high throughput. Label-free detection generally involves a transducer capable of directly measuring some physical property of the chemical compound, DNA molecule, peptide, protein, virus, or cell. A well-known example is the glucose sensor, this is an ‘enzyme-based’ biosensor. It uses an enzyme (glucose oxidase) that breaks the glucose down into gluconic acid and  $H_2O_2$ , under consumption of  $O_2$ . The glucose sensor will produce a transducer signal proportional to either the  $H_2O_2$  concentration, the pH of the gluconic acid or the  $O_2$  consumption. This signal relates thus directly to the original glucose concentration [4].

The type of biosensor handled in this work is an affinity-based biosensor. Affinity biosensors are analytical devices composed of a biological recognition element, the so-called ‘receptor’ or ‘ligand’, interfaced to a transducer which responds to the affinity interaction of the receptor with an analyte. The receptor molecule can be an antibody, receptor protein, biomimetic material or DNA. In analogy with ELISAs, in Fig. 1.1(b) we illustrate a label-free biosensor for detection of antibodies in a sample. Identical sensors are placed in an array, each of them coated with a different antigen. When immersed in a sample, the complementary antibodies will bind to the antigens resulting in an output signal of the corresponding sensor. In contrast to labeled detection, the formation of the complexes is now monitored continuously and many interactions can be followed simultaneously. This real-time data results in information on the kinetics of the reaction as well as on the concentration of the antibodies in the sample. More detail on affinity binding is given in chapter 4.

Below we list a number of biosensor requirements. Depending on the application area, the tolerances on the requirements differ. The terms that are introduced here will be used throughout the next chapters and will be related to the SOI ring resonator biosensor where appropriate. Some metrics, such as sensitivity or cost, can be defined numerically. Others, such as portability, are subjective but can have a significant impact on the commercial success of a method.

- **Sensitivity** is defined as the amount of change in sensor output response resulting from a molecular change on the sensor surface.
- **Resolution** is the smallest change in output signal that can be observed.

It depends on transducer, read-out equipment, overall noise level and data processing.

- **Limit of detection (LOD)** refers to the minimum detectable concentration or mass amount of an analyte, such as a protein, in a test sample. It can be expressed with various quantities: minimum bulk refractive index change [RIU], minimum surface coverage [ $\text{pg}/\text{mm}^2$ ], minimum analyte concentration [ $\text{ng}/\text{ml}$ ], minimum detectable molecular mass [g]... The detection limit depends on intrinsic transducer properties as well as on surface chemistry, sample delivery, affinity of the analyte for the receptor, buffer conditions etc.
- **Selectivity** is the sensor characteristic that prevents molecules other than the analyte to attach or adsorb to the surface and cause a large background signal, thus deteriorating the biosensors detection limit. Selectivity is provided by an appropriate surface coating.
- The **dynamic range** is the ratio of the largest measurable target concentration to the limit of detection.
- High **throughput** or **multiplexed** screening of biomolecular interactions in arrays is crucial. For example, researchers working in pharmaceutical discovery and life science perform large numbers of assays in parallel to understand how many molecular permutations affect the efficacy of a drug candidate.
- **Cost** breakdown has two components: cost of the disposable and cost of the instrumentation. Adoption of biosensor technology for most applications in diagnostics or pharmaceutical screening will be driven to some extent by the cost of performing an individual assay. The cost of a read-out instrument is related to its complexity and the cost of the components required to reach a specified level of performance.
- **Portability** is important for detection systems that need to serve in a range of locations (e.g. diagnostics in the doctor's office or at the patients' bed) and in time-restricted settings where real-time detection offers considerable advantages over transportation of the sample to the lab (e.g. environmental pollution control).
- The **sample volume** a biosensor consumes in order to make a reliable measurement can be important when measuring rare or expensive samples.

## 1.2 Application areas

The study of biomolecular interaction finds applications in many fields. Here we discuss some emerging applications for label-free biosensors.

### 1.2.1 Drug discovery

The analysis of molecular interactions is a key part of the drug discovery process; many millions of dollars are spent early in drug development on screening compounds for receptor binding *in vitro*. Biosensors with fluorescent or radioactive labels are nowadays commonly used for such tasks, but label-free biosensors are increasingly deployed for their high information content on affinities and kinetics, and flexibility to the process of assay design and quality control. High throughput is currently important to a lesser extent. An information-rich assay that gives a quantitative ranking of interaction affinities and the active concentration of an expressed receptor or ligand can be extremely valuable in the early stages of drug discovery, including target identification, ligand fishing, assay development, lead selection, early ADME<sup>4</sup> and manufacturing quality control. In [5], Cooper et al. give an overview of the use of biosensors at all stages in drug discovery and give indications on where label-free sensors might become indispensable, some of which have already been implemented today.

### 1.2.2 Point-of-care diagnostics

Biosensors for multiplexed diagnostics are currently attracting the most commercial interest [6]. Point-of-care (POC) systems are designed to process clinical samples for a number of different types of biomarkers<sup>5</sup> and to work in a variety of settings, such as clinical laboratories, doctors offices and eventually, at home. Basically, POC systems make state-of-the-art technology platforms accessible to a large population pool. This can be achieved by integrated systems that combine biosensor technology with sample preparation. Instead of sample pre-treatment (including for example cell lysing and extraction) in room-sized laboratories, all preparation steps have to be performed on-chip. These technologies can contribute to the realization of personalized medicine by creating a link between the diagnosis of disease and the ability to tailor therapeutics to the individual. Aside from the technological difficulties, another bottleneck diagnostic biosensors face is the additional regulatory challenge of demonstrating that the information provided is of clinical significance.

Biosensors in point-of-care systems for cancer diagnostics are believed to be very promising [5]. Cancers arise as a result of the disruption of normal cell signaling pathways, which can produce cells (cancer cells) that exhibit a decisive growth advantage compared to their neighbors. The common method for cancer diagnosis and prognosis relies heavily on technologies that are over 100 years old (visual

---

<sup>4</sup>A drug compound with poor ADME (absorption, distribution, metabolism and excretion) binds a high level of serum proteins and therefore scores low on the delicate balance between intended physiological activity, long term efficacy and potential side effects of the drug.

<sup>5</sup>A biomarker for diagnostics is a term used to refer to a protein measured in blood whose concentration reflects the severity or presence of some disease state.

inspection of cell morphology by a pathologist). Unfortunately in terms of diagnosis, there is not one molecular marker that can provide sufficient information to assist the clinician in making effective prognoses or even diagnoses. Large panels of markers must typically be evaluated. Therefore, new technology platforms must possess the capability to provide data on a large panel of markers across several different classes of biomarkers. Multiplexing becomes thus very important. It is likely that the concentration of biomarkers in either serum or urine will be very low. This will require that biosensors for cancer diagnostics will have to possess excellent sensitivity. It also imposes very stringent specificity requirements for the biological recognition elements.

The goal of using optical biosensors for diagnostics in developing countries [7] has become an important driver for engineering more cost-effective systems. Technologies for cheap, robust, low-cost, user-friendly diagnostics with minimal requirements for external energy sources are in the development and clinical testing phase. Successful approaches will work just as well in technologically advanced cultures and be more rapidly accepted due to the lower cost of use.

### **1.2.3 Environmental control and food testing**

Environmental concerns are driving the development of on-site monitoring systems to reduce the response time and cost of pollution control in comparison to shipping samples to a central laboratory. Label-free biosensors are being tested for monitoring air, water, and soil, with the primary interest coming from environmental regulatory agencies, for example online screening of water quality for both household and industrial use [8].

Food processing companies are interested in automated monitoring systems to promote safer products and reduce liability. A few companies have already replaced optical biosensors for food testing, but the efficacy of these systems for process monitoring is just beginning to be investigated [6].

## **1.3 Silicon-on-insulator microring biosensor platform**

### **1.3.1 Towards integrated optical biosensors**

From the wide variety of applications for label-free biosensors, we can extract a few key requirements: low detection limit, high throughput, portable systems, integration with sample preparation and low cost of the disposable. Depending on the actual application, some requirements are more stringent than others.

Optical label-free biosensors have received considerable attention over the past years. The key behind optical biosensors' ability to detect biological analytes is that biological molecules, including proteins, cells, and DNA, all have a permittivity  $\epsilon$  greater than that of air and water. Therefore, these materials all possess the

intrinsic ability to reduce the propagation velocity of electromagnetic waves that pass through them. Optical biosensors translate changes in the propagation speed of light into a quantifiable signal proportional to the amount of biological material present on the sensor surface.

In this category, there exist a number of detection methods, including refractive index (RI) detection, optical absorption detection, and Raman spectroscopic detection. RI and absorption are the real and imaginary part of the more general complex refractive index constant  $n = \sqrt{\epsilon/\epsilon_0}$  and are related to each other via the Kramers–Kronig relations [9]. Raman detection is unique in that, on one hand, like RI and absorption detection, target molecules are not labeled, on the other hand, emitted Raman light is used for sensing, similar to fluorescence-based detection. All optical biosensors are immune to electromagnetic interference. The biosensor platform we developed is based on RI detection.

Commercially available optical label-free biosensors exist in free-space beam sensing configurations, where discrete optical components such as mirrors, lenses, and spatial filters are used to define the wave front and the trajectory of the beam. A well-known example are SPR (surface plasmon resonance) biosensors by Biacore and other companies. Coupling light from one component to another in free-space setups typically requires accurate and therefore time consuming and expensive mechanical alignment. For the same reason portability of the equipment is low and its use is limited to dedicated lab or clinical environments. Expanding the optical sensing principle to multiplexed sensing is not straightforward as the complexity and cost of the optical components of the read-out equipment scales with the degree of multiplexing (see also section 1.5).

Over the past decade there has been a vast research effort in integration of optical label-free biosensors on photonic chips. Photonic integrated circuits (PIC) consist of optical components, such as light sources, detectors, data processing units or sensors, that are integrated on one single chip. The integrated approach allows for a significant simplification of the optical system, since the light routing and processing can be accomplished by a waveguide circuit that is fabricated by a collective lithography process. The sensing part is fully decoupled from the optical read-out part and can thus be optimized separately. Extension to multiplexed sensor arrays is simply attained by arraying one sensor next to the other and connecting them with source and detector through integrated waveguides. Most importantly, additional levels of integration with electronic and biologic functions are possible. The ultimate goal is to integrate several laboratory functions in a single chip, a so-called lab-on-a-chip. These functions can be diverse, like cell lysis, sample amplification and dilution, sample cleaning, labeling etc. Biosensors can be included in various functions of the lab-on-a-chip, for example for quality control or real-time detection.

### 1.3.2 Working principle

In Fig. 1.2 the basic working principle of an integrated ring resonator biosensor is illustrated. The ring resonator consists of a waveguide that can confine light within the submicron scale. The resonator supports circulating waveguide modes with resonant wavelengths that are related to the effective optical path length within the resonator:

$$\lambda_{res} = \frac{Ln_{eff}}{m}$$

where  $L$  is the circumference of the ring,  $m$  is an integer and  $n_{eff}$  the effective refractive index of the circulating mode. When the refractive index near the ring resonator surface is modified due to the capture of target molecules on the surface,  $n_{eff}$  will change which in turn leads to a shift in the resonance wavelength  $\lambda_{res}$ . This wavelength shift is a quantitative measure for the number of binding events near the surface.

In a wavelength interrogation setup the spectrum is scanned repeatedly and the location of the resonance is tracked, while in an intensity interrogation setup the output intensity is monitored at one specific wavelength. For sharp peaks, intensity interrogation can be more sensitive, however it is largely dependent on the peak shape and thus very susceptible to slight shape variations and noise. On top of that intensity interrogation offers a limited dynamic range. For these reasons we applied wavelength interrogation in all experiments.

### 1.3.3 Silicon photonics for biotechnology

Unlike in electronic integration, where silicon is the dominant material, photonic integrated circuits have been fabricated from a variety of material systems like silica-on-silicon, polymers, III–V semiconductors, SiON (silicon-oxynitride), silicon-on-insulator etc. Aside from ease and cost of fabrication, the number of components per surface area (the integration density) is a key issue for the choice of material. This is related to the minimal waveguide bend radius that supports guiding without substantial losses and the minimal device separation that avoids mode coupling. Essentially this relates to the degree of confinement in the waveguides. As higher confinement is achieved in material systems with larger index contrast, platforms consisting of semiconductor materials like silicon or III–V semiconductors with refractive index around 3 offer the highest degree of integration, in contrast to glasses or polymers with indices in the range of 1.5–2. In literature integrated biosensors based on resonant cavities are demonstrated with different material systems such as hydrex glass [10, 11], polymers [12] and silicon nitride [13]. In this section we will argue that silicon-on-insulator (SOI) as a material system for integrated biosensors is a valuable option.

An SOI wafer consists of a silicon membrane and a buried silicon-oxide layer

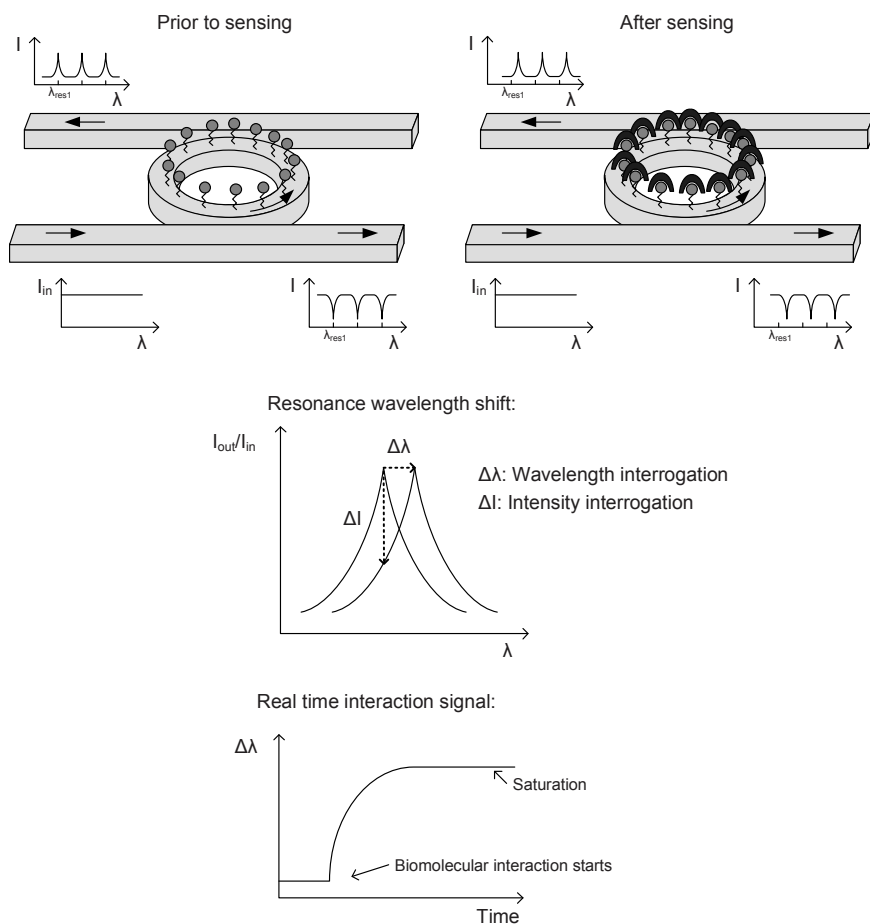


**Figure 1.2:** Basic principle of a ring resonator biosensor. A ring resonator supports resonating modes with wavelengths determined by the optical path length  $Ln_{eff}$ . Upon biomolecular at the ring surface, the effective index of the resonating mode will change which in turn leads to a measurable resonance wavelength shift.

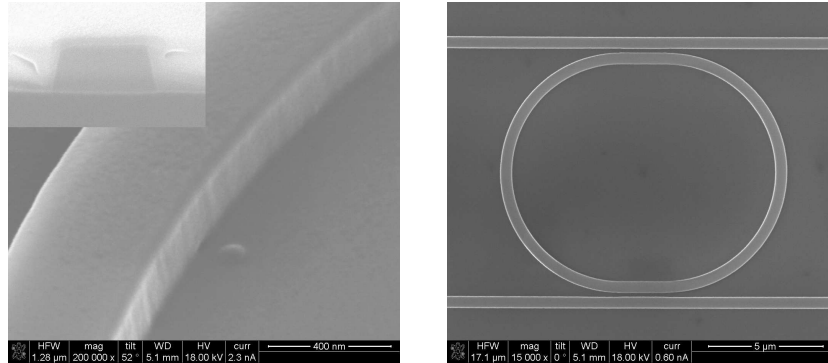


**Figure 1.3:** SEM picture of SOI waveguide for monomodal operation with width = 450 nm, height = 220 nm. SOI ring resonator with radius 5  $\mu\text{m}$  and straight section 2  $\mu\text{m}$ .

(BOX) on a supporting substrate. Silicon is transparent in the near infra-red (NIR) beyond 1.2  $\mu\text{m}$ , which includes the main telecom wavelengths 1.30  $\mu\text{m}$  and 1.55  $\mu\text{m}$ . The silicon membrane is of sub-wavelength height, lateral confinement is achieved by etching fully through the silicon membrane. In this way, a high omnidirectional index contrast ( $n_{Si}=3.46$ ,  $n_{SiO_2}=1.44$ ) is achieved which enables guiding through sharp bends and thus large density sensor integration. Fig. 1.3 shows a SEM picture of a fabricated SOI wire with typical dimensions. The silicon membrane of our fabricated devices measures 220 nm in height, and monomodal operation is achieved for waveguide widths around 450 nm (depending on the top cladding -often watery solutions in biosensing- and the polarization).

**Low detection limit** The high index contrast of SOI thus results in micron-sized ring resonator biosensors, which is of importance when detecting very small amounts of molecules. The resonance wavelength shift does not scale with the size of the cavity, hence the smaller the cavity, the less molecules are needed to cover its entire surface, while the response does not decrease with decreasing surface area. This is treated in more detail in chapter 2. There, we will also show that not only the small surface area but also the high mode confinement itself is beneficial for highly sensitive detection.

**Integration density** Because of the high index contrast, the ring resonators cover only a  $10 \times 14 \mu\text{m}^2$  area. One square millimeter on a photonics chip can thus contain over 1,000 biosensors. When each of them is covered with different receptor molecules large sets of biomarkers can be screened simultaneously within very small sample volumes. Today very few techniques exist to address surfaces this small with molecules. Thanks to advances in genome screening with microarrays,



*Figure 1.4: SOI microring resonators of  $10 \times 14 \mu\text{m}$  area addressed separately with liquid drops of compatible dimensions produced with a Bioforce ‘Nanospotter’.*

there has been vast investment in tools that produce molecular sample spots with a few hundred micron radius. SOI compatible molecular spots of a few tenths micron radius however can only be made with few commercial tools, amongst them ‘Bio-jet’ nanodispensing system of Olivetti and ‘Nanospotter’ of Bioforce. Fig. 1.4 shows pictures of SOI ring resonators with liquid drops of  $15 \mu\text{m}$  radius produced with the Bioforce ‘Nanospotter’.

**Fabrication** Using silicon as a photonics platform offers the advantage of reuse of extensively developed CMOS processing technology. Typical minimum SOI photonic feature sizes are around 100 nm, which fits well within the capacities of today’s industrial fabrication tools based on 193 nm optical projection lithography and dry etching. As a consequence of the high index contrast and the waveguide dimensions being close to the diffraction limit, device responses are very sensitive to minimal dimensional variations. Therefore, an accurate dimensional control in the range of 1-5 nm is needed. To achieve such requirement a high resolution fabrication process is needed. In [14–16], members of our group gave a detailed description on how industrial techniques are adapted for fabrication of high quality SOI photonic integrated circuits. All test devices used in this work are fabricated with the research facilities of IMEC (Interuniversity Microelectronics Center), Leuven, Belgium.

Fabrication of photonic chips with nanoscale reliability and with no extra equipment development cost is a major asset for SOI biosensors. It allows for mass production and economics of scale. For point-of-care diagnostics the availability of cheap disposables is a prior requirement, since reuse of the sensor chip is excluded. Also in drug discovery where immense numbers of test assays are run, cheap disposables can increase efficiency and keep down the development costs of the drugs.

**Active–passive integration** We mentioned that label-free biosensors can be integrated in a lab-on-a-chip. A first additional level of integration is between optical structures and microfluidics. Microfluidics can serve for a number of applications like cell sorting and cell manipulation required for the sample preparation prior to diagnostic biosensing. A second level of integration, namely the integration of the sensors with light sources, and detectors, as well as the corresponding on-board or on-chip optical and electronic controls is the next step towards fully integrated hand-held sensor systems.

While SOI is a promising platform for passive functions like sensing, the fabrication of active optoelectronic devices (light emission, amplification and detection) at telecom wavelengths using electrically contacted devices is difficult. The integration of active optical functions on a silicon platform is an active area of research. This implies the integration of silicon-based modulators, SiGe photodetectors and silicon light sources. A literature review of state-of-the-art in silicon photonics is given in [17].

A second route to achieve active functionality is heterogeneous integration of silicon with III–V material systems. As state-of-the-art active optoelectronic components are fabricated in InP/InGaAsP, heterogeneous integration with silicon results in exploitation of advantages of both material systems. Various routes towards integration are possible: one can integrate preprocessed III–V devices onto the silicon host substrate or one can integrate the material first and process the devices after. Both approaches offer advantages and have drawbacks. At Intec, the second option has led to a number of publications [18–22]. By integration of InP/InGaAsP as individual dies on the silicon host and processing them subsequently, tolerances on the misalignment of positioning is very high and positioning can thus be done quickly and cost effectively. This approach leads to efficient use of expensive InP/InGaAsP material. In this work we do not address the integration with active components. Various functional components have been developed in parallel to this work and integration of passive sensors and light guiding with active sources and detection will ultimately lead to fully integrated biosensors.

## 1.4 Outline of the manuscript

For an innovative biosensor platform like the SOI ring resonator biosensor, not only the sensor technology needs to be developed. Basically there are four parts contributing to a successful detection: the sensor, the coupling chemistry, fluid delivery and read-out system. They are schematically pictured in Fig. 1.5. In general, the quality of the weakest part will be the limiting factor for the overall quality of the system. For instance, high-quality read-out can never compensate for a bad-quality sensor chip. Separate chapters are devoted to the various aspects. The sensor element is discussed in chapter 2. Chapter 3 introduces a new technique

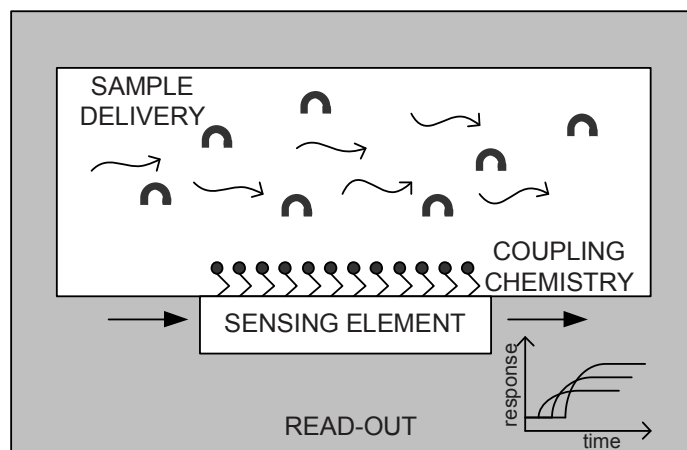


*Figure 1.5:* A biosensor platform consists of four parts contributing to a successful molecular detection: the sensing element, the coupling chemistry, sample fluid delivery and read-out system.

to extract additional data from ring resonator biosensors. Chapter 4 overviews the work we performed to obtain high quality coupling of receptor molecules to SOI biosensors. The development of microfluidics delivery and a read-out system for low noise and parallel detection is described in chapters 5 and 6. Chapter 8 gives an overview of possible routes for continuation of this work, some of which have already been initiated. It also introduces an alternative implementation of SOI ring resonator biosensors, namely transfer of a resonator to an optical fiber facet for extreme portability and in-vivo sensing.

## 1.5 Competing technologies

Detection via the optical properties of biomolecules is only one of the many options that are considered for label-free biosensors. The two other main categories are electrical and mechanical sensors based on electrical molecular properties or mass. We will briefly give an overview of the three main label-free biosensor classes in a current commercial context. Only affinity-based biosensors are listed, other mechanisms -like the enzyme-based glucose sensor we discussed earlier- are not discussed here. We intentionally choose a technological point of view and do not discuss other metrics such as time-to-result and specificity. While these metrics are critically important to sensor utility, as will become clear in chapter 4 and 5, they can be complicated by other factors that are not related to the fundamental physical performance of the device. For the same reason it is hard to compare detection limits of the different platforms. No standard evaluation exists

and performance numbers in literature reflect not only the technology, but also the quality of the interfacial layer, the fluidics and the kinetics of biomolecular pairs. Moreover different figures of merit can be used such as concentration detection limit, surface coverage etc. They are discussed in chapter 2, section 2.4. Lists on published detection limits for various sensing platforms and additional information can be found literature reviews [23–25]. We only discuss affinity-based biosensors.

### 1.5.1 Optical biosensors

Optical biosensors were already introduced in section 1.3.1. They have a long history in biosensing, since most labeled biosensors are also optical in nature. We categorize optical biosensors in 3 categories: plasmonic biosensors, interferometer-based biosensors and cavity biosensors. Each of them can have a number of different implementations (free space optics, integrated waveguides, photonic crystals, fibers...) and material systems. We will briefly introduce the main working principles, which can be used to understand many other implementations not mentioned here. Plasmonic biosensors can also be combined with interferometer or cavity biosensors, but we will treat them separately for their fundamentally different nature. Photonic crystals can be part of an interferometer or a cavity but can also serve as a biosensor as such and will also be treated separately. For a discussion on fiber optic sensors, we refer to chapter 8.

#### Plasmonic biosensors

Undoubtedly the most established label-free optical biosensor is based on surface plasmon resonances (SPR). A surface plasmon wave (SPW) is a charge density oscillation that occurs at the interface of two media with dielectric constants of opposite signs, such as a metal and a dielectric. There exist many implementations of SPR biosensors that mainly differ in the method to excite the SPR: prism coupling, waveguide coupling, fiber optic coupling, grating coupling... In the prism coupling configuration an incident light beam is totally reflected at the prism-metal interface and generates an evanescent field penetrating into the metal layer. At the resonant angle (or resonant wavelength), the propagation constant of the evanescent field matches that of the SPW and the photon will be coupled into the SPW. This angle is dependent on the refractive index of the environment and can be used for sensing. This principle first got commercialized by Biacore and generally has a good detection limit. However it is bulky and it is difficult to integrate. Fig. 1.6 illustrates a prism coupled label-free optical biosensor. Multiplexed sensing with imaging prism coupled SPR (SPRi) was first introduced in [26]. A CCD camera is used to image the intensity of light reflected off the surface. However this comes with a cost: SPRi typically has a limit of detection 10–100 times worse than stan-

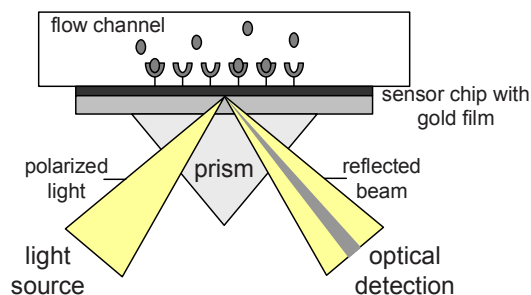


*Figure 1.6: Prism coupled SPR sensor configuration, based on [5].*

standard SPR biosensors [23]. Today, the list of SPR biosensor manufacturers and the range of products is extensive. In the past few years, SPR and SPRi have been applied in molecular biology for the detection of proteins with a detection limit ranging from picomolar to nanomolar. Generally commercial systems are capable of detecting  $1 \text{ pg/mm}^2$  surface coverage of molecules. This detection limit depends on many parameters, but particularly on surface functionalization. We refer to [27, 28] for reviews on SPRi technology literature.

Waveguide coupling offers an integrated alternative to the prism: a SPW is excited at the interface where a metal strip is included in the waveguide. This way multiplexing will be achievable at virtually no cost by simply integrating more sensors on one chip. At Intec, Peter Debackere examined guided SPR modes for biosensing, this work is published in [29–31].

### **Interferometer-based biosensors**

The phase change introduced by molecular interaction at the biosensor's surface is transduced in a spectral shift of the interference when recombining the sensor signal with a reference signal. In general the sensitivity of an interferometer increases with longer interaction length. This principle can be implemented in a Mach-Zehnder interferometer, a Young interferometer or backscattering interferometer.

In a Mach-Zehnder interferometer the sensing and reference branch are recombined and the output intensity is monitored. Mach-Zehnders can be fully integrated on chip, and will be discussed in more detail at the end of chapter 2. A Hartman interferometer is a type of Mach-Zehnder implementation, receptor molecules are patterned on top of a planar slab waveguide. Light is recombined on the chip which creates interference patterns between pairs of functionalized strips and is then coupled out of planar waveguides using gratings. A Hartman interferometer has been used by Schneider et al. for immunoassays for human chorionic gonadotropin (hCG) [32]. They achieved  $5 \text{ ng/ml}$  detection limit and improved it



biosensor will be extensively discussed in the next chapter. A high number of revolutions in the cavity results in sharp resonance peaks which enlarges the sensor performance. A ring resonator can deliver sensing performance similar or superior to an interferometer while using orders of magnitude less surface area and sample volume. The sensors have been implemented in ring-, disk- and microtoroid-shaped resonators on a chip. Since the concept was first described by Boyd et al. [41], over 100 papers have been published on ring resonators for various sensing applications, even showing single molecule detection [42]. Chao et al. showed biomolecular detection with planar polymer microring resonators, fabricated by a direct imprinting technique, with a detection limit of  $250 \text{ pg/mm}^2$  [12]. In [10, 11] planar glass-based microring arrays with 5 microrings were sequentially scanned for rapid detection of whole bacterial cells, proteins and nucleic acids. [43, 44] published results on SOI microring resonator biosensing. Washburn et al. recently reported a limit of detection of  $2 \text{ ng/ml}$  for an SOI microring resonator sensor applied to a clinically relevant cancer biomarker [43].

**Microsphere resonators** An optical WGM may be represented by a light wave that travels around near the surface of a glass sphere and returns back upon itself in phase. The optical effect of binding a compact monolayer of proteins is to increase the average radius of the sphere. Because the resonance wavelength is proportional to the radius, the fractional shift in the wavelength is equal to the fractional change in the radius. In contrast to circulating waveguide modes in ring resonators, the sensitivity in whispering gallery mode biosensors depends on the sphere radius. A comprehensive work on viral detection with a microsphere sensor that includes theoretical discussion as well as experimental results was published in [36]. It predicts that the microsphere is capable of detecting a single virus.

**Liquid-core ring resonators** The liquid core optical ring resonator (LCORR) utilizes a thin-walled micro-sized capillary. As illustrated in Fig. 1.8, the circular cross section of the capillary forms the ring and supports a WGM. The capillary wall is sufficiently thin ( $< 4 \text{ }\mu\text{m}$ ) so that the WGMs of high Q-factors ( $> 10^6$ ) are exposed to the core and interact with the analyte in proximity of the capillary inner surface [45]. The LCORR was used for quantitative detection of DNA sequences with base-mismatch studies. DNA concentration down to  $10 \text{ pM}$  was experimentally detected and the estimated surface coverage detection limit is  $4 \text{ pg/mm}^2$  [46].

### Photonic crystals

A photonic crystal (PC) has a periodic dielectric structure with a periodicity on the order of the wavelength, from which forms the photonic bandgap. Incident light whose wavelength lies within the photonic bandgap cannot propagate through

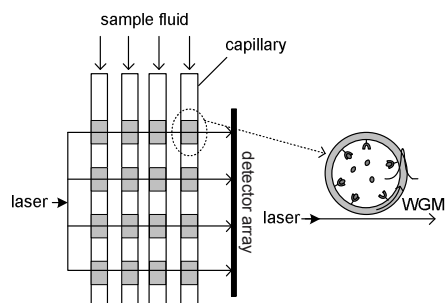


**Figure 1.8:** Conceptual illustration of a liquid core optical ring resonator sensor array from [47].

the PC and a wide bandgap emerges in the transmission (or reflection) spectrum. However, a photonic ‘defect’ within the bandgap can be introduced by locally disturbing the PCs periodic structure, leading to the formation of the defect mode. Light resonant with the defect mode can propagate in the PC. As a result, in the transmission (or reflection) spectrum, the defect mode appears as a relatively sharp peak within the bandgap. Since the spectral position of the defect mode is highly sensitive to the change in the local environment around the ‘defect’, it can be used as the sensing transduction signal when the refractive index changes as a result of the binding of the molecules to the defect.

Lee et al. for the first time demonstrated a PC microcavity biosensor that is capable of monitoring protein binding on the walls of the defect hole and quantitatively measuring the protein diameter [48]. Mandal et al. recently demonstrated a novel sensor array based on the use of arrays of 1D photonic crystal resonators and a single bus waveguide (Fig. 1.9). Using the streptavidin/anti-streptavidin model, they characterized the dose-response of the device and observed a dynamic range of 1 to 100  $\mu\text{g/ml}$  [50].

The directionality of 1D grating couplers has also been used for biosensing, upon biomolecular interaction at a grating surface, the angle or the wavelength shift of the guided mode resonance can be interrogated. In this case the optical layout of the sensor system is almost identical to that used in SPR systems, with a free space laser beam incident on the sample from above or below the substrate [49].

## 1.5.2 Mechanical biosensors

Two classes of mechanical biosensors have been successfully implemented and are commercialized: acoustic wave biosensors and microcantilevers.

Acoustic wave biosensors include quartz crystal microbalances (QCM) and integrated surface acoustic wave technologies. Both approaches utilize a piezoelectric quartz crystal connected to an oscillating external circuit that is able to measure the

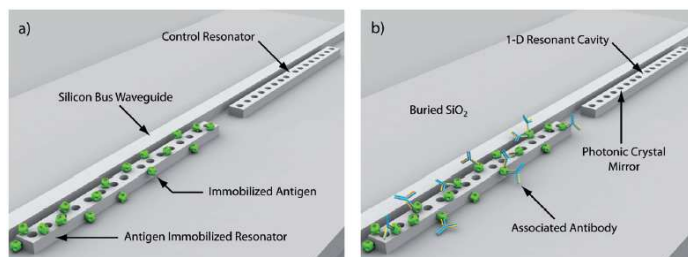


**Figure 1.9:** Photonic crystal sensor array: 1D photonic crystals are evanescently coupled to a bus waveguide from [50].

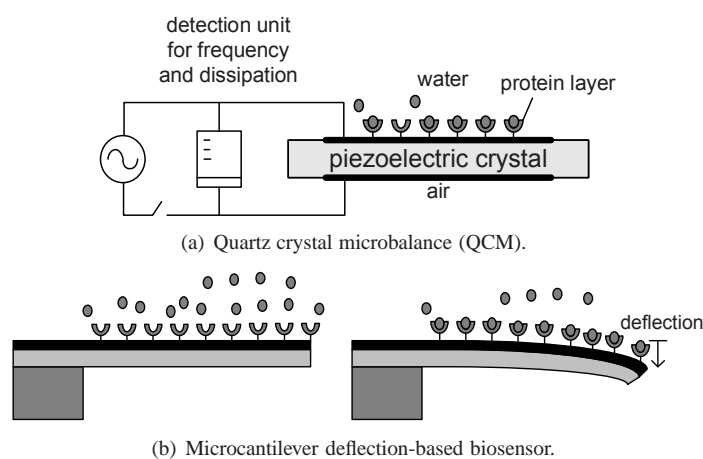


**Figure 1.10:** Illustration of two classes of mechanical biosensors.

resonant oscillatory frequency of the system (Fig. 1.10(a)). Binding of molecules to the surface of the sensor is measured as a shift in the resonance frequency of the device [51–53]. By collecting both the dissipation and the resonance frequency of a quartz crystal, kinetics of both structural changes and mass changes are obtained simultaneously. The dissipation is an indication for whether a soft film (water rich) has formed on the surface or if the film is rigid (less water). One key advantage of this class of sensors is that it is amenable to a wide range of surface coatings. QCM technology has been commercialized, a.o. by ‘Q-sense’, and can be used to characterize the formation of thin films (nm) such as proteins, polymers and cells onto surfaces in liquid [54].

Microcantilevers are a second class of mechanical biosensors, illustrated in Fig. 1.10(b). A binding event near a cantilever surface can be transduced with three methods: deflection of the cantilever [55], a change in the resonance frequency of the cantilevers [56], or a change in the stress exerted on the cantilever, which in turn

generates an electric current in an attached piezoelectric element. To achieve great sensitivity, especially when working in liquids, it is necessary to pre-energize the cantilevers by using alternating electric, magnetic, or acoustic fields. The simplest transduction event to monitor is the change in deflection, measured by reflecting a laser beam off the back of a cantilever and measuring the position with a split photodiode.

A review by Carrascosa et al. [57] covers the basic working principles and the types of cantilever sensor formats, the fabrication and the reported applications in chemical and biological analysis, trends in cantilever fabrication, examples of the commercial instrumentation available, and future developments.

Recently, report [58] demonstrated sensitive protein detection using very large arrays of up to 960 individually readable microcantilevers with 1 ng/ml PSA (prostate-specific antigen) detection limit and minimal response to non-specific proteins at much higher concentration. Currently, several companies are developing commercial microcantilever-based systems, including Cation [59], BioScale [60] and Concentris [61].

### 1.5.3 Electrical biosensors

Electrical biosensors relate on a binding-induced change in some electrical property of a circuitry of which the sensor is a vital component. A common mode of electrical biosensing is based on the principles of the field effect transistor (FET). In normal transistor operation, a semiconducting element is attached to a source and a drain electrode, and current flowing through the element is modulated by changing the voltage applied to a gate electrode. In a FET-based nanowire biosensor configuration, the SiNW (silicon nanowire), functionalized with appropriate receptor molecules is connected to a source and drain electrode (see Fig. 1.11). Binding of target biomolecules changes the dielectric environment around the nanowires and plays a role similar to that of the gate electrode. Thus, molecular binding can be directly quantitated as a change in the conductivity of the nanowires [62]. The small size of nanowires means that individual binding events result in a more significant change in the electrical properties of the circuit. This unique feature of nanowire FETs provides ultrahigh sensitivity down to a single virus [63]. A significant challenge of multiplexed biosensing with nanowire FETs however, relates to the integration of nanowires on substrates with reproducibility and uniformity [64, 65].

Carbon nanotubes (CNTs) and electrochemical impedance spectroscopy (EIS) are two alternative electrical biosensing implementations. CNTs have been investigated for a number of applications because of their unique structure-dependent electronic and mechanical properties [66]. CNT arrays in FET configuration have shown potential for biological detection. However, widespread utility has been

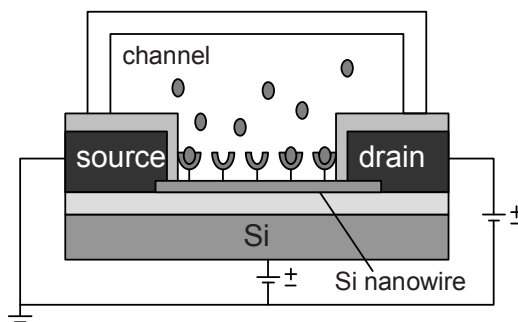


**Figure 1.11:** A silicon nanowire based field effect transistor as a biosensor. A binding event with a net positive charge yields a decrease in the conductance.

limited to date by difficulties in controlling the physical parameters relevant to biosensing: length, diameter and chirality. In EIS, sensing is accomplished by measuring changes in the resistance and/or capacitance of the electrode/solution interface upon binding of a target molecule to a receptor-functionalized surface [67, 68]. At this stage, several commercialized systems are already available for cell-based screening (ACEA Bioscience [69], Applied BioPhysics [70]).

In general, electrical detection methods have been suggested as attractive alternatives to optical readouts owing to their low cost, low power consumption, ease of miniaturization, and potential multiplexing capability. However some significant challenges are to be addressed. One inherent challenge is that they suffer reduced sensitivity when operated at physiological ionic strengths (approximately 0.15 M). Ions in solution respond similarly to the biomolecular target, and thus the device can experience a much diminished response to the binding event [71]. This can be avoided by desalting the sample prior to analysis, but introduces an additional preparative step prior to analysis.

A second challenge is to avoid disturbing the receptor molecule layer: covalent bond energies are on the order of 13 eV but biomolecule binding energies can be much less, and applied voltages will apply a force on charged molecules [68]. EIS performs best on that front, the applied voltage can be quite small, an important advantage over voltammetry or amperometry where more extreme voltages are applied.

## 1.6 Conclusion

In this chapter we introduce the concept of this work: label-free optical biosensing with microring resonators. We started with a general introduction on biosensors, with a focus on affinity biosensors and the main biosensor requirements. The most

promising application areas include drug discovery, point-of-care diagnostics, environmental control and food testing. The basic working principle of biosensing with ring resonator biosensors was explained and we justified the choice of silicon-on-insulator as a material platform for integrated biosensors. The high index contrast enables achievement of a low detection limit and high integration density. On top of that, the possibility of reuse of CMOS electronics fabrication equipment leads to mass fabrication of biochips at very low cost. Integrated biosensing has become a vast area of research and many configurations have started to be commercially implemented. We gave an overview of the three main biosensor categories: optical, electrical and mechanical biosensors with several sub-classes.

## References

- [1] M. A. Cooper. *Label-free biosensors Techniques and Applications*. Cambridge University Press, New York, USA, 2009.
- [2] W. E. Moerner. *New directions in single-molecule imaging and analysis*. Proceedings of the National Academy of Sciences of the United States of America, 104(31):12596–12602, 2007.
- [3] X. B. Yu, D. K. Xu, and Q. Cheng. *Label-free detection methods for protein microarrays*. Proteomics, 6(20):5493–5503, 2006.
- [4] C. H. Ahn, J. W. Choi, G. Beaucage, J. H. Nevin, J. B. Lee, A. Puntambekar, and J. Y. Lee. *Disposable Smart lab on a chip for point-of-care clinical diagnostics*. Proceedings of the IEEE, 92(1):154–173, 2004.
- [5] M. A. Cooper. *Optical biosensors in drug discovery*. Nature Reviews Drug Discovery, 1(7):515–528, 2002.
- [6] F. S. Ligler. *Perspective on Optical Biosensors and Integrated Sensor Systems*. Analytical Chemistry, 81(2):519–526, 2009.
- [7] P. Yager, T. Edwards, E. Fu, K. Helton, K. Nelson, M. R. Tam, and B. H. Weigl. *Microfluidic diagnostic technologies for global public health*. Nature, 442(7101):412–418, 2006.
- [8] K. R. Rogers. *Recent advances in biosensor techniques for environmental monitoring*. Analytica Chimica Acta, 568(1-2):222–231, 2006.
- [9] B.E.A. Saleh and M.C. Teich. *Fundamentals of Photonics*. John Wiley and Sons, Inc, Hoboken, New Jersey, 2007.
- [10] A. Yalcin, K. C. Papat, J. C. Aldridge, T. A. Desai, J. Hryniewicz, N. Chbouki, B. E. Little, O. King, V. Van, S. Chu, D. Gill, M. Anthes-Washburn, and M. S. Unlu. *Optical sensing of biomolecules using micro-ring resonators*. IEEE Journal of Selected Topics in Quantum Electronics, 12(1):148–155, 2006.
- [11] A. Ramachandran, S. Wang, J. Clarke, S. J. Ja, D. Goad, L. Wald, E. M. Flood, E. Knobbe, J. V. Hryniewicz, S. T. Chu, D. Gill, W. Chen, O. King, and B. E. Little. *A universal biosensing platform based on optical micro-ring resonators*. Biosensors & Bioelectronics, 23(7):939–944, 2008.
- [12] C. Y. Chao, W. Fung, and L. J. Guo. *Polymer microring resonators for biochemical sensing applications*. IEEE Journal of Selected Topics in Quantum Electronics, 12(1):134–142, 2006.

- 
- [13] A. Ksendzov and Y. Lin. *Integrated optics ring-resonator sensors for protein detection*. Optics Letters, 30(24):3344–3346, 2005.
- [14] S. K. Selvaraja, P. Jaenen, W. Bogaerts, D. Van Thourhout, P. Dumon, and R. Baets. *Fabrication of Photonic Wire and Crystal Circuits in Silicon-on-Insulator Using 193-nm Optical Lithography*. Lightwave Technology, Journal of, 27(18):4076–4083, 2009.
- [15] W. Bogaerts, R. Baets, P. Dumon, V. Wiaux, S. Beckx, D. Taillaert, B. Luysaert, J. Van Campenhout, P. Bienstman, and D. Van Thourhout. *Nanophotonic waveguides in silicon-on-insulator fabricated with CMOS technology*. Journal of Lightwave Technology, 23(1):401–412, 2005.
- [16] S. K. Selvaraja, W. Bogaerts, P. Dumon, D. Van Thourhout, and R. G. Baets. *Subnanometer Linewidth Uniformity in Silicon Nanophotonic Waveguide Devices Using CMOS Fabrication Technology*. Journal of selected topics in quantum electronics, 2010.
- [17] G. Roelkens. *Heterogeneous III-V/Silicon photonics: bonding technology and integrated devices*. PhD thesis, Ghent University, 2006-2007.
- [18] L. Liu, J. Van Campenhout, G. Roelkens, R. A. Soref, D. Van Thourhout, P. Rojo-Romeo, P. Regreny, C. Seassal, J. M. Fedeli, and R. Baets. *Carrier-injection-based electro-optic modulator on silicon-on-insulator with a heterogeneously integrated III-V microdisk cavity*. Optics Letters, 33(21):2518–2520, 2008.
- [19] J. Van Campenhout, L. Liu, P. R. Romeo, D. Van Thourhout, C. Seassal, P. Regreny, L. Di Cioccio, J. M. Fedeli, and R. Baets. *A compact SOI-integrated multiwavelength laser source based on cascaded InP microdisks*. IEEE Photonics Technology Letters, 20(13-16):1345–1347, 2008.
- [20] J. Brouckaert, G. Roelkens, S. K. Selvaraja, W. Bogaerts, P. Dumon, S. Verstuyft, D. Van Thourhout, and R. Baets. *Silicon-on-insulator CWDM power monitor/receiver with integrated thin-film InGaAs photodetectors*. IEEE Photonics Technology Letters, pages 1423–5, 2009.
- [21] G. Roelkens, J. Van Campenhout, J. Brouckaert, D. Van Thourhout, R. Baets, P. R. Romeo, P. Regreny, A. Kazmierczak, C. Seassal, X. Letartre, G. Hollinger, J. M. Fedeli, L. Di Cioccio, and C. Lagahe-Blanchard. *III-V/Si photonics by die to wafer bonding*. Materials Today, 10(7-8):36–43, 2007.
- [22] L. Liu, R. Kumar, K. Huybrechts, T. Spuessens, G. Roelkens, E.-J. Geluk, T. de Vries, P. Regreny, D. Van Thourhout, R. Baets, and G. Morthier. *An ultra-small, low-power, all-optical flip-flop memory on a silicon chip*. Nature Photonics, 2010.

- [23] A. J. Qavi, A. L. Washburn, J. Y. Byeon, and R. C. Bailey. *Label-free technologies for quantitative multiparameter biological analysis*. Analytical and Bioanalytical Chemistry, 394(1):121–135, 2009.
- [24] X. D. Fan, I. M. White, S. I. Shopoua, H. Y. Zhu, J. D. Suter, and Y. Z. Sun. *Sensitive optical biosensors for unlabeled targets: A review*. Analytica Chimica Acta, 620(1-2):8–26, 2008.
- [25] P. V. Lambeck. *Integrated optical sensors for the chemical domain*. Measurement Science & Technology, 17(8):R93–R116, 2006.
- [26] E. Yeatman and E. A. Ash. *Surface-plasmon microscopy*. Electronics Letters, 23(20):1091–1092, 1987.
- [27] E. A. Smith and R. M. Corn. *Surface plasmon resonance imaging as a tool to monitor biomolecular interactions in an array based format*. Applied Spectroscopy, 57(11):320A–332A, 2003.
- [28] C. T. Campbell and G. Kim. *SPR microscopy and its applications to high-throughput analyses of biomolecular binding events and their kinetics*. Biomaterials, 28(15):2380–2392, 2007.
- [29] P. Debackere. *Nanophotonic biosensor based on surface plasmon interference*. PhD thesis, Ghent University, 2009-2010.
- [30] P. Debackere, S. Scheerlinck, P. Bienstman, and R. Baets. *Surface plasmon interferometer in silicon-on-insulator: novel concept for an integrated biosensor*. Optics Express, 14(16):7063–7072, 2006.
- [31] P. Debackere, R. Baets, and P. Bienstman. *Bulk sensing experiments using a surface-plasmon interferometer*. Optics Letters, 34(18):2858–2860, 2009.
- [32] B. H. Schneider, E. L. Dickinson, M. D. Vach, J. V. Hoijer, and L. V. Howard. *Optical chip immunoassay for hCG in human whole blood*. Biosensors & Bioelectronics, 15(11-12):597–604, 2000.
- [33] [www.farfieldgroup.com](http://www.farfieldgroup.com), 2010.
- [34] M. M. Varma, H. D. Inerowicz, F. E. Regnier, and D. D. Nolte. *High-speed label-free detection by spinning-disk micro-interferometry*. Biosensors & Bioelectronics, 19(11):1371–1376, 2004.
- [35] E. Ozkumur, J. W. Needham, D. A. Bergstein, R. Gonzalez, M. Cabodi, J. M. Gershoni, B. B. Goldberg, and M. S. Unlu. *Label-free and dynamic detection of biomolecular interactions for high-throughput microarray applications*. Proceedings of the National Academy of Sciences of the United States of America, 105(23):7988–7992, 2008.

- [36] S. Arnold, R. Ramjit, D. Keng, V. Kolchenko, I. Teraoka. *MicroParticle photophysics illuminates viral bio-sensing*. Faraday Discussions, 137:65–83, 2008.
- [37] [www.quadraspec.com](http://www.quadraspec.com), 2010.
- [38] [www.siliconkinetics.com](http://www.siliconkinetics.com).
- [39] V. S. Y. Lin, K. Motesharei, K. P. S. Dancil, M. J. Sailor, and M. R. Ghadiri. *A porous silicon-based optical interferometric biosensor*. Science, 278(5339):840–843, 1997.
- [40] F. Vollmer and S. Arnold. *Whispering-gallery-mode biosensing: label-free detection down to single molecules*. Nature Methods, 5(7):591–596, 2008.
- [41] R. W. Boyd and J. E. Heebner. *Sensitive disk resonator photonic biosensor*. Applied Optics, 40(31):5742–5747, 2001.
- [42] A. M. Armani, R. P. Kulkarni, S. E. Fraser, R. C. Flagan, and K. J. Vahala. *Label-free, single-molecule detection with optical microcavities*. Science, 317(5839):783–787, 2007.
- [43] Adam L. Washburn, L. Cary Gunn, and Ryan C. Bailey. *Label-Free Quantitation of a Cancer Biomarker in Complex Media Using Silicon Photonic Microring Resonators*. Analytical Chemistry, 81(22):9499–9506, 2009.
- [44] D. X. Xu, A. Densmore, A. Delage, P. Waldron, R. McKinnon, S. Janz, J. Lapointe, G. Lopinski, T. Mischki, E. Post, P. Cheben, and J. H. Schmid. *Folded cavity SOI microring sensors for high sensitivity and real time measurement of biomolecular binding*. Optics Express, 16(19):15137–15148, 2008.
- [45] H. Y. Zhu, I. M. White, J. D. Suter, P. S. Dale, and X. D. Fan. *Analysis of biomolecule detection with optofluidic ring resonator sensors*. Optics Express, 15(15):9139–9146, 2007.
- [46] J. D. Suter, I. M. White, H. Y. Zhu, H. D. Shi, C. W. Caldwell, and X. D. Fan. *Label-free quantitative DNA detection using the liquid core optical ring resonator*. Biosensors & Bioelectronics, 23(7):1003–1009, 2008.
- [47] I. M. White, H. Oveys, and X. D. Fan. *Liquid-core optical ring-resonator sensors*. Optics Letters, 31(9):1319–1321, 2006.
- [48] M. Lee and P. M. Fauchet. *Two-dimensional silicon photonic crystal based biosensing platform for protein detection*. Optics Express, 15(8):4530–4535, 2007.

- [49] J. H. Schmid, W. Sinclair, J. Garcia, S. Janz, J. Lapointe, D. Poitras, Y. Li, T. Mischki, G. Lopinski, P. Cheben, A. Delage, A. Densmore, P. Waldron, and D. X. Xu. *Silicon-on-insulator guided mode resonant grating for evanescent field molecular sensing*. *Optics Express*, 17(20):18371–18380, 2009.
- [50] S. Mandal, J. M. Goddard, and D. Erickson. *A multiplexed optofluidic biomolecular sensor for low mass detection*. *Lab on a Chip*, 9(20):2924–2932, 2009.
- [51] K. Lange, B. E. Rapp, and M. Rapp. *Surface acoustic wave biosensors: a review*. *Analytical and Bioanalytical Chemistry*, 391(5):1509–1519, 2008.
- [52] E. Zampetti, S. Pantalei, A. Macagnano, E. Proietti, C. Di Natale, and A. D’Amico. *Use of a multiplexed oscillator in a miniaturized electronic nose based on a multichannel quartz crystal microbalance*. *Sensors and Actuators B-Chemical*, 131(1):159–166, 2008.
- [53] B. Zhang, Q. G. Mao, X. Zhang, T. L. Jiang, M. Chen, F. Yu, and W. L. Fu. *A novel piezoelectric quartz micro-array immunosensor based on self-assembled monolayer for determination of human chorionic gonadotropin*. *Biosensors & Bioelectronics*, 19(7):711–720, 2004.
- [54] [www.qsense.com](http://www.qsense.com), 2010.
- [55] N. V. Lavrik, M. J. Sepaniak, and P. G. Datskos. *Cantilever transducers as a platform for chemical and biological sensors*. *Review of Scientific Instruments*, 75(7):2229–2253, 2004.
- [56] B. Ilic, D. Czaplewski, M. Zalalutdinov, H. G. Craighead, P. Neuzil, C. Campagnolo, and C. Batt. *Single cell detection with micromechanical oscillators*. *Journal of Vacuum Science & Technology B*, 19(6):2825–2828, 2001.
- [57] L. G. Carrascosa, M. Moreno, M. Alvarez, and L. M. Lechuga. *Nanomechanical biosensors: a new sensing tool*. *Trac-Trends in Analytical Chemistry*, 25(3):196–206, 2006.
- [58] M. Yue, J. C. Stachowiak, H. Lin, R. Datar, R. Cote, and A. Majumdar. *Label-free protein recognition two-dimensional array using nanomechanical sensors*. *Nano Letters*, 8(2):520–524, 2008.
- [59] [www.cantion.com](http://www.cantion.com), 2010.
- [60] [www.bioscale.com](http://www.bioscale.com), 2010.
- [61] [www.concentris.com](http://www.concentris.com), 2010.

- 
- [62] F. Patolsky and C. M. Lieber. *Nanowire nanosensors*. *Materials Today*, 8(4):20–8, 2005.
- [63] F. Patolsky, G. F. Zheng, O. Hayden, M. Lakadamyali, X. W. Zhuang, and C. M. Lieber. *Electrical detection of single viruses*. *Proceedings of the National Academy of Sciences of the United States of America*, 101(39):14017–14022, 2004.
- [64] Z. Y. Fan, J. C. Ho, Z. A. Jacobson, R. Yerushalmi, R. L. Alley, H. Razavi, and A. Javey. *Wafer-scale assembly of highly ordered semiconductor nanowire arrays by contact printing*. *Nano Letters*, 8(1):20–25, 2008.
- [65] N. A. Melosh, A. Boukai, F. Diana, B. Gerardot, A. Badolato, P. M. Petroff, and J. R. Heath. *Ultrahigh-density nanowire lattices and circuits*. *Science*, 300(5616):112–115, 2003.
- [66] J. Wang. *Nanomaterial-based electrochemical biosensors*. *Analyst*, 130(4):421–426, 2005.
- [67] F. Lisdat and D. Schafer. *The use of electrochemical impedance spectroscopy for biosensing*. *Analytical and Bioanalytical Chemistry*, 391(5):1555–1567, 2008.
- [68] J. S. Daniels and N. Pourmand. *Label-free impedance biosensors: Opportunities and challenges*. *Electroanalysis*, 19(12):1239–1257, 2007.
- [69] [www.aceabio.com/](http://www.aceabio.com/), 2010.
- [70] [www.biophysics.com](http://www.biophysics.com/), 2010.
- [71] E. Stern, R. Wagner, F. J. Sigworth, R. Breaker, T. M. Fahmy, and M. A. Reed. *Importance of the debye screening length on nanowire field effect transistor sensors*. *Nano Letters*, 7:3405–3409, 2007.



# 2

## Evanescent field sensing with SOI microring resonators

This chapter is devoted to a study of the key device in this PhD project: a single microring resonator, used as a sensor. In the first section, we study the relation between the design parameters of a single ring microresonator and its performance. We examine silicon-on-insulator (SOI) microring resonators with a focus on their sensing capabilities. However, at the same time we aim to give a useful overview with generic design guidelines for microring filters.

All devices are fabricated using standard CMOS processing tools, in particular 193nm deep-UV lithography and dry etching. Throughout this work, the fabrication process has evolved immensely [1–4]. The experiments in chapter 7 are performed in the course of several years and thus make use of optical chips that are fabricated in different optimization stages. In this chapter we discuss the performance of the devices as they are today, anno 2009. All devices are fabricated according to the processing steps described by Selvaraja et al. in [4].

When using a ring resonator as a sensor, one has to track wavelength shifts caused by refractive index changes of the environment. This resonance wavelength shift is studied in section 2.2.

The detection resolution, being the minimum detectable wavelength shift, is an important property of a sensor system. In section 2.3 we search for the resolution for resonators with various spectral parameters and various interrogation methods. The measurement setups employed to obtain the results described in chapter 7 are compared in terms of the measurement resolution they provide.

Combination of the results of sections 2.3 and 2.2 leads to a conclusion on the overall detection limit of SOI microring resonator biosensors (section 2.4).

At the end of this chapter other optical waveguide configurations for sensing are briefly discussed and their performance is compared to the performance of a single ring microresonator biosensor.

## 2.1 SOI microring resonators

Optical microresonators are extensively described in literature [5–8]. In general a ring resonator consists of a loop and a coupling mechanism to access the loop. When waves that travel in the loop have a round trip phase shift that equals an integer times  $2\pi$ , the waves interfere constructively and the cavity is in resonance. From this condition we can calculate the resonance wavelength:

$$\lambda_{res} = \frac{n_{eff}L}{m} \quad m = 1,2,3... \quad (2.1)$$

, where  $L$  is the cavity length and  $n_{eff}$  is the effective index of the resonant mode. In what follows, we will briefly summarize all concepts and formulas that are needed for understanding the rest of the manuscript: all-pass and add-drop configuration, photonic wires, coupling section and spectral characteristics. After that, the performance of fabricated SOI ring resonators is discussed (section 2.1.4).

**All-pass ring resonators** In its simplest form a ring resonator can be constructed from feeding one output of a directional coupler back into its input, the so-called all-pass or notch filter configuration (see Fig. 2.1 A). The basic spectral properties can easily be derived by assuming continuous wave (CW) operation and matching fields. Under the assumption that reflections are negligible, from the ratio of the transmitted and the incident field, we obtain the transmission  $T_n$ <sup>1</sup>:

$$T_n = \frac{I_{pass}}{I_{input}} = \frac{a^2 - 2r \cos \phi + r^2}{1 - 2r \cos \phi + (ra)^2} \quad (2.2)$$

$\phi = \beta L$  is the single-pass phase shift, with  $L$  the round trip length and  $\beta$  the propagation constant of the circulating mode.  $a$  is the single-pass amplitude transmission, including both propagation loss in the ring and loss in the couplers. It relates to the power attenuation coefficient  $\alpha$  [1/cm] as  $a^2 = \exp(-\alpha L)$ .  $r$  and  $k$  are the self- and cross-coupling coefficients. Hence  $r^2$  and  $k^2$  are the power splitting ratios of the coupler, they are assumed to satisfy  $r^2 + k^2 = 1$ . This assumption causes a small error on the transmission power levels. The width of the

<sup>1</sup>Notation: we use subscript  $n$  from *notch* not to confuse with the pass transmission  $T_p$  from an add-drop filter in the next paragraph.

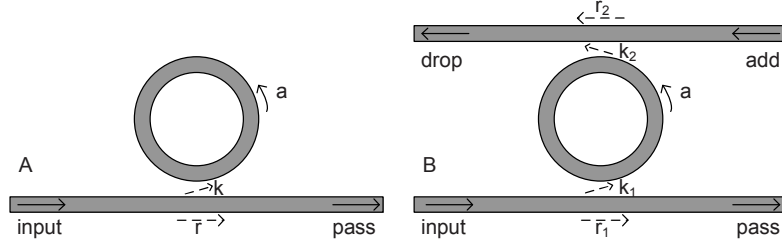


Figure 2.1: (A) All-pass and (B) add-drop ring resonator.

resonance remains correct, as long as the losses that are introduced by the couplers are included in the resonator round trip loss coefficient  $a$ .

When the cavity is in resonance the phase shift equals an integer times  $2\pi$ . For ideal cavities with zero attenuation,  $a \approx 1$ , the transmission is unity for all values of detuning  $\phi$ . Under critical coupling, when the coupled power is equal to the power loss in the ring  $1 - a^2 = k^2$  or  $r = a$ , the transmission at resonance drops to zero.

The phase argument of the field transmission varies periodically for different frequencies. All-pass resonators delay incoming signals via the temporary storage of optical energy within the resonator.

**Add-drop ring resonators** When the ring resonator is coupled to two waveguides, the incident field is partly transmitted to the drop port (see Fig. 2.1 B). The transmission to the pass and the drop port can also be derived from CW operation and matching the fields.

$$T_p = \frac{I_{pass}}{I_{input}} = \frac{r_2^2 a^2 - 2r_1 r_2 a \cos\phi + r_1^2}{1 - 2r_1 r_2 a \cos\phi + (r_1 r_2 a)^2} \quad (2.3)$$

$$T_d = \frac{I_{drop}}{I_{input}} = \frac{(1 - r_1^2)(1 - r_2^2)a}{1 - 2r_1 r_2 a \cos\phi + (r_1 r_2 a)^2} \quad (2.4)$$

If the attenuation is negligible ( $a \approx 1$ ), critical coupling occurs at symmetric coupling ( $k_1 = k_2$ ). For a lossy resonator, critical coupling occurs when the losses match the coupling as  $r_2 a = r_1$ . The shape of the transmission curves approximates a Lorentzian curve around resonance.

### 2.1.1 Photonic waveguides

SOI waveguides channel light through transverse and lateral confinement in a silicon 'core' of refractive index 3.47 surrounded by a bottom silicon oxide cladding with index 1.44 and a low index top cladding. A SEM picture of a fabricated SOI

wire was shown in chapter 1, Fig. 1.3. In most of the biosensing applications, the top cladding consists of an aqueous solution like serum, with an index of approximately 1.31 at 1550 nm wavelength [9]. The index contrast between core and cladding is very high, this gives rise to very strong confinement which enables light guiding in bends with very small radii without radiation losses. The criteria for single mode operation are met for a limited range of waveguide dimensions. An SOI photonic wire with a core thickness of 220 nm and width around 450 nm guides a single TE mode. An in-depth study of the dimensions for single mode operation is performed in chapter 3.

**Propagation losses in straight SOI wires** Propagation losses originate from multiple sources and were measured to be  $2.7 \pm 0.06$  dB/cm [4]. *Bulk absorption*, mainly caused by Boron-dopants in the crystalline silicon membrane, accounts for an absorption of 0.02 dB/cm [7]. Dangling bonds and bonded elements at the sidewall introduce *surface state absorption*. For high powers, two-photon absorption and free carrier absorption contribute to the *non-linear absorption*. In the device used in this work, power levels are low enough to avoid non-linear absorption. During propagation, part of the power is coupled to radiative modes in the substrate, this *substrate leakage* is expected to decrease exponentially with bottom cladding thickness. For the bottom oxide of this devices ( $2 \mu\text{m}$ ), these losses are negligible for the TE<sub>00</sub> mode and in the order of 0.001 dB/cm for the TM<sub>00</sub> mode, which was calculated in the PhD thesis of P. Dumon [7]. The fundamental lower limit of propagation losses is associated to *Rayleigh scattering*, caused by deep sub-wavelength index perturbations in the bulk of the waveguides. Thanks to the high quality SOI material, the Rayleigh scattering for the measured devices is expected to be extremely low. *Light scattering at sidewall roughness* is the main propagation loss contributor. The losses are correlated with the periodicity of the roughness as well as its dimensions. In [7] the author elaborates on the effect of sidewall roughness on scattering and phase deviations of the propagating modes in SOI wires. A last small loss figure comes from *scattering at top surface roughness*. Depending on the polishing process that was used for wafer fabrication, top surface roughness can be induced. The rms roughness of the SOI wafers is about 0.1 nm [7], and its calculated loss contribution is negligible.

**Bend losses** The strong mode confinement in SOI wires allows for very sharp bends (radius down to  $3 \mu\text{m}$ ) with still low radiation as compared to bends in conventional waveguides (radius down to  $100 \mu\text{m}$ ). However, both the substrate leakage and scattering loss might be influenced by waveguide bending, as the mode is slightly pushed outwards. Excess bending losses of 500 nm wide SOI waveguides fabricated with 193 nm deep-UV lithography are reported by Selvaraja et al. in [4]. A  $4.5 \mu\text{m}$  radius bend induces 0.01 dB/90° loss. For bend radii below

3  $\mu\text{m}$  the losses increase rapidly to 0.071 dB/90° for a 1  $\mu\text{m}$  radius bend. The excess bending loss of a circular 90° bend includes mode mismatch at the straight-bend interface, coupling to TM and higher order modes in the bend section and propagation loss in the bends.

**Dispersion** Because of the high index contrast, silicon wires are highly dispersive. This means that the effective index of the propagating mode is frequency dependent so that monochromatic waves of different frequencies will travel through the waveguide with different velocities. This causes propagating pulses (that comprise a sum of monochromatic waves) to broaden and to be delayed.

The group velocity  $\nu$  is the velocity at which the envelope of a propagating pulse travels and is a characteristic of the dispersive medium. Since the refractive index is mostly measured as a function of optical wavelength rather than frequency, it is convenient to express the group velocity  $\nu$  at a central frequency  $\omega_0$  in terms of  $n(\lambda)$ :  $\nu = \frac{c}{n_g}$  with  $n_g$  the group index of SOI waveguide mode:

$$n_g = n_{eff} - \lambda_0 \frac{dn_{eff}}{d\lambda_0} \quad (2.5)$$

where  $\lambda_0 = 2\pi c/\omega$ .

An SOI photonic wire has a normal first-order dispersion in the wavelength range of interest and for the dimensions we performed the characterization on:  $\frac{dn_{eff}}{d\lambda} < 0$  [7, 10, 11]. The group index is almost twice as large as the effective index. This has a large impact on the spectral characteristics of a resonator and on the sensitivity of the sensor. SOI resonator sensors rely on the resonance wavelength shift when the effective index of the mode changes. Because of dispersion, this wavelength shift will induce an additional effective index change. Unfortunately both effects counteract. The influence of the dispersion on the sensitivity of an SOI waveguide will be discussed in section 2.2.

### 2.1.2 Coupling section

A good understanding of the behavior of the coupling section is crucial for ring resonator filter design. Especially for multistage ring resonators (section 2.5), the design of directional couplers is one of the main bottlenecks to achieve accurate operation. Two coupling schemes are commonly used for coupling light from a waveguide to a resonator: multimode interferometers (MMIs) and directional waveguide couplers.

Although MMIs [12] can provide 50% coupling with high tolerance to dimensional variations, they are much more unstable when used for very low coupling as required for near critical coupling in low loss ring resonators. Moreover they are typically larger than directional couplers and they require a two-step etch process [13]. A study on MMIs in SOI is ongoing within our research group.

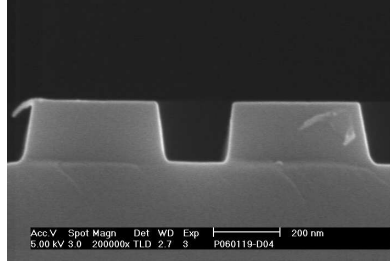


**Figure 2.2:** SEM cross section of typical SOI directional coupler.

Directional waveguide couplers consist of two waveguides in close proximity. A typical SEM cross section is shown in Fig. 2.2. Their theoretical behavior is well documented [14, 15], however few experimental studies are reported in literature. In this section, the coupling between a straight waveguide and a bend-straight-bend waveguide is determined experimentally. This is the configuration that was mostly used for the racetrack resonators in this work. Its compactness ensures coupling control with conservation of a high FSR (the FSR scales inversely with the total resonator length  $L$ ).

**Method** A waveguide-based Mach-Zehnder interferometer (MZI) was used as a test device for this study. It consists of a splitter, two waveguides with a given group delay, and a combiner. The splitter is a directional waveguide coupler, the combiner is a balanced MMI with 50% combining ratio. Fig. 2.3 shows the device with a zoom on the directional coupler. When both the splitting and combining ratios are 50%, the MZI is balanced. In this case, complete destructive interference occurs when the phases in both arms are opposite. When the splitting or combining ratios are different, we can extract the imbalance from the wavelength dependent ratio between adjacent minima and maxima of the output spectrum. The output field  $E_{out}$  is calculated using the matrix formalism<sup>2</sup> [16]:

$$[T_{E_{out}}] = [T_{combiner}] \cdot [T_{interferometer}] \cdot [T_{splitter}] \cdot [T_{E_{in}}]$$

$$E_{out} = \begin{bmatrix} \frac{1}{\sqrt{2}} & \frac{1}{\sqrt{2}} \end{bmatrix} \begin{bmatrix} e^{-j\phi_1} & 0 \\ 0 & e^{-j\phi_2} \end{bmatrix} \begin{bmatrix} \sqrt{1-k^2} & jk \\ jk & \sqrt{1-k^2} \end{bmatrix} \begin{bmatrix} 0 \\ E_{in} \end{bmatrix}$$

<sup>2</sup>The transfer matrix of an electromagnetic circuit is a matrix that describes the relation between the output quantities and the input quantities. When cascading different circuits, the transfer matrix of the entire system is found by multiplication of the individual matrices of the cascade. More information can be found in various text books.

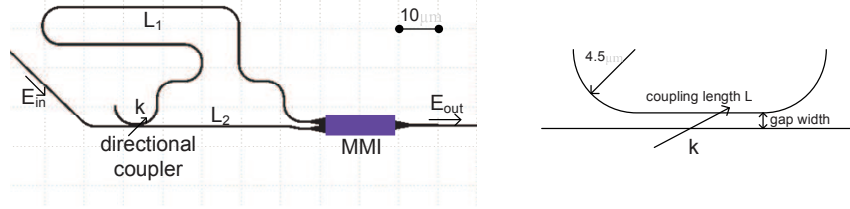


**Figure 2.3:** Left: A Mach-Zehnder Interferometer (MZI) was used as a test device for the study of directional waveguide couplers. From the adjacent minima and maxima of its spectrum we can extract the coupling coefficient of the splitter or combiner. Right: Zoom on the directional waveguide coupler.

$$E_{out} = \frac{1}{\sqrt{2}} j k e^{-j\phi_1} E_{in} + \frac{1}{\sqrt{2}} \sqrt{1-k^2} e^{-j\phi_2} E_{in}$$

$$I_{out} = |E_{out}|^2 = \frac{1}{2} \left( 1 + 2k\sqrt{1-k^2} \sin(\Delta\phi) \right) I_{in}$$

$$I_{out_{dBm}} - I_{in_{dBm}} = 10 \log \left( \frac{1}{2} + k\sqrt{1-k^2} \sin(\Delta\phi) \right)$$

With  $\phi_1 = \beta L_1$ ,  $\phi_2 = \beta L_2$  and  $\Delta\phi = \phi_1 - \phi_2$ . The directional couplers are assumed to be lossless. The method is illustrated in Fig. 2.4. From the wavelength dependent extinction ratio (ER) between the upper and lower envelope of the normalized intensity, we can determine the wavelength dependent amplitude cross-coupling coefficient  $k$ :

$$ER_{dB} = 10 \log \left( \frac{\frac{1}{2} + k\sqrt{1-k^2}}{\frac{1}{2} - k\sqrt{1-k^2}} \right) \quad (2.6)$$

$$ER = 10^{\frac{ER_{dB}}{10}} = \frac{\frac{1}{2} + k\sqrt{1-k^2}}{\frac{1}{2} - k\sqrt{1-k^2}} \quad (2.7)$$

$$\Leftrightarrow k^2 = K_{\pm} = \frac{1}{2} \pm \frac{1}{2} \sqrt{1 - \left( \frac{ER-1}{ER+1} \right)^2} \quad (2.8)$$

For our experiments, the coupling length ( $L$ ) and the gap width ( $G$ ) are swept. This way we obtain a two-dimensional sweep of the coupling coefficient. Of course, by scanning a broad spectrum, the wavelength dependence is studied as well. The  $L$  sweep was used to fit the power coupling coefficient to a sine squared and obtain the coupling coefficient per unit distance  $\kappa$  [ $1/\mu m$ ] and the offset coupling

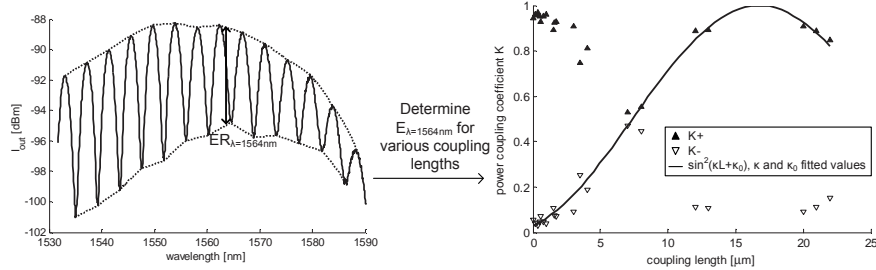


**Figure 2.4:** Method to obtain the wavelength dependent coupling coefficient per unit distance  $\kappa$  [ $1/\mu\text{m}$ ] as well as the initial coupling coefficient  $\kappa_0$  of a directional waveguide coupler from the output intensity of a Mach-Zehnder interferometer.

coefficient due to the bend sections  $\kappa_0$ <sup>3</sup>:

$$K(\lambda) = k(\lambda)^2 = \sin^2(\kappa(\lambda)L + \kappa_0(\lambda))$$

This fitting was performed for all wavelengths and for all gap widths.

**Results** We compared coupling coefficients of symmetrical and asymmetrical SOI waveguide directional couplers, i.e. with  $\text{SiO}_2$  and air cladding respectively. From fabrication data we know the waveguide widths are 427 nm and gap widths are 195, 226, 239 and 261 nm. Results are shown in Fig. 2.5. The first graphs show  $\kappa$  [ $1/\mu\text{m}$ ] and  $\kappa_0$  as a function of wavelength. As expected, the coupling increases with longer wavelengths because of the lower mode confinement.  $\kappa_0$  is very sensitive to dimensional deviations, wavelength and fitting errors and hence displays a larger variation. Fig. 2.6 compares  $\kappa$  at 1550 nm wavelength for a waveguide with air and oxide cladding. Waveguides that are covered with  $\text{SiO}_2$  have a lower index contrast, hence the mode is less confined and coupling coefficients are higher.

The beat length is the propagation length after which all optical power is transferred to the other waveguide and is equal to  $\frac{\pi}{2\kappa} - \frac{\kappa_0}{\kappa}$ . The beat length of a directional coupler with an air cladding is about 1.5 times longer than the beat length of a directional coupler with an  $\text{SiO}_2$  cladding because of the stronger mode confinement.

Fitting of a sine squared to the data obtained from the extinction ratio is not trivial for two reasons. A first issue is that equation 2.7 has two solutions  $K_+$  and  $K_-$ . For all lengths  $L$  one of them has to be discarded. Second, the accuracy of measured spectra is limited because of the limited resolution of the Agilent Spectrum Analyzer used for the experiments (60 pm). This limited resolution results in larger errors on the sharpest features. The error is thus larger on higher extinction ratios,

<sup>3</sup>This situation solely describes coupling with zero phase mismatch, meaning the propagation constants of the ground modes of both waveguides are equal.

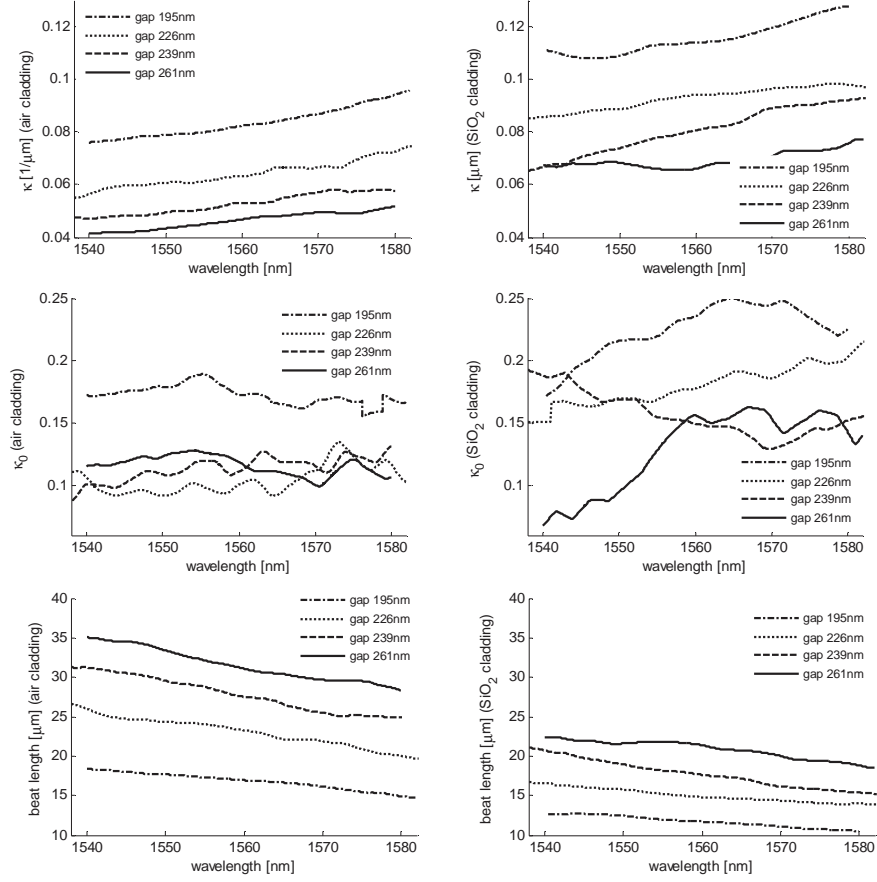


**Figure 2.5:** Directional waveguide coupler study. Measured coupling coefficient per unit length  $\kappa$  [ $1/\mu\text{m}$ ], initial coupling coefficient  $\kappa_0$  and beat length  $L_{\pi/2}$  versus wavelength. Waveguide widths=427 nm, left: air cladding, right: SiO<sub>2</sub> cladding.

corresponding to coupling coefficients near 50%. However, for the experiments presented here, fewer data points were taken around 50% coupling, which naturally decreases the impact of the larger error for most of the results. These fitting complexities cause the small defects in the fitting results of Fig. 2.5.

### 2.1.3 Spectral characteristics

The spectrum of a ring resonator is depicted in Fig. 2.7. When the round trip phase shift equals an integer times  $2\pi$ , the cavity is in resonance. The resonance wavelength equals:

$$\lambda_{res} = \frac{n_{eff}L}{m} \quad m = 1,2,3... \quad (2.9)$$

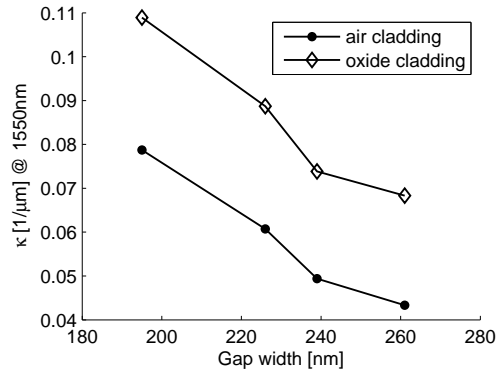


**Figure 2.6:** Measured coupling coefficient per unit length  $\kappa [1/\mu\text{m}]$  at 1550 nm as a function of gap width for directional couplers with air and  $\text{SiO}_2$  cladding.

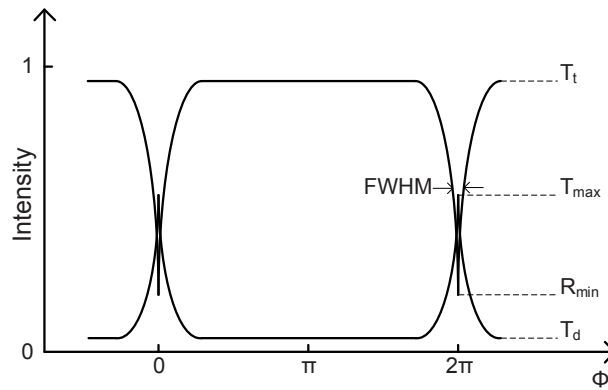


**Figure 2.7:** General spectrum of a ring resonator with important parameters.

The characteristic parameters are indicated in the figure. They depend on the losses and coupling coefficients and can be extracted directly from the formulas for transmission (2.2), (2.3) and (2.4). The results are listed below. In section 2.1.4 we will perform the reverse operation: starting from the measured spectral characteristics, the losses and coupling coefficients of SOI ring resonators will be determined.

**Resonance width** From expressions (2.2) (2.3) and (2.4) we can derive the full width at half maximum (FWHM) of the resonance spectrum<sup>4</sup>:

$$\text{All-pass ring resonator: } FWHM = \frac{(1-ra)\lambda_{res}^2}{\pi n_g L \sqrt{ra}} \quad (2.10)$$

$$\text{Add-drop ring resonator: } FWHM = \frac{(1-r_1 r_2 a)\lambda_{res}^2}{\pi n_g L \sqrt{r_1 r_2 a}} \quad (2.11)$$

**Free spectral range** Within a first order approximation of the dispersion, the wavelength range between two resonances or free spectral range (FSR) in function of wavelength equals<sup>5</sup>:

$$FSR = \frac{\lambda^2}{n_g L} \quad (2.12)$$

with L the round trip length. The strong confinement in SOI wires allows for very sharp bends (radius down to 3  $\mu\text{m}$ ) with still low radiation. This largely increases the potential FSR of SOI ring resonators as compared to conventional optical resonators.

**Extinction ratio** The on-off extinction ratio of through, respectively drop transmission is equal to  $\frac{T_t}{R_{min}}$ , respectively  $\frac{T_{max}}{T_d}$ . The extinction ratio at resonance between through and drop port of an add-drop resonator is given by  $\frac{T_{max}}{R_{min}}$ .  $T_t$ ,  $R_{min}$ ,  $T_{max}$  and  $T_d$  are defined as:

<sup>4</sup>Possible derivation method: use third order Taylor series around resonance and substitute  $\sin(\phi/2) = 0$ ,  $\cos(\phi/2) = 1$ ,  $\frac{dn_{eff}}{d\lambda} = -\frac{n_g - n_{eff}}{\lambda}$ .

<sup>5</sup>Possible derivation method: start with the definition,  $FSR(\lambda_m) = \lambda_m - \lambda_{m+1} = L \left( \frac{n_{eff}(\lambda_m)}{m} - \frac{n_{eff}(\lambda_{m+1})}{m+1} \right)$ . In first order approximation:  $n_{eff}(\lambda_{m+1}) = n_{eff}(\lambda_m) + \left( \frac{dn}{d\lambda} \right)_{\lambda_m} (\lambda_{m+1} - \lambda_m) = n_{eff}(\lambda_m) + \left( \frac{dn}{d\lambda} \right)_{\lambda_m} FSR(\lambda_m)$ . Substitution of this formula in the formula for FSR and including the definition of the group index (2.5), returns formula (2.12).

$$\text{All-pass ring resonator: } T_t = \frac{(r+a)^2}{(1+ra)^2} \quad (2.13)$$

$$R_{min} = \frac{(r-a)^2}{(1-ra)^2} \quad (2.14)$$

$$\text{Add-drop ring resonator: } T_t = \frac{(r_2a+r_1)^2}{(1+r_1r_2a)^2} \quad (2.15)$$

$$R_{min} = \frac{r_2^2a^2 - 2r_1r_2a + r_1^2}{(1-r_1r_2a)^2} \quad (2.16)$$

$$T_{max} = \frac{(1-r_1^2)(1-r_2^2)a}{(1-r_1r_2a)^2} \quad (2.17)$$

$$T_d = \frac{(1-r_1^2)(1-r_2^2)a}{(1+r_1r_2a)^2} \quad (2.18)$$

**Finesse and Q-factor** The finesse is defined as the ratio of FSR and resonance width,

$$\text{Finesse} = \frac{\text{FSR}}{\text{FWHM}} \quad (2.19)$$

It is thus a measure of the sharpness of resonances relative to their spacing. The quality factor (Q-factor) is a measure of the sharpness of the resonance relative to its central frequency,

$$\text{Q-factor} = \frac{\lambda_{res}}{\text{FWHM}} \quad (2.20)$$

The physical meaning of the finesse and Q-factor relates to the number of round-trips made by the energy in the resonator before being lost to internal loss and the bus waveguides. This is a temporal phenomenon and must be examined with the transient response. The mathematics are described in numerous text books and publications [5, 8, 17, 18]. The finesse is found to represent within a factor of  $2\pi$  the number of round-trips made by light in the ring before its energy is reduced to  $1/e$  of its initial value. The Q-factor represents the number of oscillations of the field before the circulating energy is depleted to  $1/e$  of the initial energy. To define the Q-factor, the microring is excited to a certain level and the rate of power decay is considered. From this point of view it is understood that round trip losses as well as coupling in the directional couplers are loss factors that need to be reduced to obtain high-Q resonances. Therefore an all-pass resonator typically exhibits a higher Q-factor than an add-drop resonator (when both devices operate close to critical coupling).

The unloaded Q of a resonator is the Q-factor when the resonator would not be coupled to waveguides. We always mean *loaded Q* when referring to Q-factor, unless it is specifically mentioned otherwise. The importance of Q-factor for the

sensor resolution is addressed in section 2.3. How to design ring resonators for optimized Q-factor and finesse is discussed in the next section.

#### 2.1.4 Performance of SOI ring resonators

We will examine the performance of SOI ring resonators that were fabricated with 193 nm deep-UV lithography and dry etching (details in chapter 1, section 1.3.3). In the first paragraph we search for the group index of the resonating mode, an important factor for the sensitivity of the resonator biosensor. The spectral characteristics, FWHM and extinction, are used to determine the losses and the coupling in the resonators. The last paragraph deals with Q-factor and finesse. We discuss possible optimization of the device with an eye on its application for biosensing.

All measurements are performed with TE input polarization (dominant  $E$ -field parallel to wafer plane). For our waveguide dimensions TM polarized light would provide an enhanced sensor performance, as we will demonstrate in section 2.2. However, all test devices were designed and optimized for TE polarization, as well as the grating couplers that transfer light from the horizontal waveguide direction to the vertical fiber direction<sup>6</sup>. Characterization of TM polarized ring resonator modes is ongoing at the time of writing.

The spectra are obtained with the measurement setup described in chapter 6, section 6.4.

When used as a biosensor, the ring resonator will most likely be immersed in an aqueous solution like serum. The optical properties of water will affect the spectrum of the ring resonator. Water has a refractive index of 1.311 [9] and absorption of 10.9/cm [19] at 1550 nm. We performed the characterization of a ring resonator both immersed in water and exposed to air, and we will discuss to what extent the water cladding influences the spectrum.

#### Group index of resonating modes

The group index can be determined experimentally by measuring the FSR of ring resonators with various round trip lengths. Fig. 2.8 (left) shows the FSR as a function of the round trip length of a racetrack add-drop resonator. The waveguide dimensions are 220x486 nm.  $n_g$  is determined by fitting formula (2.12) to the measured values of the FSR (measured  $n_g = 4.55$ ). The group index obtained with FimmWave (vectorial mode solver software) simulations differs slightly from the measured group index in a straight wire with the same dimensions (simulated  $n_g = 4.39$ ). This difference can be attributed to an altered mode profile in the coupling sections, where the waveguides are typically slightly smaller due to the optical

---

<sup>6</sup>More on grating couplers can be found in chapter 6, section 6.3

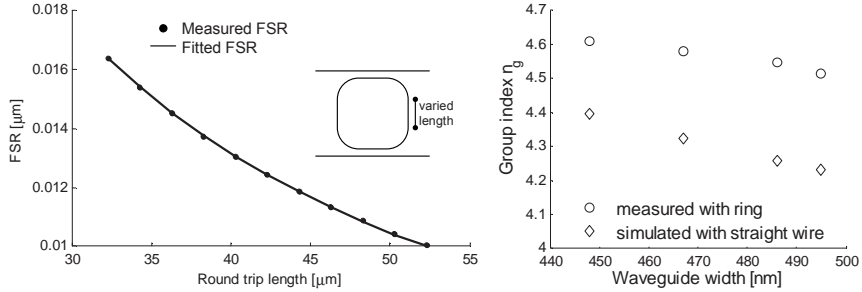


**Figure 2.8:** Left: Measurement of FSR for varying round trip lengths of an add-drop racetrack resonator with waveguide dimensions of 220x486 nm. A group index of 4.55 was determined after fitting  $FSR = \lambda_0^2 / (L \cdot n_g)$  to the measurements. Right: Measurement of group index of photonic wires width different widths (wire height=220 nm).

proximity effect<sup>7</sup>, and in the bend sections. For the rest of the chapter we use values of  $n_g$  that were measured on each set of rings before the characterization experiments.

The group index is extremely dependent on waveguide dimensions and wavelength. With the same experimental method the group indices for waveguide widths of 448, 467, 486 and 495 nm are plotted in Fig. 2.8 (right). Over this range  $n_g$  varies by 2%. Simulation of the group index of straight wires provides us with the other values on the graph. They are consistently lower, but follow the same trend as the measured group indices in ring resonators. The bandwidth of the grating couplers that were used to couple light into and out of the photonic circuit was not large enough (as compared to the ring FSR) to perform an investigation of the group index as a function of the wavelength with this method.

### Losses and coupling

**Method** The test device is a rectangular resonator, with a variation of the total round trip length  $L$ , Fig. 2.9 (left). The vertical straight length is altered, this way the coupling sections remain unaffected. All dimensions are indicated on the figure: waveguide dimensions are 448x220 nm, horizontal straight sections are 2  $\mu\text{m}$ . We measured symmetrical add-drop filters ( $r_1 = r_2$ ) with all gap widths  $w_g$  equal to 281 nm. To obtain spectra like in Fig. 2.9 (right), the spectrum is scanned with 1 pm resolution, fitted to a Lorentzian with a least-squares fitting method and scaled before determining the FWHM and the extinction parameters  $R_{min}$  and  $T_{max}$ . We

<sup>7</sup>The optical proximity effect (OPE) is defined as the change in feature size as a function of the proximity of nearby features. When an isolated line comes in close proximity with another line (e.g. in an directional coupler), the line widths of both lines reduce as a function of the distance between them. OPE can be partially corrected (optical proximity correction - OPC) at the mask level.

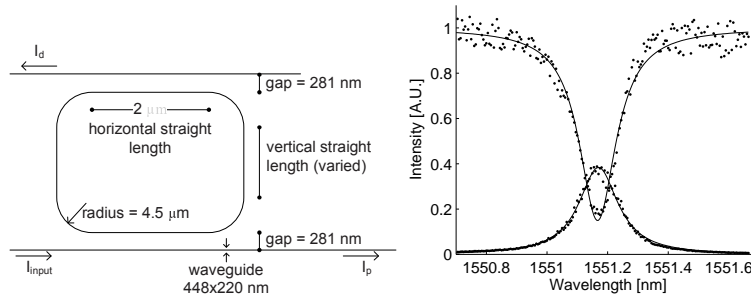


**Figure 2.9:** Left: Test ring resonator with typical dimensions indicated and a variation on the vertical straight length. Right: Exemplary add-drop ring resonator spectrum, scaled to one and fitted to a Lorentz function.

did not examine asymmetrical ring resonators because the error on measurements and fitting was too large to solve the system with three equations for  $a$ ,  $r_1$  and  $r_2$ . Therefore, we simplified the situation by using a symmetrical add-drop resonator. For all-pass filters  $a$  and  $r$  are interchangeable, so it is not possible to distinguish them from the spectral characteristics. A way of circumventing this issue was published by Mc-Kinnon et al. in [20]. They measure the transmission over a broad wavelength range and disentangle  $a$  and  $r$  based on how these parameters vary with wavelength. Another possibility is to determine  $a$  and  $r$  when  $r$  is assumed to be known from add-drop resonators with the same dimensions. However, this way errors are accumulated, leading to large errors on the results.

**Results and discussion** The losses are caused by three mechanisms: propagation losses, bend losses including mismatch losses at the straight-bend transition and losses in the coupling section. Propagation and bend losses were already described in section 2.1.1. Losses in the coupling section<sup>8</sup> are not fully characterized yet. They originate from propagation losses, from additional sidewall roughness affecting the distributed intensity, from a mismatch in wire width caused by the optical proximity effect or from a combination of these factors.

Fig. 2.10 plots values of the power round trip losses  $A = a^2$  [dB] and the power self coupling coefficient  $R = r^2$  [dB] as a function of round trip length  $L$ . The range of round trip lengths  $L$  was not large enough to draw a conclusion on the losses as a function of  $L$ . For future work several new device sweeps are designed based on these results to obtain more data. For now, we use the measurements for different  $L$  values to calculate the standard deviation on the results below.

<sup>8</sup>Sometimes the term coupling loss is used for the coupling power transmission  $t^2$ , because  $t^2$  is also a loss factor from the resonator's point of view. To avoid confusion we will not use it in this context.

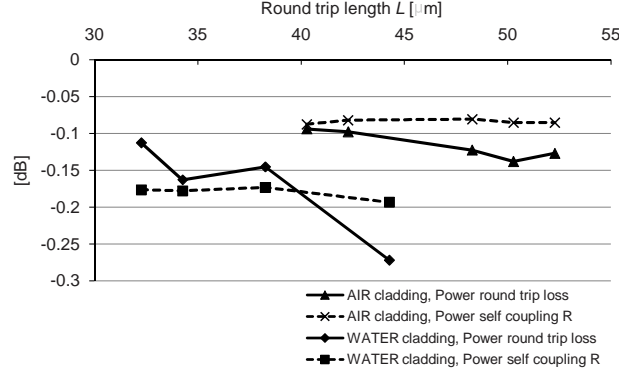


**Figure 2.10:** Experimentally determined power round trip loss [dB] ( $a^2$ ) and power self coupling [dB] ( $r^2$ ) for the test ring resonator with air and water cladding. The dimensions are indicated in Fig. 2.9.

	$n_g$	$A$ [dB]	$T$ [dB]
Air cladding	4.61	-0.11	$-17.16 \pm 0.15$
Water cladding	4.34	-0.17	$-13.91 \pm 0.21$

**Table 2.1:** Ring resonator distributed propagation losses and cross power coupling of a directional coupler with gap 281 nm. Values for devices with air and water cladding.

We list typical numbers for the round trip loss  $A$  [dB] and the coupling  $T = t^2 = 1 - r^2$  in [dB] in table 2.1. Group indices that were used for the calculations are also listed in the table.

The loss includes the three loss contributors summarized above:

$$A[\text{dB}] = A_{\text{propagation}}L_{\text{vertical}} + 4A_{\text{bend}} + 2A_{\text{coupler}} \quad (2.21)$$

An overview of the loss distribution in SOI ring resonators with air cladding is shown in Fig. 2.11. The contributions from different loss mechanisms was determined as follows. Propagation losses of SOI straight wires are measured to be  $2.7 \pm 0.06$  dB/cm [4]. Multiplying this value with the twice the length of the straight vertical ring resonator sections provides us with the total straight wire propagation loss. Each bend induces an excess loss of 0.01 dB [4]. We assume all ‘unknown’ losses to be loss factors in the coupler sections. The coupler section loss of each directional coupler with air cladding is thus  $0.04 \pm 0.01$  dB. This is a significant fraction of the total loss in the resonator, and therefore a prime candidate to focus on when trying to increase the Q-factor of the rings in the future.

For molecular sensing, the ring resonators will most likely be immersed in a aqueous environment like serum, while for telecom applications a wider range of cladding materials can be chosen according to the requirements (thermal, optical,

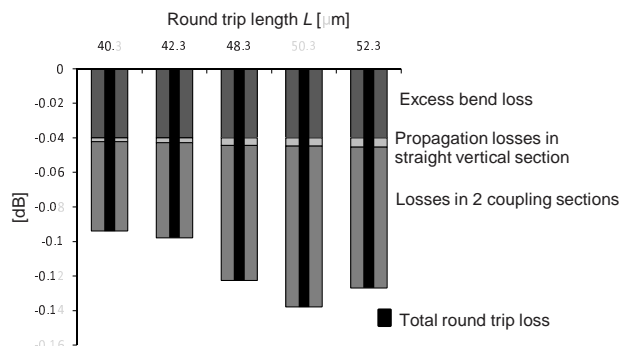


**Figure 2.11:** Experimentally determined total round trip losses of ring resonators with air cladding. Fractions of propagation losses in straight sections (from [4]), excess bend losses (from [4]) and losses in the coupling sections are indicated. The dimensions of the ring resonator test devices are indicated in Fig. 2.9.

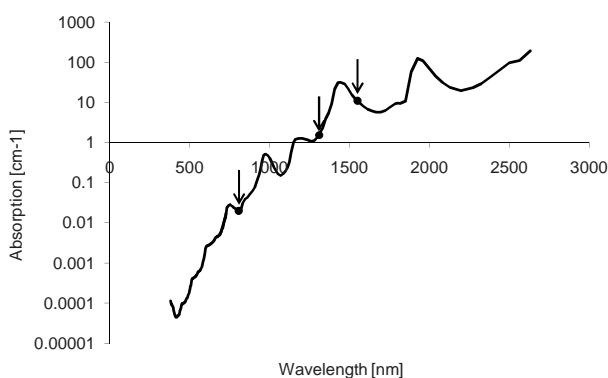


**Figure 2.12:** Water absorption spectrum across the visible and near-IR range [19]. Telecom wavelengths 800, 1310 and 1550 nm are indicated.

electrical...). If excess bend losses and couple section losses are assumed to remain constant when immersing the resonator in water, the propagation losses due to the water absorption increases from  $2.7 \pm 0.06$  dB/cm to  $52 \pm 20$  dB/cm. Despite the large error on the water propagation loss, it will give an idea on the limitation a water cladding imposes on the Q-factor. This increase of losses is mainly attributed to the water absorption. As we can see in Fig. 2.12, the water absorption at 1550 nm is as large as 10.9/cm [19]. For this reason it might be advisable to work at 1310 nm, the other commonly used telecom wavelength for which a broad range of commercially available read-out equipment exists.

A directional coupler with 2  $\mu\text{m}$  straight section couples on average 2.0 $\times$  more power to the ring when the coupler is immersed in water (Fig. 2.10). This is in

good agreement with the values obtained in the directional coupler study in section 2.1.2, where we saw that a coupler with SiO<sub>2</sub> couples about 2.2× more light to the ring resonator than a coupler with an air cladding would. The refractive index of water at 1550 nm (1.311, [9]) is situated in between the refractive index of air (1) and SiO<sub>2</sub> (1.44).

### Q-factor and finesse

**Results and discussion** When a biomolecule binds to the sensor surface, the resonance wavelength shift needs to be determined with high accuracy. A good quality biosensor has a high measurement resolution, which scales linearly with the Q-factor, under the assumption that read-out equipment is capable of scanning the spectrum with high enough spectral resolution (details in section 2.3.3).

From equation (2.20) and (2.19) the Q-factor and finesse can be rewritten as a function of the physical parameters of the ring resonator:

$$\text{All-pass ring resonator: Q-factor} = \frac{\pi n_g L \sqrt{ra}}{\lambda_{res}(1-ra)} \quad (2.22)$$

$$\text{Finesse} = \frac{\pi \sqrt{ra}}{1-ra} \quad (2.23)$$

$$\text{Add-drop ring resonator: Q-factor} = \frac{\pi n_g L \sqrt{r_1 r_2 a}}{\lambda_{res}(1-r_1 r_2 a)} \quad (2.24)$$

$$\text{Finesse} = \frac{\pi \sqrt{r_1 r_2 a}}{1-r_1 r_2 a} \quad (2.25)$$

$$(2.26)$$

For use as a sensor, a resonator does not only need to have a high Q-factor, the on-off resonance extinction needs to be large enough as well. In section 2.3.3 we find that the extinction has a low impact on the measurement resolution as long as it exceeds 15 dB. Below 15 dB however the extinction deteriorates the sensor performance. For this reason ring resonators for sensing need to be designed for close-to critical coupling operation. This limits the free design parameters; the coupling coefficients will be adapted to the losses to reach critical coupling.

The Q-factor of the measured devices is between 10,000 and 15,000 with an air cladding and around 5,000 when the resonator is immersed in water. The finesse is around 60 for air cladding and around 50 for water cladding.

In order to increase the Q-factor, it is crucial to reduce the losses in the cavity. Propagation losses are diminished by high quality SOI material and high quality processing [4]. However high water absorption at 1.55 μm increases the propagation loss dramatically, which fundamentally limits the Q-factor as will be discussed below. Bend losses might be further reduced by design of adiabatic bends that curve smoothly instead of 90° bends. The losses in the coupling section are under investigation as well as methods to decrease them.

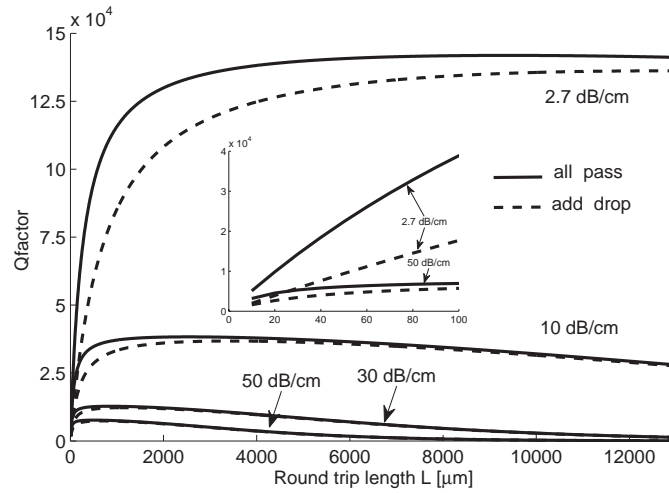
**Q-factor and finesse as a function of round trip length** The formula for Q-factor suggest that a better Q is obtained for large  $L$  and small cavity loss, but these two terms are not independent since the propagation loss increases with the cavity length. Fig. 2.13(a) and 2.13(b) present theoretical calculations of the variation of Q-factor and finesse as a function of cavity length for different propagation losses and for add-drop and all-pass configurations. An initial loss factor is added on top of the propagation losses that accounts for bend losses (four  $90^\circ$  bends have 0.04 dB of loss) and losses in the coupling sections (0.035 dB in the all-pass resonator, 0.07 dB in the add-drop resonator). The resonators operate at critical coupling,  $r_1 = a$  in the all-pass configuration,  $r_1 = r_2 a$  in the add-drop configuration.  $r_2$  was set to 0.99.

As the propagation losses in air equal 2.7 dB/cm, the highest Q-factor that can be obtained under the given conditions is about  $1.42 \cdot 10^5$  with a 9.39 mm long all-pass resonator. The highest Q-factor for an add-drop resonator would be  $1.36 \cdot 10^5$  if the length is 12.75 mm. However, a larger length also leads to a lower finesse, which is detrimental for sensing. The finesse corresponding to the maximum Q-factor for all-pass and add-drop are 5.15 and 3.64 respectively. A finesse of 5 is said to be the minimum needed for realistic sensing applications [21], because for lower finesse the peak separation is too small in comparison with the peak width and shifts can not be easily resolved. Therefore the length of the add-drop resonator needs to be limited to 9.20 mm, and the Q-factor will be limited to  $1.35 \cdot 10^5$ .

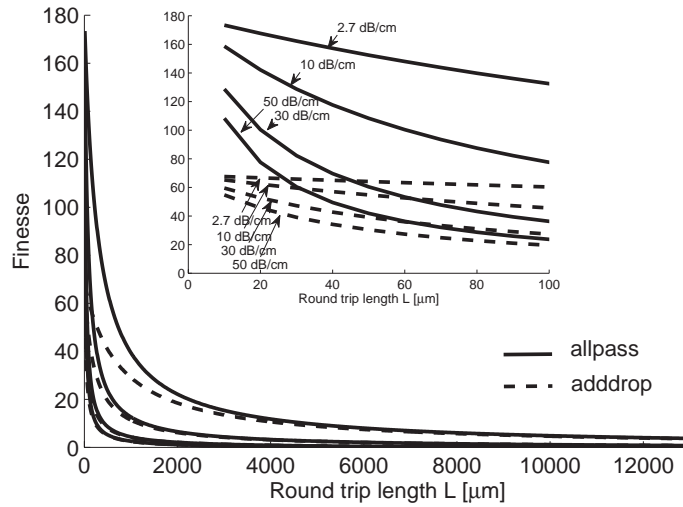
The propagation losses of a wire immersed in water are roughly estimated to be 50 dB/cm. From graphs 2.13(a) and 2.13(b) we learn that the maximal Q-factor in an all-pass configuration is  $7.66 \cdot 10^3$  and  $7.36 \cdot 10^3$  in an add-drop configuration for 510  $\mu\text{m}$  and 690  $\mu\text{m}$  respectively. However for these round trip lengths, the finesse drops below one and the signal becomes useless. The lengths for which the finesse is above 5 are 500  $\mu\text{m}$  and 520  $\mu\text{m}$  respectively. The water absorption induces a two-orders of magnitude reduction of the Q-factor, and thus of the sensor resolution.

## 2.2 Sensitivity

This section deals with the intrinsic sensitivity of a ring resonator: how much does the resonance wavelength shift when biomolecular interaction occurs around the waveguide. A formula for the shift is derived in section 2.2.1, as well as a discussion on the advantage of high index contrast waveguides for biosensing. The optical model that translates biomolecular interaction in a configuration consisting of dimensions and refractive indices is described in section 2.2.2. The last section (section 2.2.3) examines the sensitivity of SOI single ring resonator biosensors.



(a) Quality factor as a function of cavity length for four propagation loss figures.



(b) Finesse as a function of cavity length for four propagation loss figures.

**Figure 2.13:** Calculation of  $Q$ -factor and finesse as a function of cavity length  $L$ . Initial losses were set equal to the losses induced by four bends ( $0.01$  dB/bend) and one or two coupling sections ( $0.035$  dB/coupling section). All cavities operate at critical coupling,  $a = r$  in the all-pass configuration,  $r_1 = r_2 a$  in the add-drop configuration with  $r_2 = 0.99$ .

### 2.2.1 Resonance wavelength shift

A shift of the resonance wavelength  $\lambda_{res}$  is essentially caused by a change of the effective index of the resonant mode  $n_{eff}$ .

$$\Delta\lambda = \frac{\Delta n_{eff} L}{m}, m=1,2,3\dots$$

where  $m$  is the order of the resonant mode.  $n_{eff}$  is influenced by the refractive index of the cladding, which is altered upon sensing. Because of the large index contrast of SOI, the waveguide dispersion can not be neglected. A change of  $n_{eff}$  will primarily alter  $\lambda_{res}$ , which in turn will influence  $n_{eff}$  due to the non-zero slope of  $\frac{\partial n_{eff}}{\partial \lambda}$ . In a first order approximation both effects can be decoupled:

$$\Delta\lambda_{res} = \frac{\left[ \left( \frac{\partial n_{eff}}{\partial n_{env}} \right)_{\lambda_{res}, n_{env}^0} \Delta n_{env} + \left( \frac{\partial n_{eff}}{\partial \lambda} \right)_{\lambda_{res}, n_{env}^0} \Delta\lambda_{res} \right] \cdot L}{m}$$

With  $n_{eff}^0$  at the initial resonance wavelength. After substitution in formulas (2.9) and (2.5) at  $\lambda = \lambda_{res}$ , a compact formula for the resonance wavelength shift with first order dispersion will appear:

$$\Delta\lambda = \frac{\Delta_{env} n_{eff} \cdot \lambda_{res}}{n_g} \quad (2.27)$$

where  $\Delta_{env} n_{eff}$  is the effective index shift caused by an environmental change,  $\Delta_{env} n_{eff} = \left( \frac{\partial n_{eff}}{\partial n_{env}} \right)_{\lambda_{res}, n_{env}^0} \Delta n_{env}$ .

From the variational theorem of waveguides,  $\Delta_{env} n_{eff}$  caused by a local change of dielectric constant  $\Delta\epsilon(x, y)$ , can be expressed as [22–24]

$$\Delta_{env} n_{eff} = c \int \Delta\epsilon E_v \cdot E_v^* dx dy$$

where  $E_v(x, y)$  is the normalized modal electric field vector of the waveguide mode in the ring.

The sensor response scales with the squared amplitude of the electric field at the perturbation and, therefore, with the fraction of the total modal power contained in the surface volume where the dielectric constant is modified. This fraction can be increased by reducing the waveguide core dimensions to delocalize or expand the waveguide mode, thereby increasing the interaction with the surrounding cladding materials. In the case of surface layer sensing it is advantageous if the electric field decays rapidly near the surface, since a relatively larger fraction of the field will be located where the layer forms. For this reason the sensitivity for adlayers increases as the index contrast increases. A rigorous derivation of the sensitivity of  $n_{eff}$  of slab waveguides for variations of the environment was performed by Tiefenthaler et al. in [23].

The normal component of displacement  $D = \epsilon E$  must be continuous across an interface. Therefore the field amplitude above the surface is increased when using the mode for which the dominant field component is polarized normal to the sensing surface. If the waveguide height is considerably smaller than its width (top surface area  $>$  side walls area), the sensing surface will mostly be at the top surface and the  $TM_{00}$  mode is more sensitive to index variations. If the waveguide height is larger than its width (top surface area  $<$  side walls area), the  $TE_{00}$  mode will be most sensitive. Fig. 2.14(a) and 2.14(b) illustrate the mode profiles for a waveguide with 480 nm width and 220 nm height. From the figures we clearly see that the  $TM_{00}$  mode is more sensitive for this configuration.

Because of fabrication restrictions, all experiments are carried out with waveguides of 220 nm height (see chapter 1, section 1.3.3). Although it would be more beneficial to use TM polarization, most experiments are carried out with TE polarization because the grating coupler design was optimized for  $TE^9$ . Numbers on SOI evanescent field sensor sensitivity are given in the next sections.

## 2.2.2 Optical model for biomolecular interaction

Biomolecular interaction between a receptor molecule, previously deposited on the waveguide surface, and its complementary analyte, produces a change in refractive index at the sensor surface that induces a variation in the optical properties of the guided light via the evanescent field (Fig. 2.15). A biomolecular layer is optically modeled as a uniform layer with a certain thickness  $t_L$  and a certain refractive index  $n_L$ . The refractive index of the layer is between the index of dry molecules and index of the solvent or buffer solution.  $n_L$  relates to the molecular density in the layer  $\rho_L$  [g/cm<sup>3</sup>] as [25]:

$$\rho_L = \rho_{protein} \frac{n_L - n_B}{n_{protein} - n_B} \quad (2.28)$$

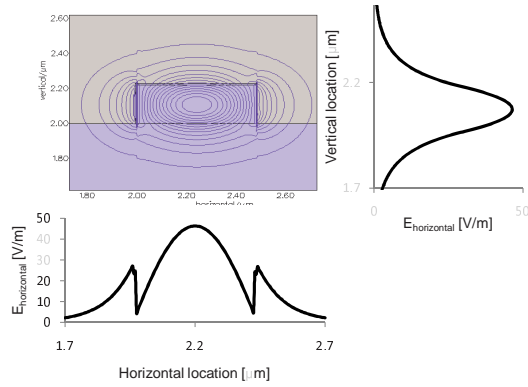
$n_B$  is the refractive index of the bulk cover medium (mostly buffer or solvent).  $\rho_{protein}$  is the density of dry proteins [g/cm<sup>3</sup>] (we work with values for proteins, but the formulas hold for DNA or other molecules). We use a literature value of  $\rho_{protein} = 1.33$  g/cm<sup>3</sup> [26, 27].  $n_{protein}$  is the refractive index of the dry molecules and has been reported to be between 1.45 and 1.48 [28].

With information on the thickness and the index of the layer, using formula (2.28) the mass of the layer  $M_L$  [g/cm<sup>2</sup>] can be calculated:

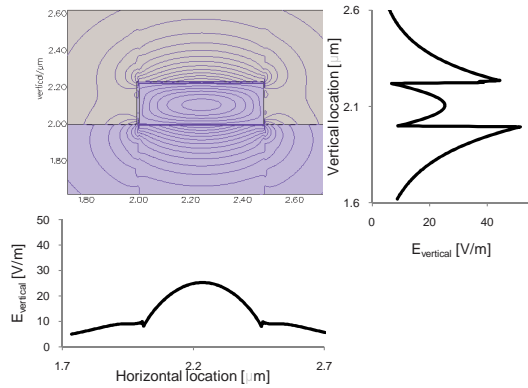
$$M_L = t_L \rho_L \quad (2.29)$$

Several groups have quantified the density of molecular layers, mostly with the use of combined techniques. Some investigators have modeled the molecular layer as

<sup>9</sup>More information on grating couplers can be found in chapter 6, section 6.3



(a) TE<sub>00</sub> mode profile.



(b) TM<sub>00</sub> mode profile.

**Figure 2.14:** Electric field distribution at 1550 nm for an SOI waveguide with dimensions of  $220 \times 480 \text{ nm}^2$ . The lower cladding is SiO<sub>2</sub>, the upper cladding is water with  $n_c = 1.311$ . The waveguide is surrounded with a 10 nm thick layer with index 1.45.

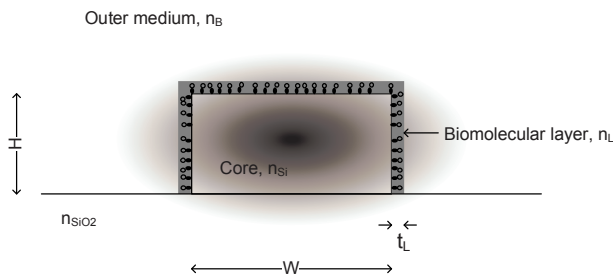


**Figure 2.15:** Optical model of a layer in which biomolecular interaction takes place.

an adlayer of fixed-height with a refractive index that varies linearly from the bulk solution index to a saturating index for a monolayer [28–30]. Alternatively, a fixed refractive index for the adsorbed layer can be assumed, typically  $n = 1.45$ , and the measured output is related to an effective thickness, as we do here [31–34]. Ultimately, both approaches are approximations and a calibration with known concentrations of biomolecules on the surface is required [32]. Accurate information on the conformational situation of the proteins in the layer can only be obtained using a combination of techniques, or alternatively with a one system that can resolve  $n_L$  and  $t_L$  independently. Chapter 3 will be devoted to this study, using dual polarization in the ring resonator biosensors we will determine  $n_L$  and  $t_L$  simultaneously.

For the rest of this chapter, we will use the model with a fixed layer refractive index of  $n_L = 1.45$  for theoretical characterization of the system.

### 2.2.3 SOI ring resonator sensitivity

**Surface sensitivity** With the optical model described above we can simulate the wavelength shift that occurs upon molecular interaction. We simulated the effective index change  $n_{eff}$  using FimmWave, a vectorial mode solver, and calculated the corresponding resonance wavelength shift with formula (2.27), see Fig. 2.16(a). The simulation parameters are  $W = 480$  nm,  $H = 220$  nm,  $n_{Si} = 3.467$ ,  $n_{SiO_2} = 1.444$ . The refractive index of the water environment is 1.311 at 1.55  $\mu\text{m}$  [9]. For layer thicknesses up to 40 nm the sensor response is linear. This thickness is far beyond the thickness of molecular layers and forms no limitation. The validity of this model was verified experimentally. When a layer with known parameters  $n_L$  and  $t_L$  surrounds the waveguides, the measured shift agrees well with the simulations, see chapter 7, section 7.3. From graph 2.16(a) the sensitivity for thin layers is determined to be 0.290 nm/nm for the  $\text{TM}_{00}$  mode and 0.158 nm/nm for the  $\text{TE}_{00}$  mode. TM polarization is more sensitive for this waveguide dimensions for the reasons described earlier.

In Fig. 2.16(b) the calculated sensitivity is plotted for single mode waveguides with varying core width and fixed core height of 220 nm, corresponding to the height of the silicon membrane of all wafers used for the experiments. Indeed, reducing the waveguide core dimensions will expand the waveguide mode, thereby increasing the interaction with the surrounding cladding material and increasing the sensitivity. However when the mode expands further in the aqueous environment, propagation losses due to water absorption will increase. The resulted decreased Q-factor might reduce the minimum detectable wavelength shift and eventually the overall detection limit of the system. These two concepts will be further explained in sections 2.3 and 2.4. For different waveguide dimensions, the group index will vary as well, but only over about 2%. The effective index differ-

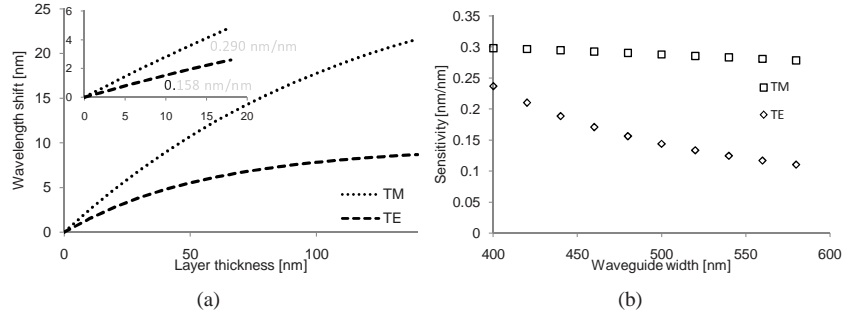


**Figure 2.16:** (a)  $\Delta\lambda$  in function of layer thickness for a waveguide with dimension  $480 \times 220$  nm, (b) Surface sensitivity in [nm shift/nm layer thickness] for a layer ( $n_{\text{layer}} = 1.45$ ) in an aqueous solution ( $n_B = 1.311$ ) on a waveguide as a function of the core width of the waveguide.

ence  $\Delta_{env} n_{eff}$  varies by about 50% for this parameter space and is dominant. With more flexibility on the height of the waveguide, we find different areas in the (width, height) plane for which either TE or TM sensitivity is maximal, depending on the amount of interaction on the sidewalls versus the top surface. This is extensively discussed in chapter 3, where we perform an analysis of the influence of waveguide dimensions on the sensitivity and additional numbers for sensitivity are given. We find the maximum TE sensitivity for an optimal TE configuration to surpass the maximum TM sensitivity for an optimal TM configuration.

**Bulk sensitivity** Fig. 2.17(a) shows the calculated sensitivity of an SOI ring resonator for bulk refractive index changes, the refractive index of the entire upper waveguide cladding is homogeneously altered. The waveguide dimensions are  $220 \times 480$  nm. From the slope of the curve, we extract a 64 nm/RIU (refractive index units) TE sensitivity and a TM sensitivity that is 3.5 times higher, 219 nm/RIU. Fig. 2.17(b) shows the simulated sensitivity for waveguides with increasing widths and fixed height of 220 nm. Again we find the sensitivity to increase upon decreasing waveguide core width.

### 2.3 Measurement resolution

For a sensor used in wavelength interrogation, the sensor resolution is the accuracy with which a wavelength shift can be determined, in other words, the minimum detectable wavelength shift  $\Delta\lambda_{min}$ . Together with the sensor sensitivity discussed in the next section (2.2) it determines the overall detection limit (section 2.4).  $\Delta\lambda_{min}$  depends on the shape of the resonance spectrum, the noise, the fitting procedure and the measurement resolution. The measurement resolution will be

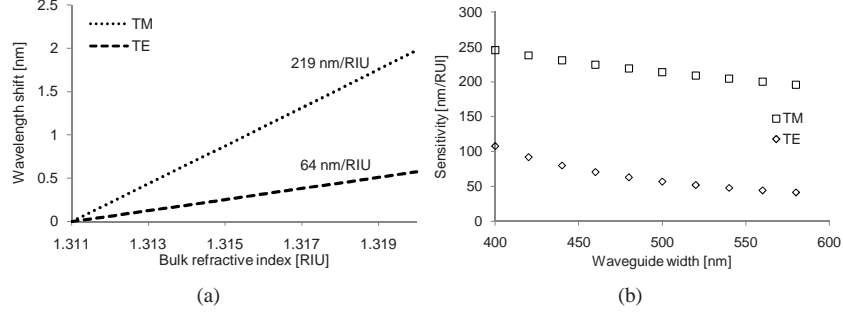


**Figure 2.17:** (a)  $\Delta\lambda$  as a function of bulk refractive index  $n_B$  for waveguide dimensions  $480 \times 220$  nm, (b) Bulk sensitivity in [nm/RIU] as a function of the core width of the waveguide. Height = 220 nm.

referred to as ‘wavelength step’, so as not to confuse it with ‘resolution’ in the sense we use it here. We focus on the impact of resonator parameters (section 2.3.3) and instrumentation factors (section 2.3.2).

Intensity interrogation, tracking of the intensity at fixed wavelength, is another option to measure resonant cavity sensors. Because the dynamical range is limited and the method is less flexible it will not be discussed.

### 2.3.1 Simulation method

To determine the minimum wavelength shift  $\Delta\lambda_{min}$  that can be resolved by the system, Monte Carlo simulations are performed. During simulation, theoretical transmission spectra are constructed first, for certain chosen values of FWHM and extinction ratio, with following formulas:

$$T_n = \frac{R_{min} + F \sin^2\left(\frac{\phi}{2}\right)}{1 + F \sin^2\left(\frac{\phi}{2}\right)} \quad (2.30)$$

$$T_p = \frac{R_{min} + F \sin^2\left(\frac{\phi}{2}\right)}{1 + F \sin^2\left(\frac{\phi}{2}\right)} \quad (2.31)$$

$$T_d = \frac{T_{max}}{1 + F \sin^2\left(\frac{\phi}{2}\right)} \quad (2.32)$$

$$F = \left( \frac{2\lambda^2}{\pi L_{eff} FWHM} \right)^2 \quad (2.33)$$

$$\phi = \frac{2\pi L_{eff}}{\lambda} \quad (2.34)$$

In a second step randomly generated Gaussian intensity noise was superimposed onto the spectra. Subsequently the noisy signals are discretized with a wavelength

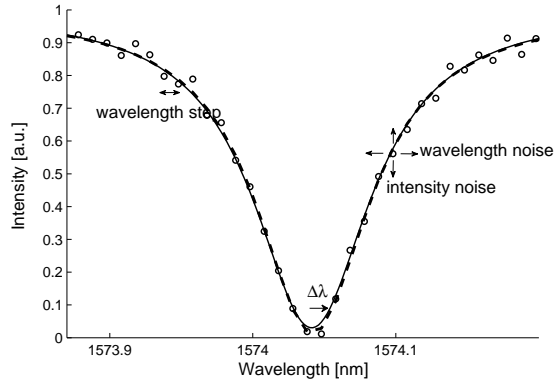


**Figure 2.18:** Transmission spectra of a resonator sensor.

step randomly chosen around the start of the measurement window. The wavelength step corresponds, for example, with the wavelength step of a tunable laser. Finally the data points are fitted to a Lorentz curve with a least-squares fitting method to extract the measured resonant wavelength. Spectra as in Fig. 2.18 are obtained. The minimum detectable wavelength shift  $\Delta\lambda_{min}$  is then calculated as the variance of the fitting error over a large number  $N$  of Monte Carlo experiments:

$$\Delta\lambda_{min} = \sqrt{\frac{\sum (\lambda_{\text{fitted resonance}} - \lambda_{\text{theoretical resonance}})^2}{N}} \quad (2.35)$$

where  $N$  is the number of iterations. We set  $N = 1000$  for all simulations below. A similar method was used by Hu et al. [35] and by Claes et al. [36].

A different approach that only requires measured data to determine  $\Delta\lambda_{min}$ , is to start from the assumption that the actual resonance wavelength is normally distributed with its mean equal to the fitted wavelength and its standard deviation equal to half of the 68.28% confidence interval of the fitted wavelength. Half of the 68.28% confidence interval can then serve as a measure for the minimum resolvable wavelength shift. We will later show that these two methods are in very good agreement.

### 2.3.2 Resolution versus instrumentation

In this section we discuss how the measurement resolution is influenced by the measurement setup, more in particular by the wavelength step and the noise levels.

**Noise** Noise sources can have two different types: intensity noise, which affects the transmitted optical signal intensity, and wavelength noise, which leads to a

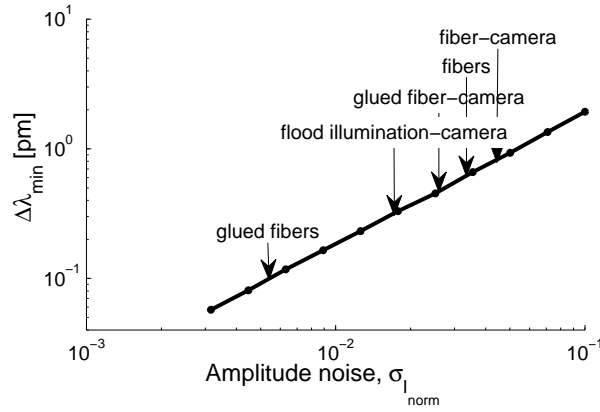


**Figure 2.19:** Minimum detectable wavelength shift  $\Delta\lambda_{min}$  versus square root of intensity noise (i.e. amplitude noise) shows a linear relation. FWHM = 100 pm, extinction ratio = 15 dB, wavelength step = 5 pm.

spectral shift of the resonance wavelength (see Fig. 2.18) [37]. The former category includes photodetector noise, light source intensity fluctuation, and possible coupling variations, whereas the latter is due mainly to light source wavelength shift (i.e., source wavelength repeatability) and resonant wavelength change of the optical resonator, often due to temperature fluctuations. Hu et al. [35] demonstrate that intensity noise and wavelength noise are orthogonal in terms of their impact on the sensor wavelength resolution  $\Delta\lambda_{min}$  and can be considered separately in sensor performance evaluation.

In chapter 6, we introduce the different measurement setups we use to determine the resonance wavelength shift of SOI ring resonator biosensors. Section 6.5 is devoted to the characterization of the intensity noise of the various detection systems. There, intensity noise is defined as the variance of the normalized intensity,  $\text{noise} = \sigma_{I_{norm}}^2 = \frac{\langle \Delta I^2 \rangle}{I^2}$ . Different instantiations of Gaussian noise with standard deviation  $\sigma_{I_{norm}}$  were added to the signal for the Monte-Carlo simulations. The absolute value of the constructed signal was further used, because negative intensities are non-physical. In Fig.2.19,  $\Delta\lambda_{min}$  is shown versus the square root of the intensity noise (referred to as amplitude noise) and realistic noise values of our equipment are indicated. We find a linear correspondence between measurement resolution and this amplitude noise  $\sigma_{I_{norm}}$ . These simulations are performed for resonances with FWHM of 100 pm, 5 pm wavelength step and 15 dB extinction ratio.

Similarly, 1000 instantiations of Gaussian distributed wavelength noise were added for simulations of the impact of wavelength noise on  $\Delta\lambda_{min}$ . In Fig.2.20 we find a linear correlation between spectral noise and measurement resolution.

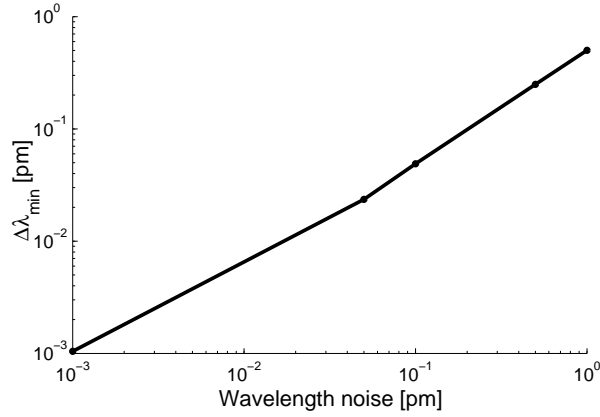


**Figure 2.20:** Simulated resonator sensor resolution  $\Delta\lambda_{min}$  versus wavelength noise shows a linear relation. These simulations are performed for resonances with FWHM of 100 pm ( $Q$ -factor of  $1.5 \cdot 10^4$ ), 5 pm wavelength step and 15 dB extinction ratio.

We also simulated the impact of the wavelength noise and intensity noise for resonant cavities with different  $Q$ -factors (see Fig. 2.21). The wavelength step was adapted to the resonance width so that always 20 data points per FWHM were recorded. Both curves show opposite behavior with respect to the resonance line width. This can be understood intuitively as follows: wavelength noise translates into intensity noise with increased amplitude for sharp (high- $Q$ ) peaks because of the large curve slope. High- $Q$  resonators are thus more susceptible to wavelength noise interference. Only for  $Q$ -factors over  $10^5$  wavelength noise needs to be considered. Within the  $Q$ -factor range of SOI microring resonators, intensity noise decreases the sensor resolution about 5 times more than wavelength noise does. Therefore, for simulations in the following sections, only intensity noise will be considered.

We mentioned the use of confidence intervals for determination of  $\Delta\lambda_{min}$  with one single measurement. In Fig. 2.22 this method is compared to the Monte Carlo method and both methods are found to be in good agreement.  $\Delta\lambda_{min}$  was plotted as a function of intensity noise  $\sigma_{I_{norm}}^2$ .

**Wavelength step** Fig. 2.23(a) shows the dependence of the measurement resolution  $\Delta\lambda_{min}$  on the wavelength step. The other ring resonator parameters are chosen as follows: extinction ratio = 15 dB, intensity noise =  $\sigma_{I_{norm}}^2 = 0.5 \cdot 10^{-4}$ . Initially we find  $\Delta\lambda_{min}$  to increase with the square root of the wavelength step. For very small wavelength steps the slope of the curve decreases, so the influence of the step diminishes. In fig.2.23(b), we plot the same information, but this time

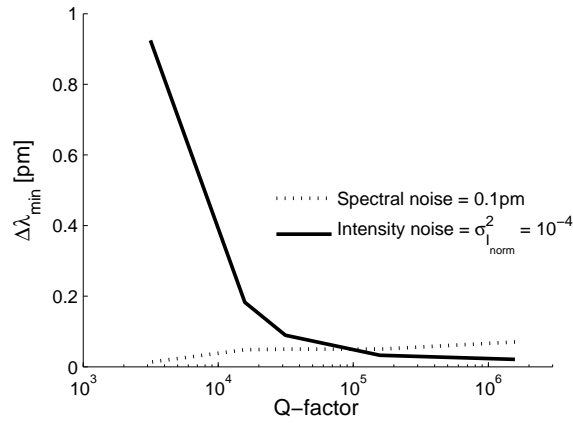


**Figure 2.21:** Simulated resonator sensor wavelength resolution  $\Delta\lambda_{min}$  at different resonance line widths, both the influence of intensity noise and wavelength noise is simulated.  $\sigma_{I_{norm}}^2 = 0.5 \cdot 10^{-4}$ , wavelength noise = 1 pm, extinction ratio = 15 dB, wavelength step = FWHM/20.

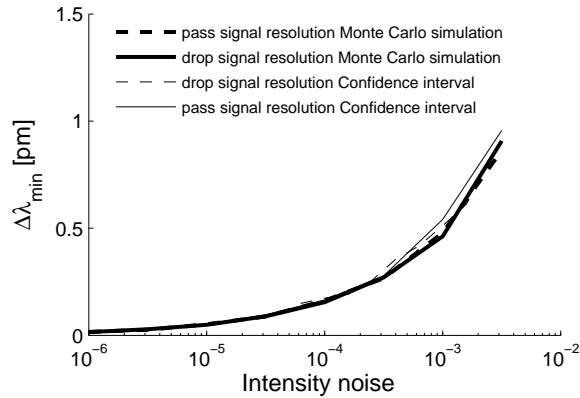


**Figure 2.22:**  $\Delta\lambda_{min}$  as a function of intensity noise  $\sigma_{I_{norm}}^2$  determined with Monte Carlo simulations and with half of the 68% confidence interval. All simulations gave similar results.

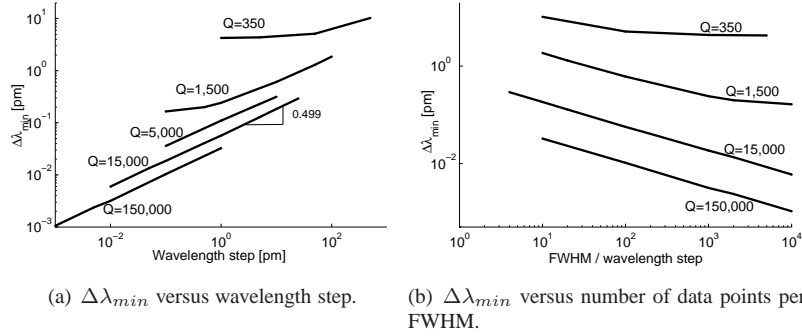


**Figure 2.23:** Simulation of measurement resolution  $\Delta\lambda_{min}$  as a function of wavelength step for different resonance line widths (variable  $Q$ -factors). Other simulation parameters: extinction ratio = 15 dB, intensity noise =  $\sigma_{Inorm}^2 = 0.5 \cdot 10^{-4}$ .

as a function of the number of data points per FWHM, and this for different  $Q$ -factors. With a low  $Q$ -factor of 350, 100 data points per FWHM are enough to get the best possible resolution. With a  $Q$ -factor of 1500, 1000 points are needed. This means that high quality cavities demand read out equipment with a very high spectral resolution if one wants to get the most information out of it. Notice however that due to the overall impact of the  $Q$ -factor on  $\Delta\lambda_{min}$ , the measurement resolution remains better for cavities with high  $Q$ -factors, even when a lower number of data points per resonance is recorded. No wavelength noise was included, the results for the highest  $Q$ -factor might change slightly when including wavelength noise.

In reality, the wavelength step is determined by the quality of the available optical equipment (resolution of the tunable laser source or optical spectrum analyzer), and it might be compromised by the required scan speed as imposed by the application. For example when an array of ring resonators is scanned simultaneously (see chapter 6 for details), we set the tunable laser wavelength step to 5 pm. This way one spectral scan of 10 nm, comprising 4 resonances, is performed within less than one minute. For kinetic monitoring of extremely fast molecular binding rates, one data point per minute might not be sufficient. A larger wavelength step might be needed, at the cost of a reduced measurement resolution. Our ring resonators have a  $Q$ -factor of about 5,000 when immersed in water. This means we record about 60 data points per FWHM with 5pm step size. From the curve for  $Q = 5,000$  on Fig. 2.23(a) we can determine that 5 pm step size is not enough to extract the minimum resolution. Even the lowest simulated wavelength step of 0.1 pm is not sufficient for an optimal measurement resolution, but below 0.1 pm step simulation times are unrealistically long.

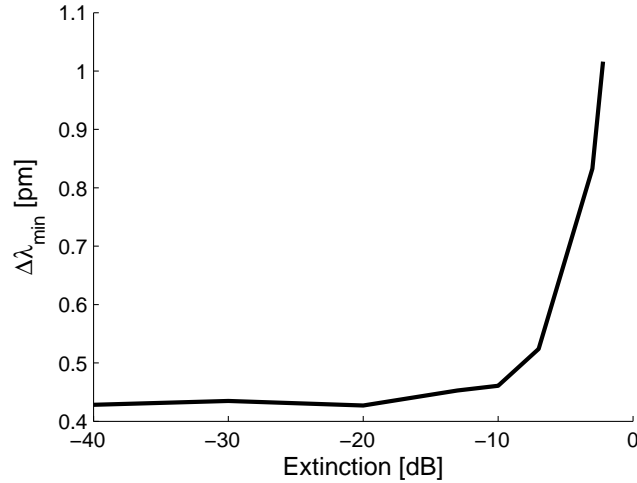


**Figure 2.24:** Simulation of  $\Delta\lambda_{min}$  as a function of resonance extinction ratio. With extinction ratios above 15 dB, the measurement resolution is independent of the extinction ratio. Other parameters: FWHM = 100 pm, intensity noise =  $\sigma_{I_{norm}}^2 = 0.5 \cdot 10^{-4}$ , wavelength step = FWHM/20.

### 2.3.3 Resolution versus resonance shape

The shape of the resonance spectrum is defined by two parameters: full width at half maximum (FWHM) and the extinction ratio. The Q-factor is related to the FWHM via Q-factor =  $\frac{\lambda_{res}}{FWHM}$ . The relation between FWHM, extinction ratio and the physical parameters of the resonator was previously discussed in section 2.1.3. The Q-factor of SOI ring resonators immersed in water is typically around 5,000 and for an SOI ring resonator with an air cladding the Q-factor is between 10,000 and 15,000 (although these last values can be improved by increasing the length of the resonator). For all simulations the intensity noise is set to  $\sigma_{I_{norm}}^2 = 0.5 \cdot 10^{-4}$  and wavelength noise was discarded.

**Extinction ratio** In Fig. 2.24 we plotted the measurement resolution as a function of the on-off resonance extinction ratio (with FWHM = 100 pm). Above 15 dB extinction ratio the measurement resolution  $\Delta\lambda_{min}$  becomes nearly independent of the extinction ratio. Below 15 dB,  $\Delta\lambda_{min}$  increases rapidly with decreasing extinction ratio. It is important to design the coupling section of the ring resonator such that coupling and round trip losses match well and thus a high extinction ratio is obtained.

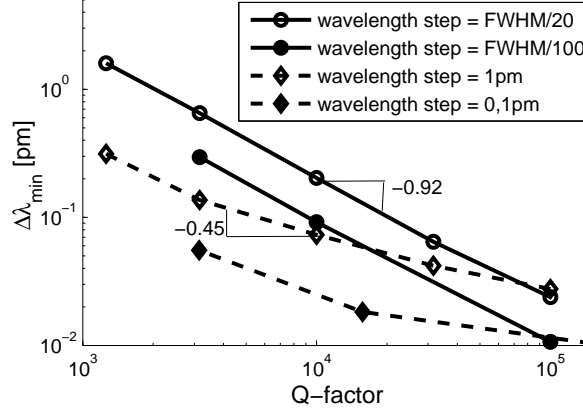


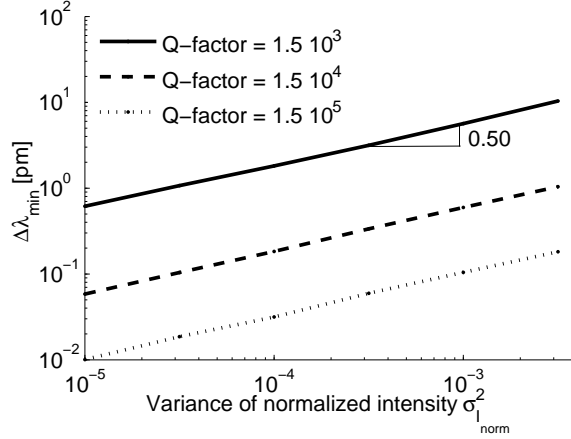
**Figure 2.25:** Simulation of  $\Delta\lambda_{min}$  as a function of  $Q$ -factor.  $\Delta\lambda_{min}$  varies linearly with the  $Q$ -factor when a fixed number of data points per resonance line width is recorded.  $\Delta\lambda_{min}$  varies with the square root of the  $Q$ -factor when a fixed wavelength step is used regardless of the resonance line width. Other simulation parameters: extinction ratio = 15 dB, intensity noise =  $\sigma_{I_{norm}}^2 = 0.5 \cdot 10^{-4}$ .

**Resonance width** In Fig. 2.25 we observe a linear dependence of the measurement resolution  $\Delta\lambda_{min}$  on the  $Q$ -factor: the smaller the resonance width, the better least-squares fit to a Lorentzian. In the first curve, we assume that always 20 data points are recorded per FWHM, so higher  $Q$ -resonance are measured with higher spectral resolution equipment. The measurement resolution scales linearly with the inverse of the  $Q$ -factor in this case. When a larger number of data points per FWHM would be recorded, the curve for  $\Delta\lambda_{min}$  shifts to lower values but the slope of the curve remains around 1. The second line in Fig. 2.25 depicts the situation in which equipment with a fixed spectral resolution of 1 pm is used (this corresponds to the resolution of the measurement equipment used for this work).  $\Delta\lambda_{min}$  scales inversely with the square root of the  $Q$ -factor for this case. In other words, when cavities with higher  $Q$ -factors are developed it is beneficial to invest in higher resolution measurement equipment as well.

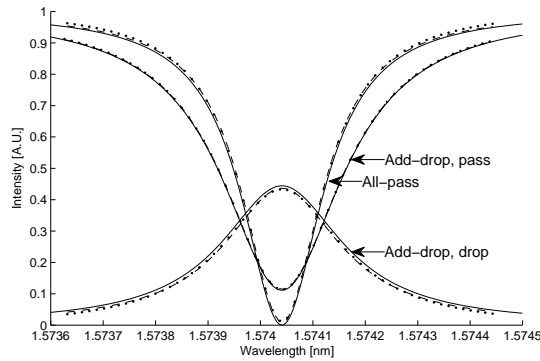
Finally, in Fig 2.26 we plot the influence of intensity noise on  $\Delta\lambda_{min}$  at different  $Q$ -factors, just like in Fig. 2.21, but this time for different noise levels. It can be seen that the higher the  $Q$ -factor, the more robust the sensor becomes with respect to intensity noise.

### 2.3.4 Add-drop or all-pass resonator?

What configuration offers the best detection resolution for a given set of physical parameters (round trip transmission  $a$  and coupling coefficient  $r$ ) of a ring resonator? Is the minimum detectable wavelength shift  $\Delta\lambda_{min}$  smaller for the signal



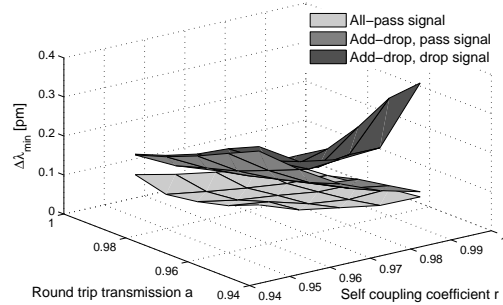
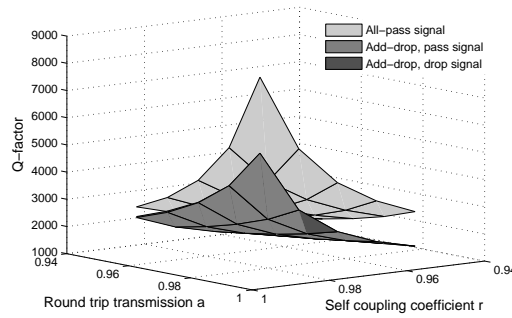
**Figure 2.26:** Influence of noise on  $\Delta\lambda_{min}$  for different  $Q$ -factors. Other simulation parameters: wavelength step =  $FWHM/20$ , extinction ratio = 15 dB.



**Figure 2.27:** Spectra of all-pass and add-drop resonator with the same physical parameters,  $a = r_1 = r_2 = 0.99$ .

on the pass or drop port of an add-drop filter, or on the output of an all-pass filter? In either configuration the ring resonator is characterized by the round trip amplitude transmission  $a$  and the amplitude self coupling coefficients  $r_1$  and  $r_2$  ( $r_2 = 1$  in an all-pass configuration). Instead of constructing the signals from the resonance shape characteristics FWHM and extinction ratio, the signals are constructed directly with formulas (2.2), (2.3) and (2.4). See Fig. 2.27 for an example of the generated spectra with  $a = r_1 = r_2 = 0.99$ .

In the same manner as described earlier, 1000 different instantiations of Gaussian intensity noise were added to the the signals. Then, a discretization with a given wavelength step is performed and a Lorentzian was fitted to all spectra. The

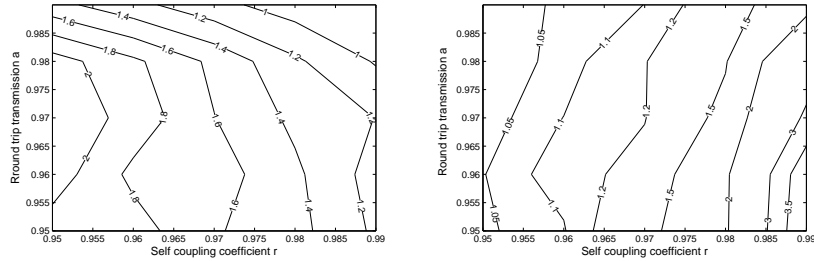
(a) Measurement resolution  $\Delta\lambda_{min}$ 

(b) Q-factor

**Figure 2.28:** Simulation of measurement resolution  $\Delta\lambda_{min}$  and  $Q$ -factor as a function of the physical parameters  $a$  and  $r$  of the resonator in all-pass configuration and symmetrical add-drop configuration.

measurement resolution was defined with formula (2.35). The wavelength step is set so that 20 data points per FWHM are recorded. The noise is constant at  $\sigma_{I_{norm}}^2 = 10^{-4}$ .

In Fig. 2.28(a) we see the measurement resolution  $\Delta\lambda_{min}$  as a function of  $a$  and  $r$  for an all-pass, pass and drop signal. The add-drop resonator was assumed symmetrical ( $r_1 = r_2 = r$ ). As expected, an all-pass filter has the best detection resolution for every combination of  $a$  and  $r$ . This is because an all-pass resonator always displays a higher  $Q$ -factor as compared to an add-drop resonator. The  $Q$ -factor of all configurations is shown in Fig. 2.28(b). The ratio of all-pass resolution to pass resolution ranges from almost 1 for high quality cavities to 2 for low quality cavities, see Fig. 2.29(a). When the ring resonator is immersed in water,  $a$  and  $r$  are roughly around 0.98 for the test devices in the previous sections (depending on the



(a) Ratio of the measurement resolution  $\Delta\lambda_{min}$  of the pass signal of a symmetrical add-drop resonator to an all-pass signal. The all-pass signal always has a better resolution. (b) Ratio of the measurement resolution  $\Delta\lambda_{min}$  of the drop to pass signal of a symmetrical add-drop resonator. The pass signal always has a better resolution.

**Figure 2.29:** Simulation of measurement resolution  $\Delta\lambda_{min}$  as a function of the physical parameters  $a$  and  $r$  of the resonator in all-pass configuration and symmetrical add-drop configuration.

round trip length), so only a  $1.2\times$  improvement can be expected when substituting the add-drop resonators with an all-pass resonator.

A closer look at  $\Delta\lambda_{min}$  at the pass and drop port of an add-drop resonator is presented in Fig. 2.29(b). Interestingly, the signal on the drop port of a symmetrical add-drop resonator always has a worse detection resolution than the signal on the pass port of the same resonator despite the fact that their resonance signals have the same Q-factor. As the self coupling coefficient  $r$  increases (higher Q-factors), the relative benefit of using the pass signal increases as well (up to  $3.5\times$  for the simulated values). This is explained by the influence of the ‘contrast’ of the peak or dip rather than by the influence of the extinction ratio. The ‘contrast’ is defined by the surface area within the peak or dip, which relates to the maximum value minus the minimum value (while the extinction ratio equals the maximum value divided by the minimum value). The fitting algorithm performs better in the presence of larger contrasts. Using the extinction ratio to measure the influence of the resonance shape is valuable when comparing signals that are all measured at the ‘pass’ port (or that are all measured on the ‘drop’ port), like we did earlier. When comparing resonance shapes with different orientation towards a bias level (like drop versus pass signal), the influence of the surface area within the peak or dip is important.

This also holds when the add-drop resonator is asymmetrical. In Fig. 2.30 the ratio of  $\Delta\lambda_{min}$  at the drop and the pass port of an asymmetrical resonator is shown. The round trip transmission  $a$  was set to 0.99.

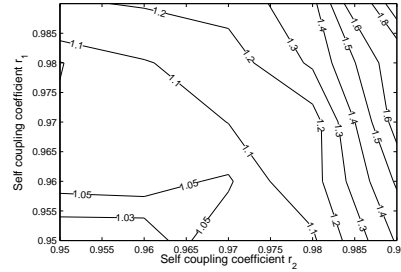


**Figure 2.30:** Ratio of drop and pass signal resolution of an asymmetrical add-drop resonator. Round trip transmission  $a = 0.99$ . The signal on the pass port always has a better measurement resolution than the signal on the drop port.

### 2.3.5 Conclusion

The simulation results show that it is possible to obtain a measurement resolution  $\Delta\lambda_{min}$  much smaller than both the light source line width and the resonant peak FWHM by using the peak fitting algorithm.

$\Delta\lambda_{min}$  decreases linearly with the Q-factor if the wavelength step is adapted to smaller line widths. For extinction ratios above 15 dB, the extinction ratio does not influence  $\Delta\lambda_{min}$  anymore.

Both spectral and amplitude noise have a linear impact on the measurement resolution. High-Q cavities are more tolerant to intensity noise and less tolerant to spectral noise.  $\Delta\lambda_{min}$  was determined for the different measurement setups we used in this work.

For a ring resonator with given physical parameters  $a$  and  $r$ , it is generally better to apply it in an all-pass configuration. Moreover when measuring on the pass port of an add-drop resonator a better measurement resolution is obtained than when measuring the drop signal.

With the spectral characteristics obtained in the previous section, we can now determine the measurement resolution of our devices. The simulation parameters are listed in the first part of table 2.2. These values are also used in table 2.2 in the next section. Two situations are listed: characteristics of the average SOI ring resonator we used for our biological experiments and an optimal SOI ring resonator with realistic improvements that were suggested throughout this chapter. This is also discussed in the next section. The measurement resolution was found to be between 0.062 and 0.672 pm.

## 2.4 Detection limit

With the sensor resolution  $\Delta\lambda_{min}$  and the sensor sensitivity considered in the previous sections, the detection limit (DL) is defined as [37]:

$$DL = \frac{\Delta\lambda_{min}}{sensitivity} \quad (2.36)$$

For bulk refractometric sensing, the DL reports the smallest bulk RI change that can be measured. For biomolecular sensing, the DL can correspond to either the thinnest layer the sensor can accurately detect, the smallest amount of molecules, the lowest concentration [ng/ml] or the smallest surface coverage [pg/mm<sup>2</sup>]. The bulk index DL and the thinnest layer DL are intrinsic properties of the optical sensor and the setup and can be accurately simulated. Molecular coverage and concentration DL however, are strongly dependent on the surface chemistry and the fluidic sample delivery. The density of the receptor molecules and the transport time of the molecules to the sensor surface influence the resonance shift upon molecular binding. Chapter 4 and 5 elaborate on surface chemistry and fluidics of the SOI ring resonator biosensor platform. As a measure for the sensitivity for molecular concentration, we use the measured resonance shift for avidin-biotin interaction with receptor anchoring through a PEG<sup>10</sup> coating, shown in chapter 7 Fig. 7.4. 2  $\mu\text{g/ml}$  avidin concentration causes the resonance wavelength to shift over 350 pm, the sensitivity was thus found to be approximately 175 pm/ $\mu\text{g/ml}$ . Assuming a linear sensor response to molecular concentrations is an approximation. This is further explained in chapter 7, section 7.4.2 and the curves are compared to sensor responses in literature.

Table 2.2 gives an overview of the detection limit of the SOI ring resonator biosensor platform. Two situations are listed: characteristics of the average SOI ring resonator we used for our biological experiments and an optimal SOI ring resonator with realistic improvements that were suggested throughout this chapter. Characteristic parameters for both configurations are listed first, followed by the measurement resolution  $\Delta\lambda_{min}$  and the sensitivity for bulk RI changes and for layers at the surface with fixed refractive index  $n_L$  and varying thickness  $t_L$ . The intensity noise level was set to the noise measured with the setup with a collimator and an infra-red (IR) camera (details in chapter 6, section 6.5) because this setup was used for the main part of the experiments. For the optimized configuration we used the lowest noise level, measured with glued fibers. The Q-factor was set to the optimal Q-factor as calculated in Fig. 2.13(a), but even in an optimal configuration the Q-factor is low because of the high water absorption. The main improvement in detection limit comes from the reduced intensity noise.

In the last part of the table we list the DL for six commonly used criteria: RI, layer thickness, surface coverage, total detectable mass, number of molecules and

<sup>10</sup>Details on surface functionalization with a poly(ethylene glycol) layer are given in chapter 4.

molecular concentration. The DL for bulk RI changes and for layer thickness is directly extracted from simulated sensitivity<sup>11</sup> and measurement resolution. The values for surface coverage and total detectable mass are extracted from the minimum detectable thickness with the optical model (fixed index) described above, with  $n_L = 1.45$ ,  $\rho_L = \rho_{protein} = 1.3 \text{ g/cm}^3$ .

The surface area of a ring resonator with  $5 \mu\text{m}$  radius,  $2 \mu\text{m}$  straight section and waveguide dimensions  $450 \times 220 \text{ nm}$  measures  $31.5 \mu\text{m}^2$ . The high index contrast of SOI results in micron-sized ring resonator biosensors, while the resonance wavelength shift (sensitivity) does not scale with the size of the cavity. Because of this, the minimum detectable mass is extremely low (in the order of  $100 \text{ ag}$ ). This is in contrast to interferometer biosensors. As explained in section 2.5 of this chapter, the sensitivity of an interferometer typically scales with the length of its sensing surface.

The threshold number of molecules was calculated from the total detectable mass, with the molecular weight of avidin ( $66 \text{ kDa}$ )<sup>12</sup>. The minimum detectable concentration was extrapolated from measurement data of Fig. 7.4 as explained above. This value was not measured for TM polarized light, therefore one DL value is missing.

In general, the optimal configuration is 1.5 orders of magnitude better than the configuration we used for most of our experiments. Thanks to the combination of high measurement resolution and extremely small sensor surface area theoretically about 100 avidin molecules should be detectable.

## 2.5 Other sensor configurations

Essentially integrated optical biosensors consist of two concepts: the 'sensing element', an optical mode that experiences a phase or amplitude change, and the 'transducer', here a ring resonator that translates the phase change in a resonance wavelength shift. Both concepts exist in many variations.

The waveguide can be replaced by a slot waveguide that guides modes through a low index slot. Because a vast fraction of the quasi-TE mode will be concentrated in the slot, it will have more interaction with analyte molecules binding in the slot region which will improve the sensitivity of the sensor. However slot waveguides have a few drawbacks: slot waveguide fabrication technology is less mature, filling of the slot with liquids is not trivial and additional propagation losses cause decreasing of the Q-factor and the measurement resolution. In the course of the master thesis of Jeroen Van Lysebettens and the PhD thesis of Tom Claes, we in-

<sup>11</sup>Validation of the simulations with experiments is described in chapter 7, section 7.2 and 7.3

<sup>12</sup>1 Da is the atomic mass unit corresponding to one twelfth of the mass of an isolated atom of carbon-12 ( $^{12}\text{C}$ ) at rest and in its ground state. With Avogadro's number, the mass of one avidin molecule is calculated to be  $1.095956532 \cdot 10^{-19} \text{ g}$ .

	Average SOI ring resonator	SOI ring resonator with realistic improvements
Polarization	TE	TM
FWHM [pm]	300	200
Q-factor	$5.2 \cdot 10^3$	$7.5 \cdot 10^3$
Extinction [dB]	15	20
Noise ( $\sigma_{I_{norm}}^2$ )	$3.4 \cdot 10^{-4}$	$3 \cdot 10^{-5}$
Wavelength step [pm]	5	1
$\Delta\lambda_{min}$ [pm]	0.672	0.063
Bulk RI sensitivity [nm/RIU]	75.4	227.4
Layer thickness sensitivity [nm/nm]	0.178	0.294
Surface area [ $\mu\text{m}^2$ ]	31.5	445
Minimum RI change [RIU]	$8.91 \cdot 10^{-6}$	$2.77 \cdot 10^{-7}$
Minimum layer thickness [pm]	3.78	0.21
Surface coverage [pg/mm <sup>2</sup> ]	5.02	0.28
Minimum detectable mass [ag]	158.17	8.96
Threshold number of avidin molecules	1,440	82
Concentration limit [ng/ml]	3.84	

**Table 2.2:** Detection limit of SOI ring resonators for two cases: an average SOI ring resonator used for our biological experiments and an optimal SOI ring resonator with realistic improvements that were suggested throughout this chapter.

vestigated slot waveguide based biosensors. Results are published in [36] and [38] and will not be discussed here. Various groups investigated the use of integrated periodical structures such as a grating or a photonic crystal [39–42]. Surface Plasmon Resonance modes (SPR) are also widely investigated for their sensitivity to environmental changes. At INTEC, Peter Debackere examined guided SPR modes for biosensing, this work is published in [43–45].

The transducer element can consist of a single ring resonator like the one applied for this work, of an interferometer in multiple appearances, or of more complex filters. In principle they all share the same advantage: the read-out is completely decoupled from the sensing element and transducer. This work deals with one of the most basic transducer principles, but the knowledge and infrastructure can now relatively easy be transferred to various other filter types in the search for the most sensitive and accurate sensing mechanism. We will list a few other transducers that were proposed in literature and that can consist of basic SOI waveguides.

### **Mach-Zehnder interferometer**

The operation principle of an integrated Mach-Zehnder interferometer (MZI) is illustrated in Fig. 2.31(a). Coherent, single frequency, single polarization light from a laser enters the single-mode input waveguide and is split equally at a Y-junction. One branch has a window over the top of it allowing the evanescent field of that branch to interact with the sample while the reference arm is protected from the sample with a thick cladding layer. The two branches recombine at the output, resulting in interference, and a photodetector measures the output intensity. A change in the RI at the surface of the sensor arm results in an optical phase change on the sensing arm and a subsequent change in the light intensity measured at the photodetector, as described by:

$$I(\Delta n_{eff}) \propto \cos(\Delta n_{eff} k_0 L)$$

where  $\Delta n_{eff}$ ,  $k_0$ , and  $L$  are the RI change, the amplitude of the wave vector, and the length of the sensing region, respectively. In contrast to resonator biosensors, increasing the length of the sensing window increases the sensing signal. Note that because of the cosine-dependent intensity function, the signal change is not easily resolvable near the maximum and minimum of the cosine function.

Various groups demonstrated bulk RI sensing and basic molecular sensing with  $\text{Si}_3\text{N}_4$  or  $\text{SiON}$  waveguides on a silicon substrate [46, 47]. Densmore et al. specifically worked on SOI MZI biosensors [22, 48]. They measured a phase response of  $460(2\pi)/\text{RIU}$ .

Other interferometers such as the Young interferometer [49] and Hartman interferometer [50] are not considered here, because although the sensing element is integrated, the recombination of the signal occurs outside of the optical chip or

with additional optical elements. The possibilities of parallel read-out and miniaturization are not similar to fully integrated SOI biosensors.

### Multiple ring resonators

**Vernier ring resonators** A digital optical sensor based on two cascaded rings with different FSRs is pictured in Fig. 2.31(c). Because of their different FSRs, the major peak of the spectral response from the output port shifts digitally when the effective refractive index of ring #2 changes. The shift of the major peak is equal to multiple FSRs of ring #1. In addition the combined resonance of ring resonators in the so-called Vernier configuration have an enhanced Q-factor as compared to single-ring resonators. This might enhance the measurement resolution. Dai et al. reported enhanced sensitivity of over two orders of magnitude as compared to a single-ring resonator [51].

**Concentric ring resonators** Fig. 2.31(b) is a schematic of a concentric ring resonator. The transfer function is determined by the characteristics of both rings plus the ring-ring distributed coupling. When the two rings resonate at the same frequency (which can be realized by fine tuning the FSR of the individual rings), the resonance depths are much enhanced as compared with the single ring resonator. The reduced measurement resolution results in a better detection limit [52].

### Ring-coupled Mach-Zehnder interferometers

A ring-coupled MZI is shown in Fig. 2.31(d). This device exhibits sharp Fano resonances, and the steep slope of the resonance can be used for sensing. Fan et al. show that when properly optimized, a ring-coupled MZI allows at most a 30.5% enhancement in sensitivity over a conventional ring resonator (used in intensity interrogation), as well as a 25% decrease in the power circulating in the ring. However the introduction of an MZI adds another source of thermal instability to the sensor, which aggravates the inherent thermal instability of the ring itself [53].

### Nested-ring Mach-Zehnder interferometers

Fig. 2.31(e) pictures an MZI-coupled microring, which includes a microring and a feedback line. The feedback line is one of the arms of the MZI coupler and the other arm is formed by part of the microring. By optimizing the length difference between the two arms of the MZI coupler, an MZI-coupled microring with a high Q-factor and high extinction ratio is obtained. Dai et al. demonstrate refractive index sensing with  $10^{-6}$  detection limit [54]. Because the coupling ratio of the MZI coupler is wavelength-dependent, one can greatly depress the dips at the resonant

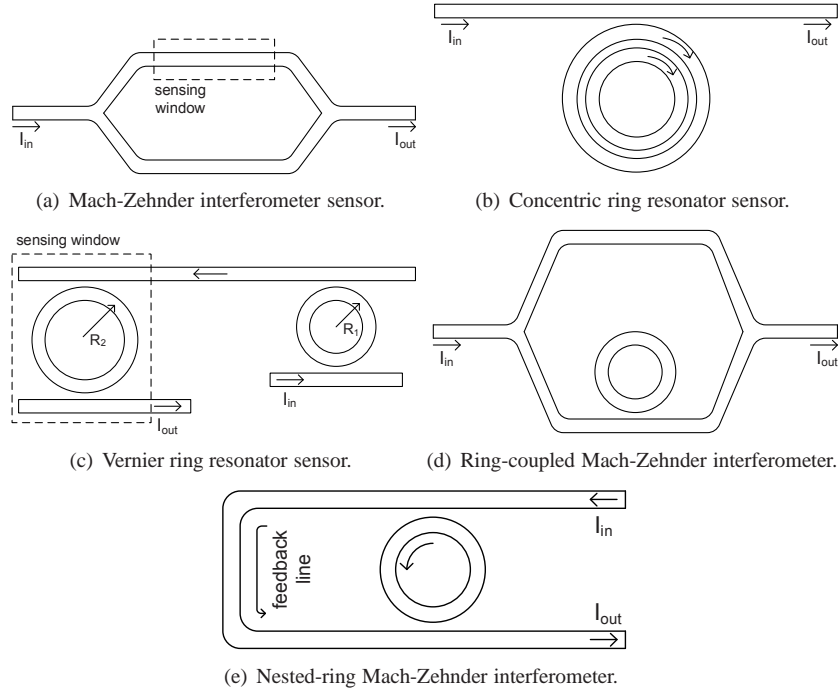


**Figure 2.31:** Other sensing configurations that can be composed of simple SOI waveguides and implemented in the same platform as described in this work (more details on the platform are found in chapter 6).

wavelengths except the considered one by correctly choosing the interference order of the MZI coupler. This way there is only one resonant wavelength with a high extinction ratio in a very large wavelengths span and the dynamic measurement range is expanded to  $0 \leq \Delta n < 0.48$ .

## 2.6 Conclusion

Throughout this chapter a single ring resonator was studied. All aspects with respect to its biosensor performance were discussed. The physical limitations of SOI ring resonators were discussed as well as methods to optimize Q-factor and finesse. We determined losses and coupling of SOI waveguides and directional couplers. We found a large discrepancy between the performance of ring resonators with an air cladding versus a water cladding. The water cladding causes absorption of IR light, which intrinsically lowers the Q-factor about 1.5 times.

The sensitivity of an SOI ring resonator biosensor depends on the fraction of light in the sensing material and on the group index of the resonant mode. The sensitiv-

ity was simulated for various waveguide dimensions. We discussed a commonly used optical model for biomolecular interaction.

The measurement resolution  $\Delta\lambda_{min}$  or the minimum detectable wavelength shift, can be much smaller than the light source line width and the resonance peak FWHM by using a peak fitting algorithm and suppressing wavelength and intensity noise. We simulated the impact of resonance shape and measurement equipment on  $\Delta\lambda_{min}$  and found  $\Delta\lambda_{min}$  to improve linearly with square root of intensity noise and with Q-factor, provided that wavelength step is adapted to the FWHM of the resonance.

Finally, the detection limit of the device can be determined with the ratio of  $\Delta\lambda_{min}$  and sensitivity. The detection limit for bulk index sensing, layer detection, surface coverage, absolute mass and molecular concentration are listed for our current devices as well as for devices with an optimal performance. The optimal performance is restricted by the limitations on resonance shape that can be obtained with SOI and the available equipment. We find the current system being capable of detecting a surface coverage of 5.02 pg/mm<sup>2</sup>, a concentration of 3.8 ng/ml and molecular mass of 158 ag. The optimal device performs more than 10 times better and can detect a threshold of 100 avidin molecules.

## References

- [1] W. Bogaerts, V. Wiaux, D. Taillaert, S. Beckx, B. Luyssaert, P. Bienstman, and R. Baets. *Fabrication of photonic crystals in silicon-on-insulator using 248-nm deep UV lithography*. IEEE Journal of Selected Topics in Quantum Electronics, 8(4):928–934, 2002.
- [2] P. Dumon, W. Bogaerts, V. Wiaux, J. Wouters, S. Beckx, J. Van Campenhout, D. Taillaert, B. Luyssaert, P. Bienstman, D. Van Thourhout, and R. Baets. *Low-loss SOI photonic wires and ring resonators fabricated with deep UV lithography*. IEEE Photonics Technology Letters, 16(5):1328–1330, 2004.
- [3] W. Bogaerts, R. Baets, P. Dumon, V. Wiaux, S. Beckx, D. Taillaert, B. Luyssaert, J. Van Campenhout, P. Bienstman, and D. Van Thourhout. *Nanophotonic waveguides in silicon-on-insulator fabricated with CMOS technology*. Journal of Lightwave Technology, 23(1):401–412, 2005.
- [4] S. K. Selvaraja, P. Jaenen, W. Bogaerts, D. Van Thourhout, P. Dumon, and R. Baets. *Fabrication of Photonic Wire and Crystal Circuits in Silicon-on-Insulator Using 193-nm Optical Lithography*. Lightwave Technology, Journal of, 27(18):4076–4083, 2009.
- [5] Tarek Ibrahim John Heebner, Rohit Grover. *Optical Microresonators: Theory, Fabrication and Applications*. Springer Series in Optical Sciences. Springer, 1st edition, 2008.
- [6] O. Schwelb. *Transmission, group delay, and dispersion in single-ring optical resonators and add/drop filters - A tutorial overview*. Journal of Lightwave Technology, 22(5):1380–1394, 2004.
- [7] P. Dumon. *Ultra-compact integrated optical filters in silicon-on-insulator by means of wafer-scale technology*. PhD thesis, Ghent University, 2007.
- [8] I. Christiaens. *Vertically coupled microring resonators fabricated with wafer bonding*. PhD thesis, Ghent University, 2005.
- [9] H. Su and X. G. Huang. *Fresnel-reflection-based fiber sensor for on-line measurement of solute concentration in solutions*. Sensors and Actuators B-Chemical, 126:579–582, 2007.
- [10] A. C. Turner, C. Manolatu, B. S. Schmidt, M. Lipson, M. A. Foster, J. E. Sharping, and A. L. Gaeta. *Tailored anomalous group-velocity dispersion in silicon channel waveguides*. Optics Express, 14(10):4357–4362, 2006.

- 
- [11] E. Dulkeith, F. N. Xia, L. Schares, W. M. J. Green, and Y. A. Vlasov. *Group index and group velocity dispersion in silicon-on-insulator photonic wires*. *Optics Express*, 14(9):3853–3863, 2006.
- [12] L. B. Soldano and E. C. M. Pennings. *Optical multimode interference devices based on self-imaging - principles and applications*. *Journal of Lightwave Technology*, 13(4):615–627, 1995.
- [13] W. Bogaerts, S. K. Selvaraja, P. Dumon, J. Brouckaert, K. De Vos, D. Van Thourhout, and R. Baets. *Silicon-on-Insulator Spectral Filters Fabricated With CMOS Technology*. *Selected Topics in Quantum Electronics, IEEE Journal of*, 16(1):33–44, 2010.
- [14] Madsen C.K. and Zhao J.H. *Optical Filter design and Analysis*. Wiley Series in Microwave and Optical Engineering. John Wiley & Sons, Inc., New York, 1999.
- [15] Q. Wang, G. Farrell, and T. Freir. *Effective index method for planar light-wave circuits containing directional couplers*. *Optics Communications*, 259(1):133–136, 2006.
- [16] D. Van Thourhout, R. Baets, Stijns. E., and H. Ottevaere. *Microphotronics Textbook*. Universiteit Gent & Vrije Universiteit Brussel, 2008.
- [17] B. E. Little, S. T. Chu, H. A. Haus, J. Foresi, and J. P. Laine. *Micro-ring resonator channel dropping filters*. *Journal of Lightwave Technology*, 15(6):998–1005, 1997.
- [18] C. Manolatou, M. J. Khan, S. H. Fan, P. R. Villeneuve, H. A. Haus, and J. D. Joannopoulos. *Coupling of modes analysis of resonant channel add-drop filters*. *IEEE Journal of Quantum Electronics*, 35(9):1322–1331, 1999.
- [19] K. F. Palmer and D. Williams. *Optical properties of water in near-infrared*. *Journal of the Optical Society of America*, 64(8):1107–1110, 1974.
- [20] W. R. McKinnon, D. X. Xu, C. Storey, E. Post, A. Densmore, A. Delage, P. Waldron, J. H. Schmid, and S. Janz. *Extracting coupling and loss coefficients from a ring resonator*. *Optics Express*, 17(21):18971–18982, 2009.
- [21] A. Delage, D. X. Xu, R. W. McKinnon, E. Post, P. Waldron, J. Lapointe, C. Storey, A. Densmore, S. Janz, B. Lamontagne, P. Cheben, and J. H. Schmid. *Wavelength-Dependent Model of a Ring Resonator Sensor Excited by a Directional Coupler*. *Journal of Lightwave Technology*, 27(9):1172–1180, 2009.

- [22] A. Densmore, D. X. Xu, P. Waldron, S. Janz, P. Cheben, J. Lapointe, A. Delage, B. Lamontagne, J. H. Schmid, and E. Post. *A silicon-on-insulator photonic wire based evanescent field sensor*. IEEE Photonics Technology Letters, 18(21-24):2520–2522, 2006.
- [23] K. Tiefenthaler and W. Lukosz. *Sensitivity of grating couplers as integrated-optical chemical sensors*. Journal of the Optical Society of America B-Optical Physics, 6(2):209–220, 1989.
- [24] G. J. Veldhuis, O. Parriaux, H. J. W. Hoekstra, and P. V. Lambeck. *Sensitivity enhancement in evanescent optical waveguide sensors*. Journal of Lightwave Technology, 18(5):677–682, 2000.
- [25] B. Lillis, M. Manning, H. Berney, E. Hurley, A. Mathewson, and M. M. Sheehan. *Dual polarisation interferometry characterisation of DNA immobilisation and hybridisation detection on a silanised support*. Biosensors & Bioelectronics, 21(8):1459–1467, 2006.
- [26] F. Hook, J. Voros, M. Rodahl, R. Kurrat, P. Boni, J. J. Ramsden, M. Textor, N. D. Spencer, P. Tengvall, J. Gold, and B. Kasemo. *A comparative study of protein adsorption on titanium oxide surfaces using in situ ellipsometry, optical waveguide lightmode spectroscopy, and quartz crystal microbalance/dissipation*. Colloids and Surfaces B-Biointerfaces, 24(2):155–170, 2002.
- [27] J. Tsai, R. Taylor, C. Chothia, and M. Gerstein. *The packing density in proteins: Standard radii and volumes*. Journal of Molecular Biology, 290(1):253–266, 1999.
- [28] J. Voros. *The density and refractive index of adsorbing protein layers*. Biophysical Journal, 87(1):553–561, 2004.
- [29] J. A. Defejter, J. Benjamins, and F. A. Veer. *Ellipsometry as a tool to study adsorption behavior of synthetic and biopolymers at air-water-interface*. Biopolymers, 17(7):1759–1772, 1978.
- [30] T. M. Davis and W. D. Wilson. *Determination of the refractive index increments of small molecules for correction of surface plasmon resonance data*. Analytical Biochemistry, 284(2):348–353, 2000.
- [31] P. I. Nikitin, B. G. Gorshkov, E. P. Nikitin, and T. I. Ksenevich. *Picoscope, a new label-free biosensor*. Sensors and Actuators B-Chemical, 111:500–504, 2005.
- [32] E. Ozkumur, A. Yalcin, M. Cretich, C. A. Lopez, D. A. Bergstein, B. B. Goldberg, M. Chiari, and M. S. Unlu. *Quantification of DNA and protein*

- adsorption by optical phase shift*. *Biosensors & Bioelectronics*, 25(1):167–172, 2009.
- [33] J. Piehler, A. Brecht, and G. Gauglitz. *Affinity detection of low molecular weight analytes*. *Analytical Chemistry*, 68(1):139–143, 1996.
- [34] L. Moiseev, M. S. Unlu, A. K. Swan, B. B. Goldberg, and C. R. Cantor. *DNA conformation on surfaces measured by fluorescence self-interference*. *Proceedings of the National Academy of Sciences of the United States of America*, 103(8):2623–2628, 2006.
- [35] J. J. Hu, X. C. Sun, A. Agarwal, and L. C. Kimerling. *Design guidelines for optical resonator biochemical sensors*. *Journal of the Optical Society of America B-Optical Physics*, 26(5):1032–1041, 2009.
- [36] T. Claes, J. G. Molera, K. De Vos, E. Schacht, R. Baets, and P. Bienstman. *Label-free biosensing with a slot-waveguide-based ring resonator in silicon on insulator*. *IEEE Photonics Journal*, pages 197–204, 2009.
- [37] I. M. White and X. D. Fan. *On the performance quantification of resonant refractive index sensors*. *Optics Express*, 16(2):1020–1028, 2008.
- [38] J. Schrauwen, J. Van Lysebettens, T. Claes, K. De Vos, P. Bienstman, D. Van Thourhout, and R. Baets. *Focused-Ion-Beam Fabrication of Slots in Silicon Waveguides and Ring Resonators*. *IEEE Photonics Technology Letters*, 20(21-24):2004–2006, 2008.
- [39] M. Lee and P. M. Fauchet. *Two-dimensional silicon photonic crystal based biosensing platform for protein detection*. *Optics Express*, 15(8):4530–4535, 2007.
- [40] N. Skivesen, A. Tetu, M. Kristensen, J. Kjems, L. H. Frandsen, and P. I. Borel. *Photonic-crystal waveguide biosensor*. *Optics Express*, 15(6):3169–3176, 2007.
- [41] J. H. Schmid, W. Sinclair, J. Garcia, S. Janz, J. Lapointe, D. Poitras, Y. Li, T. Mischki, G. Lopinski, P. Cheben, A. Delage, A. Densmore, P. Waldron, and D. X. Xu. *Silicon-on-insulator guided mode resonant grating for evanescent field molecular sensing*. *Optics Express*, 17(20):18371–18380, 2009.
- [42] S. Mandal, J. M. Goddard, and D. Erickson. *A multiplexed optofluidic biomolecular sensor for low mass detection*. *Lab on a Chip*, 9(20):2924–2932, 2009.
- [43] P. Debackere. *Nanophotonic biosensor based on surface plasmon interference*. PhD thesis, Ghent University, 2009-2010.

- [44] P. Debackere, S. Scheerlinck, P. Bienstman, and R. Baets. *Surface plasmon interferometer in silicon-on-insulator: novel concept for an integrated biosensor*. Optics Express, 14(16):7063–7072, 2006.
- [45] P. Debackere, R. Baets, and P. Bienstman. *Bulk sensing experiments using a surface-plasmon interferometer*. Optics Letters, 34(18):2858–2860, 2009.
- [46] F. Brosinger, H. Freimuth, M. Lacher, W. Ehrfeld, E. Gedig, A. Katerkamp, F. Spener, and K. Cammann. *A label-free affinity sensor with compensation of unspecific protein interaction by a highly sensitive integrated optical Mach-Zehnder interferometer on silicon*. Sensors and Actuators B-Chemical, 44(1-3):350–355, 1997.
- [47] R. G. Heideman and P. V. Lambeck. *Remote opto-chemical sensing with extreme sensitivity: design, fabrication and performance of a pigtailed integrated optical phase-modulated Mach-Zehnder interferometer system*. Sensors and Actuators B-Chemical, 61(1-3):100–127, 1999.
- [48] A. Densmore, D. X. Xu, S. Janz, P. Waldron, T. Mischki, G. Lopinski, A. Delage, J. Lapointe, P. Cheben, B. Lamontagne, and J. H. Schmid. *Spiral-path high-sensitivity silicon photonic wire molecular sensor with temperature-independent response*. Optics Letters, 33(6):596–598, 2008.
- [49] A. Ymeti, J. Greve, P. V. Lambeck, T. Wink, Swfm van Hovell, T. A. M. Beumer, R. R. Wijn, R. G. Heideman, V. Subramaniam, and J. S. Kanger. *Fast, ultrasensitive virus detection using a young interferometer sensor*. Nano Letters, 7(2):394–397, 2007.
- [50] B. H. Schneider, J. G. Edwards, and N. F. Hartman. *Hartman interferometer: versatile integrated optic sensor for label-free, real-time quantification of nucleic acids, proteins, and pathogens*. Clinical Chemistry, 43(9):1757–1763, 1997.
- [51] Daoxin Dai. *Highly sensitive digital optical sensor based on cascaded high-Q ring-resonators*. Opt. Express, 17(26):23817–23822, 2009.
- [52] X. H. Li, Z. Y. Zhang, S. Y. Qin, T. Wang, F. F. Liu, M. Qiu, and Y. K. Su. *Sensitive label-free and compact biosensor based on concentric silicon-on-insulator microring resonators*. Applied Optics, 48(25):F90–F94, 2009.
- [53] M. Terrel, M. J. F. Digonnet, and S. H. Fan. *Ring-coupled Mach-Zehnder interferometer optimized for sensing*. Applied Optics, 48(26):4874–4879, 2009.

- [54] D. X. Dai and S. L. He. *Highly sensitive sensor based on an ultra-high- $Q$  Mach-Zehnder interferometer-coupled microring*. Journal of the Optical Society of America B-Optical Physics, 26(3):511–516, 2009.

# 3

## Dual polarization ring resonator sensor

In this chapter we introduce a novel technique to extract additional data on biomolecular interactions from ring resonator biosensors. The technique is described in section 3.1 and we discuss the added value it can offer for biosensing applications. Section 3.2 clarifies the working principle. Design and implementation of the device are considered in sections 3.3 and 8.3.2 respectively.

### 3.1 Introduction

Up until now we have discussed the detection of biomolecular interaction by tracking the wavelength shift of one resonant ring resonator mode. The optical model<sup>1</sup> which links the output of the sensor to the molecular interaction consists of a layer with thickness  $t_L$  and refractive index  $n_L$ . Most biosensing techniques cannot distinguish between both parameters, and the output is linked to either one of them or to another calibration parameter such as the molecular concentration. However, access to both  $t_L$  and  $n_L$  would yield information on the density as well as on the thickness of the layer via formula (3.1):

$$\rho_L = \rho_{protein} \frac{n_L - n_B}{n_{protein} - n_B} \quad (3.1)$$

where  $\rho_{protein}$  is the density of dry proteins [ $\text{g}/\text{cm}^3$ ], generally accepted to be  $\rho_{protein} = 1.33 \text{ g}/\text{cm}^3$  [1, 2]. This formula was discussed in chapter 2, section 2.2.

---

<sup>1</sup>The optical model for biomolecular interaction is described in chapter 2, section 2.2.2.

In all biological experiments we performed, we measured only one parameter: the resonance wavelength shift of the  $TE_{00}$  resonating mode when biomolecular interaction occurs. For some waveguide dimensions however, the  $TM_{00}$  mode is also guided. When  $TE_{00}$  and  $TM_{00}$  are simultaneously excited in a ring resonator, they will propagate orthogonally with a different effective index and a different group velocity. Hence they will resonate at different resonance wavelengths. The sensitivity of their effective indices  $n_{eff,TE}$  and  $n_{eff,TM}$  to environmental changes will differ depending on the field distribution (chapter 2, section 2.2). For all of these reasons, the resonance wavelength of  $TE_{00}$  and  $TM_{00}$  will shift a different amount when biomolecular interaction takes place at the resonator surface. Measurement of both wavelength shifts will allow us to disentangle  $n_L$  and  $t_L$  and hence obtain conformational information on the biomolecular layer.

A commercial implementation based on a similar principle was done by Farfield Scientific Ltd., Manchester, UK, called the Analight®Bio200 Dual Polarization Interferometer. This is an interferometer-based sensor constructed from two optical waveguides stacked one on top of each other and an array photodiode. When polarized light (TM) is introduced to the end of the stack, single mode excitations in sensing and reference waveguides are formed and propagate through the structure. At the output, they form the well-known pattern of Youngs interference fringes on an array photodiode. On exposing the sensing waveguide to a biomolecule that attaches to it, the phase will change in the sensing waveguide while the effective index of the reference waveguide does not change. Monitoring the relative phase position of the fringe pattern will reveal the TM output. Subsequently, a second polarization of light (TE) is introduced into the waveguide stack. As explained, this responds differently to biomolecule adsorption or removal, and provides a second independent measurement. For each polarization there are an infinite number of refractive index/film thickness combinations that will produce the observed effect. However, when both polarizations are taken together a unique solution is resolved.

Conformational information of the molecules is of major importance in genomics<sup>2</sup> and proteomics<sup>3</sup>. The folding and misfolding of proteins, for example, are increasingly topics of study in their connection with the onset of degenerative diseases such as Alzheimers disease [3]. In genomics, finding information on DNA probe orientation, probe mobility and surface coverage and assessing the impact they have on hybridization efficiency are of critical importance in the development of immobilization methods [4]. Lillis et al. used the Analight to show that it was possible to elucidate probe orientation and measure probe coverage at different stages of each immobilization process and concluded on the direct impact that probe mo-

---

<sup>2</sup>Genomics is a general term for the study of the genomes of organisms. The field includes intensive efforts to determine the entire DNA sequence of organisms and fine-scale genetic mapping efforts.

<sup>3</sup>Proteomics is a general term for the large-scale study of proteins, particularly their structures and functions.

bility has on hybridization efficiency [5].

## 3.2 Measurement principle

The  $TE_{00}$  and  $TM_{00}$  modes are measured simultaneously and two wavelength shifts  $\Delta\lambda_{TE}$  and  $\Delta\lambda_{TM}$  are monitored:

$$\Delta\lambda_{TE} = \frac{\Delta_{env} n_{eff,TE} \cdot \lambda_{res}}{n_{g,TE}} \quad (3.2)$$

$$\Delta\lambda_{TM} = \frac{\Delta_{env} n_{eff,TM} \cdot \lambda_{res}}{n_{g,TM}} \quad (3.3)$$

After measurement of  $\Delta\lambda_{TE}$  and  $\Delta\lambda_{TM}$ , the experimental results will be mapped to simulations. All possible wavelength shifts are simulated for the  $(t_L, n_L)$  parameter space, see Fig. 3.1(a). The results in the graph are shifts obtained for a ring resonator with waveguide dimensions  $220 \times 450$  nm. Measured values of  $\Delta\lambda_{TE}$  and  $\Delta\lambda_{TM}$  form two horizontal planes that intersect with the simulated surfaces. The intersection line of the measured and simulated TE-planes and the measured and simulated TM-planes can now be mapped onto a  $(t_L, n_L)$  space, see Fig. 3.1(b). The intersection of both curves reveals the index and thickness of the layer unambiguously.

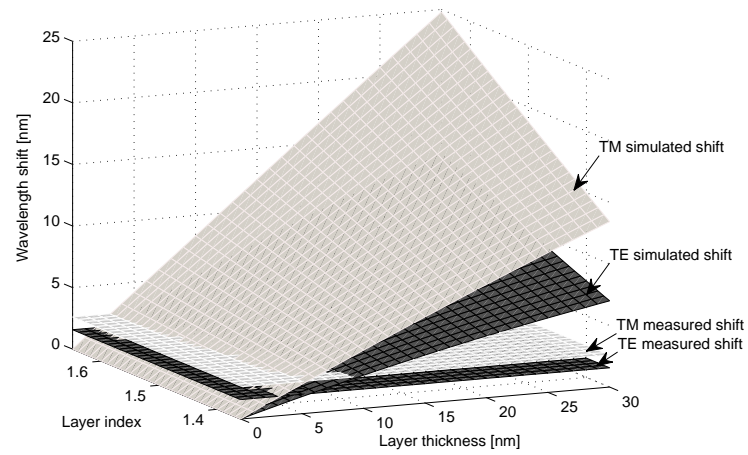
A good simulation model is crucial for accurate results. Before starting thorough examination of this sensor principle, we verified the validity of the layer simulations with experiments. For that we coated the SOI sensors with  $SiO_2$  layers with known refractive index and thickness. The wavelength shift that resulted from the coating was compared with the wavelength shift simulated with FimmWave, a vectorial mode solver. The simulation resonance shift was calculated with formula (3.2). We found good correspondence between measurement and simulations. A graph of the results and technical details are given in the experimental chapter 7, section 7.3.

## 3.3 Design considerations

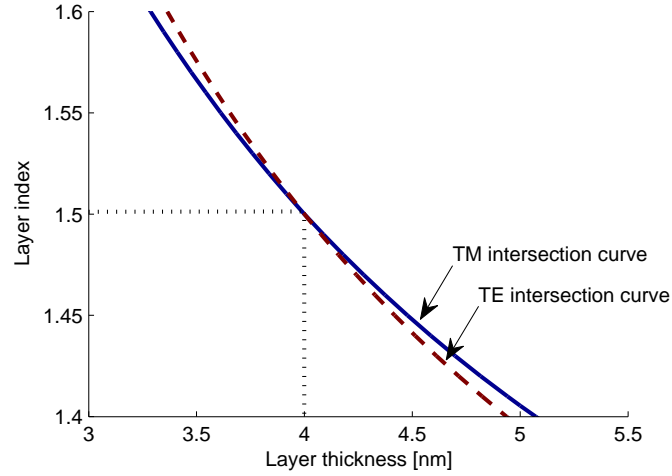
### 3.3.1 Sensor quality defined by detection limit and accuracy

The dual-polarization biosensor needs optimization for two figures: low detection limit and good  $(t_L, n_L)$  accuracy.

A low detection limit imposes on the sensor to have a good measurement resolution  $\Delta\lambda_{min}$  and large wavelength shifts  $\Delta\lambda_{TE}$  and  $\Delta\lambda_{TM}$ . The formula for detection



(a) Measured and simulated wavelength shifts for the  $TE_{00}$  and  $TM_{00}$  mode.



(b) TE and TM lines of intersection between measured and simulated wavelength shifts. The intersection of both lines provides us with the layer thickness and layer index.

**Figure 3.1:** Working principle of dual polarization ring resonator biosensor.

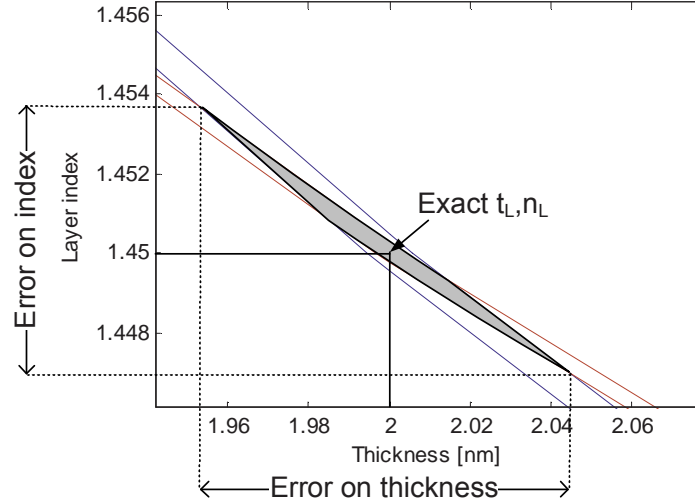


**Figure 3.2:** Illustration of the effect of a limited measurement resolution  $\Delta\lambda_{min}$  on the accuracy on thickness  $t_L$  and index  $n_L$  determination.

limit was discussed in detail in the previous chapter:

$$DL = \frac{\Delta\lambda_{min}}{sensitivity} \quad (3.4)$$

A wavelength shift can only be resolved within the measurement resolution  $\Delta\lambda_{min}$ . This translates into an uncertainty on the location of the horizontal ‘measured’ TE- and TM-planes (horizontal planes on Fig. 3.1(a)). This uncertainty is transferred in a spread on the intersection lines and hence in an area of possible  $(t_L, n_L)$  values, see Fig. 3.2. Depending on the slope of the simulated TE- and TM-planes and on the angle between the intersection lines, this area is increased or reduced. Apart from a low detection limit, the  $(t_L, n_L)$  uncertainty area is an additional measure for the quality of the sensor and has to be minimized. Both figures depend on measurement resolution  $\Delta\lambda_{min}$  and sensitivity.

### 3.3.2 Waveguide design

The measurement resolution  $\Delta\lambda_{min}$  is determined by resonance shape and instrumentation factors and was discussed extensively in chapter 2, section 2.3. The resonance shape of the TE and TM resonances will depend on losses and coupling of the two resonating modes. For now we will assume  $\Delta\lambda_{min}$  to be equal to 1 pm for the TE<sub>00</sub> and TM<sub>00</sub> modes.

The design parameters are limited to width  $W$  and height  $H$  of the waveguide. In the search for a high quality dual polarization sensor, we do not limit ourselves to

the SOI layer stack dimensions determined by the manufacturer of the wafers all our chips are processed with. Instead we will consider all  $(W, H)$  combinations. How to fabricate waveguides with a wide range of  $(W, H)$  values is discussed in the section ‘Implementation’ (section 8.3.2).

### Single mode wires

The primary requisite is single mode guiding of the  $TE_{00}$  and the  $TM_{00}$  mode. Only for a limited range of  $W$  and  $H$  values,  $TE_{00}$  and  $TM_{00}$  will be guided while  $TE_{01}$ ,  $TM_{01}$  and higher order modes will be in cut-off. Modes with effective indices above  $n_{SiO_2}$  will not be radiated into the buffer layer and will be guided. Simulation of the effective index of the modes across the  $(W, H)$  parameter space provides us with the correct  $(W, H)$  values. Note that all simulations are performed for a configuration with a water cladding ( $n_{water} = 1.311$  [6]).

### Low detection limit

The detection limit is determined by the measurement resolution  $\Delta\lambda_{min}$  and the sensitivity. As already mentioned,  $\Delta\lambda_{min}$  is set to 1 pm for all simulations. The sensitivity however, will largely depend on the waveguide dimensions because of the strong dimensional influence on the mode distribution. This was previously explained in chapter 2, section 2.2. Designing a high quality dual polarization biosensor imposes that we search for  $W$  and  $H$  that provide optimal sensitivity for the  $TE_{00}$  mode as well as for the  $TM_{00}$  mode. For all single mode  $(W, H)$  values we simulated the TE and TM wavelength shift induced by a layer of thickness  $t_L = 4$  nm and refractive index  $n_L = 1.45$  and calculated the sensitivity [nm/nm/RIU] for both modes as:

$$\text{Sensitivity} = \frac{\text{shift}}{\text{thickness} \cdot \text{layer index}} = \frac{\lambda_{res}(n_{eff,layer} - n_{eff,0})}{t_L(n_L - n_{water})} \quad (3.5)$$

$$(3.6)$$

When considering small layers the shift is linear with refractive index and layer thickness (Fig. 3.1(a)). Simulated results for the sensitivity of both modes are presented in Fig. 3.3(a) and 3.3(b).

The sensitivity trends as a function of  $W$  and  $H$  can be understood with the reasoning in chapter 2, section 2.2. With a larger fraction of the field in the layer, the effective index is more sensitive to layer variations. For TM polarized light, the effective index is more sensitive to changes on the top waveguide surface. Hence waveguides with a relatively large top surface area as compared to the sidewall surface area ( $H < W$ ) are more sensitive. A maximal TM sensitivity of 2.252 nm/nm/RIU was found for  $W = 420$  nm and  $H = 210$  nm.

The reverse reasoning holds for TE polarized light; when  $W < H$  the influence of the field discontinuity at the side walls dominates and waveguides with a large side wall surface area are more sensitive. A maximal TE sensitivity of 4.126 nm/nm/RIU was found for  $W = 220$  nm and  $H = 430$  nm<sup>4</sup>.

This reveals that, although the TM sensitivity is larger for our photonic wires (with fixed height of 220 nm), the maximal sensitivity of the TE<sub>00</sub> mode can be about twice as large as the maximal obtainable sensitivity of the TM<sub>00</sub> mode when having full flexibility on the waveguide dimensions.

For a wire with dimensions  $W = 240$  nm and  $H = 280$  nm, the product of TE and TM sensitivity was found to be optimal. TE and TM sensitivity are respectively 3.295 and 2.117 nm/nm/RIU. As expected this optimum occurs for a nearly square wire configuration. With this sensor configuration the minimum detectable mass equals 91 and 142 ag for the TE and TM mode respectively and minimum detectable surface coverage equals 2.9 and 4.5 pg/mm<sup>2</sup> respectively. These numbers are calculated with  $\Delta\lambda_{min} = 1$  pm, layer index = 1.45,  $\rho_{protein} = 1.33$  g/cm<sup>3</sup> and surface area = 31.5  $\mu\text{m}^2$ . The detection limit is slightly worse than the detection limit of the Analight@ (0.1 pg/mm<sup>2</sup>)<sup>5</sup> [7].

### Good $t_L$ and $n_L$ accuracy

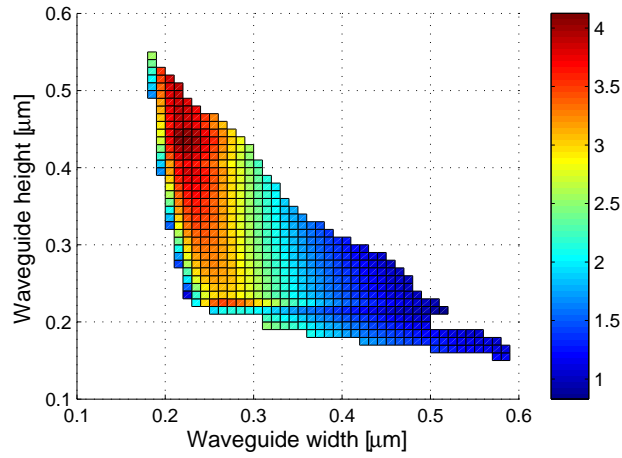
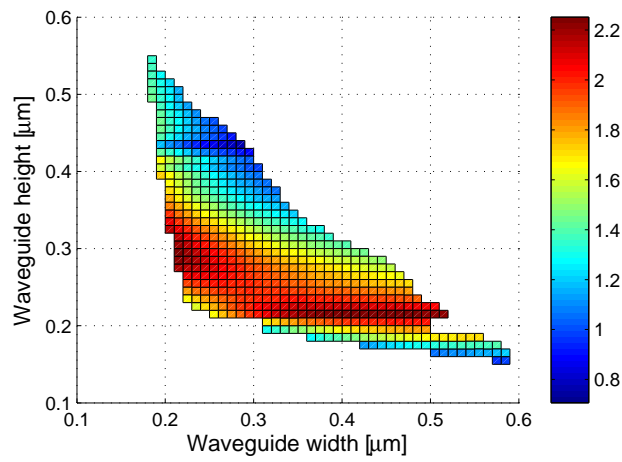
We calculate the  $t_L$  and  $n_L$  accuracy as described above by investigating the spread of the intersection lines for a change in wavelength of 1 pm, and translating this to a spread on the intersection points ( $t_L, n_L$ ), as shown in Fig. 3.2. For a certain waveguide configuration, the accuracy of both  $t_L$  and  $n_L$  also depends on the actual  $t_L$  and  $n_L$  values. The slopes of the TE and TM wavelength shift surfaces differs at all positions, and the angle formed by the intersection lines varies as well. A full investigation of all accuracy values for all waveguide configurations would require immense amount of simulations with considerable simulation time. Instead we calculated the accuracy for three configurations determined in the previous paragraph: maximal TE sensitivity, maximal TM sensitivity and optimal TE and TM sensitivity (TE×TM maximal).

The results are listed in table 3.1. We found the range of accuracies over the  $n_L$  and  $t_L$  parameter space to be worse for the first two configurations. With optimal TE and TM sensitivity, the layer thickness and index can be determined with the highest accuracy. For this configuration we plotted the thickness accuracy and the index accuracy over the  $t_L$  and  $n_L$  space in Fig. 3.4(a) and 3.4(b).

The layer thicknesses of layers with a low refractive index are resolved with the largest error. A low layer index is generally caused by low molecular density or large water content. For example, a layer with index 1.37 and thickness 5 nm

<sup>4</sup>Note that fabrication of wires with these dimensions is not trivial and requires dedicated processes.

<sup>5</sup>However as their sensor surface is much larger, they need an overall bigger amount of molecules to reach the surface coverage detection limit.

(a)  $TE_{00}$ (b)  $TM_{00}$ 

**Figure 3.3:** Sensitivity: wavelength shift per nm layer thickness ( $t_L$ ) and per refractive index unit ( $n_L - n_{water}$ ) in [nm/nm/RIU] as a function of waveguide width  $W$  [ $\mu\text{m}$ ] and height  $H$  [ $\mu\text{m}$ ].

	$W$ [nm]	$H$ [nm]	Error range on $t_L$ [nm]	Error range on $n_L$ [RIU]
Maximal TE sensitivity	220	430	$7.07 \cdot 10^{-7} - 5.10 \cdot 10^0$	$5.40 \cdot 10^{-8} - 2.34 \cdot 10^{-1}$
Maximal TM sensitivity	420	210	$1.50 \cdot 10^{-2} - 1.54 \cdot 10^1$	$2.96 \cdot 10^{-6} - 2.08 \cdot 10^{-1}$
Maximal TE×TM sensitivity	240	280	$2.46 \cdot 10^{-2} - 2.65 \cdot 10^{-1}$	$4.12 \cdot 10^{-8} - 1.55 \cdot 10^{-3}$

**Table 3.1:** Error range on layer thickness  $t_L$  and layer index  $n_L$  for three configurations: maximal TE sensitivity (4.126 nm/nm/RIU), maximal TM sensitivity (2.252 nm/nm/RIU) and optimal sensitivity for TE and TM polarization (TE, TM sensitivity = 3.295, 2.117 nm/nm/RIU).

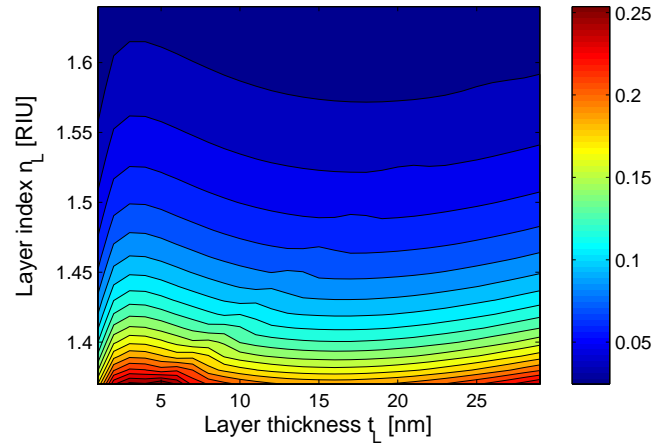
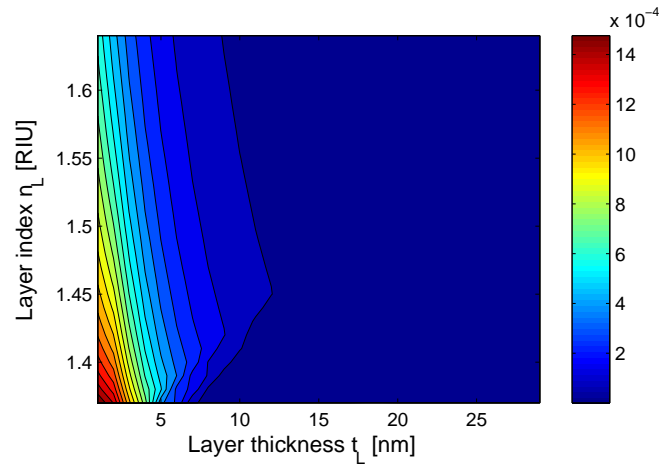
will be determined as  $1.37 \pm 0.00019$  RIU,  $5 \pm 0.13$  nm or a thickness error of 5.2%. While a layer with index 1.6 and thickness 5 nm will be determined as  $1.6 \pm 0.00010$  RIU,  $5 \pm 0.019$  nm or an thickness error of 0.76%. This is comparable with the resolution of the Analight® (0.01 nm) [7].

As for the error on index determination, a thicker layer can be determined with greater accuracy as compared to a thinner layer. A layer with thickness 2 nm and index 1.45 will be measured as  $2 \pm 0.048$  nm and  $1.45 \pm 0.00045$  RIU, an index error of 0.062%. On the other hand, a layer with thickness 10 nm and index 1.45 will be measured as  $10 \pm 0.042$  nm and  $1.45 \pm 0.000053$  RIU, thus with an index error of 0.0073%.

For this configuration, the uncertainty on the layer index  $n_L$  is always lower than 0.11% while the uncertainty on the layer thickness  $t_L$  can rise up to 26%. These large errors on determinations of the thickness only occur for layers with very low index (thus very low molecular density). As soon as the index surpasses 1.40, the maximal error on layer thickness  $t_L$  is 4%.

### 3.4 Implementation: SOI ring resonator with polarization duplexer

In the search for the best waveguide dimensions for dual polarization biosensing, we investigated all possible dimensional ( $W, H$ ) combinations. A wide variety of techniques exists for SOI layer stack fabrication, with membranes of monocrystalline, polycrystalline or amorphous silicon. All results presented in this PhD thesis are obtained with processed wafers from SOITEC with a standard mem-

(a) Error on layer thickness  $t_L$ .(b) Error on layer index  $n_L$ .

**Figure 3.4:** Thickness and waveguide accuracy for a ring resonator with wire dimensions  $W = 240$  nm and  $H = 280$  nm. These dimensions correspond with the values for optimal sensitivity for both the  $TE_{00}$  and  $TM_{00}$  mode.

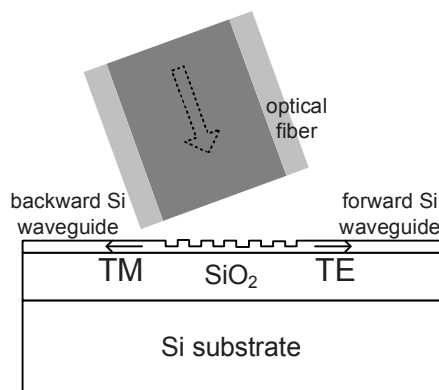


**Figure 3.5:** Dual polarization grating coupler.  $TE_{00}$  and  $TM_{00}$  modes are coupled in opposite directions.

brane height of 220 nm. An introduction to the fabrication process we apply is given in chapter 1, section 1.3.3. At Intec, Selvaraja et al. presented results on amorphous silicon deposited by a PECVD process using CMOS manufacturing tools [8]. Propagation loss measurements show a loss of 3.46 dB/cm for photonic wires (480×220 nm). This process could be attractive for our application because it allows for more flexibility on the height  $H$  of the silicon membrane.

To couple TE and TM polarized light simultaneously to a ring resonator we will make use of both waveguides that originate from a 1D grating coupler. This is in contrast with the Analignt@commercial tool where TE and TM polarization are alternated and thus real-time measurements performed with half the frequency.

A cross section of the dual polarization grating coupler is pictured in Fig. 3.5. This structure is used to spatially separate two polarizations in the same wavelength band. Due to reciprocity, the same device can recombine both polarizations. Analogously, this so-called ‘duplexer’ has been used to spatially separate two wavelength bands with the same polarization for telecom applications in the 1300 nm and 1550 nm wavelength band. The same working principle of a grating coupler as explained in chapter 6, section 6.3 applies here. We performed an optimization procedure similar to the description by G. Roelkens in [9]. By optimizing the grating coupler period and tilt angle of the optical fiber, the grating will have an optimal efficiency for TE polarized light in the forward direction, and for TM polarized light in the backward direction. The coupling was simulated with Camfr (vectorial mode solver) and Omnisim (FDTD simulation software), resulting in TE coupling efficiency of 47% and TM coupling efficiency of 27%. A similar structure for polarization splitting at 1300 nm wavelength was reported by D. Vermeulen in [10].

The implementation of the dual polarization ring resonator for real-time moni-

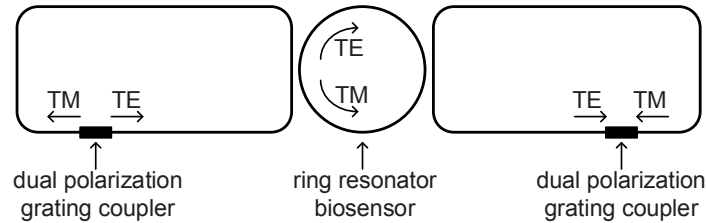


*Figure 3.6: Implementation of dual polarization ring resonator biosensor.*

toring of conformational changes of bilayers is shown in Fig. 3.6. The drop signal is monitored instead of the pass signal to avoid large reflections between the duplexers. Experimental characterization of the ring resonators is ongoing. A good knowledge of propagation properties of SOI wires for TM and TE modes is needed for design of the resonator and the directional couplers. TE mode propagation has been studied extensively (see e.g. the previous chapter), however our knowledge on TM mode propagation in wires so far was insufficient to obtain good resonances in a ring resonator. Based on simulations we made estimations on the dimensions for the first design but no resonance peaks could be observed for the  $TM_{00}$  mode. Recent progress on TM propagation in SOI wires has been published by Vermeulen et al. in [11].

### 3.5 Conclusion

We presented a novel method that allows to extract more information on biomolecular interaction with a single ring resonator. Interrogation of the wavelength shift of two orthonally resonating modes provides us with the thickness as well as with the refractive index of a layer at the sensor surface. This can be translated in information on the molecular density and thus on the conformation of the molecules which is crucial in many genomics and proteomics applications.

We searched for a sensor configuration that offers a low detection limit and a good accuracy on the thickness and the refractive index determination of the adlayers. This configuration was found to consist of waveguides with width  $W = 240$  nm and height  $H = 280$  nm. With a minimum detectable wavelength shift of 1 pm, the minimum detectable surface coverage equals 2.9 and 4.5  $\mu\text{g}/\text{mm}^2$  for the  $TE_{00}$  and  $TM_{00}$  mode respectively. The error on resolving thickness and index of the layer depends on the actual thickness and index values, but is always lower than 0.11% on the index and 4% on the thickness (when the layer index  $> 1.40$ ).

We described a possible implementation of this dual polarization ring resonator. Using a grating duplexer that spatially separates both polarizations, the two wavelength shifts can be monitored simultaneously. This device has the same integra-

tion possibilities concerning read-out and fluidics as further detailed in the next chapters. It is a robust biosensor that can be integrated in a lab-on-a-chip and that provides the user with real-time conformational information on the molecules.

## References

- [1] F. Hook, J. Voros, M. Rodahl, R. Kurrat, P. Boni, J. J. Ramsden, M. Textor, N. D. Spencer, P. Tengvall, J. Gold, and B. Kasemo. *A comparative study of protein adsorption on titanium oxide surfaces using in situ ellipsometry, optical waveguide lightmode spectroscopy, and quartz crystal microbalance/dissipation*. *Colloids and Surfaces B-Biointerfaces*, 24(2):155–170, 2002.
- [2] J. Tsai, R. Taylor, C. Chothia, and M. Gerstein. *The packing density in proteins: Standard radii and volumes*. *Journal of Molecular Biology*, 290(1):253–266, 1999.
- [3] S. E. Radford. *Protein folding: progress made and promises ahead*. *Trends in Biochemical Sciences*, 25(12):611–618, 2000.
- [4] J. Watterson, P. A. E. Piunno, and U. J. Krull. *Practical physical aspects of interfacial nucleic acid oligomer hybridisation for biosensor design*. *Analytica Chimica Acta*, 469(1):115–127, 2002.
- [5] B. Lillis, M. Manning, H. Berney, E. Hurley, A. Mathewson, and M. M. Sheehan. *Dual polarisation interferometry characterisation of DNA immobilisation and hybridisation detection on a silanised support*. *Biosensors & Bioelectronics*, 21(8):1459–1467, 2006.
- [6] H. Su and X. G. Huang. *Fresnel-reflection-based fiber sensor for on-line measurement of solute concentration in solutions*. *Sensors and Actuators B-Chemical*, 126:579–582, 2007.
- [7] <http://www.farfieldgroup.com/>, 2010.
- [8] S. K. Selvaraja, E. Sleenckx, M. Schaekers, W. Bogaerts, D. Van Thourhout, P. Dumon, and R. Baets. *Low-loss amorphous silicon-on-insulator technology for photonic integrated circuitry*. *Optics Communications*, 282(9):1767–1770, 2009.
- [9] G. Roelkens. *Heterogeneous III-V/Silicon photonics: bonding technology and integrated devices*. PhD thesis, Ghent University, 2006-2007.
- [10] Diedrik Vermeulen. *Ontwerp en Fabricage van een Geïntegreerde Zender voor Fiber-To-The-Home (FTTH) Optische Netwerken*. Master thesis, Ghent University, 2008.
- [11] D. Vermeulen, K. Van Acoleyen, S. Ghosh, S. K. Selvaraja, W. De Cort, N. Yebo, E. Hallynck, K. De Vos, P. Debackere, P. Dumon, W. Bogaerts, G. Roelkens, D. Van Thourhout, and R. Baets. *Efficient Tapering to the Fundamental Quasi-TM Mode in Asymmetrical Waveguides*. In 15th European

Conference on Integrated Optics, Cambridge, United Kingdom, 2010. Submitted.



# 4

## (Bio)Chemistry for engineers

An affinity-based biosensor consists of two parts: the transducer that converts a binding event into a read-out signal and a biological receptor layer that is responsible for the affinity-based interactions. This is schematically pictured in figure 4.1. The properties of a biosensor critically depend on the quality of the biological receptor layer, especially for detection in complex samples. The interfacial layer has to allow for immobilization of receptor molecules and at the same time effectively block non-specific interactions with the macromolecular components of the analyzed sample. In addition it must be stable, must not affect the transducer sensitivity and must not hinder transport of the chemical or biological compounds to the transducer surface. Since refractive index sensors directly respond to a change in layer thickness or density, very homogeneous and thin interfacial layers are required.

Throughout the course of this PhD, we closely collaborated with different chemistry research groups for the surface functionalization of SOI photonic chips. Our main collaborators were Dr. Jordi Girones Molera, Dr. Stepan Popelka and Dr. Irene Bartolozzi from the *Polymer Material Research Group* at *Ghent University* with Prof. Em. Etienne Schacht. They are responsible for all surface modifications for the detection of protein interaction.

This chapter starts with a general introduction to affinity-based biomolecular interaction at a transducer surface. The sections that follow will specifically focus on surface modification of silicon surfaces. We describe the chemistry applied to couple protein receptor molecules to the surface, with a focus on reduction of non-specific adsorption, which is a crucial aspect of affinity-based biosensors. This

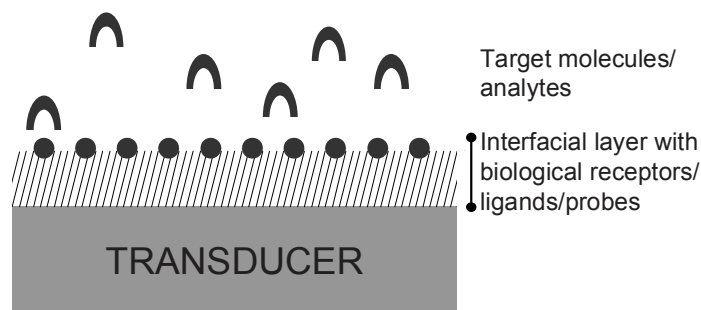


*Figure 4.1: Schematic view of an affinity-based biosensor.*

chapter is meant as a guideline for an engineering audience. Although we take care to be precise about all chemistry statements, chemists might feel different about the amount of detail for one subject and the lack of detail for another. During this work, we realized that communication across different fields is not a trivial thing, but it is of crucial importance in multidisciplinary research.

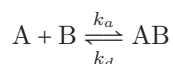
## 4.1 Biomolecular interactions at surfaces

### 4.1.1 General model

In a direct biosensor, one of the interaction partners (the ligand, receptor or probe) is immobilized on the sensor surface. When the other component (the analyte or target) is flowed across the ligand surface, the direct biosensor response can be divided into three essential phases (Fig. 4.2):

1. *Association* of analyte with ligand during sample injection.
2. *Equilibrium* or steady state during sample injection, where the rate of analyte binding is balanced by the dissociation from the complex.
3. *Dissociation* of analyte from the surface when the sample is no longer injected and buffer is flowed.

The association and dissociation phases provide information on the *kinetics* of the analyte-ligand interaction (the rates of complex formation and dissociation). The equilibrium phase provides information on the *affinity* of the analyte-ligand interaction (the strength of binding). The reaction can be described as a simple bimolecular complex formation



<i>Force</i>	<i>Energy (kJ/mol)</i>
Hydrophobic interaction	Up to 15
Electrostatic interaction	Up to 12.5
Hydrogen bonding	Up to 4
Van der Waals forces	Up to 0.4

**Table 4.1:** Molecular forces contributing to biomolecular interaction processes.

where A is the analyte and B is the surface-bound ligand.  $k_a$  and  $k_d$ , sometimes denoted as  $k_{on}$  and  $k_{off}$ , are the association and dissociation rate constants.

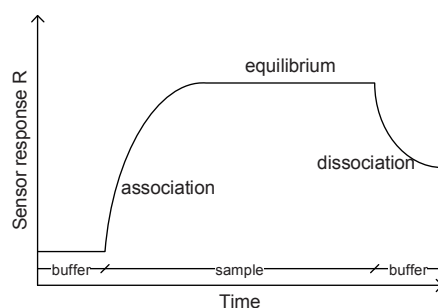


**Figure 4.2:** Schematic response of a biosensor, showing association, equilibrium and dissociation phases.

The basic forces that determine the interaction of biomolecules at the molecular level are listed in Table 4.1. The electrostatic (ionic) and the hydrophobic interaction account for approximately 85% of the interactions and are therefore the most relevant [1].

In general, a real-time biosensor provides information on three aspects of biomolecules and their interactions: the concentration (how many analyte molecules are present in a complex sample), the affinity (how strong the interaction is) and the kinetics (how fast an interaction is).

**Association phase** Assuming pseudo-first order interaction kinetics, the rate of complex formation during sample injection is given by

$$\frac{d[AB]}{dt} = k_a[A][B] - k_d[AB]$$

Under the assumption of a linear response  $R$  of the direct biosensor, a good approximation for SOI ring resonator biosensors and most other biosensors, the rate of complex formation can be expressed as:

$$\frac{dR(t)}{dt} = k_a C R_{max} - (k_a C + k_d) R(t)$$

$R$  is the biosensor signal at time  $t$ , it corresponds to  $[AB]$ .  $C$  is the concentration of analyte, corresponding to  $[A]$ .  $R_{max}$  is the response when the maximum binding capacity of the sensor is reached.  $[B]$ , the concentration of available ligand binding sites, therefore corresponds to  $R_{max} - R(t)$ .

According to this model, a plot of  $dR/dt$  against  $R$  or a plot of  $\ln(dR/dt)$  against  $t$  will be a straight line with slope  $-(k_a C + k_d)$ . Plotting the slope values obtained at different analyte concentrations will give the values  $k_a$  and  $k_d$ .

**Dissociation phase** In theory  $k_d$  can be obtained as described above, in practice however  $\ln(dR/dt)$  against  $t$  is frequently dominated by  $k_a$  ( $k_a C \gg k_d$ ) and the intercept is unreliable. The values of  $k_d$  can be preferably calculated from the dissociation phase:

$$\frac{dR}{dt} = -k_d R$$

**Equilibrium phase** At equilibrium, association and dissociation rates are equal, so

$$k_a[A][B] = k_d[AB]$$

which can be rearranged to

$$K_D = \frac{k_d}{k_a} = \frac{[A][B]}{[AB]} \quad \text{the equilibrium dissociation constant} \quad (4.1)$$

$$K_A = \frac{k_a}{k_d} = \frac{[AB]}{[A][B]} \quad \text{the equilibrium association constant} \quad (4.2)$$

The equilibrium constants define the balance between complex and free components at equilibrium, while the rate constants define how fast the interaction occurs. Two interactions may have the same equilibrium constant and widely different rate constants, or conversely may have the same rate constant in one direction and widely different equilibrium constants.

**Heterogeneous interaction** A simple model as described above will not apply when heterogeneous reactions are involved, e.g. independent interactions with multiple analytes and/or ligands, multiple analyte species competing for binding to a homogeneous ligand, homogeneous analyte species binding competitively to ligands immobilized on the surface and in the solution... Rigorous derivations of non-linear models can be found in [1–3].

### 4.1.2 Mass transport to the surface

The accuracy for determining rate constants for fast binding reactions is limited, because the reactant in the solution must first be transported to the surface in order

to bind to its immobilized partner. In our biosensor setup, the analyte is passed over the sensor surface using a small flow cell or microfluidic channels.

The velocity profile of a fluid flowing over a stationary surface approaches zero at the contact with the surface. A so-called stagnant layer of a few micrometers is formed. High flow rates induce small stagnant layers; however, a stagnant layer of less than  $2\mu\text{m}$  is hard to achieve. The analyte is more or less efficiently transported to a distance of a few micrometers from the sensor surface, but this is still relatively far away from the evanescent field. From there, transport is solely effected by diffusion, as depicted schematically in Fig. 4.3. The diffusion rate through this layer depends largely on the diffusion constant of the analyte molecules, which varies from  $3 \times 10^{-6}$  to  $6 \times 10^{-6} \text{ cm}^2 \text{ s}^{-1}$  for low weight substances to below  $10^{-7} \text{ cm}^2 \text{ s}^{-1}$  for macromolecules with molecular weights of several hundred kDa. This corresponds to an average diffusion time through the unstirred layer from less than 1 s for small molecules up to several seconds for macromolecules. The effective concentration  $[A]$  of the still unbound analyte in the evanescent field will then typically be lower than the concentration in the bulk solution  $[A_0]$ . In order to accurately determine rate constants in such systems, the data needs to be analyzed with a model that includes mass transport of analyte to the surface:



where  $k_{tr}$  is the rate constant for mass transport to and from the surface. Several methods with more complicated models are reported in literature [4, 5].

For kinetic analyses, diffusion limitation should be avoided, such that  $[A_0] \approx [A]$ . A way to circumvent diffusion-related problems is to decrease the density of the immobilized ligand and/or increase the analyte concentration. However, it remains difficult to analyze the kinetics of binding pairs with high association and low dissociation constants. For concentration determination though, a mass transport limited binding is desired, since the slope of the initial stage of the binding curve is then proportional to the analyte concentration. A low flow rate and high immobilization densities of the ligand should be chosen.

### 4.1.3 Bulk refractive index effect

The signal of SOI microring biosensors originates from a change in refractive index of the environment, both due to binding events near the surface and a bulk index effect when switching from buffer to analyte solution. The bulk contribution can easily be subtracted, as shown in Fig. 4.4. With an array of biosensors, bulk refractive index contributions can be monitored with an uncoated sensor and can be subtracted from the signal during post-processing.

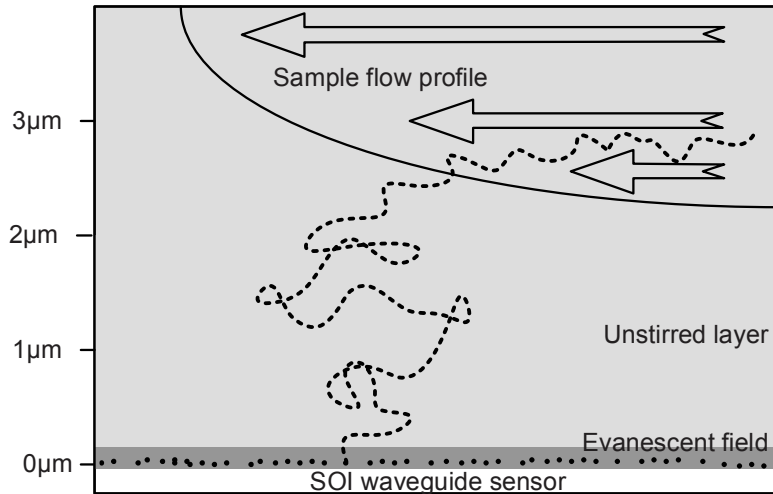


**Figure 4.3:** The evanescent field and the unstirred diffusion layer of an SOI micro-ring biosensor. Analyte molecules are transported first mostly by convection and then solely by diffusion.

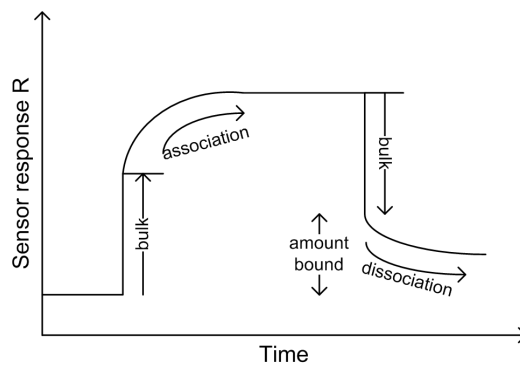


**Figure 4.4:** Schematic response of a biosensor, illustrating the bulk refractive index contribution.

#### 4.1.4 Molecular interactions studied with label-free biosensors

Some application fields of label-free biosensors are listed in chapter 1. Here we discuss immunoassays, because that is the application we studied with the SOI ring resonator biosensor platform.

An immunoassay is a technique based on the binding between an antigen and its homologous antibody in order to identify and quantify the specific antigen or antibody<sup>1</sup> in a sample. It is used to diagnose infectious diseases, (auto)immune disorders<sup>2</sup> or cancers [6]. In classical immunoassays, the detection of the concentration of an analyte relies on signals generated by various labels attached to antigens or antibodies (see for example ELISAs in chapter 1, section 1.1). Figure 4.5 shows some typical configurations of label-free immunoassays. In direct assays (a) and (b) the signal increase resulting from antigen/antibody binding directly correlates with the amount of antigen or antibody in the sample. Competition (c) or sandwich (d) assays are typically used to detect low molecular weight antigens that do not generate sufficient signal. To enhance the signal, the antigen in the sample solution is mixed with an antigen conjugate or with a secondary antibody. Only highly specific capture antibodies should be used, in order to avoid a mixture of affinities of each component in the sandwich [1]. The experiments with the SOI microring biosensor platform described in chapter 7 are conducted with a direct assay of type (b), we detect antibodies in serum by immobilizing the complementary proteins on the surface.

## 4.2 Surface characterization techniques

Satisfactory characterization of the interfacial layers with thicknesses of just a few nanometers can only be obtained by combining several techniques, each providing specific information. This section covers a brief description of the chemical surface characterization techniques employed for development of the surface chemistry of the SOI ring resonator biosensor platform. The list does not cover all possible methods, only the techniques that provided us with information for the next sections are detailed. Except for fluorescence microscopy, all techniques imply the use of flat surfaces. We have tried many of the functionalization steps both on flat surfaces of an SOI layer stack and on flat silicon surfaces of bulk silicon wafers. We found good correspondence of the results and concluded that cheap

---

<sup>1</sup>Antibody/Antigen: Antibodies or immunoglobulins (Ig) are the proteins at the heart of the human immune system. They bind bacteria, viruses or other foreign molecules and target them for destruction. An antigen is any molecule or pathogen capable of eliciting an immune response, it may be a virus, a bacterial cell wall or another macromolecule. An individual antibody binds only one particular antigen, more specifically, it binds to one particular molecular structure within the antigen.

<sup>2</sup>Autoimmune disorder: an autoimmune disorder is a condition that occurs when the immune system mistakenly attacks and destroys healthy body tissue. Well known examples are allergies, Type I diabetes, rheumatoid arthritis, multiple sclerosis (MS)...

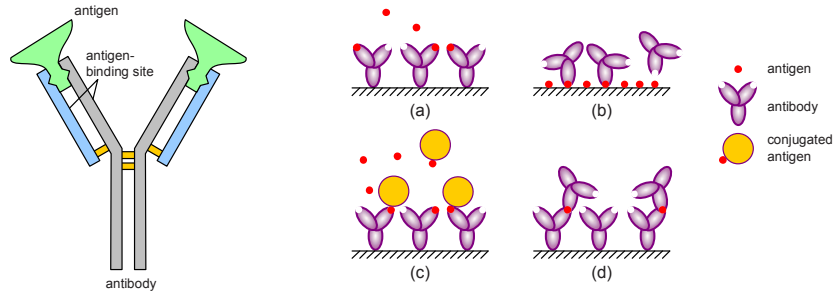


**Figure 4.5:** (left) Antibody/antigen. (right) Immunoassay formats used for label-free biosensors. (a) Direct assay: the antibody is immobilized on the sensor surface, interaction with the antigen yields a detectable refractive index shift. (b) Direct assay: the antigen is immobilized on the sensor surface, interaction with the antibody yields a detectable refractive index shift. (c) Competition assay for measuring small molecules, the conjugated antigen is large enough for a measurable shift. (d) Sandwich assay with secondary antibody.

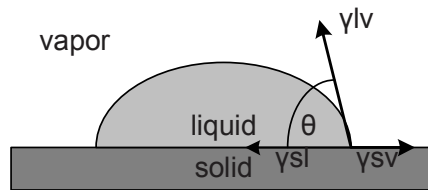


**Figure 4.6:** Contact angle  $\theta$  between solid surface and a droplet.  $\gamma_{sl}$  is the solid/liquid free energy,  $\gamma_{sv}$  is the solid surface free energy,  $\gamma_{lv}$  is the liquid surface free energy.

bulk silicon substrates can be used for characterization and optimization of the surface chemistry instead of the expensive SOI layer stack.

**Contact angle** The contact angle is the angle between, in our case, a solid surface and the tangent line to the upper surface of a droplet on that surface. It is a measure for the surface free energies between liquid and solid surrounded by vapor. The free energies are indicated in Fig. 4.6 and are related via Young's equation:  $\gamma_{sv} = \gamma_{sl} + \gamma_{lv} \cos \theta$ . From measuring the contact angle of a surface in contact with a water drop, we determine the hydrophobicity or hydrophilicity of the surface. Bare silicon surfaces were examined by static and dynamic contact angle using the drop shape analysis apparatus OCA 20 from Dataphysics. For static contact angle, a  $2 \mu\text{l}$  DI water droplet was placed on the surface of the sample and imaged using a video camera. At least three measurements per sample were performed; results from two to five samples were averaged. For dynamic contact angle measurements,  $5 \mu\text{l}$  DI water was added to a  $2 \mu\text{l}$  drop at  $0.5 \text{ ml/min}$ . Dynamic

measurements monitor the contact angle and thus the reformation, reorientation and stability of the layer over time.

**X-ray Photoelectron Spectroscopy** X-ray Photoelectron Spectroscopy (XPS) is based on the ejection of electrons from a surface when X-ray photons collide with it. The energy of the photoelectrons leaving the sample forms a spectrum with a series of photoelectron peaks that are specific for atomic binding energy. Hence XPS serves to analyze the elemental composition of a material in 1-10 nm under the surface.

The silicon samples were analyzed by XPS using a Fissions S-probe apparatus provided with a fine focus AlK source with a quartz monochromator.

**Ellipsometry** Ellipsometric techniques analyze the elliptically polarized light of a beam (initially linearly polarized) that is reflected at a surface to obtain the thickness and the refractive index of thin films.

The thicknesses of the different coatings on silicon substrates were determined by means of an M-2000FI Spectroscopic Ellipsometer (J.A. Woollam) at an angle of incidence of 75°. Ellipsometric data was acquired and evaluated by Complete EASE software (J.A. Woollam). The optical model of the multilayered substrates consisted of the software built-in optical functions of silicon, native silicon oxide and thermal silicon oxide [7]. Optical constants of silicon oxide were also used for silane layers. The index of refraction of a PEG layer (section 4.3.2) was modeled by a Cauchy dispersion function  $A_n + B_n/\lambda^2$  [8]. The extinction coefficient was taken to be zero since this polymer is a dielectric with negligible absorption in the UV/vis range used for the measurements. The Cauchy parameters  $A_n = 1.5$  and  $B_n = 0.0059\mu m^2$  were obtained from a simultaneous fit of thickness,  $A_n$  and  $B_n$  to ellipsometric data acquired from an auxiliary PEO layer (ca. 100 nm thick), spin cast on a bare silicon wafer.

**Fluorescence microscopy** Although parallel treatment of structured and bare wafers for chemical characterization is a commonly used approach, to confirm the actual presence of functional groups on the waveguides we attached fluorophores to the structured samples and observed their distribution over the surface with confocal fluorescence microscopy. Fluorescence tests were performed with a confocal Carl Zeiss LSM 510 microscope equipped with an argon laser module (Carl Zeiss Inc., Thornwood, NY) using a 10 × 0.25-NA objective. We used Alexa-fluor®555 fluorophores that were excited at 543 nm with a HeNe laser.

### 4.3 Protein coupling to a silicon surface

Straightforward surface coatings of silicon are based on assemblies of silane reagents that can bear a wide range of functional groups (-COOH, -NH<sub>2</sub>...). We make use of the -OH groups of silicon's native oxide for coupling silanes to the SOI waveguides. The covalent nature of the assembly process results in superior stability, which allows extensive handling and further modification steps without deterioration of the silane layer. In the next section we describe a one-step method that couples the proteins directly to the functional groups of a silane layer.

While anchoring proteins to silicon oxide surfaces with silanes is a convenient and reproducible method, silanes typically do not have sufficient resistance to non-specific interaction. Non-specific interaction is what happens when molecules other than the biomolecule to detect attach or adsorb to the surface and cause a large background signal. This can cause 'false positive' signals which is pernicious for the biosensor's reliability.

Non-specific interaction or protein-fouling has been attributed to various causes [9]. One of the most accepted reasons for protein-fouling to surfaces is the tendency for hydrophobic materials to absorb proteins in order to decrease their surface energy. Indeed, a high hydrophobicity can be associated with a large free surface energy. Thus, strategies for minimizing the fouling of materials focus on improving the hydrophilicity of their surfaces. A common strategy of achieving this goal involves coating the surface with a layer of polymers.

We developed a two-step method: an ultra thin layer of a hydrophilic polymer, poly(ethylene glycol) (PEG), is attached to the silane layer prior to coupling the proteins. In section 4.3.2, an overview of the coupling procedures is given together with important steps we took towards optimization of the surface coatings.

We will start this section with two concepts that will be used throughout the rest of the chapter: avidin-biotin is a molecular couple for biosensor tests and NHS-EDC chemistry is a chemistry protocol that forms covalent binding between a receptor protein and the coated sensor surface.

#### The avidin-biotin complex

In the search for novel label-free biosensors avidin-biotin is regarded as the gold standard for proof-of-principle tests. The extraordinary affinity of avidin for biotin ( $K_a = 10^{15} M^{-1}$ ) is the strongest known non-covalent interaction of a protein and ligand. For that reason we also used avidin-biotin as a model couple for binding and concentration measurements. **Biotin** is a 244 dalton<sup>3</sup> vitamin found in tiny amounts in all living cells. Since it is a relatively small molecule, it can be conjugated to many proteins without significantly altering their biological activity

---

<sup>3</sup>1 dalton (Da) is the atomic mass unit corresponding to one twelfth of the mass of an isolated atom of carbon-12 (<sup>12</sup>C) at rest and in its ground state.

and is therefore widely used to increase the sensitivity of many assay procedures. **Avidin** is a glycoprotein found in the egg white and tissues of birds, reptiles and amphibians. It contains four identical subunits to each of which one biotin protein can bind. Avidin has a mass of approximately 68 kDa. In our experiments, biotin is immobilized on the surface and avidin is the analyte in the sample solution. Bovine Serum Albumin (BSA), a protein with similar molecular weight to avidin that is abundantly present in body fluids, is used as a model protein for non-specific interaction.

### **Binding through NHS-EDC chemistry**

Covalent binding of biomolecules to other molecules is an essential component of biosensor development. Despite the complexity of protein structure, defined by the composition and sequence of 20 different amino acids, only a small number of protein functional groups comprise selectable targets for practical coupling methods. Most proteins bind through a primary amine ( $-\text{NH}_2$ ). Because of their positive charge at physiologic conditions, primary amines are usually outward-facing; thus, they are usually accessible for conjugation without denaturing the protein structure. A number of chemical reactive groups have been characterized and used to target the main protein functional groups. For our experiments, we used NHS/EDC<sup>4</sup> to couple proteins to the functional groups sticking out of the biosensor surface. Fig. 4.7 illustrates this for the activation of carboxylic acids from a surface to bind to amines from a protein. Stable surfaces or stable ligands are activated with -NHS to be much more reactive towards the amines of respectively the ligand or the surface. In the next sections we use NHS/EDC chemistry in two ways. When receptor molecules are available with an -NHS group attached to them (like biotin-NHS), we couple these so-called 'activated' receptors to the surface using EDC. When the receptor molecules are not available with an -NHS group (like most proteins), we 'activate' the surface first with an -NHS group and couple the receptor molecule after that, using EDC or variants of EDC with similar functionality.

#### **4.3.1 One-step modification: reaction with aminosilane**

The formation of amine-terminated self-assembled layers on silicon oxide allows immobilization of a variety of biologically important molecules. Also in this work, the first method we used to anchor biomolecules to the SOI surface, was covalent binding of the protein (biotin) to an aminosilane (APTES) layer that was self-assembled on the surface. The procedure is schematically pictured in Fig. 4.8. Prior to the self-assembly, the surface needs to be cleaned to maximize the number

<sup>4</sup>NHS: N-hydroxysuccinimide, EDC: 1-Ethyl-3-[3-dimethylaminopropyl]carbodiimide Hydrochloride.

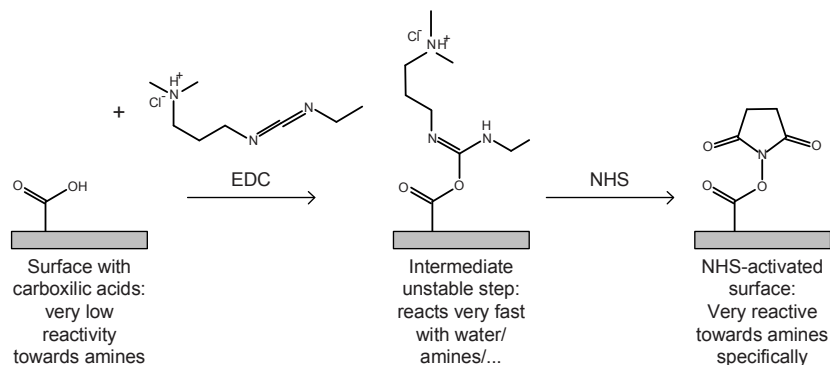


Figure 4.7: NHS activation of a carboxylic acid surface.

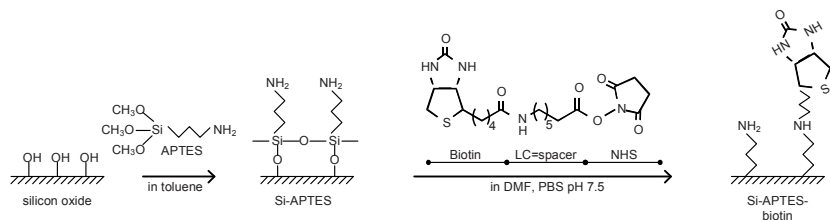


Figure 4.8: Aminosilanization and biotinylation of a silicon surface.

of silanol groups at the surface. We perform a piranha cleaning step to achieve this. The cleaned and oxidized silicon surfaces were silanized by dip-coating at room temperature in 1% dry toluene. After that, the aminosilanized surfaces (Si-APTES) were immersed in 2 ml phosphate buffer solution (PBS) with 100  $\mu\text{l}$  of E,Z link-NHS-LC-Biotin in DMF (1 mg/ml). Samples were immersed for 3 hours to allow the deposition of a layer of biotin receptors, covalently bound through NHS-EDC chemistry to the Si-APTES surface.

### Surface characterization

Contact angle measurements show an increasing hydrophobicity when the surface is coated using increasing APTES concentrations (Table 4.2). This indicates that increasing the APTES concentration results in a formation of multilayers. After silanization, the thickness increased from 2.8nm to 9.5nm. Since APTES monolayers are around 1 nm thick, this again confirms the formation of multilayers.

The surface chemical composition was determined by XPS after each reaction step (Table 4.3). After the aminosilanization step with 0.2% APTES solution, the carbon content increased from 13.7%, coming from residual contamination after the cleaning step, to 46.2%. At the same time the silicon content decreases

from 37.7% to 25.2%. Nitrogen is absent in bare silicon, while after modification, the surface nitrogen content was about 2.2%. Similar results were obtained with APTES concentrations of 1 and 2%. By increasing the concentration, a thicker surface silane layer is obtained, that shields the bulk silicon signal, which progressively decreases to 19.9 and 17.8% respectively. On the contrary, when the APTES concentration increases to 1 or 2%, the nitrogen content increases to 3.2 and 3.9% respectively. Control of concentration and deposition times minimizes the layer thickness (although never optimal), and renders the results reproducible.

	Contact angle [°]
Silicon substrate	71
Silicon oxide (after cleaning)	44.3
Si-APTES 0.2%	75.5
Si-APTES 1%	79.8
Si-APTES 2%	84.8

**Table 4.2:** Static contact angle measurements of silicon aminosilane surfaces.

	% Si	% O	% C	% N
Si substrate	27.7	10.4	54.0	-
Silicon oxide (after cleaning)	37.7	37.8	13.7	-
Si-APTES 0.2%	25.2	26.4	46.2	2.2
Si-APTES 1%	19.9	2.9	53.8	3.2
Si-APTES 2%	17.8	25.7	52.5	3.9

**Table 4.3:** XPS data of silicon aminosilane surfaces.

### 4.3.2 Two-step modification: reaction with poly(ethylene glycol)

Straightforward surface coatings of silicon are based on assemblies of silane reagents, like the one-step method described above. They can carry a wide range of functional groups for receptor molecule immobilization but they typically do not have sufficient resistance to non-specific interactions. SOI ring resonator biosensor measurements that confirm the high non-specific interaction signal of aminosilanes are presented in chapter 7, section 7.4.1.

The ability of PEG layers to reduce non-specific interactions in various detection systems is well documented [10, 11]. The PEG layer can be introduced in a single step, by using PEG bearing alkoxy silane end-groups [12, 13], or in two steps, as we did. The most frequently used two-step procedure involves the coupling of a diamino-PEG (H<sub>2</sub>N-PEG-NH<sub>2</sub>) to a silane layer bearing epoxide groups (Si-GPTS) [14, 15]. However, possible attachment to the surface through both -NH<sub>2</sub> groups would decrease the concentration of free functional groups intended for immobilization of receptor molecules, as illustrated in Fig. 4.9. Therefore, instead

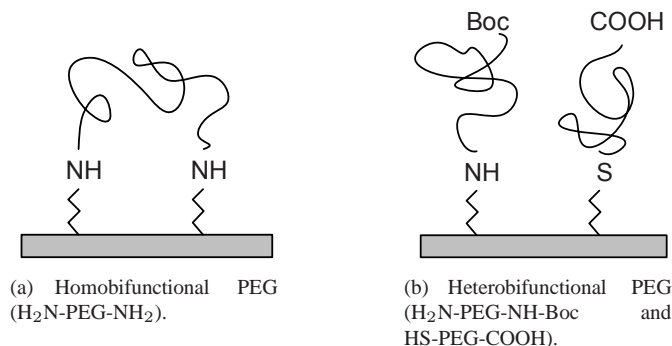


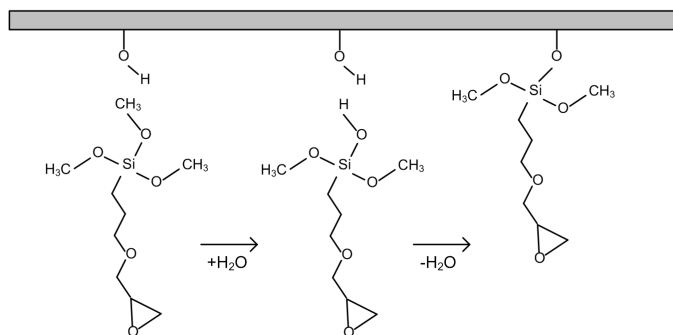
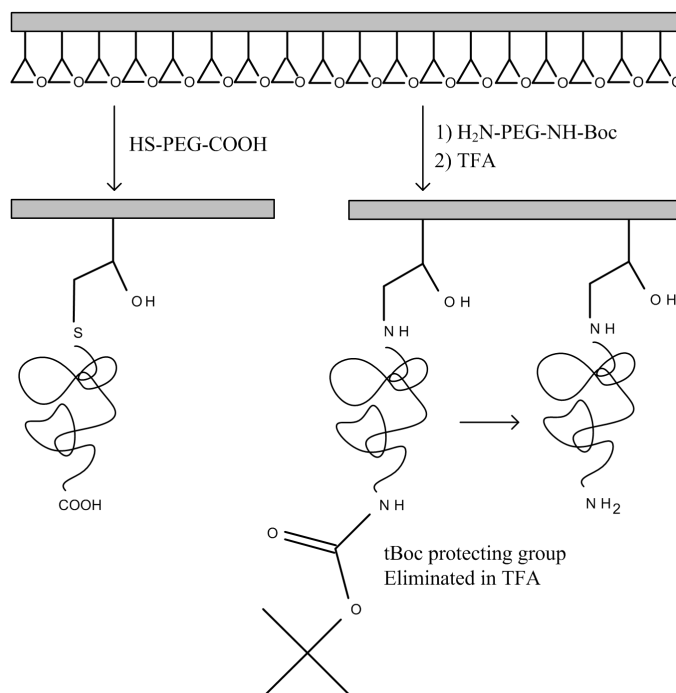
**Figure 4.9:** Using a heterobifunctional PEG instead of a homobifunctional PEG avoids attachment to the surface through both  $-\text{NH}_2$  groups.

of homobifunctional PEGs, we examined two heterobifunctional PEGs with functional end-groups of very different reactivity towards the epoxides of the silane layer.  $\alpha$ -sulfanyl- $\omega$ -carboxy PEG (HS-PEG-COOH) and monoprotected diamino-PEG ( $\text{H}_2\text{N-PEG-NH-Boc}$ ) allowed the introduction of respectively reactive carboxy ( $-\text{COOH}$ ) and amino ( $-\text{NH}_2$ ) groups on the surface of the SOI waveguides. All chemical reactions of the two-step procedure are schematically depicted in Fig. 4.10.

### Step one: GPTS layer

The first step of the procedure involves the application of a self-assembled silane layer bearing epoxide groups, 3-glycidyloxypropyltrimethoxysilane (GPTS). Notice the contrast with the silane layer bearing amino groups of the one-step procedure of the previous section. However, with different coupling chemistry and extra intermediate steps, both silanes could be used for both purposes. After oxygen plasma cleaning and activation, the substrates were immediately immersed in freshly prepared solutions of GPTS in toluene (1% w/w) and incubated overnight at room temperature (Fig. 4.10, step one). Unbound material was removed by successive sonication in pure toluene and acetone and the substrates were cured in a vacuum oven for 1 hour at  $100^\circ\text{C}$ .

Distillation of the GPTS solution prior to binding turned out to be key to obtain thin and homogeneous GPTS layers. It eliminates water traces and separates the oligomers present in the stored bottle. Fig. 4.11 shows the difference in homogeneity between a coating with and without overnight distillation of the GPTS. We clearly see the formation of agglomerates on the substrate on the left, while the surface on the right was covered with a homogeneous GPTS layer. Homogeneity of the surface chemistry is extremely important for nanostructured biosensors.

**Step 1: GPTS deposition****Step 2: PEG grafting**

**Figure 4.10:** Chemical reactions applied for the coating of cleaned silicon waveguides in a two-step procedure: GPTS deposition followed by PEG grafting. Thicknesses are not to scale.

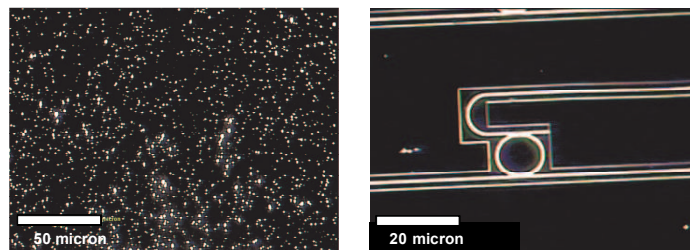


**Figure 4.11:** Reflected-light darkfield image of a silicon substrate coated with an epoxide silane (GPTS) before and after optimization of the homogeneity. Left: 1vol% non-distilled GPTS in dry toluene, 5h, ellipsometric thickness is 15nm. Right: 1vol% distilled GPTS in dry toluene, 8h, ellipsometric thickness is 1.3nm.

Unlike for many other biosensor implementations, where the response corresponds to an average of the biomolecular interaction over a large spot, a nanostructured biosensor only responds to biomolecular interaction over a very small surface area (e.g. ring surface area  $30 \mu\text{m}^2$ ). For that reason nanostructured biosensors can have very low detection limits, but the quality of the surface chemistry needs to be very high.

#### Step two: Grafting a PEG layer to GPTS

HS-PEG-COOH and  $\text{H}_2\text{N-PEG-NH-Boc}$  layers were deposited from 3 mg/ml solutions in acetone.  $100 \mu\text{l}$  of the PEG solutions was deposited on the surface of each substrate in  $20 \mu\text{l}$  portions to allow solvent evaporation. The specimens were subsequently placed in a vacuum oven at  $90^\circ\text{C}$  for 40 hours in order to enable the end groups to anchor to the epoxy-silane layer. Unbound PEG was removed by rinsing multiple times with DI water in an ultrasonic bath.

#### Coupling biotin to the PEG layer

After attaching a PEG layer to the top of our sensor using the two-step procedure above, we can proceed to attach the ligands, in this case biotin. The carboxy groups from substrates treated with HS-PEG-COOH were activated by immersing the substrates for 30 minutes in a NHS/EDC solution (0.1M/0.4M). Notice that in contrast to biotinylation of the APTES layer or the  $\text{H}_2\text{N-PEG-NH-Boc}$  layer of the next paragraph, for a HS-PEG-COOH layer the surface was 'activated'. After rinsing with DI water, the activated samples were immersed for 2 hours in 2 ml PBS to which  $100 \mu\text{l}$  of EZ-Link 5-(biotinamido) pentylamine (2 mg/ml) was added.

Deprotection of the Boc groups in substrates coated with  $\text{H}_2\text{N-PEG-NH-Boc}$  was accomplished by immersing the substrates in trifluoroacetic acid (TFA) for 10 min-

utes. After rinsing with DI water and PBS, chips were immersed in 2 ml PBS, followed by the addition of 100  $\mu$ l of EZ-Link biotin-LC-NHS in DMF (2 mg/ml). The reaction proceeded for 2 hours at room temperature. After biotin coupling, all samples were rinsed with PBS and sonicated successively in PBS and DI water.

### Surface characterization of the two-step procedure

The deposition of the GPTS layer was confirmed by ellipsometry, contact angle and XPS on model Si/SiO<sub>2</sub> substrates (see Table 4.4 and 4.5). Reproducible thicknesses of  $1.3 \pm 0.3$  nm are obtained. After GPTS treatment, the characteristic presence of 2 peaks at 284.7eV and 286.4eV, corresponding to C-C/C-H and C-O bonds respectively, was observed on the high-resolution XPS spectra of carbon (C1s) (Table 4.6). Si/SiO<sub>2</sub> wafers with smooth monolayers presented a static contact angle of  $53^\circ \pm 2^\circ$ , in good agreement with values reported in literature [16].

By characterization of the surface coating obtained after applying HS-PEG-COOH onto GPTS-treated substrates, the layers were found to be reproducible. The thickness of the PEG layer increased rapidly during the first hours and reached  $2.3 \pm 0.2$  nm after 30 hours, in line with literature values for similarly deposited PEG layers [14, 17]. Considering that the density of HS-PEG-COOH is 1.09 g/cm<sup>3</sup>, this represents a load of 2.7 ng/nm<sup>2</sup> equivalent to a chain density of 0.54 molecules/nm<sup>2</sup>. If the attachment to the surface occurred exclusively through the thiol group, one can assume a 99 pmol/cm<sup>2</sup> concentration of carboxy groups (Table 4.5). Additional characterization of the HS-PEG-COOH layer was provided by XPS analysis (Table 4.6). Reduction of the intensity of the Si peaks and a high carbon to oxygen ratio is evidence for the success of the PEG coupling. The contact angles of the grafted layers were reproducible in all experiments ( $32^\circ \pm 1^\circ$ ), lower than those of the GPTS-surface and comparable to literature values.

The thickness of H<sub>2</sub>N-PEG-NH-Boc layers was slightly higher than the thickness of HS-PEG-COOH layers, i.e. around 2.5 nm. Since the Boc-protected amino groups avoid the occurrence of any double coupling onto the chip surface, we can assume an effective concentration of amino groups equal to 97 pmol/cm<sup>2</sup> or 0.59 molecules/nm<sup>2</sup> (Table 4.5).

The comparison of the surface concentrations of functional groups indicates that the PEG brushes not only have the ability to reduce non-specific interaction but that they also have a sufficient surface concentration of functional groups, comparable to that present in mixed SAMs used as typical sensing layers of SPR immunosensors [18, 19].

The contact angle of the H<sub>2</sub>N-PEG-NH<sub>2</sub> substrates was  $21^\circ \pm 1^\circ$ . The low hysteresis observed in the dynamic contact angle ( $4^\circ$ ) is an indication of low roughness of the layer [14].

To verify the presence of reactive primary amino groups on the surface of the structured chips, we analyzed them by fluorescence confocal microscopy. Alexa-

fluor®555 cadaverine was crosslinked to the H<sub>2</sub>N-PEG-NH<sub>2</sub> surface with glutaraldehyde. The chips were partially covered with adhesive tape to set the background reference level. The fluorescence microscopy image of Fig. 4.12 shows homogeneous coloration over the surface of the chip, thus confirming a presence and homogeneous distribution of amino groups. To rule out the presence of adsorbed dye we examined negative control samples. No fluorescence signal was detected on samples covered with PEG but not pre-activated before applying the fluorophores with the same reaction and cleaning conditions. The resolution of the microscope is too low to see the 450 nm wide silicon waveguides, but we can see the fluorescence on the large silicon areas in between the etched trenches (also indicated on Fig. 4.12).

	Contact angle [°]	Thickness [nm]	Conditions
Our data	53 ± 2	1.3 ± 0.3	1% toluene, 15h
Data [16]	52 ± 1	0.85 ± 0.1	1% toluene, 24h

**Table 4.4:** Surface characteristics of the GPTS monolayer, compared with values reported in literature.

Layer	Thickness [nm]	Density [mg/ml]	Surface loading [ng/mm <sup>2</sup> ]	Chain density [molecules/nm <sup>2</sup> ]	Contact angle [°]	Hysteresis [°]
GPTS	1,4 ± 0,5	1.07	1.50	3.82	53 ± 2	16 ± 2
HS-PEG-COOH	2,3 ± 0,2	1.09	2.51	0.54	32 ± 1	8 ± 2
H <sub>2</sub> N-PEG-NH <sub>2</sub>	2,5 ± 0,2	1.09	2.73	0.59	21 ± 1	4 ± 1

**Table 4.5:** Characterization of all surface layers of the two-step procedure: ellipsometry and contact angle measurements.

	% Si (2p)	% O (1s)	% C (1s)	% N (1s)
Silicon oxide (after cleaning)	30.6	30.8	38.6	0
Si/SiO <sub>2</sub> /GPTS	26.1	28.2	45.6	0.0
Si/SiO <sub>2</sub> /GOPTS/HS-PEG-COOH	10.2	40.6	49.2	0.0
Si/SiO <sub>2</sub> /GOPTS/H <sub>2</sub> N-PEG-NH <sub>2</sub>	7.1	29.4	62.4	1.1

**Table 4.6:** Characterization of all surface layers of the two-step procedure: XPS data.

### 4.3.3 From biotin to other proteins

#### Activated surface instead of activated biotin

Tests of the SOI ring resonator biosensors modified according to the two-step procedure of section 4.3.2, revealed high specific signals to avidin and low non-specific signals to BSA, even in complex body fluids (for ring resonator binding

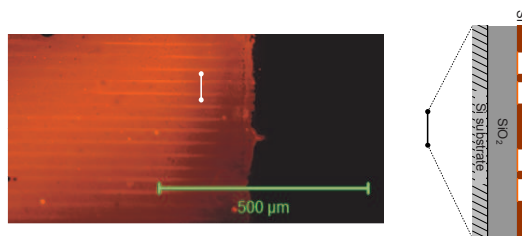


**Figure 4.12:** Fluorescence microscopy picture of a structured chip coated with  $H_2N$ -PEG-NH-Boc. Alexa-fluor@555 cadaverine was applied as described in section 4.3.2. The right side was covered with tape during the reactions to set the background reference level. The resolution of the microscope is too low to see the 450nm wide silicon waveguides, but we can see the fluorescence on the large silicon areas in between the etched trenches.

curves see chapter 7, section 7.4.2). For the coupling of biotin to a surface bearing  $H_2N$ -PEG-NH<sub>2</sub>, we used commercial biotin-LC-NHS. However, this system can not simply be applied to couple other proteins to the  $H_2N$ -PEG-NH<sub>2</sub> surface, since chemically modified proteins bearing -NHS esters are not commercially available. Consequently, the coupling system had to be altered.

Instead of coupling ‘activated’ proteins, we had to couple proteins to an ‘activated’ surface. As a model for the coupling of other proteins and antibodies, we analyzed the coupling of a non-activated biotin with terminal amino-end group ((5-biotinamido)pentylamine or further denoted as biotin-NH<sub>2</sub>). We examined two coupling methods, depicted in Fig. 4.13. Activation via glutaraldehyde has been used by other groups for coupling of fluorescent labels with excellent results [20, 21]. However, the introduction of the glutaraldehyde and the inactivation<sup>5</sup> of the aldehyde groups with ethanolamine resulted in surfaces with increased hydrophobicity (Table 4.7). This partly canceled out the advantages the PEG layer offers. Tests revealed a considerable increase in non-specific interaction when this strategy was applied.

Alternatively, we attempted the activation of the surface with disuccinimidyl carbonate (DSC) [22, 23]. With this method, the inactivation of the surface structures occurs by hydrolysis, providing hydrophilic carboxylic groups at the surface (Table 4.7). This methodology provided almost the same surface characteristics as the method used to couple activated biotin. When tested on the SOI microring biosensor platform, DSC activated surfaces interacted significantly less with non-specific molecules as compared to glutaraldehyde surfaces. DSC activation was used further for the experiments described in chapter 7, section 7.5.

<sup>5</sup>Inactivation of non-occupied reactive groups after immobilization of the receptor molecules is always necessary in order to avoid increased non-specific interaction of macromolecular components in the serum with the non-occupied reactive groups.

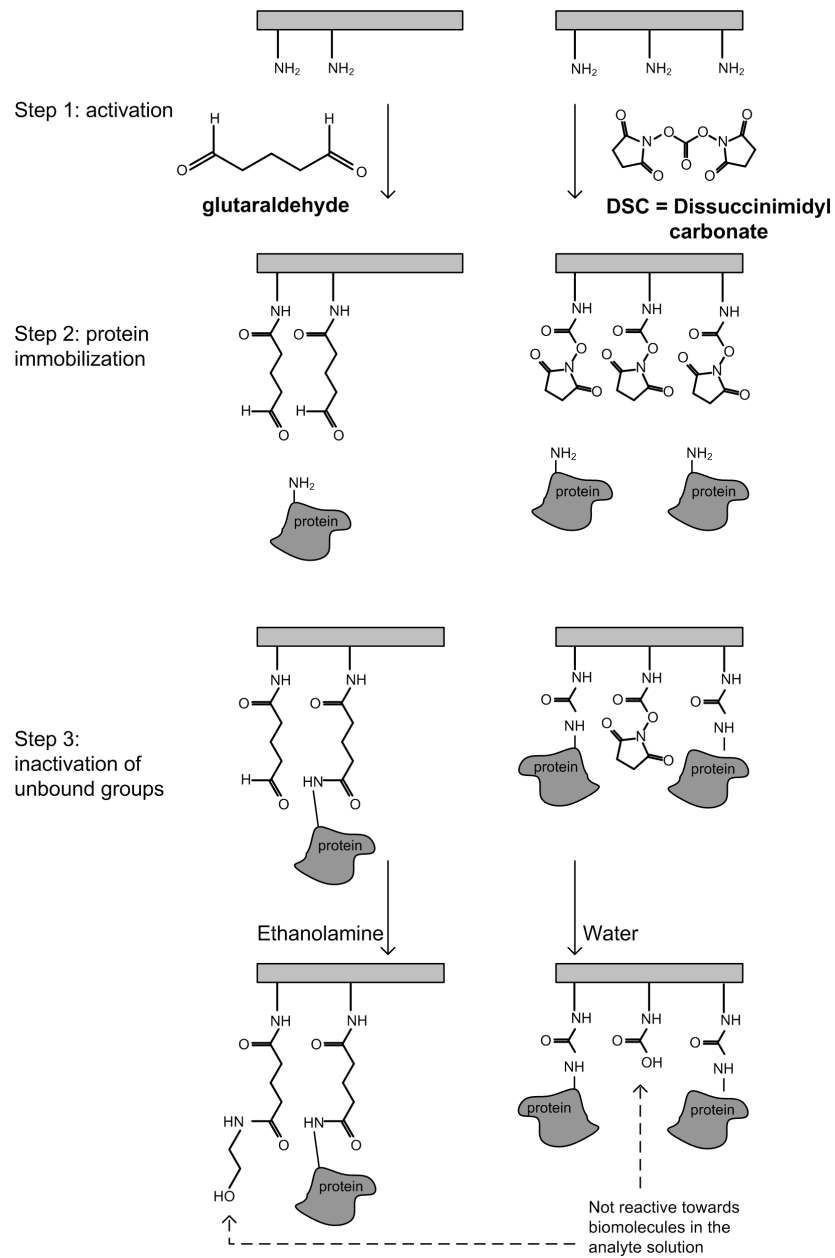


**Figure 4.13:** Surface activation with glutaraldehyde and surface activation with disuccinimidyl carbonate (DSC) of silicon surfaces coated with  $\text{H}_2\text{N}$ -PEG- $\text{NH}_2$ . Eventually DSC activation corresponded to the lowest non-specific signal.

	Contact angle [°]
GPTS	53
H <sub>2</sub> N-PEG-NH <sub>2</sub>	21
H <sub>2</sub> N-PEG-NH <sub>2</sub> /gluteraldehyde	31
H <sub>2</sub> N-PEG-NH <sub>2</sub> /DSC	24

**Table 4.7:** Static contact angle measurements of silicon substrates coated with H<sub>2</sub>N-PEG-NH<sub>2</sub> according to the two-step procedure and further activated with gluteraldehyde versus disuccinimidyl carbonate (DSC).

### Water instead of solvents

In contrast to biotin, proteins can not be dissolved in organic solvents because it would affect their structural integrity. Hence the coupling of proteins to the surface is in competition with the reaction of water with the -NHS groups of the surface. This means the hydrolysis deactivation reaction in Fig. 4.13 (step 2) is in competition with the protein coupling (step 3). The coupling procedure had to be optimized in order to minimize the hydrolysis in favor of the protein immobilization. Since most surface characterization techniques fail in quantifying the amount of proteins on a silicon surface, this optimization had to be characterized with the SOI microring biosensor platform that is described in the following chapters. See Fig. 4.14 for the results.

The highest signal depicts avidin/biotin interaction in the most ideal circumstances: activated biotin was immobilized in organic solvent. Activation of the surface with DSC is needed to couple through the amine groups of proteins, bar set 2 depicts the interaction of biotin-NH<sub>2</sub> with avidin and non-specific proteins (BSA and other components in serum I). The non-specific interaction was low as expected from the low hydrophobicity of the PEG surface. When introducing avidin to the surface however, the signal remained low which is indicative of the low density of biotin-NH<sub>2</sub> receptor molecules to the surface of the biosensor. In order to try and improve the coupling, a MES buffered saline (pH 5.5) was used as coupling buffer instead of PBS (pH=7.6). A higher pH of the solution accelerates the hydrolysis of the activated surface. At lower pH, one expects a longer reactive period for the surface towards the proteins. However, almost no difference was observed in protein receptor coverage (bar set 3). After that we turned attention to another protocol for binding proteins. The DSC activation and the subsequent protein coupling was done with the conditions described in [15]. After deprotection of the amine groups of the PEG layer, a very small volume of 50  $\mu$ l of the activation solution (DSC + DMAP + distilled TEA in distilled DMF) was placed on the SOI chip. This chip was covered with a clean and dry silicon chip and kept in a desiccator for 4 hours. This methods reduces the possible water traces during the activation. After rinsing with distilled DMF and distilled methanol the chips were ready for protein immobilization. Although not optimal yet, results improved considerably when

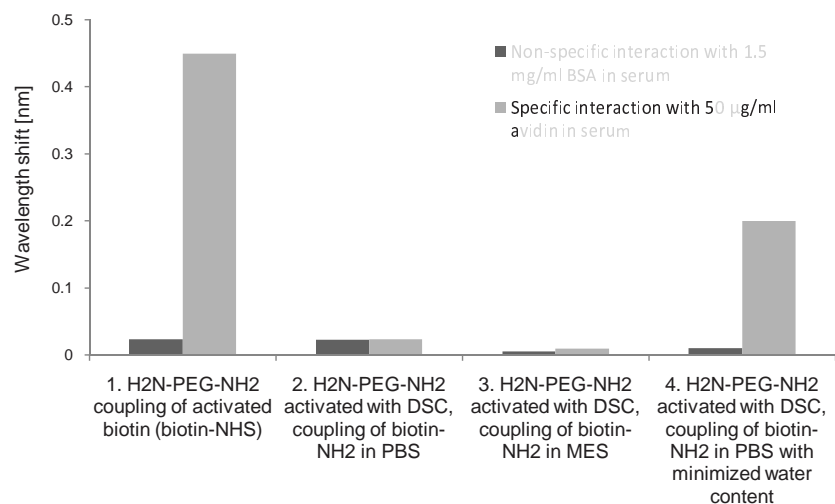


**Figure 4.14:** Optimization of the protein immobilization to obtain a high specific signal. Biotin-NH<sub>2</sub> is used as model for proteins. The serum is a 100X diluted goat serum with RaIgG, dilutions are in PBS+0.1% tween.

this methodology was applied (bar set 4).

## 4.4 Conclusion

In this chapter we aimed to explain all concepts and solutions encountered in the search of high quality biological receptor layers. Coupling of proteins to the -NH<sub>2</sub> groups of an amine silane (APTES) layer that was self-assembled on the silicon oxide surface, is a straightforward coupling procedure for dense receptor coverage. However, silanes perform poorly in terms of non-specific interactions with proteins in the analyte solution. To reduce the non-specific detection background, we introduced thin PEG layers in a two-step coupling procedure. We investigated two heterobifunctional PEG layers with different reactive groups:  $\alpha$ -sulfanyl- $\omega$ -carboxy PEG (HS-PEG-COOH) and monoprotected diamino-PEG (H<sub>2</sub>N-PEG-NH-Boc). Surface characterization tests confirmed the high quality, the reproducibility and the binding capacity of PEG layers. The thickness is in the order of a few nanometers. The contact angle decreased to 21° and 31° respectively, while the density of the functional groups remained high and comparable to the density of functional groups on commonly used SAMs for SPR sensing. Avidin/biotin was primarily used for proof-of-principle biosensor tests. To immobilize other proteins to the surface, the coupling procedure had to be slightly changed to ensure good receptor coverage and to maintain the hydrophilic character of the surface. In Fig. 4.15 the final coupling routes are schematically shown. Coupling route 1 illustrates the cou-

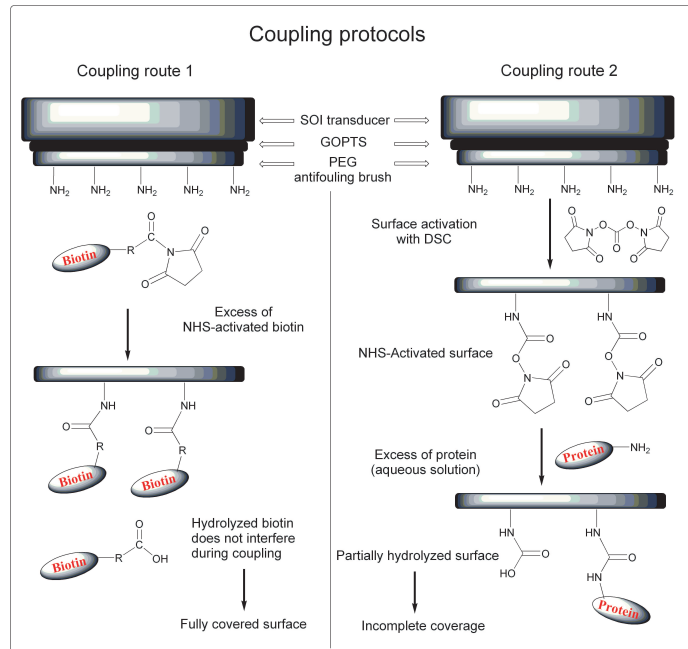


**Figure 4.15:** Employed coupling protocols for immobilization of receptor molecules (biotin and proteins) on SOI microring resonators pre-coated with a functional PEG layer.

pling of activated proteins (such as biotin-NHS) to the PEG surface, coupling route 2 shows the coupling of non-activated proteins (such as biotin-NH<sub>2</sub> and most other proteins) to a pre-activated surface. We will refer to this figure when discussing the actual binding curves for specific and non-specific interactions monitored with SOI ring resonator biosensors in chapter 7.

## References

- [1] *Handbook of Surface Plasmon Resonance*. RSC Publishing, Enschede, The Netherlands, 2008.
- [2] *BIAapplications Handbook*. Merk AB, Uppsala, Sweden, 1994.
- [3] *BIAtechnology Handbook*. Merk AB, Uppsala, Sweden, 1994.
- [4] D. G. Myszka, T. A. Morton, M. L. Doyle, and I. M. Chaiken. *Kinetic analysis of a protein antigen-antibody interaction limited by mass transport on an optical biosensor*. *Biophysical Chemistry*, 64(1-3):127–137, 1997.
- [5] D. G. Myszka, X. He, M. Dembo, T. A. Morton, and B. Goldstein. *Extending the range of rate constants available from BIACORE: Interpreting mass transport-influenced binding data*. *Biophysical Journal*, 75(2):583–594, 1998.
- [6] Michael M. Cox David L. Nelson. *Lehninger Principles of Biochemistry*. W.H. Freeman and Company, New York, 4th edition, 2005.
- [7] C. M. Herzinger, B. Johs, W. A. McGahan, J. A. Woollam, and W. Paulson. *Ellipsometric determination of optical constants for silicon and thermally grown silicon dioxide via a multi-sample, multi-wavelength, multi-angle investigation*. *Journal of Applied Physics*, 83(6):3323–3336, 1998.
- [8] William A. McGahan Harland G. Tompkins. *Spectroscopic Ellipsometry and Reflectometry: A User's Guide*. Wiley-Interscience, 1 edition edition, 1999.
- [9] D. Leckband, S. Sheth, and A. Halperin. *Grafted poly(ethylene oxide) brushes as nonfouling surface coatings*. *Journal of Biomaterials Science-Polymer Edition*, 10(10):1125–1147, 1999.
- [10] L. D. Unsworth, H. Sheardown, and J. L. Brash. *Protein-resistant poly(ethylene oxide)-grafted surfaces: Chain density-dependent multiple mechanisms of action*. *Langmuir*, 24(5):1924–1929, 2008.
- [11] W. Norde and D. Gage. *Interaction of bovine serum albumin and human blood plasma with PEO-tethered surfaces: Influence of PEO chain length, grafting density, and temperature*. *Langmuir*, 20(10):4162–4167, 2004.
- [12] Jacques Blümmel, Nadine Perschmann, Daniel Aydin, Jovana Drinjakovic, Thomas Surrey, Monica Lopez-Garcia, Horst Kessler, and Joachim P. Spatz. *Protein repellent properties of covalently attached PEG coatings on nanostructured SiO<sub>2</sub>-based interfaces*. *Biomaterials*, 28(32):4739–4747, 2007.

- [13] L. Andruzzi, W. Senaratne, A. Hexemer, E. D. Sheets, B. Ilic, E. J. Kramer, B. Baird, and C. K. Ober. *Oligo(ethylene glycol) containing polymer brushes as bioselective surfaces*. *Langmuir*, 21(6):2495–2504, 2005.
- [14] J. Piehler, A. Brecht, R. Valiokas, B. Liedberg, and G. Gauglitz. *A high-density poly(ethylene glycol) polymer brush for immobilization on glass-type surfaces*. *Biosensors & Bioelectronics*, 15(9-10):473–481, 2000.
- [15] A. Wolter, R. Niessner, and M. Seidel. *Preparation and characterization of functional poly(ethylene glycol) surfaces for the use of antibody microarrays*. *Analytical Chemistry*, 79(12):4529–4537, 2007.
- [16] I. Luzinov, D. Julthongpiput, A. Liebmann-Vinson, T. Cregger, M. D. Foster, and V. V. Tsukruk. *Epoxy-terminated self-assembled monolayers: Molecular glues for polymer layers*. *Langmuir*, 16(2):504–516, 2000.
- [17] R. Schlapak, P. Pammer, D. Armitage, R. Zhu, P. Hinterdorfer, M. Vaupel, T. Fruehwirth, and S. Howorka. *Glass surfaces grafted with high-density poly(ethylene glycol) as substrates for DNA oligonucleotide microarrays*. *Langmuir*, 22(1):277–285, 2006.
- [18] L. Strong and G. M. Whitesides. *Structures of self-assembled monolayer films of organosulfur compounds adsorbed on gold single-crystals - electron-diffraction studies*. *Langmuir*, 4(3):546–558, 1988.
- [19] L. Huang, G. Reekmans, D. Saerens, J. M. Friedt, F. Frederix, L. Francis, S. Muyltermans, A. Campitelli, and C. Van Hoof. *Prostate-specific antigen immunosensing based on mixed self-assembled monolayers, camel antibodies and colloidal gold enhanced sandwich assays*. *Biosensors & Bioelectronics*, 21(3):483–490, 2005.
- [20] Z. H. Wang and G. Jin. *Silicon surface modification with a mixed silanes layer to immobilize proteins for biosensor with imaging ellipsometry*. *Colloids and Surfaces B-Biointerfaces*, 34(3):173–177, 2004.
- [21] L. M. Lee, R. L. Heimark, J. C. Baygents, and Y. Zohar. *Self-aligned immobilization of proteins utilizing PEG patterns*. *Nanotechnology*, 17(4):S29–S33, 2006.
- [22] O. Brandt, J. Feldner, A. Stephan, M. Schroder, M. Schnolzer, H. F. Arlinghaus, J. D. Hoheisel, and A. Jacob. *PNA microarrays for hybridisation of unlabelled DNA samples*. *Nucleic Acids Research*, 31(19), 2003.
- [23] Y. Jun, T. Cha, A. Guo, and X. Y. Zhu. *Patterning protein molecules on poly(ethylene glycol) coated Si(111)*. *Biomaterials*, 25(17):3503–3509, 2004.



# 5

## Microfluidics

On top of the functionalized sensor chip, a fluidic compartment has to ensure the delivery of the sample to the sensor surface. During the course of this work, three systems were applied to guide fluids over the SOI chips: a flow cell, a cuvette and microfluidic channels.

The flow cell of Fig. 5.1(a) contains an inlet and an outlet and one single broad channel through which the sample flows and interacts with the sensor surface. It was sealed with Parafilm<sup>1</sup> and clamped to the holder.

The cuvette is a container that was mounted leak-free on the chip, Fig. 5.1(b). It contains one inlet that fits a needle, and one extra small opening through which gases can escape during filling. The openings are as small as possible to minimize sample evaporation. The cuvette can contain a sample volume of 6.3  $\mu\text{l}$ . Because this is not a flow-through system, it does not allow for switching between liquids. For practical applications it is necessary to include reference sensors to measure the background signal level. This tubing-free system was found useful when only very small sample volumes were available (e.g. when measuring DNA hybridization).

The flow cell and cuvette performed well for single ring measurements. However in order to address an array of ring resonators, it is important that the flow characteristics are equal over the entire chip. The need for compact fluidics in which the flow velocity is similar at all locations on the chip implies the use of channels with

---

<sup>1</sup>Parafilm is a product of the Pechiney Plastic Packaging Company. It consists of a flexible film and is commonly used for sealing or protecting vessels (such as flasks or cuvettes). It is stretchable, moldable, waterproof, odorless, thermoplastic, semitransparent and self-adhering.

dimensions in the order of a few tenths of microns, so-called ‘microfluidics’. Fig. 5.1(c) pictures an SOI chip packaged with PDMS microfluidics.

We will give a brief introduction on various theoretical aspects of microfluidics in section 5.1, where we also discuss microfluidics modeling techniques. Section 5.2 deals with the actual microfluidic fabrication we performed. Using channels with micron-sized dimensions adds complexity to the packaging: in contrast to the flow cell and the cuvette, the alignment of the channels can not be performed manually. Section 5.3 deals with packaging of SOI chips with microfluidics.

## 5.1 Basic concepts

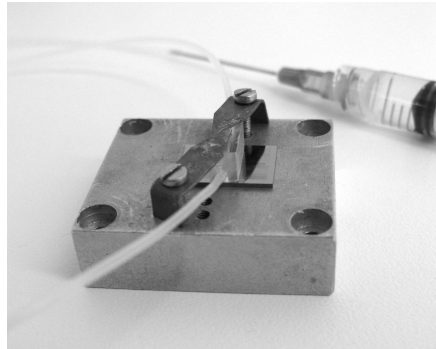
### 5.1.1 Introduction

The fundamental laws of nature underlying our understanding of the operation of liquid handling systems are all well-known. What is new in microfluidics, however, is the interplay between many different forces and the change of the relative importance of these forces in the micro-regime as compared to the macro-regime. Surface effects that often can be neglected at the macro-scale become increasingly dominant in microfluidics as size is diminished. For example, volume forces like gravity and inertia that are very prominent in our daily life become largely unimportant in lab-on-a-chip systems. Surface related forces, like surface tension and viscosity, become dominant. Microfluidic systems hold big promises for the large-scale automation of chemistry and biology, suggesting the possibility of numerous experiments performed rapidly and in parallel, while consuming little reagents. Various applications of significant scientific and practical interest have been developed over the past ten years. The study of fluid behavior in micron-scale devices is a vast research domain, and is documented in various books and publications [1–3].

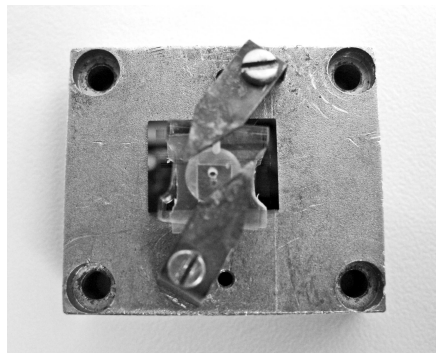
From the most general point of view, fluid flows are determined by the knowledge of velocities  $U = \{u_x, u_y, u_z\}$ , pressure  $P$ , density  $\rho$ , viscosity  $\mu$ , specific heat  $C_p$  and temperature  $T$ .  $u_x, u_y, u_z, P$  and  $T$  are related by a system of three equations: (1) a scalar equation for the mass conservation, (2) a vector equation for the conservation of momentum, and (3) a scalar equation for the conservation of energy or the Navier-Stokes (NS) equations<sup>2</sup>. If the temperature is constant, four unknowns are left and we have to solve equation (1) (conservation of mass) and (2) (conservation of momentum).

---

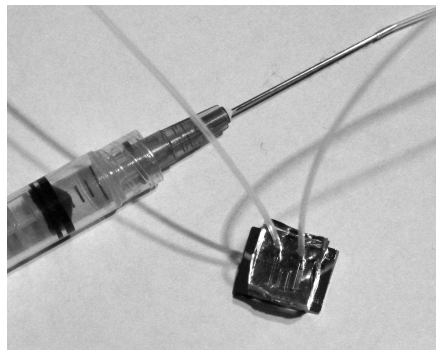
<sup>2</sup>Some authors give the name Navier-Stokes to the second equation (momentum).



(a) Flow cell with one inlet and one outlet, sealed to the SOI chip.



(b) Cuvette for zero-flow experiments, sealed to the SOI chip.



(c) SOI chip packaged with PDMS microfluidics.

**Figure 5.1:** Systems for fluid guiding over SOI chips.

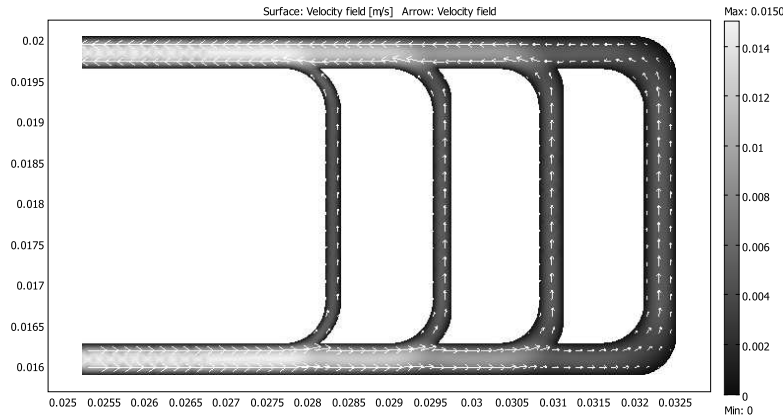


**Figure 5.2:** Typical microfluidic laminar flow with parallel flow streamlines. The dimensions are  $50 \times 192 \mu\text{m}$  for the smallest channel, and  $50 \times 400 \mu\text{m}$  for the broadest channel.

### 5.1.2 Laminarity

A flow is said to be laminar when viscous forces dominate inertia. When this is the case, turbulences cannot develop, and the fluid flow lines are, at least locally, parallel. The Reynolds number determines the ratio between inertia (convective forces) and viscous forces.

$$Re = \frac{UD}{\nu}$$

where  $U$  is the average fluid velocity,  $D$  is a characteristic dimension of the channel (or the obstacle), and  $\nu$  is the kinematic viscosity (expressed in  $\text{m}^2/\text{s}$ ). When  $Re < Re_{trans}$  the flow is said to be laminar.  $Re_{trans}$  is the transition threshold between laminar and turbulent flow. For flows in channels, tubes or pipes,  $Re_{trans}$  is of the order of 1000-2000. In microflows the velocities are mainly small. For instance, we typically use a  $5 \mu\text{l}/\text{min}$  flow rate through channels with dimensions of  $50 \times 200 \mu\text{m}$ . The flow velocity is then about  $0.8 \text{ mm/s}$ . As the kinematic viscosity of water is  $\nu = 10^{-6} \text{ m}^2/\text{s}$ , the Reynolds number is of the order of 0.008. Thus, the character of the flow is laminar, meaning that the streamlines are locally parallel. In Fig. 5.2 a typical microfluidics design is pictured, with flow arrows that are parallel as expected. The dimensions are  $50 \times 192$  to  $50 \times 400 \mu\text{m}$ .

### 5.1.3 Modeling

Because of the complex geometry of the boundaries, a finite element method is preferred to model microfluidic flows. We used commercial software COMSOL Multiphysics for that purpose (the MEMS module). Surface tension and wall adhe-

sive forces are very important for transport of fluids through microchannels, so the treatment of the boundary conditions is important. The module allows a non-zero slip velocity and includes frictional forces at the walls.

Here we briefly present the *lumped parameters model*, which is a simplified calculation method that gives very interesting and acceptable results in some cases. The model is described using the geometry of Fig. 5.2 as a working example. The aim is to calculate the width of the four channels to obtain equal flow velocities at the center of the channels. The circuit can be decomposed in connecting parts (Fig. 5.3 (top)), with nodes  $\{i = 1, N\}$  and branches  $\{j = 1, M\}$  with  $N = 6$ ,  $M = 8$ . The unknowns are the average velocities  $U_j$  and the pressure at the nodes  $P_i$ . A first set of equations is given by the mass conservation equations at each node  $i$  of the net. At a node  $i$ , the equation for the mass conservation is:

$$\sum_{j_i} U_{j_i} S_{j_i} = 0 \quad (5.1)$$

where  $j_i$  is the index corresponding to all of the branches connected to node  $i$ .  $S_{j_i}$  and  $U_{j_i}$  are the cross section and average velocities (positive or negative).

The second set of equations is given by the pressure drop relations, the Hagen-Poiseuille law. For the branch  $[i - 1, i]$ , this relation becomes:

$$P_{i-1} - P_i = R_{hydr} Q_{i-1,i} \quad (5.2)$$

where  $Q_{i-1,i}$  (in  $\text{m}^3/\text{s}$ ) is the flow rate in the channel, equal to  $U_{i-1,i} S_{i-1,i}$ , and  $R_{hydr}$  is the so-called hydraulic resistance of the channel. This equation only holds for a pressure driven, steady-state flow of an incompressible fluid, i.e. a Poiseuille flow. The hydraulic resistance is due to viscous dissipation of mechanical energy into heat by internal friction in the fluid. It can be calculated for different channel shapes.  $R_{hydr}$  of a rectangular channel with short edge  $h$ , long edge  $w$  and length  $L$  equals:

$$R_{hydr} = \frac{12\eta L}{1 - 0.63(h/w)} \frac{1}{h^3 w}$$

where  $\eta$  is the dynamic viscosity of the liquid,  $\eta_{water} = 1 \text{ mPa}\cdot\text{s}$ . More on the derivation of hydraulic resistances can be found in [3].

Solving the equations provides us with the 3 unknown widths of the channels (we set the inlet channel width equal to the width of the fourth channel to  $400 \mu\text{m}$ ). Setting a certain inlet flow rate ( $50 \mu\text{l}/\text{min}$ ) and atmospheric pressure at the outlet, we also obtain the unknown average velocities in the four channels. The height of the channels was taken to be  $50 \mu\text{m}$ , the horizontal lengths  $1.2 \text{ mm}$  and the vertical lengths  $4 \text{ mm}$ . The widths obtained by solving these equations can serve as starting values for the COMSOL model. After running the simulation, the velocities are plotted and we adapted the widths slightly to increase the velocity uniformity. Channel widths of  $192$ ,  $233$ ,  $308$  and  $400 \mu\text{m}$  were found to give nearly equal flow velocities inside the channels (Fig. 5.3 (bottom)).

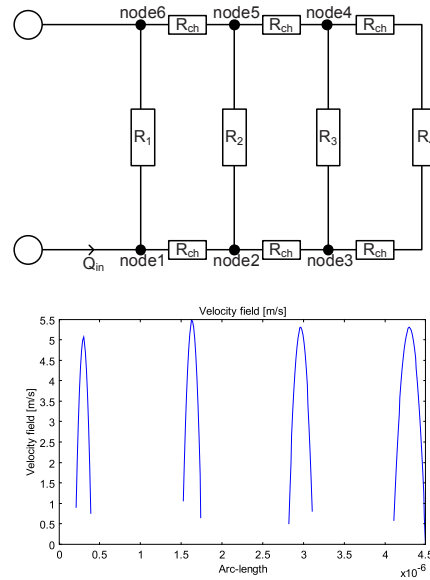


**Figure 5.3:** Top: Lumped parameter model for the channel network of Fig. 5.2, Bottom: Velocity profile in the channels.

### 5.1.4 Lab-on-a-chip

The integration of biosensors and microfluidics for point-of-care applications is still in its infancy. Microfluidic mixers, valves and pumps have to be taken to the biosensor platform to provide extra functionality for the particle delivery, or for sample pre-processing. One example of a microfluidic device is shown in Fig. 5.4. This device is used to build and maintain a concentration gradient, in this case across separate channels but the gradient would also be maintained in one output channel. The device was fabricated in PDMS with soft-lithography during this PhD work in collaboration with ONC laboratory at Boston University. Channel dimensions are  $45 \times 45 \mu\text{m}$ . In the application stage, this structure can be integrated with microring resonators to monitor biological behavior in solutions with different concentrations. Despite the importance of gradients in biology, there are only a few techniques capable of generating and maintaining them easily in solution. Using a microfluidic approach it is possible to generate spatially and temporally constant gradients extending over hundreds of micrometers and to maintain their shapes over long periods of time [4]. Interesting biological studies that are made possible by this type of devices can be found in [5–7].

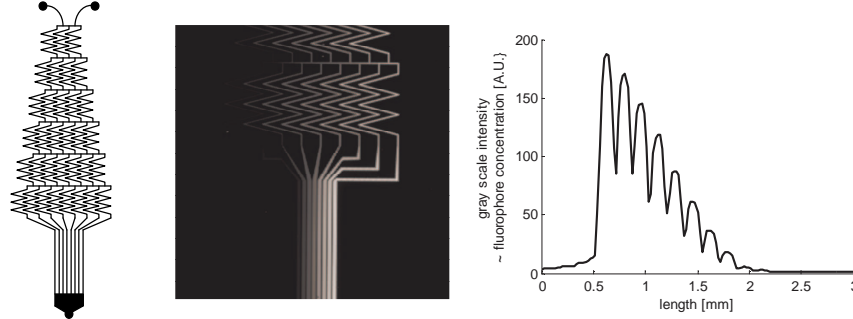


**Figure 5.4:** Microfluidic device for generating and maintaining a concentration gradient. The device was fabricated in PDMS with soft-lithography in collaboration with ONC laboratory at Boston University. Channel dimensions are  $45 \times 45 \mu\text{m}$ . The device was tested with DI water containing fluorophores. One inlet was filled with pure DI water, the other inlet was filled with DI water with a high fluorophore concentration. After passing through the channel network, a linear concentration gradient was generated.

### 5.1.5 Time to accumulate a threshold number of molecules

Sheehan et al. calculated the time for accumulation of a certain number of molecules on a sensor with a certain geometry in [8]. We apply the same model to the ring resonator biosensor. The model assumes irreversible adsorption, a reasonable approximation for strongly binding molecules such as biotin-avidin or DNA. The maximum number of molecules attached to a sensor as a function of time is then defined as

$$N(t) = \int_0^t \oint_A j d\sigma d\tau \quad (5.3)$$

where  $j$  is the flux right above the sensor normal to the sensor surface (molecules  $\text{s}^{-1} \text{m}^{-2}$ ),  $\sigma$  is the unit area,  $A$  is the sensor area and  $t$  is time. In first approximation we consider the flux to a ring, discarding molecular attachment to the side walls. Because of the zero flow velocity at the fluidic channel walls, the molecular flux to the ring surface will be determined by molecular diffusion, as was illustrated in chapter 4, Fig. 4.3.

The solution for the steady state flux to a circular area is similar to that in the ‘Weber’s disk’ problem in electrostatics,

$$j(r) = \frac{2DN_A c_0}{\pi\sqrt{a^2 - r^2}}$$

where  $N_A$  is Avogadro’s number,  $c_0$  is the initial concentration (kept constant by the flow and the assumption of zero depletion) and  $a$  the outer ring radius.  $D$  is the diffusion constant. For molecules of several kDa molecular weight such

as immunoglobulins D is approximately  $250 \mu\text{m}^2\text{s}^{-1}$ . Integrating this flux with equation (5.3) yields the steady-state accumulation of

$$N(t) = 4DN_Ac_0\sqrt{2aw - w^2t} \quad (5.4)$$

which is linear in time and varies with the square root of the ring radius.  $w$  is the waveguide width.

The ring resonator sensor requires a threshold of about 500 molecules of a few kDa molar weight to reach the detection limit (chapter 2, section 2.4). With formula (5.4) we calculate the accumulation time to capture 500 molecules to the surface of a ring resonator biosensor with radius  $5 \mu\text{m}$  and waveguide width  $500 \text{ nm}$  for increasing molecular concentrations, Fig. 5.5(a). Within the detectable concentration range of an SOI ring resonator biosensor ( $>15 \text{ pM}$ ), the time to reach the detection limit threshold is in the order of seconds and forms thus no limitations for the operation speed. From Fig. 5.5(b) we can conclude that for radii above  $3 \mu\text{m}$ , where bend losses are acceptable, the accumulation time remains below 1 s for  $15 \text{ pM}$  concentration.

From these graphs we conclude that in order to improve the sensor's performance, we should first focus on the detection limit, through improvements in transducer, read-out system and intermediate chemistry. Only when the detection limit can be decreased to the order of fM, more sophisticated molecular delivery systems are needed. For an initial concentration of  $1 \text{ fM}$ , a ring radius of  $5 \mu\text{m}$ , and  $D$  of  $250 \mu\text{m}^2\text{s}^{-1}$ , the time to accumulate 500 biomolecules approximates 60 minutes. This is not acceptable for most applications. Several methods to enhance the total flux to the sensor are proposed in literature. For instance, analyte molecules can be actively directed toward the sensor via electrostatic fields, this has been demonstrated for nucleic acids and proteins [9]. Similarly, target molecules can be attached to magnetic particles that are then directed toward the sensor via magnetic field gradients [10]. Another option could be large-scale integration of many identical sensors into a closely packed array. In all calculations the flow above the sensor was not taken into account. This is justified in chapter 4, section 4.1.2. For all practical applications studied in this manuscript, transport of the analyte to the surface is for the last few micrometers above the surface dominated by diffusion. An option to circumvent this, is to introduce convection to direct the analyte to the sensor rather than streaming it past. Simply decreasing the channel height would increase the effectiveness of fluid flow if the same volumetric flow rate could be maintained. However, the pressure required to maintain the volumetric flow rate increases as  $1/h^3$  such that, under practical pressures, the volumetric flow is reduced and the total flux to the sensor diminished.

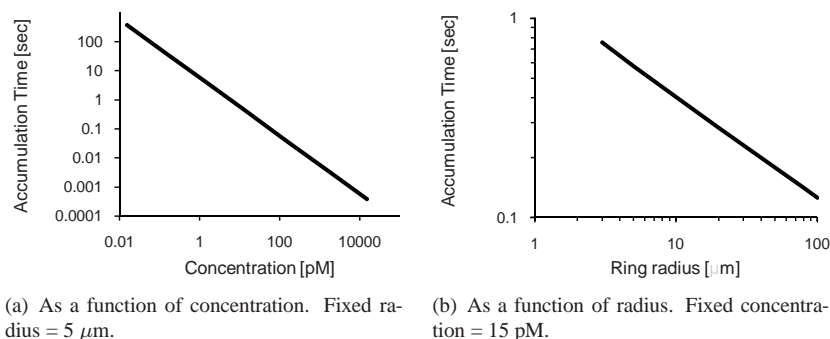


**Figure 5.5:** Calculated time to accumulate 500 molecules (of a few kDa molar weight) on a ring resonator surface with width  $500 \text{ nm}$ . Diffusion constant  $D=250 \mu\text{m}^2 \text{ s}^{-1}$ . Accumulation on the waveguide sidewalls was not taken into account.

## 5.2 Fabrication

Polymers are mostly used as substrate materials for microfluidic devices in recent years. There is a huge amount of different materials available with a broad range of chemical, mechanical, electrical and optical properties and there exist a multitude of different methods to manufacture microstructures in polymers. This allows on the one hand the selection of the optimal material for almost any given application but on the other hand this diversity often makes the correct choice of a material very difficult [11, 12].

In terms of physical parameters and thus technological pathways to fabrication, polymers can be divided into three main classes. The main parameter which has to be considered in this classification is the so-called glass transition temperature ( $T_g$ ). This parameter has its origin in the molecular behavior of the polymer material. If a polymer gets heated to a certain temperature, the energy of motion of parts of the polymer chain becomes large enough to overcome intramolecular friction. At this point in the temperature curve, larger segments of the polymer chain can suddenly start to move quite freely, leading to a significant softening of the material. Below  $T_g$ , a polymer behaves very much like a rigid, solid amorphous glass; beyond  $T_g$ , the material becomes flexible and soft. A second important parameter for technical use is the so-called heat distortion temperature (HDT). It describes the maximum temperature for structural use of the material; beyond the HDT, the polymer cannot be exposed to any mechanical stress anymore. The third temperature relevant for polymers is the decomposition temperature ( $T_d$ ), at which the polymer decomposes and the polymer chains are broken, changing the basic nature of the polymer.

So according to the value of  $T_g$  and the behavior of the polymer, the following

material classes can be defined:

1. Thermosets (duroplastic materials): in these materials, which can be liquid or solid at room temperature, the molecular polymer chains start to cross-link (cure) if the polymer is heated up or is exposed to sufficiently high doses of light or other radiation, thereby generating a rather hard and inflexible three-dimensional molecular network. If the curing process has taken place once, the polymer remains stiff even if reheated. Thermosets can therefore not be reshaped once cured.  $T_g$  typically is rather high and close to the decomposition temperature  $T_d$ . Typical examples of thermoset polymers in microfabrication are the resist materials for lithography, for microfluidic applications especially the photoresist SU-8.
2. Thermoplastic materials: these materials show a distinct softening at  $T_g$  which makes them processable around this temperature. A rather large temperature difference between  $T_g$  and  $T_d$  allows for a large process window. In thermoplastic materials, no curing takes place at elevated temperatures so the molded parts can be reshaped many times by reheating. Typical examples are poly(methyl methacrylate) (PMMA) and polycarbonate (PC).
3. Elastomers: in elastomers, the molecular chains are longer than in the other cases and typically do not show a chemical interaction but are physically entangled. If an external force is acting on the polymer, the polymer chains disentangle and allow the polymer to stretch elastically, returning to its original shape immediately if the external force is withdrawn. Owing to their low cost and easy handling, elastomeric materials, namely poly(dimethylsiloxane) (PDMS), have become a primary material for the low-volume manufacturing of microfluidic devices.

A compilation of physical and chemical properties of some polymers we tested for our microfluidic application is shown in Table 5.1 [11].

Many different fabrication methods are used to fabricate polymer microfluidics. The most commonly applied methods are photodefinable technologies, such as photolithography and laser photoablation, or replication methods, such as imprinting and hot embossing, injection molding for thermoplasts or casting for elastomers. We applied two fabrication technologies with two types of polymers, described in the next paragraphs: laser photoablation and casting for, respectively, poly-(methylmethacrylate) (PMMA) and poly-(dimethylsiloxane) (PDMS).

### 5.2.1 Excimer laser photoablation of PMMA

Photoablation was introduced in the literature as a prototyping technique for polymer microfluidic channels in 1997 by Roberts et al. [13]. In the photoablation process, a high-intensity laser beam is focused onto the material, so that the absorption

<i>Name</i>	Trade name (examples)	Density (g cm <sup>-3</sup> )	$T_g$ (°C)	Heat distortion temperature (°C)	Water absorption (%)	Thermal expansion coeff. (10 <sup>-6</sup> /K)	Resistant against	Not resistant against
PMMA	Perspex, Plexiglas	1.19	110	90	2	80	Acids, bases (medium conc.), oil, petrol	Alcohols, acetone, benzole, UV radiation, most solvents
PC	Makrolon, Calibre, Lexan, Trirex	1.19–1.24	148	125	0.30	70	Alcohols, acids	Hydrocarbons, ketones, KOH, most solvents
PI	Kapton	1.42	360–410	410	2.9–4	20	Acids, bases, solvents	
PDMS	Sylgard	1.03	120	200	0.1	960	Weak acids and bases	Strong acids, hydrocarbons
SU-8	NanoChem	1.19	210			52	Acids, bases, most solvents	
PE (LD/HD) <sup>a</sup>	Rexlon, Bapolene, Dowlex	0.91/0.967	110/140	80/100	<0.015	170/200	Acids, bases, alcohols, oil	Hydrocarbons

**Table 5.1:** Overview of polymer material properties [11].

<sup>a</sup>Low Density/High Density

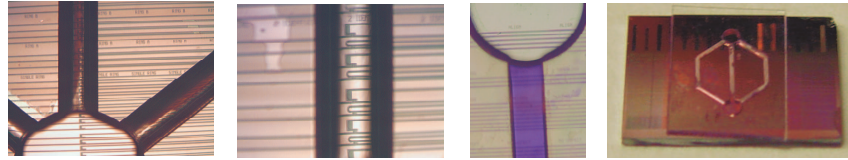


**Figure 5.6:** Poly(methyl methacrylate) (PMMA) microchannels aligned to a SOI structured chip. The PMMA channels are fabricated with laser photoablation. Dimensions of the channels are  $320 \times 65 \mu\text{m}$ .

of light induces bond-breakage in the polymer backbone [14]. The structure geometry can be realized either by using a mask and exposing the substrate through the mask or by moving either the laser beam or the substrate in x and y direction to generate the desired pattern. We used an excimer laser that emits at 193 (ArF) or 248 nm (KrF). High-power infrared Nd:YAG and CO<sub>2</sub> lasers are also used for laser ablation, but as shorter wavelengths correspond to a better optical resolution of the beam delivery system, excimer lasers are better suited for patterning with micron and even submicron accuracy. The UV excitation of organic molecules consists of certain electronic transitions in the covalent bonds. The different types of transitions are discussed in [14]. Excited electrons will relax to the ground state with different relaxation mechanisms: fluorescence, phosphorescence, internal conversion, intersystem crossing, photochemical reaction and external conversion. During ablation, polymer relaxation will be dominated by the decay process with the shortest lifetime: photochemical reaction (photodissociation) and internal conversion (heat generation).

We fabricated PMMA microchannels (Fig. 5.6) with the ‘Optec Micromaster’. This tool is equipped with optics that enable projection of a mask pattern with a chosen magnification on the material to be structured. It is coupled to a Lumonics PM848 laser that produces a power density up to  $15 \text{ J/cm}^2$  at 248 nm. Using an attenuator, the energy density can be tuned. Optimization of all working parameters such as ablation rate (in  $\mu\text{m/puls}$ ), pulse repetition rate and energy density was performed by Kris Naessens at INTEC [14].

Typical values for the ablation depth per laser shot are of the order of  $1 \mu\text{m}$ . Therefore, for deeper structures, several shots have to be fired for each location. This leads to a characteristic surface roughness of laser-ablated microchannels. The ablated material (so-called debris) has to be removed from the device by suitable means. We sonicated the structures for 10 minutes in isopropyl alcohol for that purpose.

### 5.2.2 Casting of PDMS

Although it offers a high degree of flexibility, laser ablation is a slow serial technique. Therefore we turned our attention to other fabrication methods, such as casting. Casting is by far the most widely published polymer fabrication process, also often referred to as soft lithography<sup>3</sup> [15]. Elastomer casting is a dominant fabrication method in the academic world because of its very low initial equipment cost, mainly the replication master. The dominant cost factor however, is the process time, which does not produce a significant economy of scale. Therefore casting is seen as a prototyping or low- to medium-volume production technology. For large-volume manufacturing in an industrial environment, injection molding, despite its high initial costs, is the dominating process thanks to the short cycle time.

The fabrication procedure is illustrated in Fig. 5.7. A detailed sequence of the processing parameters, together with some tips and tricks can be found in appendix A. A thin layer of photoresist is spin-coated onto a silicon wafer. We fabricated features of 50  $\mu\text{m}$  thickness with SU-8 50. The photoresist is exposed to UV light through a photomask with the inverse channel design, and an SU-8 developing reagent is used to dissolve the unexposed regions. The resulting SU-8 structures serve as a master mold for replication of PDMS microfluidics.

Before creating the PDMS microfluidics, the surface of the silicon/SU-8 master is treated with an anti-adhesive layer of fluorinated silanes. Fluorinated molecules have low surface energy, which prevents irreversible bonding of PDMS to the silicon/SU-8 master. A drop of fluorinated silane (trideca - fluoro - (1,1,2,2) - tetrahydrooctyltrichlorosilane,  $\text{C}_8\text{H}_4\text{Cl}_3\text{F}_13\text{Si}$ ) is placed on the wafer. It is deposited on the SU-8/silicon structures during overnight evaporation in a dessicator. Although anti-adhesion treatment in solvent presumably results in slightly lower surface energy [16], we prefer to use a dry method, as the solvent (pentane) destroyed the SU-8 features.

After that, we prepared a liquid PDMS prepolymer in a mixture of 1:10 base polymer:curing agent. To prevent the formation of air bubbles during mixing and casting, we thoroughly degas the mixture in a simple low vacuum system. The mixture is then poured over the master and cured at 65° for 1.5 h. The curing itself is an organometallic cross-linking reaction, where three-dimensional bonds are formed. The resulting elastomer is optically transparent (down to about 300 nm), electrically insulating and chemically inert. It is compatible with biological studies because it is impermeable to water, nontoxic to cells, and permeable to gases. After curing, the PDMS sheet is peeled away from the master. Small holes are punched into the PDMS using a flat needle to produce inlets and outlets. Many PDMS replicas can be made from a single master. The replication accuracy is extremely

<sup>3</sup>Sometimes the term soft-lithography is used to refer to all replication methods that make use of an elastomer mold (e.g. PDMS), previously casted in master mold.

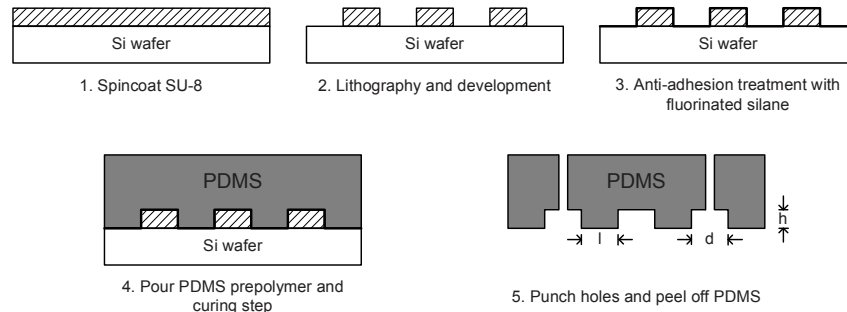


**Figure 5.7:** Fabrication steps for casting of PDMS microchannels.

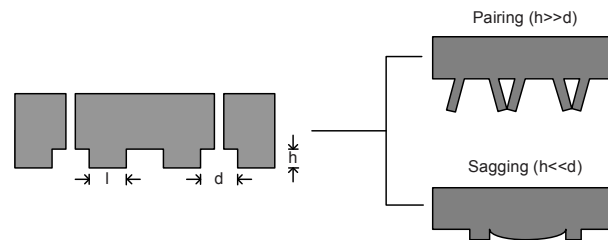


**Figure 5.8:** PDMS deformation, aspect ratios ( $h/l$ ) are limited to 0.2-2 in order to obtain defect-free features.

high; the replication of structures below 10-nm feature size with root mean squared surface roughness of 0.26 nm has been reported [17]. However aspect ratios are limited to 0.2-2 range in order to obtain defect-free features. When the aspect ratio ( $h/l$ ) is too high or too low, the elastomeric character of PDMS will cause the microstructures in PDMS to deform or distort and generate defects in the pattern, as illustrated in Fig. 5.8 [18].

### 5.3 Integration with SOI chips

Because the SOI microring biosensor platform is developed to be scalable for high throughput detection of hundreds of different molecules at once, different receptor molecules are spotted on the chip before the microfluidic channels are mounted. This is in contrast with the approach that couples receptor molecules to the surface after bonding the channels, which requires a more complex channel network with multiple in- and outlets, especially for large sensor arrays. Our approach of spotting before bonding asks for a low temperature bonding process during which contact of an adhesive glue with the receptor molecules on the SOI chip has to be prevented. A commonly used technique where both substrates are exposed to

a short oxygen plasma treatment and bonded at higher temperature for permanent sealing can therefore not be used. Still, we optimized this method as well (see next paragraph), because it is a powerful method that results in very strong bonds. It was used for all applications that did not involve biomolecules: sensing bulk refractive index changes, preliminary optical trapping experiments... In order not to damage the fragile receptor biomolecules, we used a stamp-and-stick method to transfer the channels on the SOI chip for biomolecular sensing experiments [19]. We will describe both of these techniques in more detail, but first we briefly discuss the surface properties of PDMS which are crucial for understanding bonding. PDMS consists of repeating  $-\text{OSi}(\text{CH}_3)_2-$  units; the  $\text{CH}_3$  groups make its surface hydrophobic. The surface can be made hydrophilic, thus with high surface energy, by exposure to an oxygen plasma which oxidizes the surface to silanol ( $\text{Si-OH}$ ) [20]. This will enhance the bonding capacities of PDMS with different materials. The plasma-oxidized surface remains hydrophilic if it stays in contact with water. In air, rearrangements occur within 30 min, which bring hydrophobic groups to the surface and lower the surface free energy.

### 5.3.1 Direct bonding using plasma activation of the surface

The silanol groups at the PDMS surface, induced by oxygen plasma treatment, interact with those on another surface, when two such layers are brought into conformal contact. For both PDMS and  $\text{SiO}_2$ , these reactions yield  $\text{Si-O-Si}$  bonds after loss of a water molecule. These covalent bonds form the basis of a tight irreversible seal between both materials.

Prior to the oxygen plasma treatment, the PDMS and the SOI chip were cleaned. PDMS was sonicated in IPA and DI water, the SOI chips were immersed in a piranha solution ( $\text{H}_2\text{SO}_4:\text{H}_2\text{O}_2$  in 7:3 ratio) for 5 minutes. We used the Oxford Reactive Ion Etching (RIE) or Oxford Plasmalab Inductively Coupled Plasma Reactive Ion Etching (ICP-RIE) equipment for the plasma treatment, depending on their availability. Both tools gave similar results. After plasma treatment of both materials, the channels were aligned to the SOI sensors using a flip-chip bonder from 'Microtech' and bonded at  $135^\circ\text{C}$  for 45 min. All process parameters can be consulted in appendix A. Pictures of PDMS channels sealed with direct oxygen plasma bonding to SOI photonic chips are shown in Fig. 5.9.

### 5.3.2 Adhesive bonding with stamp-and-stick method

We used a room temperature 'stamp-and-stick' bonding technique for transfer of PDMS (or PMMA) to an SOI chip covered with biomolecules. This principle has first been described by Satyanarayana et al. [21], we adapted this technique for our purpose. The procedure is illustrated in Fig. 5.10. A  $7\ \mu\text{m}$  thick SU-8 layer is first spun on a flat silicon substrate. The PDMS is given a short  $\text{O}_2$ -plasma treatment

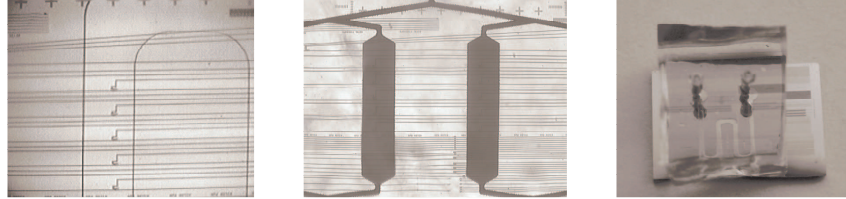


**Figure 5.9:** PDMS channels are aligned to SOI photonic chips and sealed with direct oxygen plasma bonding.

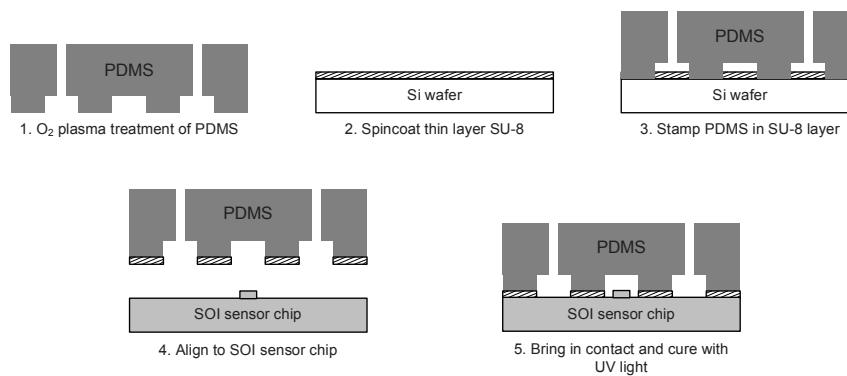


**Figure 5.10:** Stamp-and-stick method for bonding of PDMS microchannels to a structured SOI chip without exposure to aggressive surface treatment or high temperatures.

to enhance adhesion to the glue. After that the microfluidics chip is pressed in the SU-8 glue layer, after which a thin layer of glue surrounds the channels. A too thick glue layer will clog the channels, a layer that is too thin will not be transferred to the polymer. The channels are aligned to the SOI sensor array with a flip-chip bonder. Both devices are brought into contact and the SU-8 is UV-cured for 2.5 minutes. Fig. 5.11 shows pictures of the transferred PDMS microfluidics to an SOI chip. As can be observed from the pictures, the sealing might be a little irregular at the edges due to spreading of the glue. By making sure the edges are not too close to the sensors, this did not alter the biosensor's working capacity.

## 5.4 Conclusion

The sample delivery part of the SOI biosensor platform can take three forms: a flow cell, a cuvette or microfluidic channels. The former two are clamped on the chip and are reusable, the microfluidics are bonded to the SOI and are disposable with the rest of the chip. For the current concentration detection limit ( $\approx 10\text{pM}$ ),



**Figure 5.11:** Pictures of PDMS microfluidics bonded to SOI chips with the stamp-and-stick procedure using an adhesive layer. Channel dimensions range from  $50 \times 50 \mu\text{m}$  to  $200 \times 50 \mu\text{m}$ .

the time to accumulate a threshold number of molecules for sensing is not a limiting factor. Only when the detection limit decreases to fM concentration range, more sophisticated sample delivery methods need to be developed. Using finite element methods and lumped element methods the behavior of fluids on a micron scale can be predicted. We fabricated microfluidic channels with two fabrication methods: excimer laser photoablation and replication molding. After fabrication, the polymer microfluidics need to be bonded to the SOI chips. In order not to damage the fragile biomolecules on the sensor, no high temperatures or surface activation methods can be applied during the bonding step. This leaves us to adhesive bonding with an intermediate glue. To avoid contact between biomolecules and the glue, we use a stamp-and-stick bonding process.

## References

- [1] J. Berthier Silberzan and P. *Microfluidics for biotechnology*. MEMS series. Artech house, Norwood, MA, 2006.
- [2] T. M. Squires and S. R. Quake. *Microfluidics: Fluid physics at the nanoliter scale*. Reviews of Modern Physics, 77(3):977–1026, 2005.
- [3] Hendrik Bruus. *Theoretical Microfluidics*. Oxford master series in condensed matter physics. Oxford University Press Inc., New York, 2008.
- [4] S. K. W. Dertinger, D. T. Chiu, N. L. Jeon, and G. M. Whitesides. *Generation of gradients having complex shapes using microfluidic networks*. Analytical Chemistry, 73(6):1240–1246, 2001.
- [5] N. L. Jeon, H. Baskaran, S. K. W. Dertinger, G. M. Whitesides, L. Van de Water, and M. Toner. *Neutrophil chemotaxis in linear and complex gradients of interleukin-8 formed in a microfabricated device*. Nature Biotechnology, 20(8):826–830, 2002.
- [6] H. B. Mao, P. S. Cremer, and M. D. Manson. *A sensitive, versatile microfluidic assay for bacterial chemotaxis*. Proceedings of the National Academy of Sciences of the United States of America, 100(9):5449–5454, 2003.
- [7] J. Pihl, J. Sinclair, E. Sahlin, M. Karlsson, F. Petterson, J. Olofsson, and O. Orwar. *Microfluidic gradient-generating device for pharmacological profiling*. Analytical Chemistry, 77(13):3897–3903, 2005.
- [8] P. E. Sheehan and L. J. Whitman. *Detection limits for nanoscale biosensors*. Nano Letters, 5(4):803–807, 2005.
- [9] M. J. Heller, A. H. Forster, and E. Tu. *Active microelectronic chip devices which utilize controlled electrophoretic fields for multiplex DNA hybridization and other genomic applications*. Electrophoresis, 21(1):157–164, 2000.
- [10] D. L. Graham, H. Ferreira, J. Bernardo, P. P. Freitas, and J. M. S. Cabral. *Single magnetic microsphere placement and detection on-chip using current line designs with integrated spin valve sensors: Biotechnological applications*. Journal of Applied Physics, 91(10):7786–7788, 2002.
- [11] H. Becker and C. Gartner. *Polymer microfabrication technologies for microfluidic systems*. Analytical and Bioanalytical Chemistry, 390(1):89–111, 2008.
- [12] H. Becker and L. E. Locascio. *Polymer microfluidic devices*. Talanta, 56(2):267–287, 2002.

- 
- [13] M. A. Roberts, J. S. Rossier, P. Bercier, and H. Girault. *UV laser machined polymer substrates for the development of microdiagnostic systems*. Analytical Chemistry, 69(11):2035–2042, 1997.
- [14] Kris Naessens. *Excimer laser ablation of microstructures in polymers for photonic applications*. PhD thesis, Ghent University, 2003-2004.
- [15] J. C. McDonald, D. C. Duffy, J. R. Anderson, D. T. Chiu, H. K. Wu, O. J. A. Schueller, and G. M. Whitesides. *Fabrication of microfluidic systems in poly(dimethylsiloxane)*. Electrophoresis, 21(1):27–40, 2000.
- [16] Stijn Scheerlinck. *Metal grating based interfacing to and probing of nanophotonic circuits*. PhD thesis, Ghent University-IMEC, 2008-2009.
- [17] Hua Feng, A. Gaur, Sun Yugang, M. Word, Jin Niu, I. Adesida, M. Shim, A. Shim, and J. A. Rogers. *Processing dependent behavior of soft imprint lithography on the 1-10-nm scale*. IEEE Transactions on Nanotechnology, 5(3):301–308, 2006.
- [18] Y. N. Xia and G. M. Whitesides. *Soft lithography*. Annual Review of Materials Science, 28:153–184, 1998.
- [19] K. De Vos, J. Girones, T. Claes, Y. De Koninck, S. Popelka, E. Schacht, R. Baets, and P. Bienstman. *Multiplexed Antibody Detection With an Array of Silicon-on-Insulator Microring Resonators*. Photonics Journal, IEEE, 1(4):225–235, 2009.
- [20] S. Bhattacharya, A. Datta, J. M. Berg, and S. Gangopadhyay. *Studies on surface wettability of poly(dimethyl) siloxane (PDMS) and glass under oxygen-plasma treatment and correlation with bond strength*. Journal of Microelectromechanical Systems, 14(3):590–597, 2005.
- [21] S. Satyanarayana, R. N. Karnik, and A. Majumdar. *Stamp-and-stick room-temperature bonding technique for microdevices*. Journal of Microelectromechanical Systems, 14(2):392–399, 2005.



# 6

## Optical read-out

As explained in the introductory chapter, there are basically four parts contributing to a successful detection: the sensing element or transducer, the coupling chemistry, fluid delivery and read-out system. They were schematically pictured in chapter 1, Fig. 1.5.

This chapter describes the optical read-out in detail. The stability of the signal in time is very important for a low detection limit. Section 6.1 discusses how to minimize the influence of environmental parameters on the resonance wavelength of an SOI ring resonator. Light sources and detection mechanisms will be discussed in section 6.2. Part of the read-out system is integrated on-chip, see grating couplers section 6.3. Part of it consists of free-space optics, see section 6.4. A separate section is devoted to comparison of the different setups in terms of their intensity noise, section 6.5.

### 6.1 Signal stability and temperature dependence

The read-out system includes the sensor holder and the entire environment. The stability of the signal over time is very important for a low detection limit. Drift or shift of the signal when no biomolecular interaction takes place at the sensor surface is to be avoided. The resonance wavelength is susceptible to all factors that influence the effective refractive index of the optical mode  $n_{eff}$ , amongst them dimensional and refractive index changes of the core and cladding material. Stress, temperature and non-linear optical effects are the main contributors to unwanted

effective refractive index changes. Non-linear optical effects are avoided by keeping the intensity levels in the ring resonators low enough. Apart from potential conformational changes, strain induces changes in the electron density and in the average band gap in silicon [1], causing a change in the material's refractive index. However in the SOI biosensor platform, the chips are not subject to strain or stress. The main cause of unpredicted shifts are temperature fluctuations. On top of that, the temperature may be varied intentionally to induce certain biological effects (e.g. (de)hybridization of DNA). The temperature dependence of the refractive index of silicon is quite high, the thermo-optic coefficient  $dn/dT$  equals  $1.79 \times 10^{-4}/K$  at 1530 nm. This is an order of magnitude higher than the temperature dependence of the refractive index of  $SiO_2$  ( $1.2 \times 10^{-5}/K$ ). Thermal expansion has a negligible influence on the wavelength shift, although stress induced refractive index variations due to different expansion of silicon and  $SiO_2$  might contribute slightly [2].

In contrast to silicon and  $SiO_2$ , water has a negative thermo-optic coefficient ( $\approx -1 \times 10^{-4}$ ) [3], hence the red shift induced by material temperature dependence of silicon is partly neutralized. Dumon et al. reported a temperature induced wavelength shift of 83.4 pm/K for a ring resonator in air with 460 nm waveguide width [2]. We measured a wavelength shift of 66.7 pm/K for a ring resonator with the same dimensions in a water environment. Decreasing the waveguide width would increase the fraction of light in the negative thermo-optic coefficient material, further decreasing the influence of the temperature on the resonance wavelength. However, higher losses due to the water absorption would decrease the resonator's Q-factor.

The minimum detectable wavelength shift  $\Delta\lambda_{min}$  of an SOI ring resonator is lower than 1 pm (chapter 2, section 2.4). A temperature change of  $0.01^\circ C$  can already cause this shift. For that reason temperature stabilization is very important. We place the chip with the fluidics on a temperature-stabilized chuck. On top of that, when multiple rings are placed in an array, one of them can be used to compensate for temperature drift, provided that the temperature over the entire chip is equal.

## 6.2 Sources and detectors

The read-out system serves to provide light to the sensing element and process the light after passing through the sensing element. To measure a resonance wavelength shift, the spectrum of a ring resonator must be monitored. This can be done either by stepping the wavelength of a monochromatic source, in particular a tunable laser source or by excitation with a broadband source, in particular a (superluminescent) Light Emitting Diode (LED) and spectral analysis of the output with an optical spectrum analyzer (OSA) or spectrometer. An OSA typically has a higher resolution and a higher sensitivity as compared to a spectrometer. The

highest resolution OSA we have available is an Agilent 86140B spectrum analyzer with 60 pm resolution. This is insufficient to scan the resonance spectrum of a ring resonator with a FWHM of 150 pm. Hence a tunable laser is preferred. High spectral resolution comes at the cost of measurement time. Using the fastest tunable laser we had available, Santec TSL-510A, a range of 7 nm can be scanned with 5 pm resolution in about one minute. In chapter 8 we describe a method to circumvent the use of an expensive tunable laser by designing a more elaborate photonic circuit.

### 6.3 Grating couplers

Coupling light in and out of a photonic integrated circuit is an important issue: simple butt-coupling between fiber and waveguide results in unacceptable losses because of the mismatch between the fiber mode (dimension single-mode fiber core  $\varnothing \approx 10 \mu\text{m}$ ) and the waveguide mode (dimensions  $\approx 450 \times 220 \text{ nm}$ ). A lensed fiber that focuses the incoming beam on the waveguide core reduces these losses, but the alignment tolerance is too low for practical applications. The coupling problem has been tackled with different mechanisms. We will only discuss the use of integrated grating couplers. An overview of other approaches can be found in [4, 5]. Grating couplers are a substantial part of the biosensor platform, especially when multiple resonators are addressed at the same time. One- and two-dimensional grating couplers, with variations in particular designs have been demonstrated in numerous publications, amongst them [6–8]. We briefly overview the working principle of a one-dimensional grating coupler.

Waveguide gratings are structures having a periodic modulation of the refractive index, see illustration Fig. 6.1. According to the Bragg-condition, schematically shown in Fig. 6.1, this one-dimensional periodic structure will allow power exchange between particular modes of the structure. For each grating a  $\mathbf{K}$ -vector along the direction of periodicity can be defined with magnitude:

$$K = \frac{2\pi}{\Lambda}$$

in which  $\Lambda$  is the period of the grating. The fundamental waveguide mode with propagation constant  $\beta$  couples to other modes with  $k_x$  vectors given by the Bragg condition:

$$k_x = \beta + mK$$

with  $m = \dots, -2, -1, 0, 1, 2, \dots$ . From the vector diagram it is clear that vertical coupling through a grating coupler will go hand in hand with a large second order reflection back into the waveguide. To avoid this, the gratings are designed for slightly off-vertical coupling. In order to optimize the coupling efficiency, the overlap between the field profiles of an optical fiber and the upwards diffracted

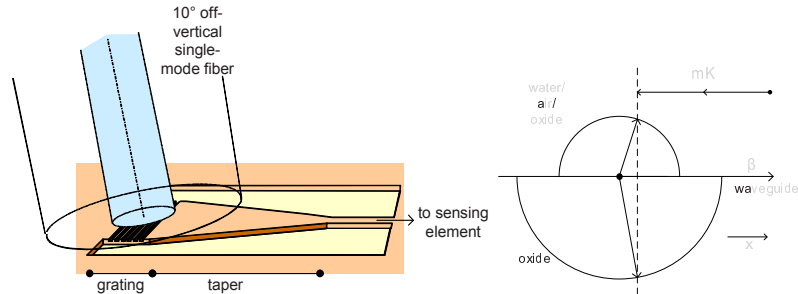


**Figure 6.1:** (Left) Coupling to integrated waveguides with near-vertical grating couplers from [4], (Right) Bragg condition for one-dimensional periodic structures.

field profile is maximized. An extensive analysis of the design of grating couplers is given by Taillaert in [9] and by Tamir in [10].

The SOI shallow etched gratings have maximal coupling efficiency of 31% at 1.55  $\mu\text{m}$  wavelength for 10° off-vertical coupling angle, with a 1 dB bandwidth of 40 nm [11]. Two mechanisms to enhance the coupling efficiency of integrated SOI grating couplers have been demonstrated by Van Laere [12] and Roelkens [13], using a gold bottom mirror or a silicon overlay layer respectively. Lateral conversion of the spot-size from the grating toward a single-mode photonic wire is performed by an adiabatic taper of  $\approx 300 \mu\text{m}$  length. The rather small bandwidth of the grating couplers forms no limitation for ring resonator sensors, as the sensing window is limited by the FSR of the resonators. As we will see below when discussing different setups, the power efficiency of the grating couplers is not a limiting factor either. We benefit from high alignment tolerances when using compact grating couplers ( $\pm 2 \mu\text{m}$  for 1 dB excess loss).

The 1D grating couplers are very polarization selective, because of the large waveguide birefringence in high index contrast material systems. The effective index is substantially different for TE and TM polarization and as a consequence a 1D grating coupler can only be designed for one polarization. The orthogonal polarization will be coupled at a completely different angle. For all measurements discussed in chapter 7, the grating couplers were optimized for TE polarization. Polarization wheels controlled the polarization at the output facet of the fiber. This polarization dependence was used in chapter 3 to launch TE and TM light in two different waveguide directions.

## 6.4 Measurement setups: fiber-based, camera-based

### 6.4.1 Fiber-based setup

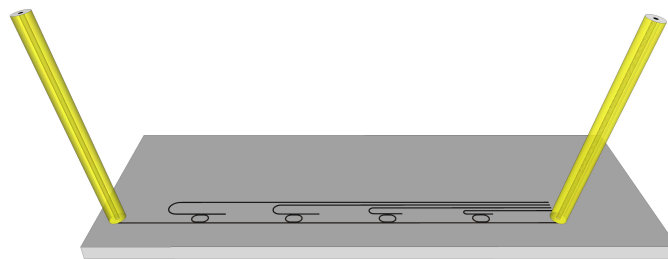
The fiber-based setup consists of two single-mode fibers, aligned to the grating couplers to transfer the input and output optical signal, Fig. 6.2(a). From the illustration it is clear that only one waveguide can be addressed at the time. Hence, only limited multiplexing is achievable. The output fiber can guide the signal of a bus waveguide that couples light to multiple ring resonators, and a spectrum like Fig. 6.2(b) is obtained. Provided that each ring resonator has a free spectral range (FSR) of 15 nm, and their resonances are separated about 1.5 nm to avoid spectral overlap and allow shifting upon molecular detection, a maximum of about 10 ring resonators can be monitored simultaneously. Post-processing involves separation of the individual signals from the common pass port signal, fitting a Lorentzian to each resonance spectrum, storing the resonance wavelength and tracing the resonance wavelength of all signals over time.

When measuring an array of ring resonator sensors simultaneously, light coming from multiple output gratings has to be detected in parallel. One possible mechanism is to align an array of fibers. However, the outer diameter of the cladding of a single mode fiber is 125  $\mu\text{m}$ , so the gratings need to be separated at least this much. This is a space consuming and fragile solution. If elaborate packaging is applied, several fibers can be packaged with the chip. However this way the fibers become part of the disposable which increases its cost unacceptably.

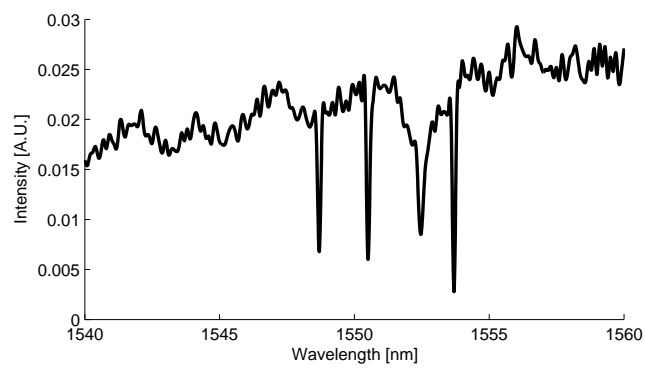
### 6.4.2 Infra-red camera setup with fiber illumination

Another option to measure many output signals simultaneously, is to monitor the light of the grating couplers by imaging them with an infra-red (IR) camera. A XenICs XEVA camera was mounted on a microscope. An illustration of this setup is shown in Fig. 6.3(a). The InGaAs camera operates from 0.9 to 1.7  $\mu\text{m}$ , has 320 $\times$ 256 pixels with 30  $\mu\text{m}$  pixel pitch and captures at a frame rate of 60 Hz. The exposure time can be set from 1  $\mu\text{s}$  to 400 s. To image the output gratings of 15 $\times$ 20  $\mu\text{m}$  on about 5 $\times$ 5 pixels, we set the magnification to 15X. Notice that we only use a small fraction of the available pixels, using a linear pixel array could reduce the system cost while maintaining similar performance.

Light is coupled into the photonics integrated circuit with a single mode fiber. In our design 3-dB MMI splitters were used as power splitters. They are about 10  $\mu\text{m}$  long, and have an excess loss of -0.2 dB. This is significantly better than an SOI Y-splitter. Although Y-splitters are more compact and have a large operation band width, because of the sharp feature in the middle, they typically cause large losses. The current generation of SOI Y-splitters has an excess loss of -1.5 dB [14]. Fig. 6.3(b) shows the spectra of a 4 $\times$ 4 ring resonator array addressed with one fiber.

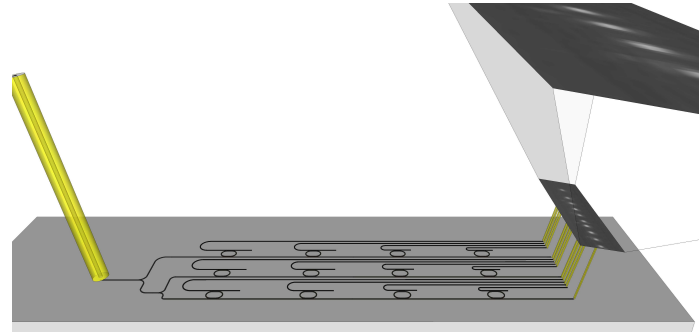


(a) Fiber-based setup.

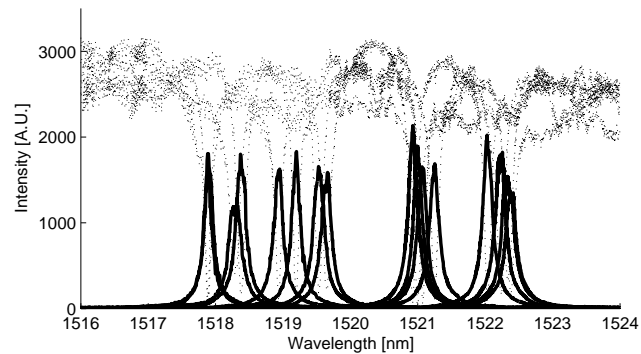


(b) Resonance spectra measured with two fibers.

**Figure 6.2:** Fiber-based measurement setup: light transfer with two single-mode fibers.



(a) Infra-red camera setup with fiber illumination.

(b)  $4 \times 4$  ring resonators are measured simultaneously with a single-mode fiber and an IR camera. Dashed lines: pass spectra, full lines: drop spectra.

**Figure 6.3:** Camera-based measurement setup: one incoupling grating is addressed with a single-mode fiber and light is captured from the outcoupling gratings with an IR camera.

A tunable laser scans the spectrum. The input power and the camera integration time was chosen so that the intensity of the resonance peaks corresponds to the pixel saturation level to obtain a maximum signal-to-noise ratio. A software framework was programmed around the camera, Fig. 6.4 shows a screen shot of the user interface. It stores the maximum pixel intensity of a window around each grating coupler. The spectrum is plotted on screen (bottom left) and the resonance spectrum of each device is stored in a separate file. By tracking only the intensity of one pixel (the maximum intensity pixel), noise due to mechanical instability is partially filtered out. A Matlab post-processing script fits a Lorentzian to the spectrum of each ring resonator per time step, so the resonance wavelength of all rings over time can be monitored.

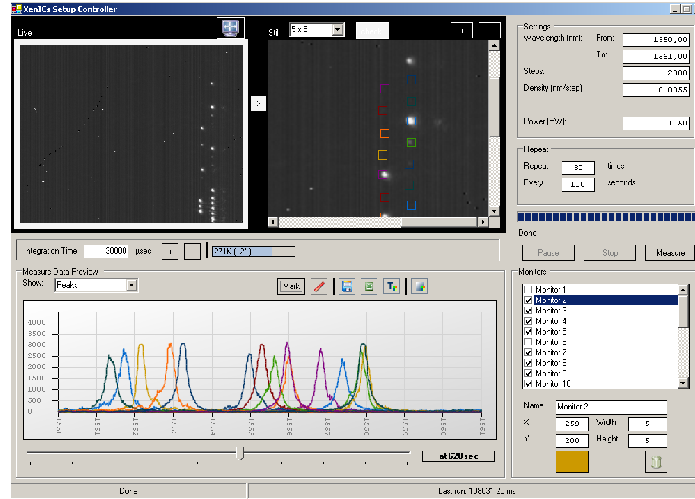
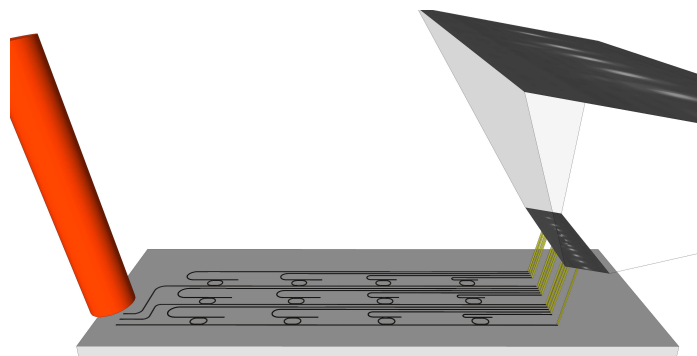


*Figure 6.4: Screen shot of the dedicated software for measuring the spectrum of multiple devices in parallel using an IR camera and a tunable laser.*

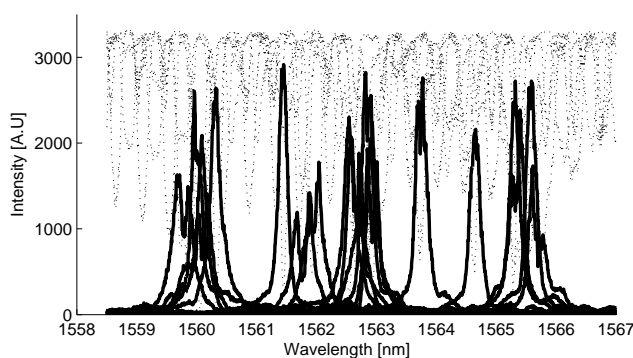
### 6.4.3 Infra-red camera setup with flood illumination

In Fig. 6.5(a) we illustrate another way to couple light into the photonic integrated circuit. Multiple grating couplers can be addressed at once with a collimated laser beam. This scheme offers the highest degree of multiplexing, since multiple input bus waveguides can be addressed, and multiple output gratings can be monitored in parallel. The spectrum of a ring resonator array of  $5 \times 4$  is shown in Fig. 6.5(b). For the experiments in chapter 7 we used a collimator that converts the fiber mode in a parallel free space beam of 2 mm diameter. This collimator could transfer light to over 100 grating couplers. If each grating coupler is tapered to a bus waveguide that serves as an input for 10 ring resonators, an array of 1000 biosensors can be monitored in parallel. On top of that, there is more flexibility in the design width of the grating couplers, since it does not have to fit to the width of a single-mode fiber core in this case. Exciting 100 waveguides with one single-mode fiber instead of with a collimated beam as discussed here would require  $71 \times 2$ -splitters. This is still feasible with respect to space and power budget, but it does not scale as easily as the flood illumination technique towards even larger arrays.

An important advantage of using flood illumination versus an optical fiber is the alignment tolerance. While the alignment of a single-mode fiber to a grating coupler has a tolerance of  $2 \mu\text{m}$  for 1 dB excess loss, the alignment of a wide parallel free space is in the order of hundreds of microns and scales with the width of the collimated beam. The overall system becomes highly tolerant to mechanical instability. For commercial applications this is a very important feature for which many



(a) Infra-red camera setup with flood illumination.

(b)  $5 \times 4$  ring resonators are measured simultaneously with flood illumination and an IR camera. Dashed lines: pass spectra, full lines: drop spectra.

**Figure 6.5:** Camera-based measurement setup: incoupling gratings are addressed with flood illumination and light is captured from the outcoupling gratings with an IR camera.

existing technologies fail.

Both with fiber coupling and flood illumination the power efficiency is rather low. However the losses in the photonic integrated circuit are low enough, and the IR camera is sensitive down to very low intensity levels so that power efficiency has not been an issue.

Despite these advantages, flood illumination comes with a drawback: the resonance spectrum is distorted by a periodic modulation with 450 pm period. In worst case, the resonance dips disappear in the oscillations and the spectrum becomes useless (e.g. Fig. 6.6). This problem was studied by M. Verbist during her master thesis work [15]. Two possible sources of this effect have been examined. The distortion might be caused by imaging imperfections. When the image

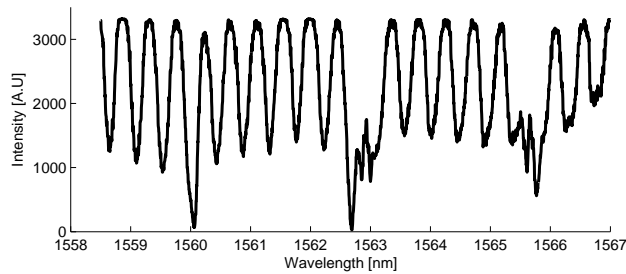


**Figure 6.6:** In worst case periodic oscillations can completely deteriorate the ring resonator spectrum.

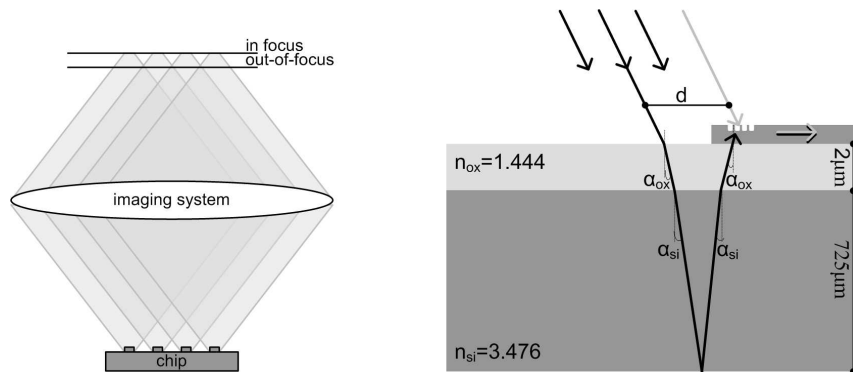


**Figure 6.7:** Possible sources of the spectral distortion observed in Fig. 6.5(b). (Left) Out-of-focus imaging of multiple output grating couplers, (Right) Reflection on the bottom of the silicon substrate.

plane does not coincide with the CCD camera plane, light coming from different gratings might interfere, Fig. 6.7 (left). However, this cause can be excluded by looking at the spectra of Fig. 6.3(b): also here multiple gratings are monitored simultaneously, but no interference patterns in the output spectrum are observed. In [15] extra experiments were performed confirming that Young-interference as a source of spectral distortion can be excluded.

A second source of the oscillations might be interference of light traveling with different optical path lengths. For example, aside from the light that couples directly to the grating, a second possibility is for light to couple via the backside of the grating, Fig. 6.7 (right). When these waves recombine, they cause interference patterns.

To confirm that the interference spectrum actually originates from a beam that is coupled through the backside of the grating coupler, we calculate the distance  $d$  where a beam should enter the chip in order to arrive at the back of the grating cou-

pler after reflection on the bottom of the substrate. From the wave vector diagram of Fig. 6.1 can be determined that the coupling efficiency from a wave coming from the back of the grating to a horizontal waveguide is maximal, when light is incident with an angle  $\alpha_{ox}$  that satisfies (with  $\alpha_{air} = 10^\circ$ ):

$$n_{air}\sin(\alpha_{air}) = n_{ox}\sin(\alpha_{ox}) \quad (6.1)$$

$$\Rightarrow \alpha_{ox} = 6.91^\circ \quad (6.2)$$

Following Snell's law, the angle of the light beam in the silicon substrate is determined:

$$n_{si}\sin(\alpha_{si}) = n_{ox}\sin(\alpha_{ox}) \quad (6.3)$$

$$\Rightarrow \alpha_{si} = 2.86^\circ \quad (6.4)$$

The most important contribution to this beam comes from the reflection of a beam incident to the bottom surface under the same angle  $\alpha_{si}$ . The distance  $d$  between the grating coupler and the location of incidence is thus:

$$d = 2(h_{ox}\tan(\alpha_{ox}) + h_{si}\tan(\alpha_{si})) \quad (6.5)$$

$$\Rightarrow d = 73\mu m \quad (6.6)$$

Interference of this beam with the beam coupled through the top of the grating coupler, will cause a sinusoidal modulation of the intensity. For the calculation of the period, we assume equal and unit intensity of both interference modes. In reality the difference in intensities will mainly depend on the grating coupler design and on the wavelength. However the interference period will not depend on the mode intensities. Under these assumptions, the interference intensity equals:

$$I = 2(1 + \cos(\Delta\Phi)) \quad (6.7)$$

where  $\Delta\Phi$  is the phase delay between both waves. The phase delay equals the acquired phase difference along propagation through the substrate plus a phase shift  $\pi$  upon reflection at the bottom substrate. For the following calculations, the propagation through the oxide is neglected<sup>1</sup>. The optical path length difference between the directly coupled mode and the backside coupled mode  $\Delta L$  is:

$$\Delta L = 2n_{si}\frac{h_{si}}{\cos(\alpha_{si})} \quad (6.8)$$

The phase delay between the interfering beams then becomes:

$$\Delta\Phi = \frac{2\pi}{\lambda}\Delta L - \pi = \frac{4\pi}{\lambda}n_{si}\frac{h_{si}}{\cos(\alpha_{si})} - \pi \quad (6.9)$$

<sup>1</sup>Including the propagation through the thin oxide layer only changes the period with a few picometers.

Plugging this into equation (6.7), we see that the intensity varies periodically as a function of  $\nu = \frac{1}{\lambda}$ , with period  $\Delta\nu = \frac{1}{\Delta L}$ . The period  $\Delta\nu$  can be converted to a period  $\Delta\lambda$  with the identity  $\frac{\Delta\lambda}{\lambda} = \frac{\Delta\nu}{\nu}$ .

$$\Delta\lambda = \lambda^2 \Delta\nu \quad (6.10)$$

$$\Rightarrow \Delta\lambda = \frac{\lambda^2 \cos(\alpha_{si})}{2n_{si}h_{si}} \quad (6.11)$$

At a central wavelength of 1550 nm, the period of the oscillation is 477 pm (with  $n_{Si}=3.47$ ,  $h_{Si}=725 \mu\text{m}$ ,  $\alpha_{Si}=2.86^\circ$ ). This corresponds well with the experimentally measured period of 450 pm.

A possible solution to avoid coupling through the backside of the grating coupler while still using flood illumination, is covering the area behind the grating couplers with an absorbing or reflecting coating. In [15] the chip was coated with a BCB polymer spacer and covered with a Au coating. A window around the grating couplers was lithographically defined and opened. In this way, no interference could occur and the spectrum was not distorted. Another solution resides in the use of a cylindrical lens and focus the laser beam to a line-shaped spot. With a high-NA lens (NA 0.55), line spots with 15  $\mu\text{m}$  line width can be obtained. This is sufficiently smaller than  $d$  (73  $\mu\text{m}$ ) and will help to avoid the oscillations in the spectra. The problem could also be tackled at the level of the grating design. Gratings with greater directionality, that couple significantly more efficiently in the upwards direction, can be fabricated with use of a bottom mirror or a silicon overlay layer [4, 5].

## 6.5 Noise

Apart from wavelength resolution, alignment tolerance and degree of multiplexing, noise is an important characteristic of the measurement equipment. The detection limit is defined by the ratio of measurement resolution and sensitivity (chapter 2, section 2.4). If infinitely small resonance width were available and absolutely zero system noise were present, the sensor performance could be characterized by the sensitivity alone. However, the resonance resolution and system noise detract from the accuracy with which the true resonance wavelength can be located. The relations between accuracy, spectral resolution, system noise and resonance shape (extinction and Q-factor) are worked out in chapter 2, section 2.3. In this section we discuss the noise of the different read-out methods that were introduced above. There are two classes of noise that contribute to errors in determining the positions of the resonant mode: intensity variations and spectral variations [16]. Intensity noise refers to the cumulative noise added to the spectral transmission characteristic. Noise sources include thermal and shot noise in the photodetector, laser relative intensity noise, quantization errors and possible fiber-to-chip coupling vari-

ation. In addition to intensity noise, there are spectral noise factors that also contribute to variation in the spectral location of the resonant mode and thus to the measurement resolution. First there is the thermal variation of the system. This was discussed in section 6.1 of this chapter. The spectral resolution is also limited by the wavelength accuracy of the laser or the optical detection mechanism. In our setup, the laser is tuned over a small spectral range while a photodetector or IR camera measures the amplitude at the output of the system. The limitation in this case is due to the linewidth of the laser, which is less than 1 MHz. At 1550 nm, 1 MHz is equivalent to about 8 fm.

Since the Q-factor of the SOI ring resonators is relatively low ( $10^4$ ), the influence of noise on the detection limit is dominated by intensity noise. In the case of high-Q sensors ( $10^7$ ), spectral noise becomes the limiting factor and controlling the temperature and laser induced spectral fluctuations is key to a high detection limit.

To determine the intensity noise of the detection system, the output intensity was measured a large number of times at constant wavelength and constant input power [17]. The intensity noise was then determined as the variance of the normalized intensity,  $\text{noise} = \sigma_{I_{norm}}^2 = \frac{\langle \Delta I^2 \rangle}{I^2}$ . This way we bring setup noise only into account, and exclude possible noise sources in the photonic integrated circuit (for example the interference mentioned in the previous section). The same definition was used for the noise in the simulations of chapter 2. Results for the different setups are in graph 6.8. A large part of the noise of the fiber-fiber setup originates from vibrations of the fibers, which causes the coupled intensity to fluctuate. When comparing the noise of a setup with two loose fibers to the noise level of a setup where the mechanical stability is enhanced by gluing both fibers to the chip with a UV curable glue,  $\sigma_{I_{norm}}^2$  decreases with a factor 50. For the IR camera setups, the measurements were done for a set of input powers to obtain the noise for the full dynamic range of the camera. No correlation was found between the input intensity level and  $\sigma_{I_{norm}}^2$ , but the standard deviation was used to indicate the error bar.  $\sigma_{I_{norm}}^2$  of the camera setup is dominated firstly by mechanical stability (the noise decreases when gluing the fiber or using flood illumination), and then by quantization errors because of the limited number of bits (12) used for analog/digital conversion.

## 6.6 Conclusion

Measuring the spectrum of a ring resonator biosensor can be performed with a number of read-out systems. They differ in light source (monochromatic or broadband), detection (spectrum analyzer, photodetector or CCD camera) or light guiding (fiber or free-space). The read-out system of an integrated optical biosensor is fundamentally different from the read-out system of commercial free-space

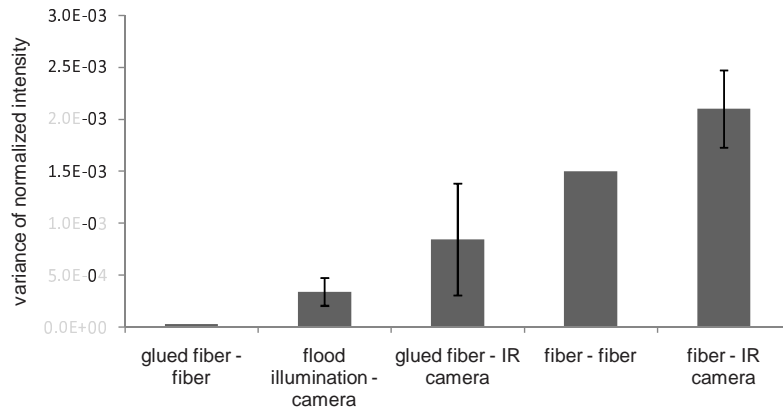


**Figure 6.8:** Comparison of the variance on the normalized intensity for different read-out systems.

biosensors like Biacore SPR. The read-out is completely decoupled from the detection, offering a much higher degree of multiplexing and a much higher alignment tolerance. The latter is important for portable applications and largely reduces the cost of the overall system. In Table 6.1 the setups we investigated are listed and compared in terms of important performance parameters. Flood illumination and detection with an IR camera offers a good trade-off between high degree of multiplexing and low noise. However precautions need to be taken to avoid oscillations originating from interference between the modes coupled directly and through the backside of the grating couplers.

	Wavelength resolution [pm]	Noise	Alignment tolerance	Multiplexing (# rings)	Cost of the disposable
Fiber-fiber (SANTEC tunable laser-photodetector)	1	high	low ( $2 \mu\text{m}$ )	10	low
Fiber-fiber glued (SANTEC tunable laser-photodetector)	1	very low		10	high
Fiber-fiber (SLED-OSA Agilent)	60		low ( $2 \mu\text{m}$ )	10	low
Fiber-fiber glued (SLED-OSA Agilent)	60			10	high
Fiber-IR camera	1	very high	low ( $2 \mu\text{m}$ )	100–1000	low
Glued fiber - IR camera	1	medium		100–1000	high
Flood illumination-IR camera	1	low	high ( $>100 \mu\text{m}$ )	$>1000$	low

*Table 6.1: Overview of the performance parameters of different read-out setups.*

## References

- [1] P. Dumon. *Ultra-compact integrated optical filters in silicon-on-insulator by means of wafer-scale technology*. PhD thesis, Ghent University, 2007.
- [2] P. Dumon, G. Priem, L. R. Nunes, W. Bogaerts, D. Van Thourhout, P. Bienstman, T. K. Liang, M. Tsuchiya, P. Jaenen, S. Beckx, J. Wouters, and R. Baets. *Linear and nonlinear nanophotonic devices based on silicon-on-insulator wire waveguides*. *Japanese Journal of Applied Physics Part 1-Regular Papers Brief Communications & Review Papers*, 45(8B):6589–6602, 2006.
- [3] G. Abbate, U. Bernini, E. Ragozzino, and F. Somma. *Temperature-dependence of refractive-index of water*. *Journal of Physics D-Applied Physics*, 11(8):1167–1172, 1978.
- [4] Frederik Van Laere. *Photonic integrated circuits and fiber couplers based on InP bonded membranes*. PhD thesis, Ghent University, 2008-2009.
- [5] G. Roelkens. *Heterogeneous III-V/Silicon photonics: bonding technology and integrated devices*. PhD thesis, Ghent University, 2006-2007.
- [6] D. Taillaert, W. Bogaerts, P. Bienstman, T. F. Krauss, P. Van Daele, I. Moerman, S. Verstuyft, K. De Mesel, and R. Baets. *An out-of-plane grating coupler for efficient butt-coupling between compact planar waveguides and single-mode fibers*. *IEEE Journal of Quantum Electronics*, 38(7):949–955, 2002.
- [7] D. Taillaert, H. Chong, P. I. Borel, L. H. Frandsen, R. M. De La Rue, and R. Baets. *A compact two-dimensional grating coupler used as a polarization splitter*. *IEEE Photonics Technology Letters*, 15(9):1249–1251, 2003.
- [8] F. Van Laere, W. Bogaerts, P. Dumon, G. Roelkens, D. Van Thourhout, and R. Baets. *Focusing Polarization Diversity Grating Couplers in Silicon-on-Insulator*. *Journal of Lightwave Technology*, 27(5-8):612–618, 2009.
- [9] Dirk Taillaert. *Grating couplers as interface between optical fibers and nanophotonic waveguides*. PhD thesis, Ghent University, 2004-2005.
- [10] T. Tamir and S. T. Peng. *Analysis and design of grating couplers*. *Applied Physics*, 14(3):235–254, 1977.
- [11] W. Bogaerts, R. Baets, P. Dumon, V. Wiaux, S. Beckx, D. Taillaert, B. Luysaert, J. Van Campenhout, P. Bienstman, and D. Van Thourhout. *Nanophotonic waveguides in silicon-on-insulator fabricated with CMOS technology*. *Journal of Lightwave Technology*, 23(1):401–412, 2005.

- 
- [12] F. Van Laere, G. Roelkens, M. Ayre, J. Schrauwen, D. Taillaert, D. Van Thourhout, T. E. Krauss, and R. Baets. *Compact and highly efficient grating couplers between optical fiber and nanophotonic waveguides*. *Journal of Lightwave Technology*, 25(1):151–156, 2007.
- [13] G. Roelkens, D. Van Thourhout, and R. Baets. *High efficiency Silicon-on-Insulator grating coupler based on a poly-Silicon overlay*. *Optics Express*, 14(24):11622–11630, 2006.
- [14] W. Bogaerts, S. K. Selvaraja, P. Dumon, J. Brouckaert, K. De Vos, D. Van Thourhout, and R. Baets. *Silicon-on-Insulator Spectral Filters Fabricated With CMOS Technology*. *Selected Topics in Quantum Electronics, IEEE Journal of*, 16(1):33–44, 2010.
- [15] Marie Verbist. *Retroreflectieve optische marker-chips met individueel afgestemde filters*. Master thesis, Ghent University, 2007-2008.
- [16] I. M. White and X. D. Fan. *On the performance quantification of resonant refractive index sensors*. *Optics Express*, 16(2):1020–1028, 2008.
- [17] K. De Vos, J. Girones, T. Claes, Y. De Koninck, S. Popelka, E. Schacht, R. Baets, and P. Bienstman. *Multiplexed Antibody Detection With an Array of Silicon-on-Insulator Microring Resonators*. *Photonics Journal, IEEE*, 1(4):225–235, 2009.



# 7

## Biosensor measurement results

### 7.1 Introduction

The previous chapters were devoted to the technical details of the SOI ring resonator biosensor platform development. This chapter will show the most important measurement results that we obtained. All measurements have been performed with the focus on characterization of the platform, including photonic chip, chemistry, fluidics and read-out system. The platform is developed to be applicable for a broad range of applications with a focus on protein detection. However, in the course of this work we did not investigate a specific diagnostic or biotechnological problem. Instead we used standard molecules such as avidin, biotin, IgGs and DNA to characterize the platform.

First we will present the sensor's ability to monitor refractive index variations of the entire environment, i.e. bulk refractive index (RI) changes (see section 7.2). In a next step we measured the thickness of thin layers with well known properties at the ring resonator surface, see section 7.3. The high affinity molecular couple avidin-biotin has been used to perform specific and non-specific binding tests. Although avidin-biotin will not be the ultimate biological system studied with these biosensor chips, it is a useful model affinity couple to demonstrate the feasibility and reproducibility of the detection. It also allowed us to characterize the sensitivity of the system and to show the efficiency of the surface chemistry coatings to reduce non-specific interactions, see section 7.4. The measurement results are structured similarly to the section structure of the chemistry chapter

(chapter 4). Ultimately we tested the system for multiplexed protein detection: different proteins were spotted on different chip locations and various antibodies could be detected simultaneously, see section 7.5.

In the theoretical chapter (chapter 2) we calculated the minimum detectable wavelength shift  $\Delta\lambda_{min}$  of the system. With the measurement results presented here, we can determine the sensor's sensitivity towards bulk RI changes or biomolecular layer changes. The ratio of  $\Delta\lambda_{min}$  and sensitivity provides us with the sensor's detection limit. The detection limits reported in this chapter are calculated for a minimum detectable wavelength shift of 0.67 pm, which was calculated in chapter 2, section 2.3.5. A list of calculated detection limits can be found in table 2.2 of the same chapter.

## 7.2 Bulk RI sensing

Although the sensitivity for bulk RI changes is not a direct measure for the sensor's sensitivity for biomolecular detection, it is important to investigate this parameter. Biomolecules appear in solutions with different refractive indices, hence sometimes causing a bulk RI contribution to the measurements. Most likely this signal is of no interest for the user, so in order to be able to compensate for it, it is advisable to predict its contribution.

Liquids with varying refractive indices (water with different sodium chloride concentrations) are flowed across the ring resonator in order to characterize the bulk refractive index sensitivity. No surface chemistry was carried out, so the refractive index is homogeneously changed above the ring resonator. Su et al. experimentally determined the refractive index of solutions at 1550nm [1]. The refractive index of an aqueous solution of NaCl varies as  $n = 0.17151C + 1.3105$ , with  $C$  the concentration in mass %. Fig. 7.1 shows a linear shift of 69 nm/RIU of the resonance wavelength with increasing salt concentration. The shifts are determined after Lorentzian fitting. All measurements are done three times to prove repeatability. The linear fit is depicted with mean wavelength shift values and weighted standard deviation error bars. The variations are very small, proving a very high stability. The sensitivity corresponds well to the simulated sensitivity values in chapter 2, section 2.2. If a shift of 0.67 pm is detectable, this results in an RI detection limit of  $9.7 \cdot 10^{-6}$  RIU.

## 7.3 Layer thickness sensing

To study molecular interaction near the sensor surface, a simple model of a layer surrounding the waveguides at three sides with constant refractive index and increasing thickness is commonly used (chapter 2, section 2.2.2) [2]. The resonance

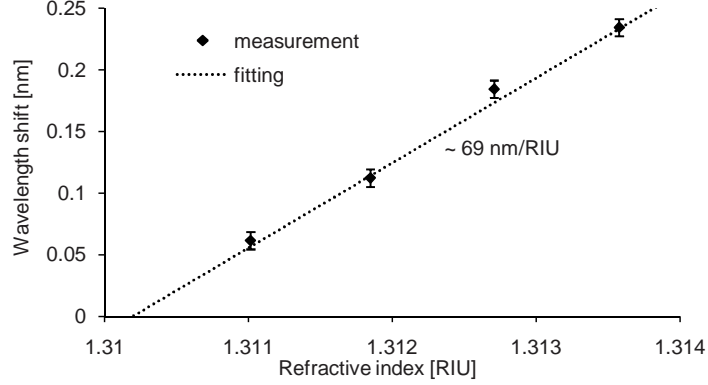


**Figure 7.1:** Resonance wavelength shift versus bulk refractive index change showing a sensitivity of 69nm/RIU or a detection limit of  $10^{-5}$  RIU.

wavelength shift is

$$\Delta\lambda = \frac{\Delta n_{eff} \lambda_0}{n_g} \quad (7.1)$$

taking first-order dispersion into account.  $n_{eff}$  is the effective index change of the resonating mode,  $\lambda_0$  the initial resonance wavelength and  $n_g$  the group index. We simulated the effective index change  $n_{eff}$ , using vectorial mode solver software Fimmwave, and calculated the corresponding resonance wavelength shift with formula (1). To verify this formula and simulations, we deposited thin layers of  $\text{SiO}_2$  on ring resonator sensors and measured the wavelength shift. The simulation parameters of the deposited layers, thickness and refractive index, were determined with a M-2000FI Spectroscopic Ellipsometer (J.A. Woollam) on flat surfaces fabricated at the same time. Sidewall layer thickness was determined by focused ion beam (FIB) cross-sectional examination of the waveguides. The expected wavelength shift induced by these layers with known parameters was simulated, and showed good correspondence with the measured wavelength shift, see Fig. 7.2. Four rings with different radii were measured for each data point. Average and standard deviation, although very small, are indicated. As expected, the shift does not vary with the ring radius. Sensing with TM polarized light would be 1.5 times more sensitive for thin layers, but the grating coupler design for these experiments was optimized for TE polarization, so we only performed TE experiments.

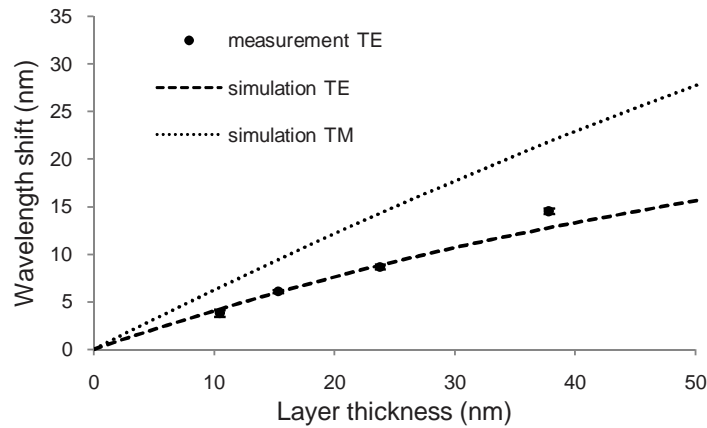


**Figure 7.2:** Comparison between theoretical and experimental response of the resonance wavelength shift to the thickness of an  $\text{SiO}_2$  overlayer.

## 7.4 Avidin-biotin characterization

### 7.4.1 One-step modification

The title 'One-step modification' refers to the chemistry described in the section with the same name, section 4.3.1 in chapter 4. A layer of APTES is anchored to the silicon waveguides, to which biotin molecules are linked with NHS/EDC chemistry. We flowed different concentrations of avidin in Phosphate Buffer Solution (PBS) across the sensor surface and plotted the wavelength shift after about 45 minutes in Fig. 7.3 (left). Each data point shows the difference in resonance wavelength of the cavity immersed in PBS, before and after being in contact with the avidin solution. Redundant avidin molecules are rinsed thoroughly with PBS, so no bulk refractive index changes are involved. All measurements are performed with at least 3 different samples, and error bars are indicated. For avidin concentrations above  $10 \mu\text{g/ml}$  the surface is fully covered, so the resonance wavelength shift saturates. This is another proof that we detect a surface modification and not a bulk liquid modification, like in Fig. 7.1. Smaller avidin concentrations cause smaller wavelength shifts which allows quantification of the avidin concentration. Starting from the lowest measured concentration, we assume a linear shift for smaller concentrations. With this assumption, the concentration corresponding to a minimal detectable shift of  $0.67 \text{ pm}$ , is a detection limit of  $5.1 \text{ ng/ml}$ <sup>1</sup>.

Assemblies of silane reagents are straightforward silicon surface coatings that can carry a wide range of functional groups for receptor molecule immobilization, but they typically do not have sufficient resistance to non-specific interactions. SOI

<sup>1</sup>Note the value of  $3.8 \text{ ng/ml}$  from table 2.2 corresponds to the PEG chemistry and not the APTES chemistry

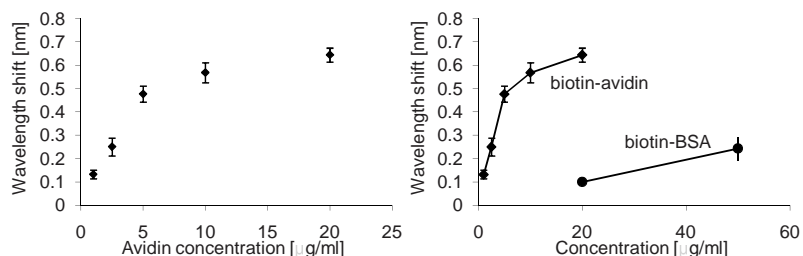


**Figure 7.3:** Left: Resonance wavelength shift corresponding to different avidin concentrations for quantitative molecular detection. Biotin was anchored to the surface through an APTES layer with the chemistry described in section 4.3.1, Right: Non-specific binding tests to show a lower response for biotin-BSA interactions compared to biotin-avidin interactions, however the response is still much too high for practical applications.

ring resonator biosensor measurements that confirm the high non-specific signal of APTES are presented in Fig. 7.3 (right). Bovine Serum Albumin (BSA), a protein with similar molecular weight to avidin but with low affinity to biotin, has been used as a model for non-specific interactions. Identically biotin-coated chips are brought into contact with avidin solutions and BSA solutions. The response to BSA concentrations is clearly lower, but not sufficiently low to be usable in practical applications with serum that typically contains BSA concentrations of at least 20 times higher than in this experiment. With a silane coating, one can not distinguish between a specific signal of 1  $\mu$ g/ml avidin and a non-specific signal of 20  $\mu$ g/ml BSA.

#### 7.4.2 Two-step modification

The low robustness against non-specific interactions of silane coatings can be improved by attaching an ultra thin layer of a hydrophilic polymer like poly(ethylene glycol) (PEG). In chapter 4, section 4.3.2 we describe how to coat the sensors with monoprotected diamino-PEG ( $\text{H}_2\text{N-PEG-NH}_2$ ) or  $\alpha$ -sulfanyl- $\omega$ -carboxy PEG ( $\text{HS-PEGCOOH}$ ) in a two-step modification procedure. Chemical characterization experiments confirming the reduced hydrophobicity and the homogeneity of the surface coatings are also presented in chapter 4. In this section sensing results of an SOI ring resonator with a PEG coating are presented.

#### Concentration measurements

After deprotection of the Boc groups, chips coated with ( $\text{H}_2\text{N-PEG-NH}_2\text{-Boc}$ ) were biotinylated and placed in the optical setup. PBS (10mM  $\text{NaHPO}_4$ , 150mM NaCl, pH 7.4) was used as running buffer. The signal of the chips immersed in

PBS was taken as a reference level. Fig. 7.4 shows the real time response signal of the chips to a range of avidin concentrations: 2, 10, 87.5 and 175  $\mu\text{g/ml}$  and two response signals of the chips to BSA at 1 mg/ml concentration. Every curve corresponds to a different experiment on a different chip. For high concentrations, a fast wavelength shift is initially recorded due to the sudden concentration gradient. Ideally, under mass-transport limiting conditions present in these interactions, the initial slope is linearly proportional to the concentration of the analyte in solution. In our experiment however, due to gradual mixing of the fluids in the tubings (it takes several minutes before the initial concentration level is reached), the slope of the curve does not directly correspond with the concentration or the kinetics of the interaction. The kink in the 2  $\mu\text{g/ml}$  signal is due to a flow problem: when an air bubble gets trapped, a short increased flow rate is needed to push it through.

Sensor calibration can be done either by monitoring the shift at a certain time, after a certain transported volume, or by calculating the slope of the S-curve. However for the last method, a valve needs to be installed that allows instant switching between liquids without gradual mixing. The initial-slope-based quantization method was used by other groups and was found to have a high precision [3]. This is mainly because more data points are taken into account to calculate the slope over a given time range as opposed to determining one data point after a certain time. We calculate the detection limit from a one-point calibration with the saturation level in time of the 2  $\mu\text{g/ml}$  curve, under the assumption that smaller concentrations cause linear shifts. 2  $\mu\text{g/ml}$  avidin concentration causes the resonance wavelength to shift over 350 pm, the sensitivity was thus found to be approximately 175 pm/ $\mu\text{g/ml}$ . We extrapolate a detection limit of 3.8 ng/ml for a measurement resolution of 0.67 pm.

No blue shift was observed when the chips were rinsed with PBS at the end of the experiment. This is in agreement with the specific binding of avidin, rather than its adsorption, due to the low dissociation constant of avidin-biotin and the absence of a bulk refractive index effect at these concentrations.

### Monitoring all coupling steps in real time

In a second set of experiments the receptor immobilization was performed inside the microchannels instead of on the bench top before sealing the channels. Fig. 7.5 is a graph of the real time sensor response to successive chemical steps. Biotin was immobilized via the free amino groups of the  $\text{H}_2\text{N-PEG-NH}_2$  layer using biotin-NHS. After rinsing the surface with buffer, a solution of BSA (1 mg/ml) was applied to block the surface and evaluate the non-specific interaction. Afterwards, a solution of 55  $\mu\text{g/ml}$  avidin in PBS was run through the system. An immediate signal shift occurs. It is a little lower than the shift of Fig. 7.4, because the biotinylation did not proceed long enough. In order to save time, we performed the receptor coupling in solution outside of the optical setup for all the experiments

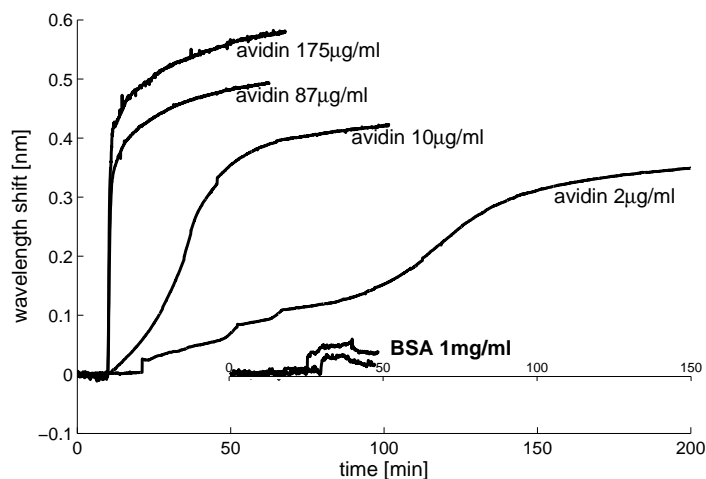


**Figure 7.4:** Specific versus non-specific binding tests: interaction of six biotinylated  $H_2N$ -PEG- $NH_2$  coated chips. Wavelength shift obtained due to the interaction with avidin (2, 10, 87,5 and 175  $\mu\text{g/ml}$ ) and with BSA (1mg/ml). For BSA interaction two signals on two separate chips are shown. The kink in the 2  $\mu\text{g/ml}$  signal was due to a flow problem: when an air bubbles gets trapped, a short increased flow rate pushes it through.

described below.

**Non-specific interaction**

In Fig. 7.4 we observe a low response to 1 mg/ml BSA as compared to a high response to 2  $\mu\text{g/ml}$  avidin. This confirms the ability of the PEG coating to reduce non-specific interactions. Further investigation of non-specific interactions with a silane coating versus a PEG coating was performed in Fig 7.6. It shows a comparison of the signal provided by chips with and without the PEG coating. Curve A is the interaction of 10  $\mu\text{g/ml}$  avidin with a biotinylated PEG coated chip. The response signal to avidin arises 210 times above the noise level. Curve C shows the interaction of 17  $\mu\text{g/ml}$  BSA with an epoxy-silane (GPTS) covered chip. It is clear that even for a BSA concentration this small, in absence of the PEG coating a rather high output is measured. This refers to the high non-specific interaction of silane coatings. Curve B shows the signal obtained by interaction of increasing BSA concentrations on a PEG coated chip. For a BSA concentration of 17  $\mu\text{g/ml}$  no distinguishable signal was measured. For 50  $\mu\text{g/ml}$  BSA, the signal exceeded only 2.5 times the noise level. 1 mg/ml BSA concentration raised the output response to only about 15 times above the noise level, taken into account the back shift after rinsing with PBS (such high molecular concentrations cause a bulk refractive index change). From these low levels of non-specific signal it is concluded

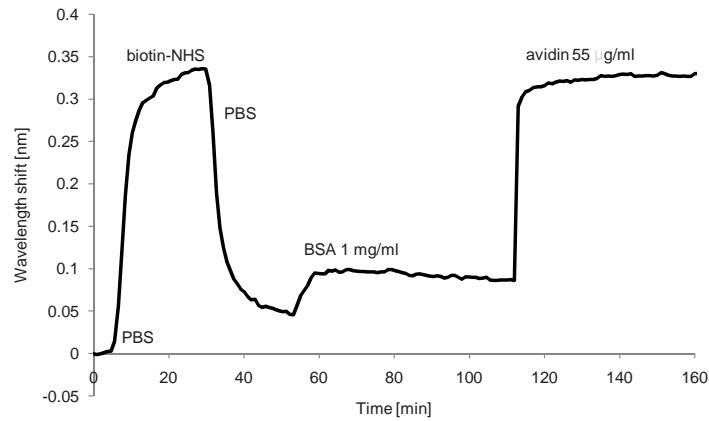


*Figure 7.5: Real time sensor response of biotin receptor binding and avidin interaction.*

that the PEG coating truly reduces the background. This is crucial towards applications with serum that contains high levels of random proteins, and only very small amounts of the analyte to detect.

## 7.5 Protein detection and multiplexing

To immobilize protein receptor molecules on the PEG-coated silicon sensor, the original coupling procedure for N-hydroxysuccinimidyl ester of biotin (biotin-NHS) had to be modified since proteins do not carry groups that react directly with the amino groups of the PEG coating. This was discussed in chapter 4, section 4.3.3. Fig. 4.15 in chapter 4 shows two different coupling routes: one route for coupling activated proteins (like biotin-NHS), and the second route for coupling non-activated proteins (like biotin-NH<sub>2</sub> as well as most proteins). The second route is the one we used for the final multiplexing experiments.

We will first introduce the SOI biosensor platform for the multiplexing experiments in section 7.5.1. The different chemistry steps for optimization of the coupling routes were characterized with the SOI ring resonator biosensor platform and results are discussed in section 7.5.2. Section 7.5.3 shows two results of multiplexed label-free biosensing of proteins.

### 7.5.1 SOI biosensor platform for multiplexed protein detection

Fig. 7.7 illustrates the biosensor platform for multiplexed protein detection. The SOI photonic integrated circuit consists of an array of 3×4 microring resonators. Four rings are connected to one common input waveguide, each of them having a

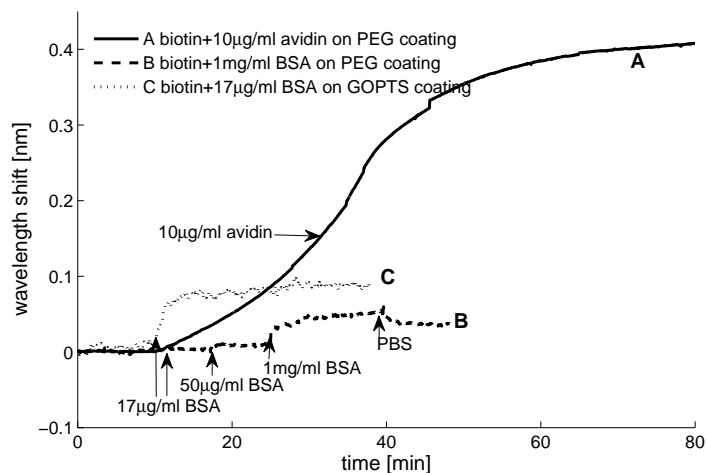


**Figure 7.6:** Comparison of chips with and without  $H_2N$ -PEG- $NH_2$  coating: (A) specific interaction on a  $H_2N$ -PEG- $NH_2$  coated surface, (B) non-specific interaction on a  $H_2N$ -PEG- $NH_2$  coated surface with increasing BSA concentrations, (C) non-specific interaction on a non  $H_2N$ -PEG- $NH_2$  coated surface.

dedicated drop signal port. Three of these four ring series are placed independently next to each other. The resonators in series differ by 30 nm in circumference to avoid spectral overlap of resonances.

The SOI chips are modified according to the coupling procedures described in chapter 4. A drop of receptor proteins was spotted to each column of rings prior to microfluidics packaging. All proteins were spotted at 1 mg/ml concentration in PBS (pH 7.4) containing 10% glycerine to prevent spot evaporation and normalize spot size [4]. The minimum spot size of the BioDot spot tool is 300  $\mu\text{m}$  in diameter, but one column of racetrack resonators occupied about a 1 mm diameter, so that is the spot size we aimed for. Samples were incubated in the fridge at 4°C overnight. Afterwards, they were rinsed thoroughly with MilliQ water and PBS.

In a next step, the samples are packaged with microfluidics according to the stamp-and-stick procedure described in chapter 5, section 5.3.2. The chip with fluidics is subsequently placed on a temperature stabilizing chuck and the sample liquids were pumped with a Harvard syringe pump at 5  $\mu\text{l}/\text{min}$  flow rate.

The three input waveguides are simultaneously addressed through vertical grating couplers with a 2 mm wide collimated beam coming from a tunable laser source. The output gratings are imaged with an IR camera. This read-out system was detailed in chapter 6, section 6.4. This way we can record the response of 12 ring resonators to different molecules in the serum in parallel.

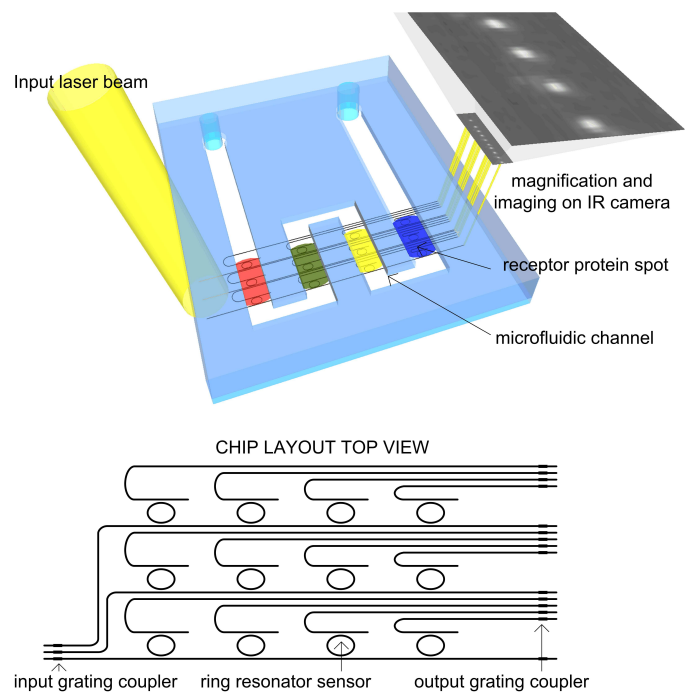


**Figure 7.7:** Illustration of the biosensor platform (not to scale).

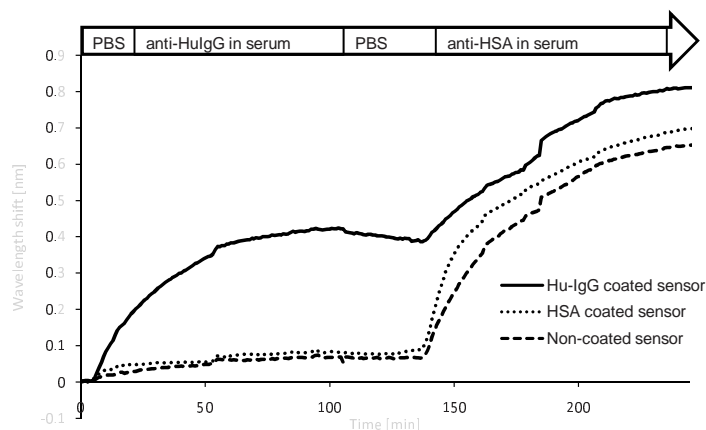


**Figure 7.8:** Experiment that proves the increased non-specific interaction when receptor proteins are coupled to the PEG layer through gluteraldehyde. The signal of three sensors coated with different proteins (Hu-IgG, HSA and one uncoated sensor) does not show sufficient specificity upon interaction with diluted goat serum.

### 7.5.2 Chemistry optimization steps

In a first attempt to couple proteins other than biotin, activation of the PEG surface was carried out by gluteraldehyde (chapter 4, Fig. 4.13 left). However as confirmed by contact angle measurements, after inactivation of the aldehyde groups with ethanolamine the hydrophobicity increased. This partly canceled out the advantages of the hydrophilic PEG surface. In Fig. 7.8 the increased non-specific interaction after coupling through gluteraldehyde is demonstrated. Three sensors with different receptor proteins are measured in parallel. One sensor was coated with Hu-IgG (Human Immunoglobuline), another sensor was coated with HSA (Human Serum Albumin) and yet another sensor was not coated. Different fluids are consecutively flowed across all sensors. The signal is stabilized in PBS. Then  $48 \mu\text{g/ml}$  of anti-Hu-IgG in 100X diluted goat serum was introduced. This serum contains about  $550 \mu\text{g/ml}$  proteins that might interact non-specifically with the sensor. The sensor that was coated with Hu-IgG features a higher response than the sensor coated with HSA and the uncoated sensor. However the non-specific signal is high if compared to the low non-specific signals in the previous paragraphs. When a solution of  $31 \mu\text{g/ml}$  anti-HSA in 100X diluted goat serum is pushed through the channels, not only the sensor coated with HSA responds, but all three sensors have a positive signal. This is caused by the non-specific interaction of the proteins in the goat serum with the aldehyde surface. Further investigation with fluorescence microscopy and contact angle measurements confirmed the poor resistance of gluteraldehyde to non-specific interactions.

Fig. 7.9 gives an overview of several experiments we performed for optimization

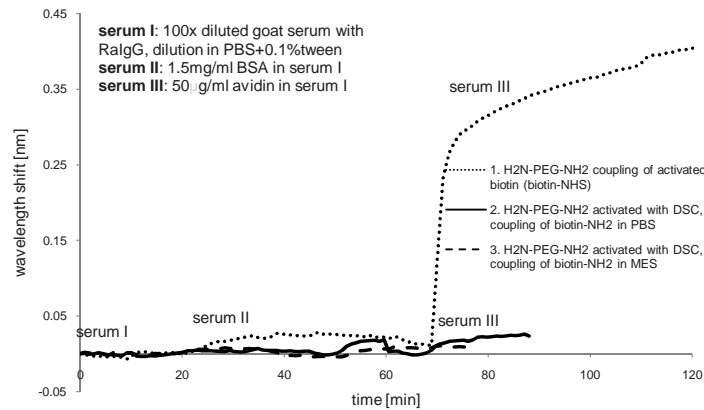


**Figure 7.9:** Immobilization of receptor proteins through DSC. Curve 1 depicts the interaction for the ideal situation where an activated protein (biotin-NHS) is coupled directly to the surface (coupling route 1). When coupling a non-activated protein (biotin-NH<sub>2</sub>) through DSC, the competition with hydrolysis decreases the receptor density, both in low and high pH buffer (curve 2 and 3). No biotin-avidin interaction can take place.

of protein coupling. Curve 1 depicts the interaction of avidin with biotin when biotin-NHS is used as receptor molecule. This is the ideal situation that was used in all previous sections to optimize the coating towards low non-specific interactions (coupling route 1). As a model for other proteins, biotin with a primary amino group (biotin-NH<sub>2</sub>) was used. Instead of using aldehydes for coupling proteins to the surface, we investigated the use of DSC (disuccinimidyl carbonate). DSC transforms the amino end-groups of the PEG coating to N-hydroxysuccinimidyl. With this method, the inactivation of the surface structures occurs by hydrolysis, providing hydrophilic carboxylic groups at the surface (chapter 4, Fig. 4.13 (right)). From curve 2 we conclude that, indeed, the non-specific interaction is low, but the specific signal is low too. The receptor coupling through DSC was not effective because of the competing interaction of water and receptor molecules with the N-hydroxysuccinimidyl (chapter 4, section 4.3.3). In order to improve the coupling, a MES buffered saline (pH 5.5) was used as coupling buffer instead of PBS. The lower pH of the solution decelerates the hydrolysis, which might extend the reaction period of the proteins with the surface. This procedure was verified in curve 3. Unfortunately, the receptor density remained very low when using a lower pH buffer resulting in a low avidin-biotin interaction and a low output signal.

Next, instead of changing the pH of the solution, we played around with the solution volume. The water content during receptor immobilization was minimized by using very low volumes and placing a second chip on top of the sensor chip (chapter 4, Fig. 4.15 coupling route 2). The efficiency of the second route was

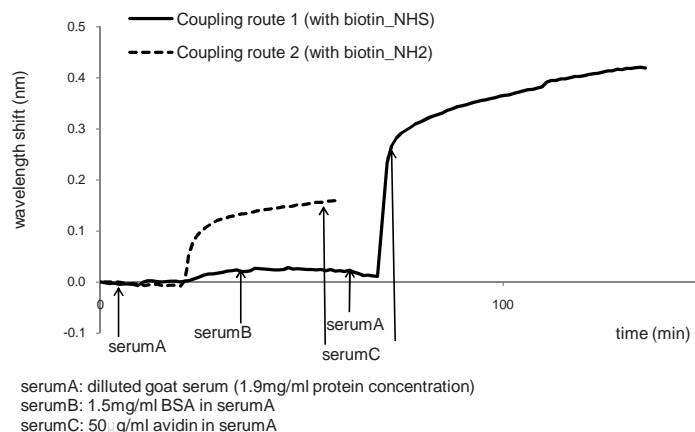


**Figure 7.10:** Biotin-NHS versus biotin-NH<sub>2</sub> as model receptor molecules. The full line depicts biotin-avidin interaction when coupling biotin-NHS with coupling route 1, the dashed line depicts biotin-avidin interaction when coupling biotin-NH<sub>2</sub> with coupling route 2.

verified and compared to that of the first route in Fig. 7.10. The full line shows the response to avidin of a sensor with biotin-NHS receptor molecules (Fig. 4.15, coupling route 1), the dashed line corresponds to the response to avidin of a sensor with biotin-NH<sub>2</sub> receptor molecules (Fig. 4.15, coupling route 2). After stabilizing the signal in PBS-diluted goat serum (1.9-mg/ml total protein concentration), a sample of the same serum fortified with 1.5 mg/ml of BSA was run through the system showing almost no response. One hour later, a sample fortified with 50 μg/ml of avidin was analyzed. Within a few minutes a sharp wavelength shift was detected, which corroborates the high selectivity and sensitivity of the system. The avidin binding test revealed that the second route is less efficient and less repeatable (dashed line), probably due to partial hydrolysis of surface NHS-ester groups during the coupling step. Although not optimal yet, this result indicates the viability of the applied methodology.

### 7.5.3 Multiplexing

Fig. 7.12 shows the result of a proof-of-principle multiplexed sensing experiment. Three different proteins are spotted on the resonators: Hu-IgG, HSA and BSA. The fourth column of resonators was left for reference. First, PBS was pumped over the sensors to determine the reference wavelength. After that, two diluted body fluids are successively pumped through the channels; goat serum with 128 μg/ml polyclonal anti-Hu-IgG (1.9 mg/ml total protein concentration) and goat serum with 82.6 μg/ml polyclonal anti-HSA (1.5-mg/ml total protein concentration). All

dilutions are made with PBS + 0.1% Tween. Notice the high concentration of non-specific proteins versus the low concentration of the specific antibodies in the serum. When the first serum is introduced, a sharp signal rise was measured for the three resonators covered with Hu-IgG. The other nine resonators barely responded, proving the absence of anti-HSA and anti-BSA in the first serum. Upon introduction of the second serum, the signals of the resonators covered with HSA rise sharply, while the other signals remain constant. This indicates the presence of anti-HSA in the second serum and the absence of anti-Hu-IgG and anti-BSA. The non-specific background signal is extremely low. No difference in background signal was detected between the reference sensors and the sensors covered with BSA. The variation between equally covered sensor signals is mainly due to a slight difference in receptor coverage, as it cannot be explained by geometrical or temperature variations. Indeed, intra-chip variations in waveguide width are very small ( $< 1$  nm) and account for less than 3 pm variation in response between different sensors. The signal differences are also too big to be attributed to intra-chip temperature variations. A difference of 0.05 nm shift would originate from a temperature variation of about  $1^{\circ}\text{C}$  over less than a millimeter on chip. A small part of the wavelength shift is due to the difference in refractive index of the diluted serums versus PBS. This difference is estimated  $2.6 \times 10^{-4}$  for the serum with 1.5 mg/ml protein concentration [2], which corresponds to a shift of 15 pm.

The reference signals, both from the BSA sensors and the receptor molecule-free sensors, can be subtracted from the positive signals. This way the non-specific interaction signal and the bulk refractive index signal are eliminated and we obtain the net shift due to specific binding.

In a second experiment, all four sensor columns were covered with receptor molecules: Hu-IgG, HSA, BSA and biotin-NH<sub>2</sub>. The exact same solutions as in the previous experiment of anti-Hu-IgG and anti-HSA in goat serum were successively pumped through the system. Again the sensors coated with Hu-IgG and HSA responded to their complementary molecules. At the end of the sample running sequence, a solution of goat serum containing 102  $\mu\text{g/ml}$  of avidin and 0.4 mg/ml other proteins was added. The biotin-NH<sub>2</sub> coated sensors responded. From the rather low signals in this experiment, we can conclude that the receptor coverage was not optimal. With sensor surface areas as small as 20  $\mu\text{m}^2$  the requirements in terms of homogeneity are very strict. Further investigation of the coupling parameters is needed to improve receptor density and repeatability.

## 7.6 Conclusion

In this chapter we listed the most important measurement results obtained with the SOI ring resonator biosensor platform. We characterized its response to bulk refractive index changes. A minimum index change of  $10^{-5}$  is detectable. However

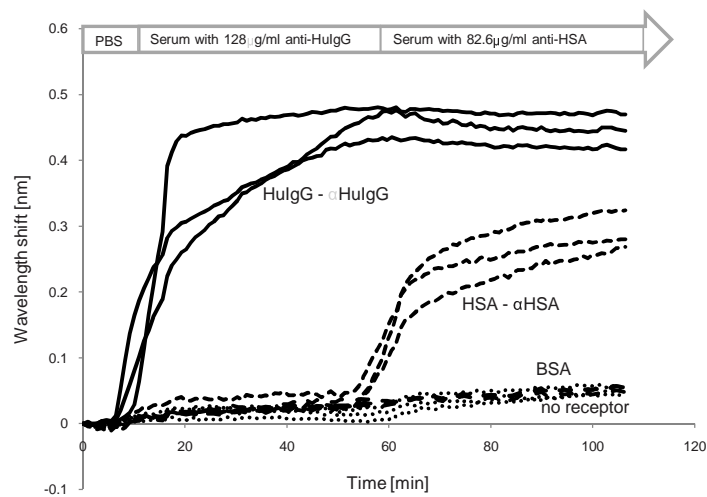


**Figure 7.11:** Experiment with three different receptor molecules spotted on the SOI chip: Hu-IgG, HSA, and BSA. PBS was introduced first to establish the reference. After that, two serums were successively pumped over the sensors. The first serum contained 128 µg/ml anti-Hu-IgG and 1.9 mg/ml other proteins, and the second serum contained 82.6 µg/ml anti-HSA and 1.5 mg/ml other proteins. The resonators spotted with the complementary proteins responded sharply, while the response of the other resonators remained low.

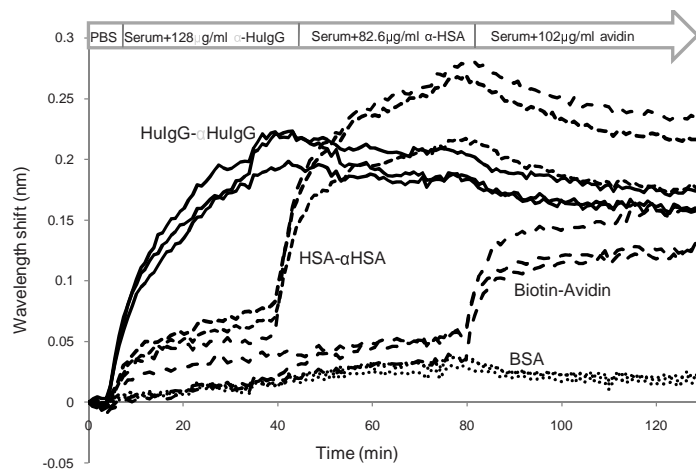


**Figure 7.12:** Experiment with four different receptor molecules spotted on the SOI chip: Hu-IgG, HSA, BSA and biotin-NH<sub>2</sub>. PBS was introduced first to establish the reference. After that, three serums were successively pumped over the sensors. The first serum contained 128 µg/ml anti-Hu-IgG and 1.9 mg/ml other proteins, the second serum contained 82.6 µg/ml anti-HSA and 1.5 mg/ml other proteins and the third serum contained 102 µg/ml avidin and 0.4 mg/ml other proteins. The resonators spotted with the complementary proteins responded sharply, while the response of the other resonators remained low.

this does not directly correspond to the sensor's performance for biomolecular detection. To verify the validity of our understanding of the wavelength shift caused by surface layers with increasing thickness, we compared simulations to measurements of the wavelength shift upon deposition of SiO<sub>2</sub> layers with known parameters. We found a good correlation. The main measurement results that have led to optimization of the surface chemistry are also presented. At first, characterization was performed with the high affinity couple biotin-avidin. We found the system being capable of detecting a few ng/ml avidin concentration. After validation of the coupling chemistry, preventing non-specific interactions of random proteins in the solutions, we coupled proteins other than biotin to the surface. The measurements presented here reveal that careful control of the water content during receptor immobilization was necessary and further optimization needs to be carried out for increased repeatability. With the final coupling procedure, multiple proteins in solution were detected in parallel in two proof-of-principle experiments.

## References

- [1] H. Su and X. G. Huang. *Fresnel-reflection-based fiber sensor for on-line measurement of solute concentration in solutions*. *Sensors and Actuators B-Chemical*, 126:579–582, 2007.
- [2] J. Voros. *The density and refractive index of adsorbing protein layers*. *Biophysical Journal*, 87(1):553–561, 2004.
- [3] Adam L. Washburn, L. Cary Gunn, and Ryan C. Bailey. *Label-Free Quantitation of a Cancer Biomarker in Complex Media Using Silicon Photonic Micro-ring Resonators*. *Analytical Chemistry*, 81(22):9499–9506, 2009.
- [4] E. W. Olle, J. Messamore, M. P. Deogracias, S. D. McClintock, T. D. Anderson, and K. J. Johnson. *Comparison of antibody array substrates and the use of glycerol to normalize spot morphology*. *Experimental and Molecular Pathology*, 79(3):206–209, 2005.

# 8

## Perspectives

Up until now we worked on the development of an integrated biosensor platform with SOI microring resonators. The current system has been characterized theoretically and experimentally. For that, we integrated the chip with microfluidics and implemented it in a read-out system. The knowledge and infrastructure we collected can now serve to improve upon the entire platform. A few suggestions are given in the section 8.1. In section 8.2.2 we discuss the first steps we took towards DNA hybridization monitoring. This fits into a bigger framework where we explore the possibilities of including SOI photonic biosensors in a point-of-care diagnostic system with on-chip sample preparation. In the last section of this chapter, a novel implementation of SOI microring resonator biosensors is introduced. Instead of detection on-chip, we transfer the SOI microrings to the facet of an optical fiber. This does not lead to higher multiplexing or point-of-care systems, but enables in-vivo label-free biosensing.

### **8.1 Towards lower detection limit, higher level of integration and reduced cost**

The detection limit of the platform is in good agreement with the detection limit of most state-of-the-art systems, but for many applications - like cancer diagnostics - a lower detection limit is desired. Instead of ng/ml, detection limits in the order of pg/ml are needed for a broad range of biomarkers. A *lower detection limit* can be obtained by reducing the measurement resolution, or increasing the

sensitivity. Reducing the measurement resolution can be achieved by increasing the resonance Q-factor and reducing the system's noise. Reduction of the wavelength step is another possibility, but that comes with an increased scan time. In chapter 2 we argue that the limitation factor for the Q-factor is the propagation loss caused by water absorption. Changing the working wavelength to 1300 nm can enhance the Q-factor. For noise reduction there are various routes. In a fiber setup, balanced detection has been used by several groups as a means to increase the signal-to-noise ratio [1]. When using an IR camera, noise reduction can be obtained by reduction of background light or analog/digital conversion with a larger number of bits. An enhanced sensitivity would be achieved when measuring with TM polarized light. Grating coupler and ring resonator design would have to be adapted to function optimally for TM polarization. Aside from that, other filter configurations can be studied. In chapter 2, section 2.5, some examples that were proposed in literature are listed. They have to be studied in terms of resolution and sensitivity.

In parallel, *higher levels of integration* are required for development of point-of-care systems. The read-out equipment, still existing of bulky tools like a tunable laser and an IR camera, can be miniaturized and integrated with the chip, preferably at reasonable additional cost. Then, the overall signal-to-noise ratio will have to be reevaluated and optimized. Various routes for passive/active integration are described in chapter 1, section 1.3.3. Integration with active microfluidics is another level of integration. Several laboratory functions can be included on the chip, like cell lysis, sample amplification and dilution or sample cleaning, to end up with a so-called lab-on-a-chip.

As an intermediate step towards *cost reduction*, we could integrate a broadband light source and make use of the directionality of the outcoupling light. This way expensive equipment with high spectral resolution can be omitted. At INTEC, Van Acoleyen et al. study integrated dispersive elements for beam steering using high order arrayed waveguide gratings (AWGs) and grating couplers. We could integrate these devices on one chip with a microring biosensor. Broadband light will be filtered by the ring resonator and send to the AWG. The directionality of the output beam will depend on the central wavelength, which corresponds to the resonance wavelength of the sensor and thus to the molecular concentration. Design and fabrication requirements are not trivial to meet, but after optimization the beam steering could run up to several degrees for wavelength shifts of less than 1 nm. This can be measured with cheap optics. The idea is analogous to a cheap implementation of SPR biosensors named SPREETA, commercialized by Texas Instruments. Using a broad band source and broad beam reflecting to a CCD camera, a cheap hand-held device was developed. This comes at the cost of worse detection limit and low throughput [2].

## 8.2 DNA hybridization

The development of nucleic acids diagnostics has become the subject of intense research. Current methods mainly consists of optical detection using labeled oligonucleotides with dyes [3], quantum dots [4], or enhanced absorption of light by oligonucleotide-modified gold nanoparticles [5]. Label-free methods that offer sensitivity, selectivity, and low cost for the detection of DNA hybridization are under investigation, especially for their implementation in point-of-care diagnostics. We started investigating the ability to monitor DNA hybridization with the SOI ring resonator platform. We successfully attached single stranded DNA (ssDNA) probes to microring resonator surfaces. The chemistry surface functionalization is briefly summarized in section 8.2.1 and ring resonator experiments are discussed in section 8.2.2. Although hybridization experiments were not fully successful yet, an important issue has been uncovered. For the surface modification we collaborated with Dr. Sylvia Wenmackers and Dr. Veronique Vermeeren from the *Institute for Materials Research at Hasselt University*.

In the future, SOI ring resonators will be integrated in point-of-care systems, amongst others during the EC funded project INTOPSENS under FP7. The project aims for point-of-care label-free identification of pathogenic bacteria strains and their antibiotic resistance for fast and low-cost diagnostics of sepsis. Sepsis is a systemic inflammatory response to infection, often associated with organ or multiorgan dysfunction. A diagnostic platform is needed that can quickly identify the presence and type of infectious micro-organisms, as well as the type of antibiotic resistance genes that it carries, so as to be able to proscribe the correct type of antimicrobial treatment.

### 8.2.1 DNA functionalization

The covalent attachment of DNA on silicon was performed through the introduction of -COOH functionalities on the surface followed by EDC-mediated coupling to NH<sub>2</sub>-terminated ssDNA. The modification steps are shown in Fig. 8.1. This procedure was published by Vermeeren et al. in [6]. Instead of coupling silane chains with -COOH end groups like described in chapter 4, for the DNA experiments we explored a different modification route. COOH-terminated lipid acids were attached to -H groups exposed at the silicon surface.

**-H termination** 20 min of SPM<sup>1</sup> and APM<sup>2</sup> standard silicon cleaning was performed first [7]. Then, the substrates are rinsed and dried with nitrogen. The chips are immersed in buffered HF (0.6 vol% HF (40%) in DI water) for 1 min to obtain

<sup>1</sup>SPM: sulfuric-peroxide mixture (4:1 H<sub>2</sub>SO<sub>4</sub> : H<sub>2</sub>O<sub>2</sub>).

<sup>2</sup>APM: ammonia-peroxide mixture (5:1:1 H<sub>2</sub>O : H<sub>2</sub>O<sub>2</sub> : NH<sub>3</sub>).

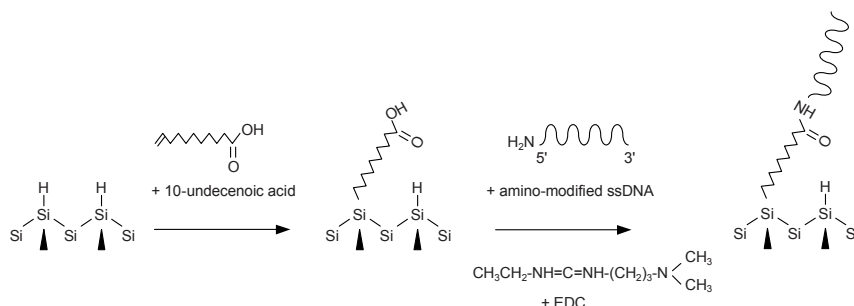


**Figure 8.1:** Schematics of the chemistry functionalization steps for covalent attachment of ssDNA to SOI chips.

-H terminated silicon surfaces. After that, the surfaces are kept in an oxygen-free environment to avoid oxidation.

**-COOH termination** The -H terminated SOI surfaces were covered with pure 10-undecenoic acid (10-UDA), an organic unsaturated fatty acid containing a carboxylic acid (COOH) functionality. The samples were subsequently illuminated for 20 h with 254 nm light from a 4W lamp ( $>2.5 \text{ mW/cm}^2$ ), under a protective nitrogen atmosphere inside a glovebox. The samples were rinsed with hot distilled water.

**DNA functionalization** To establish covalent attachment of  $\text{NH}_2$ -terminated ssDNA to the -COOH terminated samples, they were treated with  $5 \mu\text{mol}$  (0.1 M) of EDC and 30 pmol of  $\text{NH}_2$ -modified ssDNA in a 25 mM MES buffer (pH 6) for 2 h at  $4^\circ\text{C}$ . EDC as an intermediate component to couple  $\text{NH}_2$  to COOH functional groups was described in chapter 4, section 4.3. After incubation, the chips are cleaned with multiple 1xPBS rinsing steps and stored at  $4^\circ\text{C}$ .

## 8.2.2 DNA preliminary results

**Surface modification** To optimize the chemistry procedure described above we performed SOI microring resonator measurements after each modification step. The results presented in Fig. 8.2 are obtained with simultaneous measurement of 15 ring resonators. The output was averaged and standard deviation is indicated. Each bar corresponds to the resonance wavelength after treatment (on dry chips) as compared to a reference measurement on the same chip before treatment. The first bar shows to the resonance wavelength shift after surface cleaning steps, -H termination and attachment of COOH-terminated 10-UDA linkers. After covalent attachment of ssDNA with 8 and 36 base pairs, the output increases as can be observed on the second and the third bar. Together with control by confocal

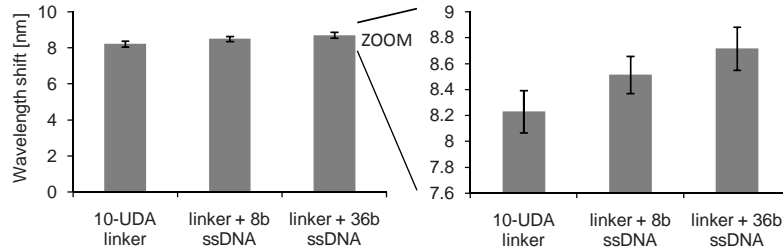


**Figure 8.2:** Ring resonator measurement of different modification steps for covalent attachment of ssDNA probes. The reference level (0 nm shift) was determined before modification. Results are averaged over 15 simultaneously measured rings and standard deviations are indicated.

microscopy using fluorescently labeled probes, this confirms the formation of a ssDNA layer on the ring resonator surface.

**DNA hybridization** For the study of DNA hybridization, we brought the chips in contact with hybridization buffer at elevated temperature (40°C). First, in order to determine the reference wavelength, hybridization buffer without complementary DNA was flown over the chip. We noticed that instead of signal stabilization, there was a large blue resonance shift, see Fig. 8.3. The experiment was performed on 15 ring resonators simultaneously and all results show the same behavior. When comparing a SEM picture of an SOI waveguide before and after immersion in hybridization buffer (Fig. 8.4), we clearly see the aggressive effect of the buffer on the waveguides. Although hybridization seemed to be successful when we performed a control experiment with confocal microscopy using fluorescently labeled DNA, the ring resonator response is dominated by a blue shift induced by waveguide damage. Investigation of the components of commercially available hybridization buffers provides us with a list of possible sources of this effect. A thorough study of the influence of the separate components is ongoing in order to find the source of damage and seek for a way to circumvent the problem.

## 8.3 Fiber probe sensor

### 8.3.1 Motivation

Optical fibers are used extensively as medical devices for viewing hard-to-reach locations, e.g. the endoscope. The property of fibers to conduct light to a remote, convenient location can be used for in-vivo biosensing. Today, commercial optical fiber biosensors require fluorescent or colorimetric labeling of one or more biomolecules [8]. Once the labeled biomolecule has interacted with its target, the

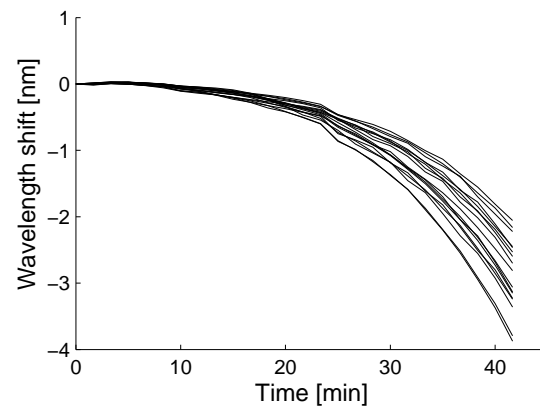


**Figure 8.3:** Wavelength shift when the chip with ssDNA probes is immersed in hybridization buffer. A large blue shift can be observed. Measurements were performed on 15 ring resonators simultaneously.

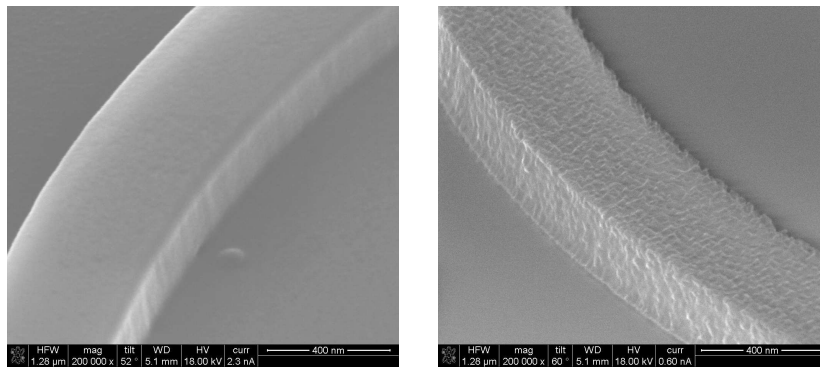


**Figure 8.4:** SEM pictures of an SOI waveguide before and after being immersed in hybridization buffer.

fluorophore is excited by the evanescent wave and the resulting fluorescence is then conducted via the fiber to an analytical device that has been equipped with appropriate wavelength filters. This area is the subject of a recent review [9].

Over the past years, optical fibers have been studied for label-free biosensing as well. They include fiber bragg gratings, long-period grating biosensors, photonic crystal fiber sensors, hollow fibers in a fabry-perot cavity, etc [10, 11]. Most applications, however, focus on bulk refractive index sensing. For biochemical detection, these sensors cannot compete with other types of optical sensors in terms of their detection limits, even though their bulk sensitivity can exceed 100 nm/RIU.

### 8.3.2 Implementation

We propose a configuration that combines the high quality of SOI ring resonator biosensors with the portability of optical fibers. An SOI membrane with integrated ring resonators will be transferred on the facet of a single mode optical fiber and form a ‘fiber probe sensor’. A top view of the design is pictured in Fig. 8.5. The chip is designed to be ‘retroreflective’: using a dedicated light coupling scheme, light will couple into and out of the integrated circuit via the same grating coupler and under the same angle. The fiber core is aligned to a grating coupler, the cladding of the fiber carries the rest of the integrated circuit comprising a 3dB MMI splitter/combiner and a ring resonator biosensor. A curved grating focuses the light onto the SOI waveguide, this circumvents the need for space consuming waveguide tapers [12]. The SOI circuit will be modified with receptor molecules. When immersed in sample solution, the resonance wavelength of the ring resonator will shift when analytes bind to the receptors. This shift is monitored by repeatedly scanning of the spectrum with a tunable laser and detection with a photodetector. As illustrated in Fig. 8.6, source and detector are connected to the device through an optical circulator<sup>3</sup>.

### 8.3.3 Fabrication

In the course of the master thesis work of C. Lerma Arce we studied several routes for fabrication of the device, in particular for the transfer of a structured SOI membrane onto a fiber facet. One of the fabrication routes is illustrated in Fig. 8.7. By making use of a thin spincoated SU-8 layer, the silicon membrane is suspended while etching the silicon oxide layer underneath. After that, the optical fiber is aligned to the grating coupler in an active way, by optimizing the reflected power. In the final step an intermediate glue is cured with UV light. The SOI membrane and the fiber facet form an angle of 10°, corresponding to the angle of optimal

<sup>3</sup>A circulator is a non-reciprocal multiple port device that transmits power entering at a port to the next port.

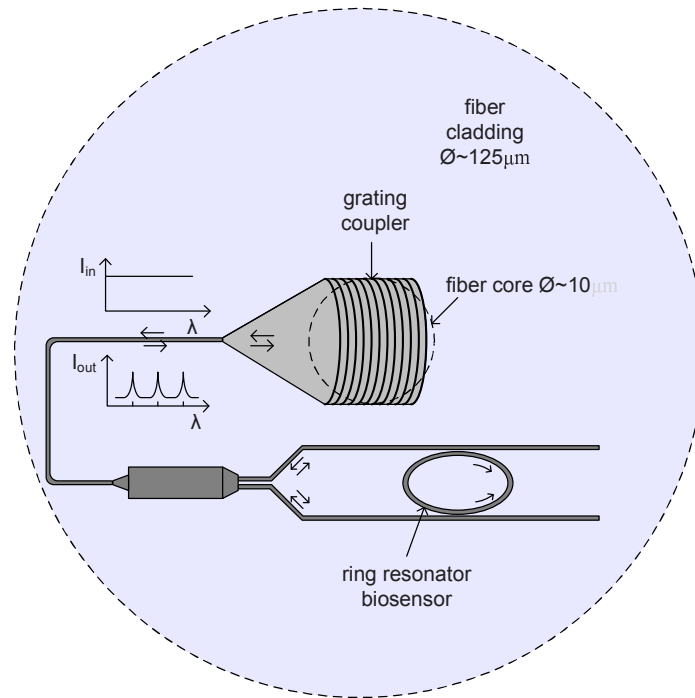


**Figure 8.5:** Top view of an optical fiber probe: a photonic integrated circuit for biosensing aligned to the core of an optical fiber.

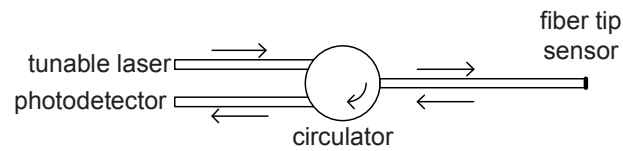


**Figure 8.6:** Optical fiber probe and read-out.

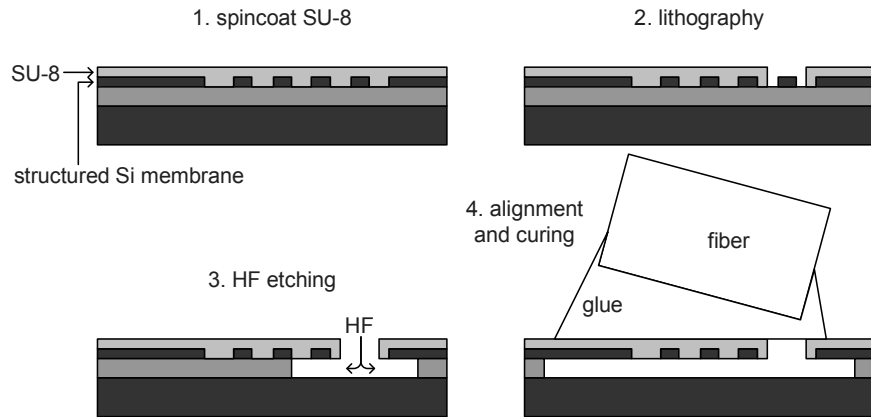


**Figure 8.7:** One of the studied fabrication routes for transfer of a structured SOI chip to a fiber facet.

efficiency and low reflection of the grating. Details on the process steps and measurement results can be found in [13]. Investigation of more efficient fabrication methods that provide a higher yield is ongoing in the PhD thesis of C. Lerma Arce, as well as characterization of the device for biosensing.

## 8.4 Conclusion

We proposed several routes for continuation of this work. So far we studied a single ring resonator biosensor on an SOI photonic chip and built a basic measurement platform for multiplexed detection around it. Now, other filter configurations and better read-out schemes can be developed to obtain lower detection limits. Higher levels of integration, with microfluidics and optoelectronic components, have to be studied as well. Ultimately the photonic chip will be integrated in a point-of-care diagnostic tool. For one specific application, sepsis diagnoses, we started investigation of DNA hybridization monitoring. The last part of this chapter deals with a novel implementation: an integrated SOI circuit is transferred to the facet of a single mode optical fiber. This can lead to a robust and portable device for in-vivo label-free biosensing.

## References

- [1] A. Yalcin, K. C. Papat, J. C. Aldridge, T. A. Desai, J. Hryniewicz, N. Chbouki, B. E. Little, O. King, V. Van, S. Chu, D. Gill, M. Anthes-Washburn, and M. S. Unlu. *Optical sensing of biomolecules using micro-ring resonators*. IEEE Journal of Selected Topics in Quantum Electronics, 12(1):148–155, 2006.
- [2] *Handbook of Surface Plasmon Resonance*. RSC Publishing, Enschede, The Netherlands, 2008.
- [3] A. C. Pease, D. Solas, E. J. Sullivan, M. T. Cronin, C. P. Holmes, and S. P. A. Fodor. *Light-generated oligonucleotide arrays for rapid DNA-sequence analysis*. Proceedings of the National Academy of Sciences of the United States of America, 91(11):5022–5026, 1994.
- [4] D. Gerion, F. Q. Chen, B. Kannan, A. H. Fu, W. J. Parak, D. J. Chen, A. Majumdar, and A. P. Alivisatos. *Room-temperature single-nucleotide polymorphism and multiallele DNA detection using fluorescent nanocrystals and microarrays*. Analytical Chemistry, 75(18):4766–4772, 2003.
- [5] T. A. Taton, C. A. Mirkin, and R. L. Letsinger. *Scanometric DNA array detection with nanoparticle probes*. Science, 289(5485):1757–1760, 2000.
- [6] V. Vermeeren, S. Wenmackers, M. Daenen, K. Haenen, O. A. Williams, M. Ameloot, M. Vandeven, P. Wagner, and L. Michiels. *Topographical and functional characterization of the ssDNA probe layer generated through EDC-mediated covalent attachment to nanocrystalline diamond using fluorescence microscopy*. Langmuir, 24(16):9125–9134, 2008.
- [7] M. Meuris, P. W. Mertens, A. Opdebeeck, H. F. Schmidt, M. Depas, G. Vereecke, M. M. Heyns, and A. Philipossian. *The IMEC clean - A new concept for particle and metal removal on Si surfaces*. Solid State Technology, 38(7):109, 1995.
- [8] J. P. Golden, C. R. Taitt, L. C. Shriver-Lake, Y. S. Shubin, and F. S. Ligler. *A portable automated multianalyte biosensor*. Talanta, 65(5):1078–1085, 2005.
- [9] A. Leung, P. M. Shankar, and R. Mutharasan. *A review of fiber-optic biosensors*. Sensors and Actuators B-Chemical, 125(2):688–703, 2007.
- [10] A. D. Kersey, M. A. Davis, H. J. Patrick, M. LeBlanc, K. P. Koo, C. G. Askins, M. A. Putnam, and E. J. Friebele. *Fiber grating sensors*. Journal of Lightwave Technology, 15(8):1442–1463, 1997.

- 
- [11] X. D. Fan, I. M. White, S. I. Shopoua, H. Y. Zhu, J. D. Suter, and Y. Z. Sun. *Sensitive optical biosensors for unlabeled targets: A review*. *Analytica Chimica Acta*, 620(1-2):8–26, 2008.
- [12] F. Van Laere, W. Bogaerts, P. Dumon, G. Roelkens, D. Van Thourhout, and R. Baets. *Focusing Polarization Diversity Grating Couplers in Silicon-on-Insulator*. *Journal of Lightwave Technology*, 27(5-8):612–618, 2009.
- [13] C. Lerma Arce. *Optical fiber probe sensors for portable and in-vivo detection of biomolecules*. Master thesis, Ghent University, 2008-2009.



# 9

## Conclusions

We studied a label-free biosensor platform based on an integrated SOI photonic circuit, in particular a ring resonator. The photonic circuit was theoretically investigated, fabricated and experimentally tested. In collaboration with the *Polymer Material Research Group* at *Ghent University* with Prof. Em. Etienne Schacht, we investigated silicon surface modification techniques for anchoring receptor molecules to the waveguides. We packaged the photonics chip with PDMS microfluidics and interrogated the sensors with a camera-based parallel read-out setup.

Important features were studied theoretically for optimization of a single micro-ring resonator. The device transduces molecular interaction at its surface into a shift of resonance wavelength, measurable by tracking the resonance peak or dip of its spectrum. The quantities to be studied include the measurement resolution  $\Delta\lambda_{min}$ , the sensitivity and the detection limit.  $\Delta\lambda_{min}$  corresponds to the minimum measurable wavelength shift. It depends on the resonance shape, determined by Q-factor and extinction, and on equipment parameters, determined by noise and wavelength step. The influence of these parameters on  $\Delta\lambda_{min}$  was simulated. We found that  $\Delta\lambda_{min}$  is linearly dependent on the Q-factor, on wavelength noise and on intensity noise squared (sometimes referred to as amplitude noise). It scales on the square root of the wavelength step and is not dependent on the peak extinction ratio for extinction ratios that surpass 15 dB. This means that improving the Q-factor and diminishing the noise will be the most efficient way to enhance the measurement resolution. We found the Q-factor to be limited by the round trip losses in the ring due to water absorption. This is inherent to the sensing mechanism and might be improved by using other working wavelengths, e.g. 1300 nm,

the other telecom wavelength. The sensitivity corresponds to the amount of shift for a unit amount of biomolecular interaction, and is expressed in shift per adlayer, absolute mass or concentration. The inherent device sensitivity (maximum sensitivity) is determined by the fraction of light in the molecular layer. This results in a large sensitivity for high index contrast waveguides. The sensitivity for absolute molecular mass is determined by the sensor's surface area: the smaller the surface area, the fewer molecules are needed to cover the entire sensor, while the resonance wavelength remains the same. A ring resonator with optimal design in a low noise setup is able to detect a minimum layer thickness of less than 1 pm and surface coverage of around 1 pg/mm<sup>2</sup>. This corresponds to a detection limit of 100 molecules with medium weight like avidin.

The material platform of choice, silicon-on-insulator, provides a high index contrast, leading to dense integration of components and high sensitivity biosensors. On top of that, it offers the advantage of reuse of extensively developed CMOS processing technology. Fabrication of photonic chips with nanoscale reliability and with no extra equipment development cost is a major asset for SOI biosensors. It allows for mass production and economics of scale.

We presented a novel method that allows to extract more information on biomolecular interaction with a single ring resonator. Interrogation of the wavelength shift of two orthonally resonating modes provides us with the thickness as well as with the refractive index of a layer at the sensor surface. This can be translated in real-time information on the molecular density and thus on the conformation of the molecules which is crucial in many genomics and proteomics applications. The error on resolving thickness and index of the layer depends on the actual thickness and index values, but is always lower than 0.11% on the index and 4% on the thickness (when the layer index > 1.40).

The inherent biosensor sensitivity can be reduced when the receptor molecule density is not optimal. Thus, the properties of a biosensor critically depend on the quality of the receptor layer, especially for detection in complex samples. The interfacial layer has to allow for immobilization of receptor molecules and at the same time effectively block non-specific interactions with the macromolecular components of the analyzed sample. In addition it must be stable, must not affect the transducer sensitivity and must not hinder transport of the chemical or biological compounds to the transducer surface. Silanization of a silicon oxide layer on top of the silicon waveguide is a straightforward coupling procedure for dense receptor coverage. However, silanes perform poorly in terms of non-specific interactions with proteins in the analyte solution. To reduce the non-specific interaction, we introduced thin PEG layers in a two-step coupling procedure. We investigated two heterobifunctional PEG layers with different reactive groups:  $\alpha$ -sulfanyl- $\omega$ -carboxy PEG (HS-PEG-COOH) and monoprotected diamino-PEG (H<sub>2</sub>N-PEG-NH-Boc). Surface characterization tests confirmed the

high quality, the reproducibility and the binding capacity of PEG layers. The thickness is in the order of a few nanometers. The contact angle was as low as  $21^\circ$  and  $31^\circ$  for both PEG coatings, while the density of the functional groups remained high.

After chemical modification of the surface, the chip is packaged with PDMS microfluidics that serve to deliver the analytes. In order not to damage the fragile biomolecules on the sensor, no high temperatures or surface activation methods can be applied during the packaging step. This implies the use of adhesive bonding with an intermediate glue. To avoid contact between biomolecules and the glue, we use a stamp-and-stick bonding process. For the current concentration detection limit ( $\approx 10\text{pM}$ ), the time to accumulate a threshold number of molecules for sensing is not a limiting factor.

Measuring the spectrum of a ring resonator biosensor was performed with a number of read-out systems. They differ in light source (monochromatic or broadband), detection (spectrum analyzer, photodetector or CCD camera) or light guiding (fiber or free-space). The read-out system of an integrated optical biosensor is fundamentally different from the read-out system of commercial free-space biosensors like Biacore@SPR. The read-out is completely decoupled from the detection, offering a much higher degree of multiplexing and a much higher alignment tolerance. The latter is important for portable applications and considerably reduces the cost of the overall system. Flood illumination and detection with an IR camera offers a good trade-off between high degree of multiplexing and low noise. Using the platform we described we performed a number of experiments to characterize the SOI microring biosensor. Avidin/biotin was initially used as a model biomolecular pair. The detection limit of the system was determined to be around  $3.8\text{ ng/ml}$ . Once the platform was found to be stable, we performed multiplexed protein detection experiments. An array of microrings was covered homogeneously with a PEG layer, on top of which different proteins were spotted on different ring resonators. After packaging with PDMS microfluidics, different diluted serums were flown over the biochip. Each analyte could be detected with high specificity. Now that a basic biosensor platform has been installed and SOI microring biosensors have been characterized, other filter configurations and better read-out schemes can be developed to obtain lower detection limits. Higher levels of integration, with microfluidics and optoelectronic components, have to be investigated as well. This will ultimately lead to integration of a disposable SOI photonics biochip in a point-of-care diagnostic tool.





# Microfluidics processing

## A.1 Introduction

Optimization of the fabrication and bonding of PDMS microfluidics went along with many trial and error phases. This appendix describes the final method that we believe can be applied with high reproducibility and yield. The first section lists the steps for fabrication of the PDMS part. It consists of 1) fabrication of the mold, and 2) casting of the PDMS. In a section step (section A.3, the surfaces are prepared for bonding. As explained in chapter 5, section 5.3 we developed two bonding methods: direct bonding at high temperature and adhesive bonding with a stamp-and-stick procedure. Depending on the bonding procedure of choice, different surface preparation steps are required. Section A.4 lists the actual bonding steps for both procedures.

## A.2 PDMS microfluidics fabrication

### Step 1: master mold fabrication

1. SU-8 lithography
  - Spin coat SU-8 50 at 500 rpm for 5 sec, then at 3000 rpm for 40 sec
  - Prebake at 65°C for 6 min, then at 95°C for 6 min
  - Exposure at 25000 mJ for 500 sec

- Postbake at 65°C for 6 min, then at 105°C for 6 min
  - Develop with SU-8 developing reagent
2. Anti-adhesion treatment with fluorinated silanes. Place a very small drop of fluorinated silanes ( $C_8H_4Cl_3F_13Si$ ) on the side of the wafer, and let evaporate overnight in a desiccator. Clean with DI water and IPA. The silicon wafer with SU-8 structures is hydrophobic now.

### Step 2: PDMS microfluidics fabrication

1. Weight PDMS and curing agent in a plastic cup. 10:1 mass ratio (ex. 30g PDMS + 3g curing agent)
2. Mix well (use kitchen mixer, clean it immediately afterwards with acetone)
3. Degas in desiccator
4. Pour on silicon/SU-8 mold
5. Degas in desiccator
6. Cure on hot plate (about 1,5 hours at 60C, depending on the thickness of the PDMS)
7. Punch holes with flat needle (pink needles)
8. Cut out the PDMS with a razor blade
9. Remove the PDMS at the holes

## A.3 Surface preparation

### Step 3 for stamp-and-stick procedure

- SOI chip: dry
- PDMS
  1. 5 min ultrasonic cleaning in DI water
  2. 5 min ultrasonic cleaning in isopropyl alcohol (IPA)
  3. 30 sec drying at high temperature
  4. Oxygen plasma treatment (ICP/RIE parameters: 15 sec, 70W, 75 mTorr plasma pressure, 20 sccm oxygen flow rate, program O2Katrien. RIE parameters: power 400 W, flow 500 sccm, time 0.3 min.)

**Step 3 for direct bonding procedure**

- SOI chip: dry
  1. 5min piranha etching ( $\text{H}_2\text{SO}_4$  :  $\text{H}_2\text{O}_2$  in 7:3 ratio)
  2. Aceton, IPA, DI water cleaning
  3. Dry with argon flow
  4. Oxygen plasma treatment (ICP/RIE parameters: 15 sec, 70W, 75 mTorr plasma pressure, 20 sccm oxygen flow rate, program O2Katrien. RIE parameters: RIE parameters: power 400 W, flow 500 sccm, time 0.3 min.)
- PDMS
  1. 5 min ultrasonic cleaning in DI water
  2. 5 min ultrasonic cleaning in IPA
  3. 30 sec drying at high temperature
  4. Oxygen plasma treatment (ICP/RIE parameters: 15 sec, 70W, 75 mTorr plasma pressure, 20 sccm oxygen flow rate, program O2Katrien. RIE parameters: RIE parameters: power 400 W, flow 500 sccm, time 0.3 min.)

**A.4 Bonding****Step 4 for stamp-and-stick procedure**

1. Spincoat SU8-10 on flat, clean Si substrate (50 sec at 4000rpm)
2. Place PDMS on bottom holder of flip-chip machine, channel side up (put glass plate underneath, to keep the machine clean).
3. Place Substrate with glue on top holder of flip-chip machine (use vacuum to seal).
4. Gently make contact between both surfaces and release.
5. Run 'stamp-and-stick' program (+/- 30 sec at 60°C to evaporate solvents of glue on PDMS chip).
6. Place SOI chip on top holder of flip-chip machine.
7. Align surfaces to each other (zoom out as far as possible)
8. Make contact
9. Take glass plate with the entire structure out of the flip-chip machine and cure with UV lamp (+/- 160 sec)

**Step 4 for direct bonding procedure**

1. Place PDMS on bottom holder of flip-chip machine, channel side up (put blue plastic foil under PDMS to make sure the PDMS does not stick to the holder after bonding).
2. Place SOI chip on top holder of flip-chip machine
3. Align surfaces to each other (zoom out as far as possible)
4. Make contact with 20 N force
5. Run 'PDMS' program (45 min at 110°C top holder/135° bottom holder)

# B

## Publications

### **B.1 Patent applications**

R. Baets, W. Bogaerts, K. De Vos, S. Scheerlinck, Retro-reflective structures, WO 2009/156410 A1.

### **B.2 International Journals**

1. W. Bogaerts, S. Selvaraja, P. Dumon, J. Brouckaert, K. De Vos, D. Van Thourhout, R. Baets, "Silicon-on-Insulator Spectral Filters Fabricated with CMOS Technology", *J. Sel. Top. Quantum Electron.*, 16(1), pp. 33-44 (2010).
2. K. De Vos, Jordi Girones Molera, T. Claes, Y. De Koninck, Stepan Popelka, Etienne Schacht, R. Baets, P. Bienstman, "Multiplexed antibody detection with an array of silicon-on-insulator microring resonators", *IEEE Photonics Journal*, 1(4), pp. 225-235 (2009).
3. T. Claes, J. Girones Molera, K. De Vos, E. Schacht, R. Baets, P. Bienstman, "Label-Free Biosensing With a Slot-Waveguide-Based Ring Resonator in Silicon on Insulator", *IEEE Photonics Journal*, 1(3), pp. 197-204 (2009).
4. K. De Vos, J. Girones, S. Popelka, E. Schacht, R. Baets, P. Bienstman, "SOI optical microring resonator with poly(ethylene glycol) polymer brush for label-free biosensor applications", *Biosensors and Bioelectronics*, 24(8), pp.

2528-2533 (2009).

5. J. Schrauwen, J. Van Lysebettens, T. Claes, K. De Vos, P. Bienstman, D. Van Thourhout, R. Baets, "Focused-ion-beam fabrication of slots in silicon waveguides and ring resonators", *IEEE Photonics Technology Letters*, 20(23), pp. 2004 (2008).
6. K. De Vos, I. Bartolozzi, E. Schacht, P. Bienstman, R. Baets, "Silicon-on-Insulator microring resonator for sensitive and label-free biosensing", *Optics Express*, 15(12), pp. 7610-7615 (2007).

### B.3 International Conferences

7. D. Vermeulen, K. Van Acoleyen, S. Ghosh, S. Selvaraja, W.A.D. De Cort, N.A. Yebo, E. Hallynck, K. De Vos, P.P.P. Debackere, P. Dumon, W. Bogaerts, G. Roelkens, D. Van Thourhout, R. Baets, "Efficient Tapering to the Fundamental Quasi-TM Mode in Asymmetrical Waveguides", accepted for publication in ECIO, United Kingdom, (2010).
8. K. De Vos, J. Girones, T. Claes, E. Schacht, R. Baets, P. Bienstman, "High throughput label-free biosensing with silicon-on-insulator microring resonators", Europt(r)ode X , Czech Republic, (2010).
9. K. De Vos, J. Girones Molera, Y. De Koninck, E. Schacht, R. Baets, P. Bienstman, "Multiplexed protein detection with an array of silicon-on-insulator microring resonators", 22nd Annual Meeting of the IEEE Photonics Society, Turkey, pp. 457-458 (2009).
10. S. Selvaraja, K. De Vos, W. Bogaerts, P. Bienstman, D. Van Thourhout, R. Baets, "Effect of Device Density on the Uniformity of Silicon Nanophotonic Waveguide Devices", The 22nd Annual Meeting of the IEEE Photonics Society, Turkey, pp. 311-312 (2009).
11. K. De Vos, P.P.P. Debackere, T. Claes, J. Girones, W.A.D. De Cort, E. Schacht, R. Baets, P. Bienstman, "Label-free biosensors on silicon-on-insulator optical chips", *SPIE Optics and Photonics*, 7397(37), United States, (2009).
12. P. Bienstman, K. De Vos, T. Claes, P.P.P. Debackere, R. Baets, J. Girones, E. Schacht, "Biosensors in silicon on insulator", *Proceedings of SPIE Photonics West 2009-OPTO: Integrated Optoelectronics Devices*, 7220, United States, pp. 722000 (9 pages) (2009).
13. T. Claes, J. Girones, K. De Vos, P. Bienstman, R. Baets, "Label-free biosensing with silicon-on-insulator slotted racetrack resonator", *Proceedings Annual Symposium of the IEEE/LEOS Benelux Chapter*, 2008, Netherlands,

pp. 23-26 (2008).

14. G. Roelkens, W. Bogaerts, D. Taillaert, P. Dumon, L. Liu, S. Selvaraja, J. Brouckaert, J. Van Campenhout, K. De Vos, P.P.P. Debackere, D. Van Thourhout, R. Baets, "Silicon nanophotonics: towards VLSI photonic integrated circuits", URSI, United States, (2008).
15. K. De Vos, P.P.P. Debackere, R. Baets, P. Bienstman, "Label-free biosensors on Silicon-on-Insulator optical chips based on microring cavities and surface plasmon interferometry", ICTON 2008, 2, Greece, pp. 88-91 (2008).
16. W. Bogaerts, P. Dumon, J. Brouckaert, K. De Vos, D. Taillaert, D. Van Thourhout, R. Baets, "Ultra-compact optical filters in Silicon-on-Insulator and their Applications", Group IV Photonics, Japan, pp. WA1 (2007).
17. P.P.P. Debackere, K. De Vos, S. Scheerlinck, P. Bienstman, R. Baets, "Silicon-on-Insulator as a Platform for Biosensors", Frontiers research Meeting, (2007).
18. K. De Vos, I. Bartolozzi, D. Taillaert, W. Bogaerts, P. Bienstman, R. Baets, E. Schacht, "Optical biosensor based on silicon-on-insulator microring cavities for specific protein detection", Proc. of SPIE Photonics West (BiOS), 6447, United States, pp. 6447DK-1 (2007).
19. P.P.P. Debackere, D. Taillaert, S. Scheerlinck, K. De Vos, P. Bienstman, R. Baets, "Si based waveguide and surface plasmon sensors", Photonics West 2007: Silicon Photonics II, 6477, United States, pp. 647719 (2007).
20. K. De Vos, I. Bartolozzi, P. Bienstman, R. Baets, E. Schacht, "Optical Biosensor based on Silicon-on-Insulator Microring Resonators for Specific Protein Binding Detection", LEOS Benelux Annual Symposium, Netherlands, (2006).
21. P. Bienstman, P. Dumon, W. Bogaerts, D. Taillaert, F. Van Laere, K. De Vos, D. Van Thourhout, R. Baets, "Silicon nanophotonics using deep-UV lithography", APOC 2006, 6351(99), South Korea, (2006).
22. P. Bienstman, F. Van Laere, D. Taillaert, P. Dumon, W. Bogaerts, K. De Vos, D. Van Thourhout, R. Baets, "High index-contrast silicon-on-insulator nanophotonics", ICTON, United Kingdom, pp. Tu.D2.1 (2006).
23. K. De Vos, I. Bartolozzi, P. Dumon, S. Scheerlinck, W. Bogaerts, D. Taillaert, E. Schacht, P. Bienstman, R. Baets, "Silicon-on-Insulator Microring for Label-Free Biosensing", NanoBioEurope, France, (2006).
24. P. Bienstman, F. Van Laere, D. Taillaert, P. Dumon, W. Bogaerts, K. De Vos, D. Van Thourhout, R. Baets, "High index-contrast silicon-on-insulator nanophotonics", PPCM, Belgium, pp. 4 (2006).

25. K. De Vos, P. Bienstman, R. Baets, "Label-free biosensor based on active and passive resonant cavities", ePIXnet Winter School, Optoelectronic Integration - Technology and Applications, Switzerland, pp. 76 (2006).

## **B.4 National Conferences**

26. K. De Vos, J. Girones, R. Baets, P. Bienstman, "Photonics microring biosensor platform", PhD Symposium, Belgium, (2008).
27. K. De Vos, I. Bartolozzi, P. Bienstman, R. Baets, E. Schacht, "Optical Biosensor based on Silicon-on-Insulator Microring Resonators for Specific Protein Binding Detection", PhD Symposium, Belgium, (2006).